

Multi-disciplinary modelling of the  
aerothermodynamically-induced fragmentation of  
re-entering bodies

PhD Thesis

Fábio Morgado

Aerospace Centre of Excellence

Department of Mechanical and Aerospace Engineering (MAE)

University of Strathclyde, Glasgow

June 1, 2025

This thesis is the result of the author's original research. It has been composed by the author and has not been previously submitted for examination which has led to the award of a degree.

The copyright of this thesis belongs to the author under the terms of the United Kingdom Copyright Acts as qualified by University of Strathclyde Regulation 3.50. Due acknowledgement must always be made of the use of any material contained in, or derived from, this thesis.

# Abstract

A globally proposed solution to remove objects from space is to make them undergo destructive atmospheric re-entry, through which they break into several fragments, eventually demising due to the high aerothermal loads experienced during the re-entry process. Therefore, accurate prediction of the destructive process and trajectory dynamics is of utmost importance to determine the re-entry safety. However, most state-of-the-art prediction tools use engineering and surrogate models that cannot capture the collision dynamics and occurring flow interactions formed by the proximity of multiple fragments in high-enthalpy regimes.

To overcome this issue, this work presents the development of a multi-fidelity based tool *TITAN* (TransatmosphEric flighT simulATIoN). The tool handles the fragments using a common spatial domain to account for the interactions due to proximity. It also employs an automated criterion to identify the level of fidelity required at each time step, enabling switching between low-fidelity and high-fidelity models to compute the aerodynamic and aerothermodynamic quantities during the reentry process. A detailed description of the framework is introduced in this work, along with various experimental and numerical test cases to verify and validate the implemented submodules, aimed to deliver the capability to perform a complete simulation from the reentry interface until the ground collision. The dynamic motion of the objects is computed using the integrated 6 Degrees of Freedom (DoF) trajectory propagator under a quasi-steady assumption, enabling the analysis of the individual fragment trajectory. The framework is finally tested against two conceptual re-entry spacecraft, and an analysis of debris dispersion due to proximity interaction is conducted.

# Acknowledgements

I would like to thank my supervisor, Dr. Marco Fossati, for this research opportunity. I am grateful for his advice and expertise, insightful feedback, and support, which were invaluable in shaping this thesis and my academic journey. Additionally, this work would not have been possible without the European Space Agency's (ESA) support through the OSIP program that co-funded the PhD (with the contract number ESA Contract No. 4000130436/20/NL/MH/ac).

My deepest appreciation goes to Dr. Thierry Magin and Dr. Cristina de Persis for their support and guidance on this project since the start. Your expertise has been invaluable for the progress of this PhD project.

I am forever grateful to my family and partner for all their support and patience over the past years. Without you, I would not have concluded this work. Thank you for believing in me, especially during the times when I doubted myself.

Finally, to the friends I met along the way, thank you for all the wonderful moments and experiences we shared. You made my days in Scotland a lot brighter and inspired me to become the person I am today.

# Contents

<b>Abstract</b>	<b>ii</b>
<b>Acknowledgements</b>	<b>iii</b>
<b>List of Figures</b>	<b>vii</b>
<b>List of Tables</b>	<b>xiii</b>
<b>1 Introduction</b>	<b>2</b>
1.1 Motivation . . . . .	2
1.2 Challenges and Research Questions . . . . .	5
1.3 Advantages of a multi-fidelity methodology . . . . .	7
1.4 Thesis Layout . . . . .	8
1.5 Publications . . . . .	9
1.5.1 Conferences . . . . .	9
1.5.2 Journals . . . . .	10
<b>2 Physics of Atmospheric Entry</b>	<b>11</b>
2.1 Atmospheric environment . . . . .	11
2.2 Physics of high-speed atmospheric re-entry . . . . .	13
2.2.1 Flow regime classification . . . . .	13
2.2.2 High-temperature effects during re-entry . . . . .	16
2.2.3 Free-molecular regime . . . . .	20
2.2.4 Continuum regime . . . . .	27

<b>3</b>	<b>Atmospheric Re-entry Analysis</b>	<b>37</b>
3.1	Key Modules for Destructive Re-entry Analysis Tools . . . . .	39
3.1.1	Geometry Modelling . . . . .	40
3.1.2	Flight Dynamics Trajectory Modelling . . . . .	40
3.1.3	Aerodynamics and Aerothermodynamics Modelling . . . . .	41
3.1.4	Structural and Fragmentation Analysis . . . . .	42
3.1.5	Thermal Analysis . . . . .	42
3.2	High-fidelity Modelling for Re-entry Analysis . . . . .	43
3.3	Inclusion of Multi-fidelity for Re-entry Analysis . . . . .	44
3.3.1	A Physics-Informed Multi-Fidelity Switch . . . . .	44
3.3.2	Billig Shock-Envelope . . . . .	46
<b>4</b>	<b>Development of a Reentry Framework</b>	<b>51</b>
4.1	Spacecraft Modelling . . . . .	52
4.1.1	Surface Mesh Handler . . . . .	54
4.1.2	Mass and Inertia . . . . .	57
4.2	Aerodynamics and Aerothermodynamics Computation . . . . .	60
4.2.1	Flow Properties Calculation . . . . .	60
4.2.2	Panel Shadowing . . . . .	63
4.2.3	Aerodynamics Calculation . . . . .	66
4.2.4	Aerothermodynamics Calculation . . . . .	68
4.3	Trajectory Dynamics . . . . .	70
4.4	Collision Dynamics . . . . .	72
4.5	Thermal and ablation modelling . . . . .	74
4.6	Material modelling . . . . .	75
4.7	Structural Analysis . . . . .	76
4.8	Verification and Validation cases . . . . .	79
4.8.1	Aerodynamic and Aerothermodynamic . . . . .	79
4.8.2	Stagnation Heat Transfer for Partially Catalytic Wall . . . . .	85
4.8.3	Structural Analysis Validation . . . . .	90
4.8.4	Collision Dynamics Validation . . . . .	93

<b>5</b>	<b>Integration of a High-fidelity Fluid Solver for Proximal Aerodynamics</b>	<b>98</b>
	<b>Interaction</b>	<b>98</b>
5.1	Coupling of SU2-NEMO and Mesh Adaptation . . . . .	99
5.1.1	Verification of Anisotropic Adaptation in Hypersonic Flows . . .	104
5.2	A Quasi-Steady Approach for the Aerothermodynamic Interaction . . .	113
5.2.1	Numerical reconstruction of two-sphere dynamical separation . .	113
5.2.2	Numerical reconstruction of a shock-interfered free flying ring . .	117
5.3	Validation of the Multi-Fidelity Criteria . . . . .	124
<b>6</b>	<b>Application to Spacecraft re-entry</b>	<b>129</b>
6.1	Automated Transfer Vehicle . . . . .	129
6.2	Attitude and Vernier Upper Module . . . . .	134
<b>7</b>	<b>Conclusions</b>	<b>141</b>
7.1	Future Work . . . . .	146
7.1.1	Improving the ablation model . . . . .	148
7.1.2	Uncertainty quantification . . . . .	148
<b>A</b>	<b>Tools for Re-Entry Simulation</b>	<b>149</b>
A.1	Object-Oriented tools . . . . .	149
A.1.1	DAS/ORSAT . . . . .	149
A.1.2	DRAMA/SESAM . . . . .	153
A.1.3	DEBRISK . . . . .	155
A.2	Spacecraft-Oriented tools . . . . .	156
A.2.1	SCARAB . . . . .	156
A.2.2	PAMPERO . . . . .	161
A.3	Hybrid tools . . . . .	163
A.3.1	FOSTRAD . . . . .	163
A.3.2	SAMj . . . . .	165
<b>B</b>	<b>Inertial tensor of a tetrahedron</b>	<b>167</b>

Contents

<b>C SU2-NEMO and anisotropic adaptation</b>	<b>169</b>
C.1 The open-source solver SU2-NEMO . . . . .	169
C.1.1 Governing equations and physical models . . . . .	170
C.1.2 Inviscid Flux Scheme . . . . .	172
C.2 Adaptive Mesh Generation . . . . .	174
<b>D 2D cases for anisotropic mesh validation in hypersonic flow</b>	<b>176</b>
D.1 2D Single Cylinder . . . . .	176
D.2 2D Proximal Cylinders . . . . .	180
<b>Bibliography</b>	<b>186</b>

# List of Figures

1.1	Evolution of the launch traffic near LEO <sub>IADC</sub> per mission funding (from [ESA Space Debris Office, 2023]). . . . .	3
2.1	Atmospheric layers and properties as a function of altitude (from [Hirschel, 2004]) . . . . .	12
2.2	Molecular dissociation, vibrational excitation and ionization for air as a function of altitude and velocity [Anderson, 2006]. . . . .	17
2.3	Effect of the wall catalycity on atoms recombination (from [Bertin, 1994]).	18
2.4	Coordinate system for surface element in free molecule flow (from [Hayes and Probstein, 1959]). . . . .	26
2.5	Typical re-entry flowfield (from [Etkin, 1972]). . . . .	27
2.6	Schematic for Newtonian impact theory (from [Anderson, 2006]). . . . .	28
2.7	Stagnation flow past a blunt body (from [Goulard, 1958]). . . . .	31
2.8	Shock stand-off distance on spheres versus density ratio and free-stream Mach number (from [Olivier, 1995]). . . . .	36
3.1	Flowchart of the multi-fidelity aerothermal modelling. . . . .	45
3.2	Visualization of the virtual sphere and the equivalent shock envelope for a cube geometry. . . . .	48
3.3	Shock envelope for cubic geometry at Mach 9.3 . . . . .	48
3.4	Shock envelope for cylindrical geometry at Mach 9.3 . . . . .	49
3.5	Representation of the sphere positioning in relation to the shock envelope.	50
4.1	High-level overview of TITAN modules flowchart. . . . .	52

## List of Figures

4.2	Overview of the primitive-joint concept in the geometry modelling of a spacecraft. . . . .	54
4.3	Illustration of a sphere subdivision into several components to increase simulation fidelity. . . . .	54
4.4	Transformation $\mathbf{g}$ and $\mathbf{g}^{-1}$ (from [Tonon, 2005]). . . . .	59
4.5	Computation of mixture properties at free-stream, boundary layer edge and wall locations using Mutation++. . . . .	62
4.6	Occlusion culling depth-sorting methodology illustration. . . . .	64
4.7	Depth-sorting methodology applied to the ATV spacecraft. . . . .	64
4.8	Comparison of pressure distribution obtained using the depth-sort algorithm (middle) and the ray-casting algorithm (right) over a sphere with a fine discretization at the stagnation area. . . . .	65
4.9	Facet subdivision for partial occlusion assessment. . . . .	66
4.10	Schematic of objects and respective collision mesh at the moment of impact. . . . .	72
4.11	Material database information flow. . . . .	76
4.12	Example of the superposition method for two cubes attached with a cylindrical joint. . . . .	78
4.13	Comparison of aerodynamic and aerothermal coefficient deviation concerning the reference DSMC solution. . . . .	81
4.14	a) Pressure and heat-flux surface distribution from sphere stagnation point at 90 km . . . . .	81
4.15	b) Pressure and heat-flux surface distribution from sphere stagnation point at 130 km . . . . .	82
4.16	c) Pressure and heat-flux surface distribution from sphere stagnation point at 200 km . . . . .	82
4.17	Pressure and heat-flux distribution for the hollow hemisphere. . . . .	83
4.18	ARD geometrical configuration [Walpot, 2002] in mm. . . . .	84
4.19	Pressure and heat-flux distribution for the ARD capsule. . . . .	84

## List of Figures

4.20	Stagnation line results for sphere with radius $R = 0.5$ m and heat flux prediction using the low-fidelity models. . . . .	87
4.21	Species molar fraction at stagnation line assuming non-catalytic wall for a sphere with radius $R = 0.5$ m. . . . .	88
4.22	Stagnation line results for sphere with radius $R = 0.05$ m and heat flux prediction using the low-fidelity models. . . . .	88
4.23	Species molar fraction at stagnation line assuming non-catalytic wall for a sphere with radius $R = 0.05$ m. . . . .	89
4.24	Heat flux at the stagnation point for the sphere with radius $R = 0.05$ m, using the boundary layer edge conditions from the stagnation line code. . . . .	89
4.25	Volume mesh with subdomain decomposition generated using GMSH. . . . .	90
4.26	Pressure distribution, displacement and von Mises solution on ATV geometry at an altitude of 82 km. . . . .	92
4.27	Evolution of the joint temperature and stress during re-entry. . . . .	92
4.28	Sphere-sphere collision arrangement. . . . .	93
4.29	Sphere-Sphere collision . . . . .	94
4.30	Multi-sphere collision arrangement. . . . .	95
4.31	Multi-sphere collision results. . . . .	95
4.32	Setup and results for the sphere-rod collision case. . . . .	96
4.33	Setup and results for the puck-wall collision case. . . . .	97
5.1	Flowchart of the quasi-steady approach for high-fidelity modelling. . . . .	100
5.2	Grid adaptation for a ring with $45^\circ$ angle of attack. . . . .	103
5.3	Ring aerodynamic coefficients for different angles of attack. . . . .	103
5.4	Heat flux (left) and pressure (right) contours of the single sphere case for different levels of adaptation (Top figures correspond to the first grid and bottom figures correspond to the final adapted grid). . . . .	106
5.5	Contours of normalized y- velocity $[v/u_2]$ (left) and z- velocity $[w/u_2]$ (right) components contours of the single sphere case for different levels of adaptation (Top figures correspond to the first grid and bottom figures correspond to the final adapted grid). . . . .	107

List of Figures

5.6 Heat flux (left) and pressure (right) plots of the different anisotropic grids for the +y and +z plane (Top figures correspond to the first adapted grid and bottom figures correspond to the final adapted grid). . . . . 109

5.7 Geometry configuration of the three-dimensional two-spheres case. . . . 110

5.8 Detailed visualization of the final anisotropic grid used for the two-spheres case. . . . . 110

5.9 Schlieren and Mach contours of the two-spheres case for different levels of adaptation (Top figures correspond to the first grid and bottom figures correspond to the last adapted grid). . . . . 111

5.10 Experimental Schlieren (left) and superposition of experimental and numerical Schlieren in green (right) at the shock-shock interaction region. 112

5.11 Pressure plot at the symmetry plane of the aft sphere. . . . . 113

5.12 Pressure contour at the surface of the aft sphere. . . . . 113

5.13 Schematic of the configuration setup and reference frame. . . . . 114

5.14 Visualization of the final adapted grid and pressure distribution at  $t' = 0, 1.04, 2.08$  and  $3.16$ . . . . . 116

5.15 Comparison of experimental Schlieren and numerical sphere position and shock front for  $t' = 0$  (left) and  $t' = 1.66$  (right) [Laurence et al., 2012]. 116

5.16 Drag coefficient (left) and Lift coefficient (right). . . . . 117

5.17 Model arrangement of the free-flight ring and steady crossflow cylinder test case. . . . . 118

5.18 Evolution of the freestream flow conditions during the useful test duration of the experiment. . . . . 119

5.19 Visualization of anisotropic grid adaptation for  $t = 10$  ms. . . . . 120

5.20 Pressure distribution over the ring's surface and correspondent last level of mesh adaptation for several instants of time. . . . . 122

5.21 Aerodynamic coefficients for different instants of time. . . . . 124

5.22 Position and attitude evolution of the ring. . . . . 125

5.23 Simplified conceptual geometry configuration of the ATV for methodology validation. . . . . 126

## List of Figures

5.24	Solar panel forces and moments comparison. . . . .	127
5.25	ATV dynamics after fragmentation. . . . .	128
6.1	ATV geometry and surface mesh details. . . . .	130
6.2	Parameters evolution until fragmentation event. . . . .	131
6.3	Post-fragmentation fidelity management. . . . .	132
6.4	High-fidelity (left) and low-fidelity (right) pressure distribution comparison. . . . .	132
6.5	Fragments disposition comparison after 5 seconds of simulation (distance in meters). . . . .	133
6.6	High-fidelity solution after 5 seconds of simulation, at 92 km of altitude. . . . .	133
6.7	AVUM model used in the re-entry simulation. . . . .	135
6.8	AVUM snapshots after skirt demise (Left panel accounts for collision, Right panel neglects collision). . . . .	137
6.9	Impact location of surviving components of the AVUM . . . . .	138
6.10	Pressure distribution over the surface of the fragments using the quasi-steady propagation with high-fidelity computation (left) and low-fidelity methods (right), and Mach distribution over a slice of the adapted mesh instants after the release of the titanium tanks. . . . .	140
A.1	Parent-child relationship of nested components in the DAS 3.0 re-entry assessment (from [Liou et al., 2021]). . . . .	150
A.2	SESAM High-level System Context (from [Kanzler et al., 2017]) . . . . .	154
A.3	Shadow analysis schematic (from [Lips et al., 2007]). . . . .	159
A.4	Heat flow balance for wall surface panel (from [Koppenwallner et al., 2005]). . . . .	160
D.1	Grids overview for the single cylinder case. . . . .	177
D.2	Normalized stream-normal velocity ( $v/u_2$ ) for the single cylinder case at the stagnation region. . . . .	178
D.3	Flow contours of the single cylinder case for the structured grid (left) and the unstructured grid (right). . . . .	179

List of Figures

D.4	Surface pressure plot for the single cylinder. . . . .	180
D.5	Surface heat flux plot for the single cylinder. . . . .	180
D.6	Geometry configuration of the two-dimensional two-cylinder case . . . .	181
D.7	Grids overview for the two-cylinder case using inviscid formulation. . . .	181
D.8	Grids overview for the two-cylinder case using viscous formulation. . . .	182
D.9	Normalized pressure contours for the structures and anisotropic grids, respectively, at the shock-shock interference region using inviscid formu- lation. . . . .	183
D.10	Normalized temperature contours for the structured and anisotropic grids, respectively, at the shock-shock interference region using inviscid formulation. . . . .	183
D.11	Surface pressure plot of the aft cylinder for the two-cylinder case using inviscid formulation. . . . .	184
D.12	Surface heat flux plot of the aft cylinder for the two-cylinder case using viscous formulation. . . . .	184
D.13	Lift coefficient of the aft cylinder for a vertical displacement of 0.3 meters.	184
D.14	Drag coefficient of the aft cylinder for a vertical displacement of 0.3 meters.	184
D.15	Normalized pressure contours for the structured and anisotropic grids, respectively, at the shock-shock interference region using viscous formu- lation. . . . .	185
D.16	Normalized temperature contours for the structured and anisotropic grids, respectively, at the shock-shock interference region using viscous formulation. . . . .	185

# List of Tables

2.1	Tauber formula correlation factor. . . . .	20
2.2	Energy accommodation coefficient $\alpha$ for air [Wiedmann and Trumpler, 2022]. . . . .	21
3.1	Uncertainties associated with physical properties involved in the destructive re-entry risk assessment [De Persis and Lemmens, 2023]. . . . .	38
4.1	Free-stream conditions for the 1.6-meter-diameter sphere case [Dogra et al., 1992]. . . . .	80
4.2	Free-stream conditions for the hollow hemisphere case. . . . .	83
4.3	Free-stream conditions for the ARD case. . . . .	84
4.4	Free-stream conditions for model verification. . . . .	86
4.5	Temperature at boundary layer edge. . . . .	86
4.6	Species mass fraction at boundary layer edge. . . . .	87
4.7	ATV trajectory at the start of the re-entry simulation. . . . .	90
4.8	Material properties of Al6061-T651 as a function of temperature [Summers et al., 2015]. . . . .	91
4.9	Geometrical, inertial and initial conditions of the cylindrical puck. . . . .	97
5.1	Ring geometrical details. . . . .	102
5.2	Freestream parameters. . . . .	102
5.3	Free-stream and wall values for the single sphere case. . . . .	105
5.4	Grid details for the single sphere case. . . . .	105
5.5	Free-stream and wall values for the two-spheres case. . . . .	110

List of Tables

5.6	Grid details for the two-spheres case. . . . .	110
5.7	Geometrical and mass properties of the model. . . . .	114
5.8	Initial conditions and free-stream parameters. . . . .	114
5.9	Properties of the annular ring and the cylinder model. . . . .	119
5.10	Initial conditions for the shock-impinged ring case. . . . .	120
5.11	Discrepancy parameters between numerical CFD and low-fidelity coefficients. . . . .	123
5.12	Initial trajectory conditions and geometry details. . . . .	125
6.1	Initial trajectory conditions for the ATV case. . . . .	130
6.2	Material list of the main AVUM components [Dumon et al., 2022] . . .	134
6.3	Trajectory conditions and geometry details at the entry interface . . . .	135
6.4	COPV and Titanium tanks release and ground spread details. . . . .	138
A.1	ORSAT object geometry and motion [Lips and Fritsche, 2005]. . . . .	151
A.2	ORSAT transition regime bridging function for aerothermal loads [Lips and Fritsche, 2005] . . . . .	152
A.3	Aerodynamic and Aerothermodynamic models in FOSTRAD. . . . .	164
D.1	Free-stream and wall values for the single cylinder case. . . . .	177
D.2	Grid details for the single cylinder case. . . . .	177
D.3	Free-stream and wall values of the two-cylinder case. . . . .	181
D.4	Grid details for the inviscid proximal cylinder case. . . . .	181
D.5	Grid details for the viscous proximal cylinder case. . . . .	182

## List of Tables

# Chapter 1

## Introduction

### 1.1 Motivation

Satellite launches have been continuously increasing due to the need for global communication and navigation services, entertainment, and Earth observation. With the miniaturisation of space systems and the rise of satellite constellations (e.g., Starlink, Kuiper, OneWeb), commercial operators have become more prominent in the space sector, which promoted a further increase in the number of launch vehicles and orbiting satellites, as illustrated in Fig. 1.1, being primarily launched into a Low-Earth Orbit (LEO).

To avoid space clusterisation from nonoperational satellites and space debris, various mitigation measures are being considered and implemented by space agencies and international communities for the control of space debris formation [Kato, 2001]. One of the recommended measures is the safe disposal of the vehicles and satellites after their end-of-life. Focusing on the LEO environment, the preferable scenario is a disposal by re-entry within 5 years from the satellite decommission [ESA Space Debris Mitigation WG, 2023], through a controlled or uncontrolled atmospheric re-entry [Pardini and Anselmo, 2019]. A controlled re-entry is normally achieved by activation of the propulsive system to make the spacecraft descent with a steeper flight path angle, for a selected latitude and longitude such that the estimated impact location has

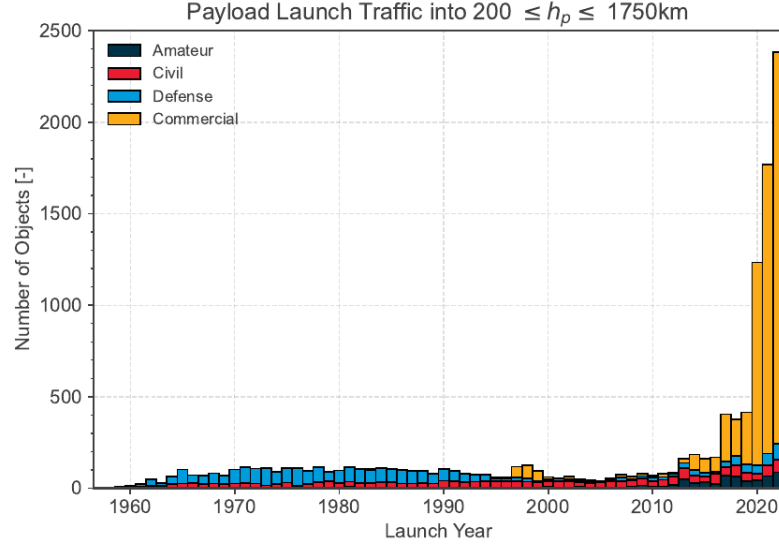


Figure 1.1: Evolution of the launch traffic near  $LEO_{IADC}$  per mission funding (from [ESA Space Debris Office, 2023]).

a minimum casualty risk, such as unpopulated areas [Park et al., 2021]. However, regarding uncontrolled re-entry, ground impact in a free-risk area can not be guaranteed. To ensure minimal risk to life and assets on Earth during an uncontrolled re-entry, the Inter-Agency Space Debris Coordination Committee (IADC) has set standards that require fragments with impact kinetic energy greater than  $15 J$  to have a casualty risk (expected number of casualties per re-entry) lower than  $10^{-4}$  [Liou et al., 2020, O'Connor, 2008, ESA Space Debris Mitigation WG, 2023, ESA Re-entry Safety WG, 2017]. Active debris removal (ADR) strategies have been envisaged to induce uncontrolled re-entry, including propulsion deorbit and drag augmentation techniques to curb the rapid growth of debris [Junfeng Zhao, 2020].

To exploit the advantages of uncontrolled re-entry in terms of simplicity and lower costs, the design-for-demise approach has been introduced to meet the casualty risk constraint. The design-for-demise concept is a strategy used in space debris mitigation to ensure that, from the early stages of mission planning, spacecraft and satellite components are designed to re-enter and burn up in the Earth's atmosphere safely. During their descent trajectory, the debris can break up into smaller parts until they

have completely demised, or reach the ground and pose a risk to the human population. Thus, re-entry analysis is required from the early planning phases.

To correctly assess the ground casualty risk, re-entry analysis tools must predict the debris trajectory and the occurring physical processes. They must consider the multiple physical models involved, such as heat transfer and thermal degradation, aerodynamics, and aerothermodynamics for multiple flow regimes, and structural dynamics and flight mechanics. These models should also be applicable to a multitude of fragments with irregular shapes and sizes [Hankey, 1988]. Improved modeling and simulation of the fragmentation induced by extreme heat and aerodynamic loads are crucial to designing systems capable of safe demise and assessing the associated risk, but accurate modelling of the break-up mechanism is challenging due to its complexity and multi-disciplinary nature. The unsteady changes in the object's shape, in addition to their orientation and relative motion, impact the local aerodynamic environment, leading to a growing uncertainty in the modelling of the loads impacting the debris.

Several space agencies and research institutes have developed fast and accurate analysis tools to check for the compliance with imposed regulations and verify the survivability of space debris [niu Wu et al., 2011, De Persis and Lemmens, 2023]. Historically, the developed tools fall into two categories: object-oriented tools that can evaluate the survivability space debris using simplified shapes, and spacecraft-oriented tools which employ detailed geometric models with meshed structures and enables more complex physical models. In recent years, an increase in experimental campaigns conducted on various material samples and shapes using wind tunnels and plasma facilities have yielded in a significant number of data increase regarding material behavior at high temperatures temperatures, and objects dynamic under high-speed flows. This increase in validation results has led to a steep improvement on the re-entry analysis tools over the last decade [De Persis and Lemmens, 2023]. Significant advancements have also been made in the last years to enhance the accuracy of re-entry simulations. New versions of space-oriented tools [Annaloro et al., 2021, Kanzler et al., 2021] have begun to incorporate aerodynamic and heat flux data-based models from Computational Fluid Dynamics (CFD) tools, which improved the fidelity of pressure and heat-flux dis-

tribution over the re-entering object surface. Additionally, new high-fidelity tools for the fast estimation of pressure loads [Ledermann et al., 2022] and data-driven machine learning methodologies for the prediction of pressure and heat-flux distribution [Graham et al., 2023] are being developed to be coupled in the next generation of analysis tools [De Persis and Lemmens, 2023].

## 1.2 Challenges and Research Questions

The instants after break-up events are characterized by the formation of a debris cloud, of which the fragments' proximity and relative dynamics are impacting factors on the evolution of the dynamics. In particular, the proximity of debris can lead to collision events, where fragments collide with each other and exchange momentum, and to the formation of complex flow structures that can influence the load distribution over the surface. However, the commonly adopted approach by the current re-entry tools follows the isolated analysis of the fragments generated during the break-up event and does not account for proximity effects. Furthermore, the simplified aerodynamic assumptions cannot consistently address the high-intensity loads generated by the complex flow features such as shock-shock interaction and shock impingement. These loads can play a major role in the debris dynamics during the instants after fragmentation. Using high-fidelity methods to predict aerothermodynamic loads, such as CFD, allows for the complex shock interference patterns arising during the re-entry process to be captured [Maier et al., 2021]. CFD solvers have been extensively used for the aerothermodynamic analysis of re-entering objects at individual trajectory points [Furudate et al., 2006, Martin et al., 2012]. However, employing these methods for the complete set of trajectory points is computationally costly, becoming prohibitively expensive given the potentially large number of fragments generated during the demise process and the required automatic mesh refinement at each analysed time-step to obtain converged solutions.

**Research question 1: Is it possible to develop a computationally efficient and accurate tool that can model flow interaction in the moments after breakup and demise events?**

Due to the computational cost of high-fidelity methods, performing a complete re-entry simulation from the entry interface until the ground using solely high-fidelity methods is not feasible. As an alternative, this project focuses on creating a new tool for re-entry simulations called TITAN, which uses a novel multi-fidelity methodology to achieve a compromise between cost and accuracy. The methodology implements a decision-making process to choose the adequate model in terms of fidelity, enabling capturing the occurring physical processes at particular instants of time. Two research questions arise from the challenges of using the proposed multi-fidelity methodology.

- *Research question 1.1: How to automatically detect the required local fidelity level in a conservative manner?*
- *Research question 1.2: Is an anisotropically adapted unstructured grid capable of adequately resolving the loads' distribution over the objects' surface?*

Regarding the former research question, the methodology must correctly choose between low- or high-fidelity models without human-in-the-loop interaction, reducing the downtime of the re-entry simulations. For this matter, a conservative physics-informed criterion based on the proximity of the objects, their velocity and known atmospheric parameters is proposed. Furthermore, the proposed criterion allows to organise the objects by which fidelity is required to capture the surrounding flow physics, based on their relative location, avoiding the use of high-fidelity methods when not required.

For the latter research point, the use of high-fidelity methods requires a computational grid to perform flow simulations. It is known that the grid cell type and alignment play a role in the computed surface distribution [Candler et al., 2007, Nompelis et al., ]. This work explores the use of unstructured tetrahedral grids with prismatic layers for CFD simulations, due to its accessibility in automating grid generation for arbitrary geometrical shapes. Therefore, the suitability of anisotropic grids for hypersonic simulations is also verified in this work.

**Research question 2: Can the implementation of a common global domain enable to capture the interference in dynamics due to the objects physical proximity?**

As an alternative to the individual analysis and propagation of fragments generated during breakup and demise events, this work explores the use of a common global domain, enabling one to account for the occurring interactions and flow interference due to physical proximity. Furthermore, its contribution to dynamics evolution and ground impact location are also assessed in this project. In this sense, the developed framework TITAN introduces two types of interaction due to proximity: aerodynamic interaction via changes in the flow structure that are dependent on the fragments' position and orientation, and collision interaction via elastic momentum exchange. To propagate the dynamics, a quasi-steady approach for time propagation is proposed in this project, assuming a steady-state solution at each time interval. This approach is validated through comparison with analytical and experimental cases.

### **1.3 Advantages of a multi-fidelity methodology**

As previously mentioned in Sec. 1.2, the development of new tools in destructive re-entry analysis, particularly those employing a multi-fidelity methodology, present advantages when compared to tools that employ only low- or high-fidelity models, such is the case for commonly used object-oriented and spacecraft-oriented re-entry analysis tools [Pontijas Fuentes et al., 2019, Koppenwallner et al., 2005, Annaloro et al., 2015]. The tools employ engineering assumptions and data-based correlations for their aerodynamic calculations, failing to capture the occurring shock interactions.

An important benefit of using a multi-fidelity is the ability to achieve a better balance between accuracy and computational costs when running the simulations by allowing to switch between models with different fidelity. The use of high-fidelity techniques like DSMC and CFD is highly costly, but by only using the more intensive methods when increased precision is required, the computational time to run a simulation can substantially decrease when compared to a full simulation using only high-fidelity mod-

## Chapter 1. Introduction

els. Furthermore, multi-fidelity tools could limit the use of high-fidelity methods until when strictly required, enabling one to capture the complex physical phenomena that otherwise would be impossible to observe using low-fidelity methods.

### 1.4 Thesis Layout

**Chapter 2** presents a detailed literature review concerning high-temperature high-speed physics occurring during a re-entry process for continuum and free-molecular regime, and common low-fidelity models to predict the acting heat flux and pressure over the re-entering objects' surface.

**Chapter 3** provides an overview on object-oriented and spacecraft oriented tools, their inherent simplified models and assumptions used in re-entry analysis and recent developments. The chapter ends with the proposal of a newly proposed multi-fidelity switch methodology for the re-entry simulation.

**Chapter 4** describes the development of TITAN, a new atmospheric re-entry framework and provides details about the implemented disciplinary modules and interdisciplinary communication between different modules. This chapter presents verification cases regarding the implemented modules, namely for low-fidelity aerodynamics and aerothermodynamics, wall catalicity effects, structural modelling and collision modelling.

**Chapter 5** explains the use of a multi-fidelity approach as an alternative to low-fidelity models in modelling the aerodynamics and aerothermodynamic loads impacting the objects. The goal of the approach is to enable the capture of complex flow structures rising from fragments proximity after break-up and demise events. A physics-informed fidelity switch is discussed, for automatically selecting the adequate level of fidelity for a given time step.

**Chapter 6** provides an analysis of two re-entry test cases using the developed frame-

## Chapter 1. Introduction

work and the proposed multi-fidelity approach: a conceptual re-entry of the Automated Transfer Vehicle, and a re-entry case of the Attitude and Vernier Upper Module. The analysis is mainly focused on the effect of accounting for higher aerodynamic fidelity in the cloud of debris spatial distribution and the effect of debris collision in the ground impact location.

**Chapter 7** contains the concluding remarks of the presented work and suggestions for further improvements.

## 1.5 Publications

The relevant methodology and results discussed in this dissertation have been presented in the following conference proceedings and accepted in the stated international journals:

### 1.5.1 Conferences

- [Morgado et al., 2022c]: Morgado, F., Peddakotla, S. A., Garbacz, C., Vasile, M. L., and Fossati, M. (2022c). Multi-fidelity approach for aerodynamic modelling and simulation of uncontrolled atmospheric destructive entry. In *AIAA SCITECH 2022 Forum*, page 1323
- [Morgado et al., 2022b]: Morgado, F., Peddakotla, S. A., Garbacz, C., Vasile, M., and Fossati, M. (2022b). Fidelity management of aerothermodynamic modelling for destructive re-entry. In *The 2nd International Conference on Flight Vehicles, Aerothermodynamics and Re-entry Missions Engineering (FAR)*. European Space Agency, DEU
- [Morgado et al., 2023]: Morgado, F., Fossati, M., Kóvacs, D., and Magin, T. (2023). Rebuilding the vki’s experiment on the interference of a free-flying ring and stationary cylinder using a multi-fidelity numerical methodology. In *AIAA SCITECH 2023 Forum*, page 1386

### 1.5.2 Journals

- [Maier et al., 2021]: Maier, W. T., Needels, J. T., Garbacz, C., Morgado, F., Alonso, J. J., and Fossati, M. (2021). SU2-NEMO: An Open-Source Framework for High-Mach Nonequilibrium Multi-Species Flows. *Aerospace*, 8(7). 10.3390/aerospace8070193
- [Morgado et al., 2022a]: Morgado, F., Garbacz, C., and Fossati, M. (2022a). Impact of anisotropic mesh adaptation on the aerothermodynamics of atmospheric reentry. *AIAA Journal*, 60(7):3973–3989
- [Peddakotla et al., 2022a]: Peddakotla, S. A., Morgado, F., Thillaithevan, D., O’Driscoll, D., Santer, M., Maddock, C., Vasile, M., and Fossati, M. (2022a). Multi-fidelity and multi-disciplinary approach for the accurate simulation of atmospheric re-entry. In *73rd International Astronautical Congress 2022*
- [Maier et al., 2023]: Maier, W., Needels, J. T., Alonso, J. J., Morgado, F., Garbacz, C., Fossati, M., Tumuklu, O., and Hanquist, K. M. (2023). *Development of Physical and Numerical Nonequilibrium Modeling Capabilities within the SU2-NEMO Code*
- [Graham et al., 2023]: Graham, J., Morgado, F., and Fossati, M. (2023). Data-driven modelling of aerothermodynamic loads during atmospheric re-entry. In *AIAA AVIATION 2023 Forum*, page 4202
- [Morgado et al., 2024b]: Morgado, F., Peddakotla, S. A., Graham, J., Vasile, M., and Fossati, M. (2024b). A multi-fidelity framework for aerothermodynamic modelling and simulation of destructive atmospheric entry. *AIAA Journal*. Accepted for publication
- [Morgado et al., 2024a]: Morgado, F., G. Kovács, D., and Fossati, M. (2024a). Modeling the interaction of proximal fragments for destructive atmospheric entry analysis. *AIAA Journal*. Accepted for publication

## Chapter 2

# Physics of Atmospheric Entry

The low Earth orbit objects that re-enter the atmosphere present high kinetic energy, reaching velocities over 7.8 km/s at the entry interface, commonly defined at an altitude of 120 km [Choi et al., 2017]. During descent, they will experience strong aerodynamic and aerothermal loads that can melt and break the structures into several fragments that need to be tracked independently. Most of the re-entering fragments will demise, but surviving ones can cause great risk to ground population, buildings and natural ecosystems. The ground footprints of the surviving debris can extend for hundreds of kilometers [niu Wu et al., 2011].

### 2.1 Atmospheric environment

The atmospheric properties determine the free-stream parameters that re-entering objects are subjected to, which in turn governs the acting aerodynamic and thermal loads. The gas composition, temperature and density vary as a function of altitude, and their variation dictates the layered division of the atmosphere, as illustrated in Fig. 2.1. The atmospheric properties are also dependent on the geographical latitude of the location and they change in time due to seasons, atmospheric tides, solar activity and geomagnetic activity.

In the homosphere layer, the composition of the atmosphere remains relatively constant up to an altitude of approximately 100 km due to the turbulent mixing of the

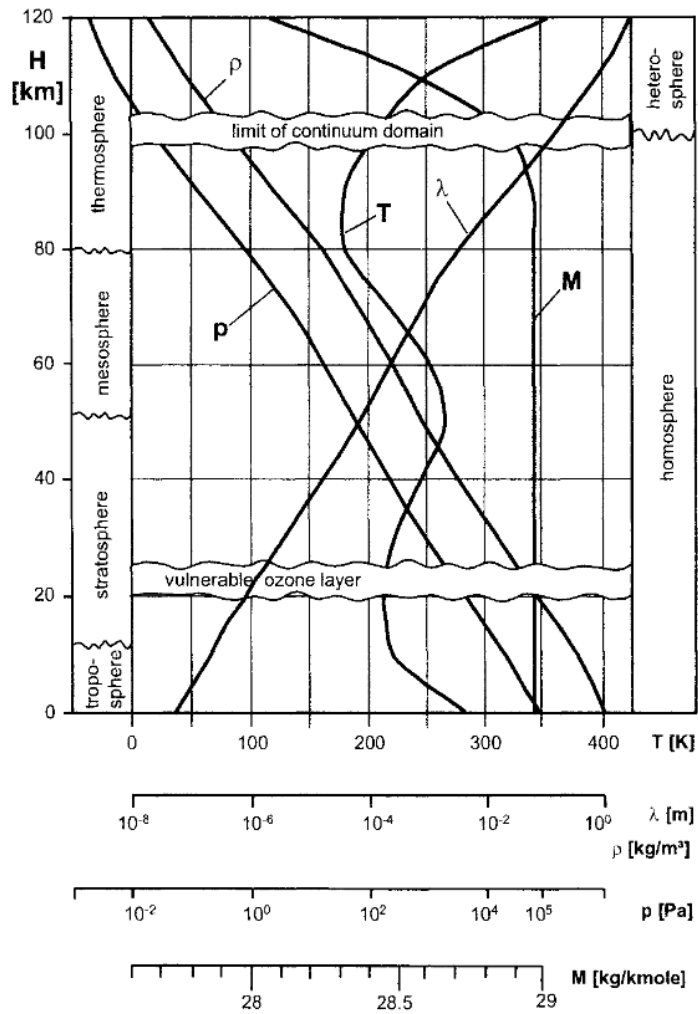


Figure 2.1: Atmospheric layers and properties as a function of altitude (from [Hirschel, 2004])

species. The gas mixture is predominantly composed of  $N_2$  and  $O_2$  molecules, with an approximate molar fraction of 78.09% and 20.95% respectively [Blay et al., 2019]. The homosphere layer consists of the troposphere from sea level up to approximately 10 km, the stratosphere between 10 km and 50 km, the mesosphere between 50 km and 80 km, and the lower part of the thermosphere between 80 km and 100 km. In addition to the atmospheric properties, the strong winds encountered in the troposphere can significantly affect the trajectory of the fragments that have not been demised and which already had their velocity drastically reduced from the entry point due to atmospheric

drag.

As for the heterosphere layer located above an altitude of 100 km (also called turbopause) until 800 km, the atmospheric composition changes with altitude. Heavier molecules and atoms tend to reside in the lower layers of the heterosphere, while the lighter species are more prevalent at higher altitudes. The heterosphere layer incorporates the rest of the thermosphere and the ionosphere. It is important to consider the changes in atmospheric composition with altitude, as it influences the computation of the aerothermodynamic loads.

Throughout the years, various models have been developed to simulate the atmosphere and retrieve the atmospheric temperature and partial densities as a function of altitude. Currently, the most commonly used global atmospheric models are the U.S. Standard Atmosphere 1976 [United States National Oceanic and Atmospheric Administration and United States Committee on Extension to the Standard Atmosphere, 1976], NRLMSISE-00 [Picone et al., 2002] and NASA GRAM [Justus et al., 2004]. Both the NRLMSISE-00 and NASA GRAM models include variations due to time, solar activity, geomagnetic activity, and location.

## 2.2 Physics of high-speed atmospheric re-entry

### 2.2.1 Flow regime classification

The local flow experienced by the debris can have different classifications according to the flow speed and rarefaction. The speed regime is defined by the Mach number  $M_\infty$ , which is expressed as the ratio between the object's speed in the undisturbed flow  $V_\infty$  and the speed of sound  $a_\infty$

$$M_\infty = \frac{V_\infty}{a_\infty}. \quad (2.1)$$

According to the free-stream Mach number, the flow can be categorized as [Anderson, 2006]:

- Hypersonic regime:  $M_\infty \geq 5$

## Chapter 2. Physics of Atmospheric Entry

- Supersonic regime,  $1.2 \leq M_\infty < 5$
- Transonic regime,  $0.8 \leq M_\infty < 1.2$
- Subsonic regime,  $M_\infty < 0.8$

The hypersonic regime is not strictly defined by a specific Mach number but is generally associated with speeds above Mach 5, where distinct physical phenomena become dominant. Such phenomena include thin shock layers, where the shock remains close to the body, and entropy layers with high entropy gradients formed as a result of variations in shock strength along different streamlines. High-temperature effects also become prominent, as the presence of high enthalpy results in molecular dissociation and ionization.

The space debris re-enter the atmosphere at hypersonic speed (around Mach 25) and remain in this regime for most of the descent, but the applied atmospheric drag slows the fragment, thus transitioning from hypersonic flow to supersonic, transonic and subsonic flow.

The debris will also experience several flow regimes, determined by the Knudsen number  $Kn$ , an indicative of the level of rarefaction in the flow, defined as,

$$Kn = \frac{\lambda}{l_{ref}}, \quad (2.2)$$

where  $\lambda$  is the molecular mean free path and  $l_{ref}$  is the reference length representative of the body, such as the diameter of a thrust chamber or the radius of a capsule. The mean free path is defined as the average distance that a molecule travels before colliding with another molecule. The following classification is generally assumed [Dongari et al., 2009]:

- $Kn > 10$  - Free Molecular Regime;
- $0.1 \leq Kn \leq 10$  - Transitional Regime;
- $0.001 \leq Kn \leq 0.1$  - Slip Regime;
- $Kn \leq 0.001$  - Continuum Regime.

At the re-entry interface, the atmosphere is highly rarefied, and the mean free path is much larger than the characteristic dimension of the body resulting in a lower number of collisions. In this regime, the gas behaves as a collection of independent molecules, and the aerodynamic forces and heat flux on the vehicle arise from direct molecular impacts. Because of this, the traditional Navier-Stokes equations no longer apply and statistical mechanics and kinetic theory must be used to model gas-surface interactions. Molecular dissociation and recombination can still occur in this regime, driven by the interaction between the molecules and the surface of the re-entry object at the time of impact.

As the object falls through the denser atmosphere, the particles' mean free path decreases, which in turn reduces the Knudsen number, entering the transitional regime. Here, the mean free path of air molecules is still comparable to the object size, but intermolecular collisions start becoming significant. This regime is challenging to model because it requires a combination of molecular kinetic theory and modified continuum approaches, such as the Boltzmann equation or direct simulation Monte Carlo (DSMC) methods. In this regime, surface interactions are still dominant, but small shock waves and localized continuum-like effects begin to emerge. The impact of aerodynamic forces and heat flux on the surface becomes significantly more pronounced as the flow becomes less rarefied. As the object continues to descend, strong shock waves start to form in the vicinity of the body, giving rise to high temperature effects in the flow mixture, which must be taken into account for the correct assessment of the heating rates and aerodynamic loads acting on the surface.

Later, the object reaches the slip flow regime, where the flow starts behaving like a continuum, but the no-slip boundary condition of classical fluid dynamics does not hold. The slip regime is a special case, which can be predicted by solving the Navier-Stokes equations for the flowfield, except near the object surfaces, where velocity slip and temperature jump phenomena occur and do not match the conditions at the surface of the object. To handle this, the simulation of the flow near the wall is treated by applying special boundary conditions. In addition, the increasing number of collisions leads to more significant aerodynamic heating.

Finally, the flow reaches the continuum regime, where the mean free path is much smaller than the vehicle dimensions, and the gas can be considered continuum. Stronger bow shocks start to form ahead of the vehicle, drastically increasing the temperature and pressure of the air, leading to higher chemistry rates in the shock and to intense aerodynamic heating, driven by convective and radiative heat transfer. In this regime, viscosity and thermal conductivity play significant roles in the boundary layer, where velocity and temperature gradients generate strong shear forces and possible shock-boundary layer interactions, which can lead to flow separation and unsteady loads on the vehicle. The traditional Computational Fluid Dynamics (CFD) methods can now be fully used to solve the Navier-Stokes equations.

### 2.2.2 High-temperature effects during re-entry

When the fluid crosses a shock wave, it is suddenly compressed and slowed down over a distance on the order of the mean free path, and a large portion of its kinetic energy is converted to internal energy with the increase of the collision rate, causing the temperature to rise. The high temperatures in hypersonic flows play a major role in the characterization of the fluid surrounding the re-entering objects, giving rise to physicochemical processes, such as vibrational and electronic energy excitation, chemical reactions, ionization, and gas-surface interactions. When these processes occur, the approximation of air as a perfect gas is no longer valid. The rates of the physicochemical processes are affected by the local thermodynamic state, and these rates increase as a function of density and temperature.

In the equilibrium resting state, atmospheric air is mostly formed by diatomic particles ( $N_2$ ,  $O_2$ ), which possess four energy modes (translation, rotation, vibration and electronic excitation) while atoms have two energy modes (translation and electronic excitation). As the molecules become excited along with the temperature increase, they undergo dissociation, forming atomic oxygen ( $O_2 \rightarrow O + O$ ) and atomic nitrogen ( $N_2 \rightarrow N + N$ ), and recombination, forming nitric oxide ( $N + O \rightarrow NO$ ). Further temperature increases lead to the removal of electrons from the electron cloud, in a process referred to as ionization ( $NO \rightarrow NO^+ + e^-$ ). The ionization process is a well-

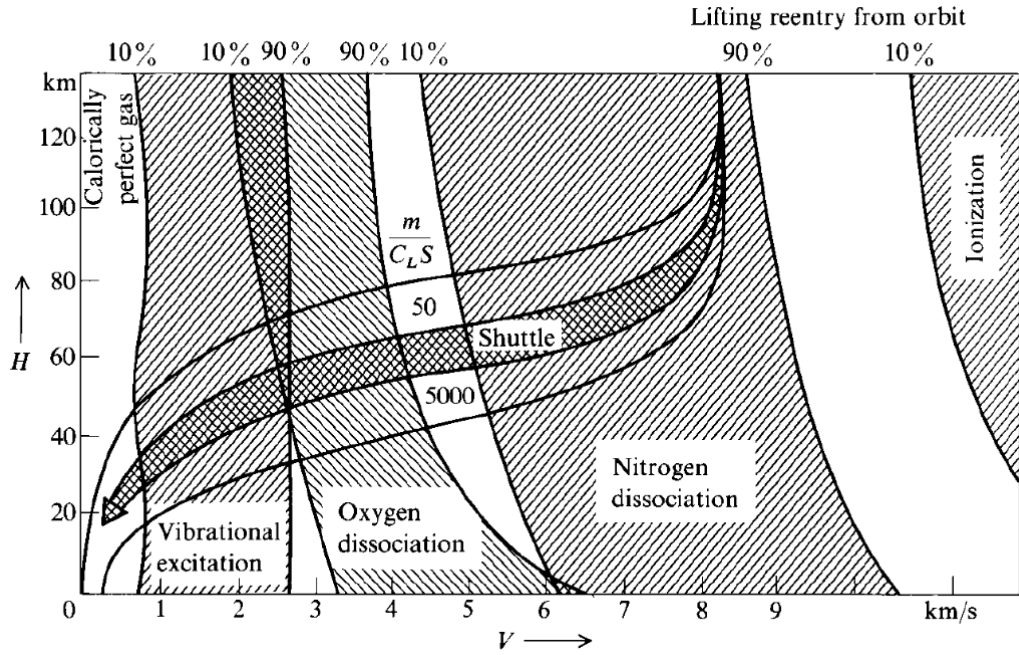


Figure 2.2: Molecular dissociation, vibrational excitation and ionization for air as a function of altitude and velocity [Anderson, 2006].

known phenomenon in re-entries of capsule or shuttle types for causing communication blackouts due to the formation of an envelope of ionized air. Figure 2.2 reports the occurrence of physicochemical processes for air as a function of re-entry velocity.

When high-temperature flow reaches the surface of the objects, the gas-surface interaction needs to be accounted for, as the heat transfer rate to the surface in the form of convective and radiative flux can be significantly affected by the occurring processes.

The characteristics of the surface material can act as a catalytic medium and promote molecular exothermic recombination. This chemical process releases energy onto the surface, contributing to the amount of heat flux transferred to the object. The level of catalicity is measured by the recombination coefficient ( $\gamma$ ), described as the ratio between the mass flux of atoms recombining at the surface and the mass flux of atoms impinging the surface. It is commonly assumed that all the energy due to recombination is transmitted to the wall [Preveraud et al., 2019].

There are three types of catalytic walls as illustrated in Fig. 2.3: non-catalytic walls,

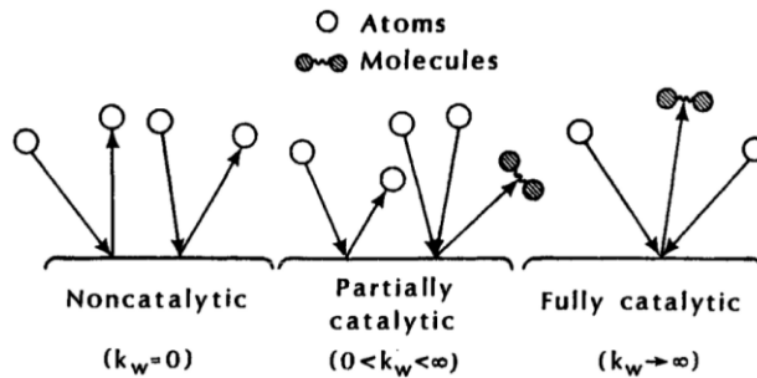


Figure 2.3: Effect of the wall catalycity on atoms recombination (from [Bertin, 1994]).

partially catalytic walls and fully catalytic walls. In non-catalytic walls, the surface of the object is chemically inert, not contributing to the molecular recombination ( $\gamma = 0$ ). On the opposite spectrum, fully catalytic walls promote the complete recombination of the  $N$  and  $O$  atoms that impinge the surface ( $\gamma = 1$ ), maximizing the energy released. In the intermediate case, the surface is considered partially catalytic ( $0 < \gamma < 1$ ). This is generally the situation found on materials used as Thermal Protection Systems (TPS). The predicted aerodynamic heat in the stagnation point could differ by a factor of 4 by using either a non-catalytic or fully catalytic assumption [Cui et al., 2022, Candler, 2019]. The catalytic properties and emissivity parameter of the material may change throughout re-entry due to the occurring physicochemical processes, including the formation of oxide layers and changes in the boundary layer gas composition due to material ablation and pyrolysis.

The energy exchange between the gas and the wall occurs through the convective and radiative heat fluxes. The convective heat flux refers to the transfer of heat between the hot gas and the cold surface and is affected mainly by the temperature gradient between the gas and the surface, and by the local radius of curvature, among other factors. The convective heat flux is also impacted by the mass diffusion of the species in the flow. The radiative heat flux also plays an important role in the energy transfer between the gas and the object. The object releases heat to the local environment in the form of radiation, in a phenomenon called radiative cooling and described by the

Stefan-Boltzmann Law,

$$\dot{q}_{r,w} = \epsilon \sigma T_w^4 \quad (2.3)$$

where  $\epsilon$  is the emissivity coefficient of the surface,  $\sigma$  is the Stefan-Boltzmann constant and  $T_w$  is the wall temperature. For high fusion temperature materials, the effects of the radiative heat flux during re-entry can lead to the survivability of the object.

Another source of non-negligible heat radiation is the gas in the shock layer when the temperature reaches values superior to 10000  $K$ . Depending on the temperature and mixture composition, the gas emits radiation to the surrounding bodies and flow regions, which is then absorbed. For the Apollo re-entry capsule, the radiative heat transfer constituted over 30% of the total heating rate [Anderson, 2006].

The Tauber correlation [Tauber and Sutton, 1991] can be used to calculate the radiative heat flux from the gas to the stagnation point, as a function of the local radius of curvature and the upstream conditions. The correlation is given as

$$\dot{q}_r = C R_n^b \rho_\infty^a f(V_\infty) \quad (2.4)$$

where  $R_n$  is the radius of curvature,  $\rho_\infty$  and  $V_\infty$  are, respectively, the density and velocity of the free-stream flow, and the parameters  $a$ ,  $b$  and  $C$  are constant values defined as

$$\begin{cases} C = 4.736 \times 10^8 \\ b = 1.22 \\ a = 1.072 \times 10^6 \times V_\infty^{-1.88} \times \rho_\infty^{-0.325} \end{cases} \quad (2.5)$$

The parameter  $a$  also needs to comply with

$$\begin{cases} \text{If } 1 \leq R_n \leq 2, & \text{then } a \leq 0.6 \\ \text{If } 2 < R_n \leq 3, & \text{then } a \leq 0.5 \end{cases} \quad (2.6)$$

The value of the function  $f(V_\infty)$  is calculated by interpolating the free-stream ve-

locity with the data in table 2.1.

Table 2.1: Tauber formula correlation factor.

$V_\infty$ (m/s)	9000	9250	9500	9750	10000	10250	10500	10750	11000	11500
$f(V_\infty)$	1.5	4.3	9.7	19.5	35	55	81	115	151	238
$V_\infty$ (m/s)	12000	12500	13000	13500	14000	14500	15000	15500	16000	
$f(V_\infty)$	359	495	660	850	1065	1313	1550	1780	2040	

It is important to note that the Tauber correlation is valid only for free-stream velocities between 9000 and 16000 m/s and for altitudes between 54 and 72 km.

### 2.2.3 Free-molecular regime

At high altitudes, the interaction of the objects with the atmospheric air is characterised by the free molecular flow. In this regime, the air molecules collide and interact with the vehicle's surface but collisions between particles are unlikely to occur and can be neglected. When the incident particles impact the debris surface, there is an energy and momentum transfer between the gas and the body. The degree of exchange is tied to the level of the particles' re-emission or reflection, which itself depends on the surface temperature. The momentum and heat transfer mechanisms in non-continuum gas flows are still not completely understood [Bayer-Buhr et al., 2022], and the assumption that the mechanics can be satisfactorily described through empirical parameters called accommodation coefficients is commonly applied [Hayes and Probstein, 1959, Rader et al., 2005].

A measure of the energy lost by the molecules due to collision is given by the energy accommodation coefficient as

$$\alpha = \frac{E_i - E_r}{E_i - E_w}, \quad (2.7)$$

where  $E_i$  is the incident energy per unit area per second of the molecule,  $E_r$  the energy carried by the re-emitted or reflected molecules and  $E_w$  is the energy that the molecules would have if all the incident molecules were re-emitted with the Maxwellian velocity distribution for the correspondent wall temperature ( $T_w$ ). The accommodation coeffi-

cient evaluates the ability of the molecules to adjust to the surface temperature during their time of contact. It is assumed that all the molecular energy modes (translational, rotation, vibrational and electronic) are accommodated to the same degree [Rader et al., 2005].

The energy accommodation coefficient varies between zero ( $\alpha = 0$ ) and unity ( $\alpha = 1$ ), ranging from a fully specular reflection where there is no energy exchange between the molecules and the body, to a fully diffusive reflection where the molecules come to complete thermal equilibrium with the surface temperature, respectively. The coefficient's value is strongly dependent on the composition and temperature of the gas and surface, the gas pressure and the conditions of the surface roughness and gas adsorption. Over the years, several experimental tests were conducted for rarefied air flow to determine the energy accommodation coefficient. Wiedmann and Trumpler [Wiedmann and Trumpler, 2022] investigated the measurement of the energy accommodation coefficient for air on metallic surfaces, reporting values between 0.87 and 0.97, as reported in Table 2.2. Moe et al. [Moe et al., 1993] have reviewed the measurements of 4 satellites in low Earth orbit at an altitude near 200 km, and reported the accommodation factor to be close to unity ( $\alpha = 0.975$ ), and only dependent on the amount of gas adsorbed on the surface.

Table 2.2: Energy accommodation coefficient  $\alpha$  for air [Wiedmann and Trumpler, 2022].

Surface material	$\alpha$
Flat lacquer on bronze	0.88 - 0.89
Polished bronze	0.91 - 0.94
Machined bronze	0.89 - 0.93
Etched bronze	0.93 - 0.95
Polished cast iron	0.87 - 0.93
Machined cast iron	0.87 - 0.88
Etched cast iron	0.89 - 0.90
Polished aluminum	0.87 - 0.95
Machined aluminum	0.95 - 0.97
Etched aluminum	0.89 - 0.97

In addition to the energy exchange, momentum transfer also needs to be considered. It has originally been proposed by Maxwell [Maxwell, 2011] the use of a single param-

eter to determine the fraction of incident molecules that are specularly or diffusely reflected from the surface, in order to determine the amount of momentum exchanged. However, as reported by Schaaf [Schaaf, 1953] and Hurlbut [Hurlbut, 1957], a single parameter is not sufficient to describe the momentum transfer process. Instead, in analogy to the energy accommodation coefficient, it's proposed the adoption of two separate accommodation coefficients to describe the normal momentum exchange

$$\sigma_n = \frac{p_i - p_r}{p_i - p_w}, \quad (2.8)$$

and the tangential ( $\sigma_t$ ) momentum exchange

$$\sigma_t = \frac{\tau_i - \tau_r}{\tau_i - \tau_w}, \quad \tau_w = 0, \quad (2.9)$$

where  $p$  and  $\tau$  are the normal and tangential momentum components to the surface. Similar to Eq. 2.7, the subscript  $i$  and  $r$  refer to the incident and reflected stream, while  $p_w$  and  $\tau_w$  refer respectively to the normal and tangential momentum components of the molecules which are re-emitted with a Maxwellian velocity distribution at the respective wall temperature.

There is little information concerning the normal accommodation coefficient  $\sigma_n$ . However, experimental measures found in Estermann [Estermann, 1955] and Millikan [Millikan, 1923] have determined that the tangential accommodation coefficient  $\sigma_t$  lies in the range between 0.8 and 1.0 for air. By inspection of the energy and tangential accommodation coefficients, the values are close to unity indicating that the molecule reflection is mainly diffusive, and therefore, the value of the normal accommodation coefficient should also be close to unity [Hayes and Probstein, 1959].

To determine the aerodynamic forces and convective heat transfer, it is usually assumed that the distribution of velocities for the incident molecules in a steady flow with mean velocity  $U$  follows a Maxwellian distribution function. By denoting the velocity of a single molecule in the x, y, and z directions by  $c_x$ ,  $c_y$ , and  $c_z$  respectively, the velocity distribution law for gas in equilibrium is defined as [Kennard, 1938]

$$f = \frac{\rho_\infty}{m(2\pi\mathcal{R})T_\infty^{\frac{3}{2}}} \exp \left[ -\frac{(c_x - U \sin \theta)^2 + (c_y + U \cos \theta)^2 + c_z^2}{2\mathcal{R}T_\infty} \right], \quad (2.10)$$

where  $T_\infty$  and  $\rho_\infty$  are respectively the free-stream temperature and density,  $m$ , is the molecular mass,  $\mathcal{R}$  is the specific gas constant and  $\theta$  is the molecular incidence angle to the surface element. The total number of particles striking a unit area per second is found by integrating over the molecular velocities.

$$\begin{aligned} N_i &= \int_{-\infty}^{\infty} \int_{-\infty}^{\infty} \int_0^{\infty} c_x f (dc_x)(dc_y)(dc_z) \\ &= \frac{\rho_\infty}{m} \sqrt{\frac{\mathcal{R}T_\infty}{2\pi}} \left\{ e^{-(\mathcal{S} \sin \theta)^2} + \sqrt{\pi}(\mathcal{S} \sin \theta)[1 + \operatorname{erf}(\mathcal{S} \sin \theta)] \right\} \end{aligned} \quad (2.11)$$

where  $\operatorname{erf}(x)$  is the error function defined as

$$\operatorname{erf}(x) = \frac{2}{\sqrt{\pi}} \int_0^x e^{-t^2} dt, \quad (2.12)$$

and  $\mathcal{S}$  denotes the molecular speed ratio as

$$\mathcal{S} = \frac{U}{\sqrt{2\mathcal{R}T_\infty}}. \quad (2.13)$$

The convective heat transfer for a steady flow over the surface is calculated by performing an energy flux balance between the energy carried by the incident and re-emitted molecules over a differential surface element. Taking into consideration the energy accommodation coefficient in Eq. 2.7, the heat transfer is expressed as

$$\dot{q} = -(E_i - E_r) = -\alpha(E_i - E_w) \quad (2.14)$$

The calculation of the incident energy flux can be simplified by breaking into contributions due to the translation motion of the molecules ( $E_{i,tr}$ ) and due to the internal degrees of freedom, such as rotation and vibration ( $E_{i,int}$ ). The kinetic energy carried per molecule is equal to  $\frac{1}{2}m(c_x^2 + c_y^2 + c_z^2)$ . Additionally, under the assumption of classical equipartition of energy, the flow carries an average amount of internal energy of  $\frac{1}{2}j_{int}m\mathcal{R}T$  per molecule, where  $j_{int}$  denotes the number of internal degrees of freedom.

Under the perfect gas assumption, the number of internal degrees of freedom is

$$j_{int} = \frac{5 - 3\gamma}{\gamma - 1}, \quad (2.15)$$

where  $\gamma$  is the specific heat ratio of the gas. It is important to note that for monoatomic mixtures, the specific heat ratio  $\gamma$  is equal to  $\frac{5}{3}$ . From Eq. 2.15 we conclude there are no internal degrees of freedom, and thus the only energy contribution is due to translation.

The flux of incident energy per unit area can be retrieved by integrating the energy components of incident molecules using Eq. 2.11 and Eq. 2.15. A more detailed deduction can be found in [Hayes and Probst, 1959, Schaaf and Chambre, 1958].

$$\begin{aligned} E_i &= E_{i,tr} + E_{i,int} \\ &= \frac{1}{2}m \int_{-\infty}^{\infty} \int_{-\infty}^{\infty} \int_0^{\infty} \left[ (c_x^2 + c_y^2 + c_z^2) + \frac{5 - 3\gamma}{\gamma - 1} \mathcal{R}T_{\infty} \right] c_x f(dc_x)(dc_y)(dc_z) \\ &= \rho_{\infty} \mathcal{R}T_{\infty} \sqrt{\frac{\mathcal{R}T_{\infty}}{2\pi}} \left\{ \left[ \mathcal{S}^2 + \frac{\gamma}{\gamma - 1} \right] \right. \\ &\quad \left. \left( e^{-(\mathcal{S} \sin \theta)^2} + \sqrt{\pi}(\mathcal{S} \sin \theta)[1 + \text{erf}(\mathcal{S} \sin \theta)] \right) - \frac{1}{2}e^{-(\mathcal{S} \sin \theta)^2} \right\} \end{aligned} \quad (2.16)$$

The component relative to the reflected energy flux is obtained assuming the molecules at the surface do not have macroscopic velocity ( $U = \mathcal{S} = 0$ ) and are in Maxwellian equilibrium at the surface temperature. Therefore, assuming a steady state flow on which the flux of incident particles is the same as the flux of reflected particles ( $N_w = N_i$ ), manipulating Eq. 2.16 yields that

$$E_w = \rho_{\infty} \mathcal{R}T_{\infty} \sqrt{\frac{\mathcal{R}T_{\infty}}{2\pi}} \left\{ \left[ \frac{\gamma + 1}{2(\gamma - 1)} \frac{T_w}{T_{\infty}} \right] \left( e^{-(\mathcal{S} \sin \theta)^2} + \sqrt{\pi}(\mathcal{S} \sin \theta)[1 + \text{erf}(\mathcal{S} \sin \theta)] \right) \right\} \quad (2.17)$$

and, combining Eq. 2.14, Eq. 2.16 and Eq. 2.17, the convective heat transfer flux can be retrieved as

$$\dot{q} = -\alpha\rho_\infty\mathcal{R}T_\infty\sqrt{\frac{\mathcal{R}T_\infty}{2\pi}}\left\{\left[\mathcal{S}^2 + \frac{\gamma}{\gamma-1} - \frac{\gamma+1}{2(\gamma-1)}\frac{T_w}{T_\infty}\right]\left(e^{-(\mathcal{S}\sin\theta)^2} + \sqrt{\pi}(\mathcal{S}\sin\theta)[1 + \operatorname{erf}(\mathcal{S}\sin\theta)]\right) - \frac{1}{2}e^{-(\mathcal{S}\sin\theta)^2}\right\} \quad (2.18)$$

The general method used for the calculation of the aerodynamic forces is to handle the force contribution of incident particles and re-emitted particles over a surface element separately. To compute the stress over the surface, it is convenient to split it into normal and tangential components, namely pressure and shear. From the definition of momentum accommodation coefficients in Eq. 2.8 and Eq. 2.9, we define

$$\begin{aligned} p_r &= (1 - \sigma_n)p_i + \sigma_n p_w \\ \tau_r &= (1 - \sigma_t)\tau_i \end{aligned} \quad (2.19)$$

and the net pressure and shear on the surface are given as

$$\begin{aligned} p &= p_i + p_r = (2 - \sigma_n)p_i + \sigma_n p_w \\ \tau &= \tau_i - \tau_r = \sigma_t \tau_i \end{aligned} \quad (2.20)$$

The parameter  $p_w$  is the pressure exerted by the molecules when re-emitted in Maxwellian equilibrium at wall temperature and with no macroscopic velocity component ( $U = \mathcal{S} = 0$ ). For a gas at rest with temperature  $T_w$ , the average normal momentum component carried by each molecule over a unit area per unit time is  $\frac{1}{2}m\sqrt{2\pi\mathcal{R}T_w}$  [Schaaf and Chambre, 1958]. Assuming a steady state, the number of molecules impacting the surface must be equal to the number of re-emitted molecules, and thus

$$p_w = \frac{1}{2}m\sqrt{2\pi\mathcal{R}T_w}N_i. \quad (2.21)$$

Each molecule transports an amount of momentum normal and tangential to the surface equal to  $mc_x$  and  $-mc_y$  respectively, as per reference to Fig. 2.4.

Combining Eq. 2.10, Eq. 2.11, Eq. 2.20, and Eq. 2.21, the total pressure and shear are retrieved by performing the integration:

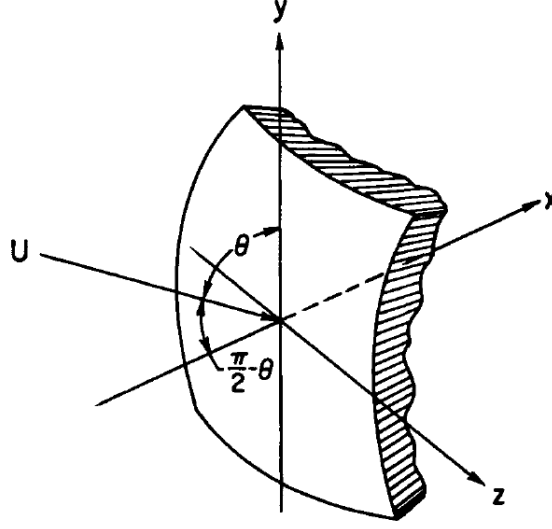


Figure 2.4: Coordinate system for surface element in free molecule flow (from [Hayes and Probstein, 1959]).

$$\begin{aligned}
 p &= \int_{-\infty}^{\infty} \int_{-\infty}^{\infty} \int_0^{\infty} \left[ (2 - \sigma_n) m c_x + \frac{\sigma_n}{2} m \sqrt{2\pi \mathcal{R} T_w} \right] c_x f(dc_x)(dc_y)(dc_z) \\
 &= \frac{\rho_{\infty} U^2}{2 \mathcal{S}^2} \left\{ \left[ \frac{(2 - \sigma_n)}{\sqrt{\pi}} (\mathcal{S} \sin \theta) + \frac{\sigma_n}{2} \sqrt{\frac{T_w}{T_{\infty}}} \right] e^{-(\mathcal{S} \sin \theta)^2} \right. \\
 &\quad \left. + \left[ (2 - \sigma_n) \left( \mathcal{S}^2 \sin^2 \theta + \frac{1}{2} \right) + \frac{\sigma_n}{2} (\mathcal{S} \sin \theta) \sqrt{\frac{\pi T_w}{T_{\infty}}} \right] [1 + \operatorname{erf}(\mathcal{S} \sin \theta)] \right\}
 \end{aligned} \tag{2.22}$$

$$\begin{aligned}
 \tau &= - \int_{-\infty}^{\infty} \int_{-\infty}^{\infty} \int_0^{\infty} \sigma_t m c_y c_x f(dc_x)(dc_y)(dc_z) \\
 &= \frac{\sigma_t \rho_{\infty} U^2 \cos \theta}{2 \mathcal{S} \sqrt{\pi}} \left\{ e^{-(\mathcal{S} \sin \theta)^2} + \sqrt{\pi} (\mathcal{S} \sin \theta) [1 + \operatorname{erf}(\mathcal{S} \sin \theta)] \right\}
 \end{aligned} \tag{2.23}$$

The total force acting on a body is obtained by integrating the pressure and shear components over the surface. Analysing Eq. 2.18, Eq. 2.22 and Eq. 2.23, the heat transfer and net force depend not only on the free-stream conditions (gas composition, temperature, density, velocity), incidence (angle  $\theta$ ) and the surface temperature, as well as on both energy and momentum accommodation coefficients. Therefore, a careful

selection of the coefficients must be performed.

### 2.2.4 Continuum regime

It is in the continuum regime that the re-entering bodies will experience the maximum inertial and thermal loads, significant for their demise. The general fluid phenomena occurring during hypersonic re-entry in the continuum regime are illustrated in Fig. 2.5. These phenomena are typically captured with the use of traditional CFD tools to solve the Navier-Stokes equation, but such tools are computationally costly. There are computationally efficient impact methods that provide reasonable accuracy in the computation of pressure and heat distribution, based on the local panel inclination.

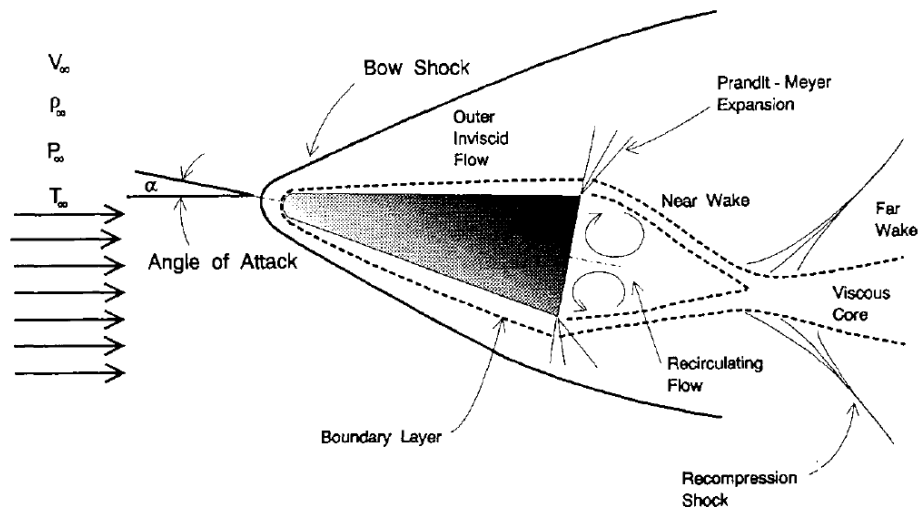


Figure 2.5: Typical re-entry flowfield (from [Etkin, 1972]).

The prediction of the aerodynamic forces acting on the body is reasonably described by the Newtonian theory, which models the flow as a stream of particles impacting the surface. According to the theory, the stream of particles does not deviate from the free-stream direction until it impacts the object's surface, after which the particles transfer the normal component of their momentum to the surface while preserving their tangential momentum, as represented in Fig. 2.6. The retrieved local pressure coefficient is given by Newton's sine-squared law, and is expressed as

$$C_p = \frac{p - p_\infty}{\frac{1}{2}\rho_\infty V_\infty^2} = 2 \sin^2 \theta, \quad (2.24)$$

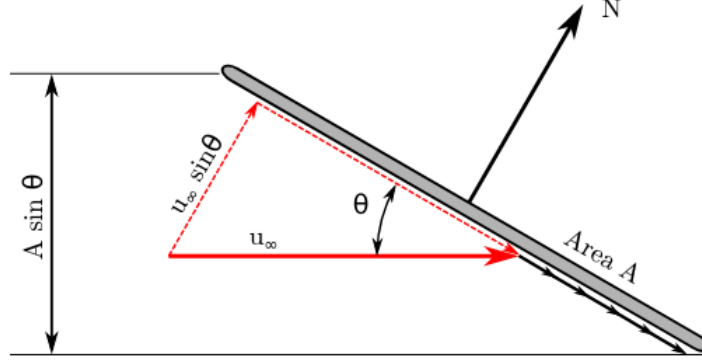


Figure 2.6: Schematic for Newtonian impact theory (from [Anderson, 2006]).

which is similar to the local pressure coefficient obtained using the free molecule regime formula (Eq. 2.22) assuming a cold wall ( $T_\infty \gg T_w$ ) and large molecular speed ratio ( $\mathcal{S} \gg 1$ ). In the Newtonian formulation, the pressure coefficient is only dependent on the local surface inclination angle and presents the maximum value of  $C_p = 2$  at the stagnation point. However, the traditional Newtonian theory does not account for the total pressure loss across the normal shock. Thus, a modification to the theory was proposed by Lees [Lees, 1955], known as the modified Newtonian theory, and expressed as:

$$C_p = C_{p,max} \sin^2 \theta. \quad (2.25)$$

where  $C_{p,max}$  corresponds to the stagnation pressure coefficient behind the normal shock, given by

$$C_{p,max} = \frac{2}{\gamma M_\infty^2} \left( \left[ \frac{(\gamma + 1)^2 M_\infty^2}{4\gamma M_\infty^2 - 2(\gamma - 1)} \right]^{\frac{\gamma}{\gamma-1}} \left[ \frac{1 - \gamma + 2\gamma M_\infty^2}{\gamma + 1} \right] - 1 \right). \quad (2.26)$$

The constant value of  $C_{p,max} = 2$  defined in the traditional Newtonian theory is obtained in the limiting case of  $M_\infty \rightarrow \infty$  and  $\gamma \rightarrow 1$ .

The pressure applied by the fluid to local panels that are not directly exposed to the flow, denoted as the shadowed region of the body, is assumed to be equal to the free-stream pressure as there are no particles impacting the surface. Therefore,  $C_p = 0$  in the shadowed regions. The pressure distribution over the discretized surface is obtained with the corresponding pressure of each local panel. Upon pressure integration over all the panels, the global aerodynamic forces and moments acting on the body can be obtained.

The high-speed flows encountered during re-entry also generate high thermal loads that need to be carefully predicted in order to assess the correct design of the thermal protective system, or to verify the full demise of the spacecraft and analyse the casualty risk. The correct prediction of heat flux in hypersonic flow is complex: the high temperatures at the shock layer may cause the dissociation and ionization of the flow molecules, which can then recombine as the flow approaches the body, given the surface catalicity and properties of the surrounding flow.

According to Lees [Lees, 1956], the convective heat transfer rate for the laminar boundary layer can be approximated as:

$$\dot{q}_{conv} = \dot{q}_{cond} + \dot{q}_{diff} = -\frac{k}{c_p} \left( \frac{\partial h}{\partial y} - \sum h_i \frac{\partial c_i}{\partial y} \right) + \rho D_{ij} \sum h_i \frac{\partial c_i}{\partial y} \quad (2.27)$$

where  $k$  is the thermal conductivity coefficient of the gas,  $c_p$  is the specific heat at constant pressure,  $h$  is the static enthalpy,  $h_i$  is the enthalpy of species  $i$ ,  $c_i$  is the species concentration by weight, and  $D_{ij}$  is the binary diffusion coefficient. Because of the close proximity between the atomic weights and properties of oxygen and nitrogen, the gas in the boundary layer can be assumed as a binary mixture, and the concentrations of nitric oxide, ions and electrons can be ignored for flight Mach below 25 [Lees, 1956]. The first term of Eq. 2.27 corresponds to heating due to conduction and the second term to heating due to diffusion. The mass diffusion due to thermal gradients is small in comparison to mass diffusion due to concentration gradients and is usually neglected [Lees, 1956].

The difference between the boundary layer edge enthalpy and the cooled wall enthalpy is the main driver of the conduction mechanism for heat convection to the

objects' surface. The diffusion mechanism is driven by the mass gradient within the boundary layer, which describes the chemical enthalpy due to the occurring processes. If atoms that diffused to the wall recombine due to the surface catalytic effect, convective heating is increased as the energy released during recombination is transferred to the surface.

Lees [Lees, 1956] studied the heat transfer over blunt-nosed bodies under typical hypersonic atmospheric re-entry conditions, making a pioneering step forward in the analysis of reacting flows, and applied a locally self-similar formulation to predict the heat transfer rate at the stagnation point for an equilibrium boundary layer and highly cooled walls, given as

$$\dot{q}_s = \frac{0.50 \times 2^{k/2}}{Pr^{2/3}} \frac{\sqrt{\rho_e \mu_e V_\infty} h_s}{\sqrt{R_N}} G(M_\infty, \bar{\gamma}, \gamma_\infty) \quad (2.28)$$

where  $k = 0$  for a planar body and  $k = 1$  for an axisymmetric body. The subscripts  $e$  and  $s$  denote the edge of the boundary layer and stagnation point respectively,  $R_N$  is the nose radius,  $Pr$  is the average Prandtl number generally assumed to be equal to 0.71, and

$$G(M_\infty, \bar{\gamma}, \gamma_\infty) = \left( \frac{\bar{\gamma} - 1}{\bar{\gamma}} \right)^{0.25} \left( 1 + \frac{2}{\gamma_\infty - 1} \frac{1}{M_\infty^2} \right)^{0.25} \left( 1 - \frac{1}{\gamma_\infty M_\infty^2} \right)^{0.25} \quad (2.29)$$

where  $\bar{\gamma}$  is the mean specific heat ratio behind the shock wave.

An alternative formulation was presented by Sibulkin [Sibulkin, 1952] and the same expression was later deduced by van Driest [van Driest, 1956, van Driest, 1958] to compute the heat flux at the stagnation point of a body of revolution in a uniform, external, steady flow. In the formulation, chemical processes occurring at the shock layer were not considered. The equation is given as

$$\dot{q}_s = 0.763 Pr^{-0.6} (\rho_s \mu_s)^{0.5} \sqrt{\left( \frac{du_e}{dx} \right)_s} (h_s - h_w) \quad (2.30)$$

where the term  $\left( \frac{du_e}{dx} \right)_s$  is the velocity gradient over the curvilinear abscissa at the

stagnation point, as illustrated in Fig. 2.7.

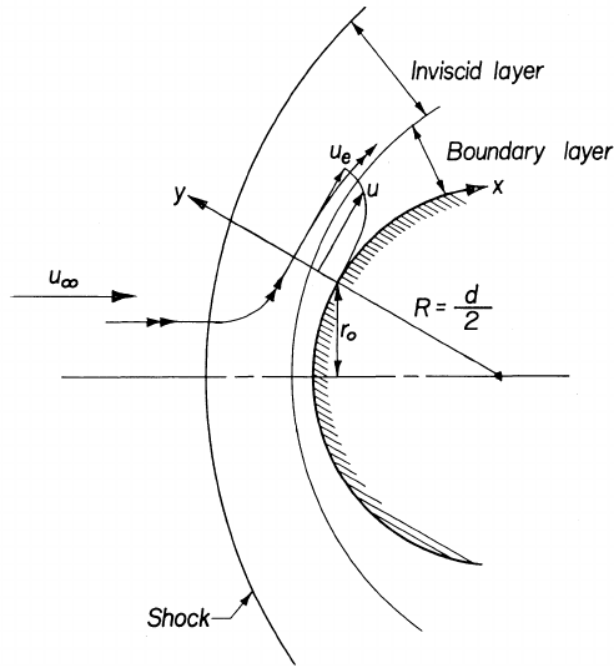


Figure 2.7: Stagnation flow past a blunt body (from [Goulard, 1958]).

Further work has been conducted by Fay and Riddell [Fay and Riddell, 1958] on the development of an empirical correlation to explain heat transfer at the stagnation point in dissociated air. The correlation was based on a large number of calculations, covering altitudes from 7.6 km to 36.6 km, flight velocities from 1.8 km/s to 7 km/s and wall temperatures from 300 K to 3000 K. The analysis has been performed for boundary layers in chemical equilibrium and for frozen boundary layers considering both fully-catalytic and no-catalytic surfaces. For a frozen boundary layer, the recombination rates ( $k_w$ ) are sufficiently small such that the occurring recombination processes occurring in the boundary layer are due to the catalicity effect of the surface, and the local temperature and species concentration are independent of one another. For a boundary layer in chemical equilibrium, the recombination rates of the atoms are sufficiently large such that the flow is always in local thermochemical equilibrium, and the boundary layer can be described using either local temperature or the concentration distribution of the chemical species. The general expression proposed by Fay and Riddell is formulated as

$$\dot{q}_s = 0.763 Pr^{-0.6} (\rho_s \mu_s)^{0.4} (\rho_w \mu_w)^{0.1} \sqrt{\left(\frac{du_e}{dx}\right)_s} (h_s - h_w) \left[1 + (Le^\alpha - 1) \left(\frac{h_D}{h_s}\right)\right] \quad (2.31)$$

where  $Le$  is the Lewis Number,  $h_D$  is the molecule dissociation enthalpy at the boundary layer edge. For the analysis conducted by Fay and Riddell, the stagnation point velocity gradient is given by the modified Newtonian theory as

$$\left(\frac{du_e}{dx}\right)_s = \frac{1}{R_N} \sqrt{\frac{2(p_s - p_\infty)}{\rho_s}}. \quad (2.32)$$

The value of  $\alpha$  determines the type of analysis the correlation predicts: for a boundary layer in chemical equilibrium  $\alpha = 0.52$ ; for a frozen boundary layer with fully catalytic wall  $\alpha = 0.63$ ; for a frozen boundary layer with no catalytic wall  $\alpha = -\infty$ . It is important to notice that the formulation proposed for boundary layers in chemical equilibrium and frozen with fully catalytic wall are similar, differing only on the exponent of the Lewis number, suggesting a similar heat transfer rate as the Lewis number tends to unity.

Sutton and Graves [Sutton et al., 1971] have further extended the theoretical analysis conducted by Lees, Fay and Riddell, and developed a general relation for arbitrary gases and gas mixtures in chemical equilibrium by analysing over 22 gas mixtures. The derived general expression was simplified by Sutton and Graves using several assumptions, arriving at a final formulation expressed as

$$\dot{q}_s = K \sqrt{\frac{p_e}{1.01325 \times 10^5 R_N}} (h_s - h_w) \quad (2.33)$$

where  $K$  is defined as the heat transfer coefficient. The constant  $(\frac{1}{1.01325 \times 10^5})$  is applied to convert the pressure from Pascal to a standard atmosphere unit, as used in the derivation of the formula. The heat transfer coefficient is given as

$$K = \frac{0.0885}{(Pr_w)^{0.6}} \left(\sum \frac{c_{0,i}}{M_{0,i} \gamma_{0,i}}\right)^{-0.5} \quad (2.34)$$

where  $c_{0,i}$  is the mass fraction of each species in the air,  $M_{0,i}$  is the molecular weight

of each species and  $\gamma_{0,i}$  is the transport parameter, where the values can be found in [Sutton et al., 1971] for the analysed gases. The subscript 0 denotes the original composition of the cold mixture, i.e. the local composition of the atmosphere.

The mentioned heat flux formulations are some of the most commonly used to predict the heat transfer rate at stagnation points. Information on alternative empirical and semi-empirical formulations can be found in [Park et al., 2021].

### Catalytic effects

Assuming a chemically frozen boundary layer, Goulard [Goulard, 1958] formulated an expression for the convective heat transfer at the stagnation region in chemically frozen boundary layers, considering the effect of partly catalytic walls in terms of a recombination coefficient. In his work, the total heat flux is divided into two main contributors: thermal energy conduction ( $\dot{q}_c$ ) and diffusive heat transfer ( $\dot{q}_d$ ) due to surface catalytic recombination. The total heat transfer is written as

$$\dot{q}_w = 0.664Pr_w^{-2/3} (\mu_e \rho_e)^{0.5} \sqrt{\left(\frac{du_e}{dx}\right)_s} h_s \left[ 1 + \left( Le^{2/3} \varphi - 1 \right) \frac{h_D}{h_s} \right] \quad (2.35)$$

where  $\varphi$  is a correction factor used to describe the effect of the catalytic rate  $k_w$  in the surface heat transfer. The correction factor is calculated as

$$\varphi = \frac{1}{1 + \frac{0.47Sc^{-2/3}(2\mu_s\rho_s)^{0.5}\sqrt{\left(\frac{du_e}{dx}\right)_s}}{\rho_w k_w}} \quad (2.36)$$

where  $Sc$  is denoted as the Schmidt number. The catalytic rate depends on the catalytic recombination coefficient ( $\gamma$ ) at the wall, given as the following equation:

$$k_w = \gamma \sqrt{\frac{k_B T_w}{2\pi m}} \quad (2.37)$$

The catalytic recombination coefficient (also known as the gamma model) handles the catalysis process in a macroscopic manner and is widely used in the analysis of thermal protection systems [Goulard, 1958, Scott, 1973].

**Velocity gradient prediction**

The equations deduced by Fay and Riddell and by Sutton and Graves strongly depend on the tangential velocity gradient at the stagnation point  $\frac{du_e}{dx}$ . According to the inherent physical assumptions, the velocity gradient calculation approaches can be divided into four methods: Newtonian theory [Lees, 1955], Fay and Riddell approximation [Fay and Riddell, 1958], Stokes and Truitt model [Truitt, 1960], and an integral method derived by Olivier [Olivier, 1993, Olivier, 1995].

The Newtonian theory suggests that the pressure results from the transfer of the normal velocity vector across a body, while the conservation of the tangential vector is maintained. The velocity gradient can be represented as

$$\left(\frac{du_e}{dx}\right)_s = \frac{u_\infty}{R_N}. \quad (2.38)$$

However, the prediction using Newton's theory is a crude approximation, and other methods should be used [Ilich et al., ].

In their work, Fay and Riddell derived a formulation for the velocity gradient prediction using a one-dimensional inviscid momentum equation and assuming a Newtonian pressure distribution. The equation is given as

$$\left(\frac{du_e}{dx}\right)_s = \frac{1}{R_N} \sqrt{\frac{2(p_s - p_\infty)}{\rho_s}}, \quad (2.39)$$

and is considered an improvement to the pure Newtonian formulation, as it accounts for post-shock conditions. To account for the dependency on the shock stand-off distance ( $\Delta$ ), Stokes and Truitt derived a new formulation, assuming an incompressible rotational flow, which is a good approximation for low temperature or equilibrium flows. The equation is given as

$$\left(\frac{du_e}{dx}\right)_s = \frac{3}{2} \frac{u_e}{R_N} \left[ \frac{(1 + \bar{\Delta})^3}{(1 + \bar{\Delta})^3 - 1} \right] \quad (2.40)$$

where  $\bar{\Delta} = \frac{\Delta}{R_N}$  is the dimensionless shock stand-off distance. To include vorticity, compressibility and high-temperature gas effects, Olivier derived an integral method

based on inviscid conservation equations. The velocity gradient can be expressed as

$$\left(\frac{du_e}{dx}\right)_s = \frac{u_\infty}{R_N} \frac{1 + \bar{\Delta}}{\bar{\Delta}} \frac{p_s - p_2}{\rho_\infty u_\infty^2} \frac{\rho_2}{\rho_s} \quad (2.41)$$

here the subscript 2 refers to the post-shock conditions, considering a normal shock relation.

Both Stokes and Truitt's method and Olivier's formulation consider the influence of the shock stand-off distance on the evaluation of the tangential velocity gradient. Figure 2.8 presents experimental as well as predicted values of the shock stand-off distance using different formulations. Several representative shock stand-off correlations based on experimental data have been proposed in the literature, such as Freeman for real gas regimes, Lobb for non-reacting or frozen flows in high Mach number regimes and Billig for perfect gas regimes [Olivier, 1995]. They are respectively expressed as

$$\bar{\Delta}|_{Freeman} = \frac{\rho_\infty}{\rho_2} \quad (2.42)$$

$$\bar{\Delta}|_{Lobb} = 0.82 \frac{\rho_\infty}{\rho_2} \quad (2.43)$$

$$\bar{\Delta}|_{Billig} = 0.143 \exp\left(\frac{3.24}{M_\infty^2}\right) \quad (2.44)$$

where  $\frac{\rho_\infty}{\rho_2}$  represents the density ratio across the shock.

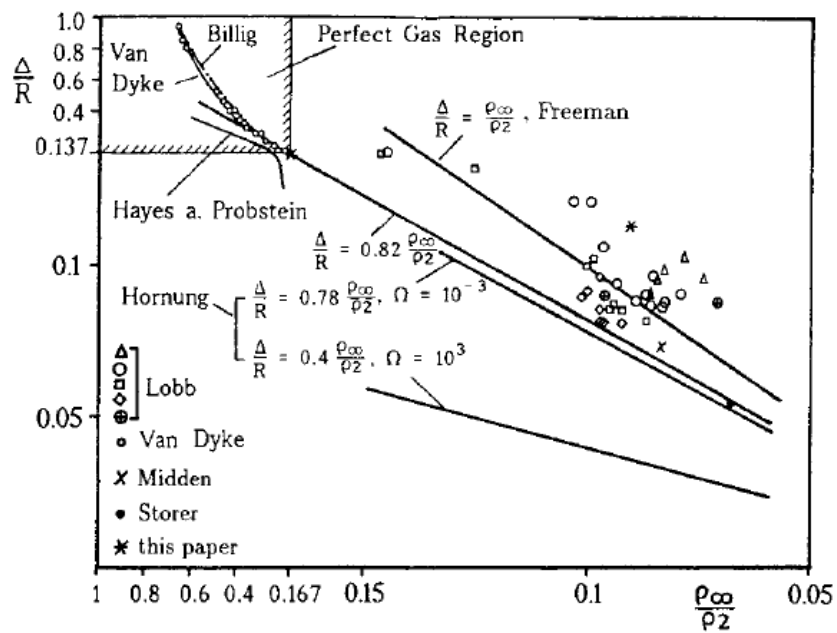


Figure 2.8: Shock stand-off distance on spheres versus density ratio and free-stream Mach number (from [Olivier, 1995]).

## Chapter 3

# Atmospheric Re-entry Analysis

Re-entry analysis and ground risk assessment have gained significant interest over the last decades. Several space agencies and research institutes have developed fast and accurate tools to assess the trajectory and demise process of spacecraft and rocket bodies during re-entry [niu Wu et al., 2011]. The objects' fragmentation and demise are determined by the flight dynamics, structural conditions, aerodynamics and heat load history during re-entry. However, surviving fragments pose a non-negligible risk to the ground population. The destruction analysis of spacecraft requires the physical and geometrical modelling of the spacecraft and its components.

Accurately predicting the re-entry time and location of uncontrolled space objects is challenging. Considerable uncertainty arises in re-entry prediction due to sparse and inaccurate position tracking and atmospheric data, complex shapes of the re-entering objects and incorrect modelling of aerodynamic and aerothermal loads [Pardini and Anselmo, 2013]. Achieving reliable results is crucial to mission planning. However, it has been noticed there is a non-negligible variation in the results produced by distinct re-entry tools for several different studies [Park et al., 2021, Annaloro et al., 2017a]. Each tool can employ different physical models, which introduces unique uncertainty profiles. To assess uncertainties and offer a set of best practices in modelling, ESA has developed a tool-agnostic framework for the probabilistic assessment of destructive re-entry, known as PADRE [Beck et al., 2019], and is based on a comprehensive review of the key variables for spacecraft demise. The baseline model for re-entry uncertainty is

reported in the ESA Demise Verification Guidelines (DIVE) [European Space Agency, 2020] for the system, equipment and material level. A summary of the uncertainties associated with the physical processes occurring during destructive re-entry is expressed in Table 3.1. It is important to notice that for more complex shapes and physical processes, the associated uncertainty may be larger [Beck et al., 2021].

Table 3.1: Uncertainties associated with physical properties involved in the destructive re-entry risk assessment [De Persis and Lemmens, 2023].

Parameter	Uncertainty
Aerodynamic drag	Continuum: $\pm 10\%$ uniform
	Transitional: $\pm 50\%$ on characteristic length scale, uniform
	Free molecular: $\pm 10\%$ uniform
Heat flux	Continuum: $\pm 30\%$ uniform
	Transitional: $\pm 50\%$ on characteristic length scale, uniform
	Free molecular: $\pm 10\%$ uniform
Oxidised emissivity	$\pm 25\%$ triangular, Maximum does not exceed 1
Specific heat capacity	$\pm 5\%$ normal three sigma limit
Latent heat of melt	$\pm 5\%$ normal three sigma limit
Alloys melt temperature	$\pm 30\text{ K}$ uniform
Atmospheric density	$\pm 10\%$ normal one sigma

The tools used to simulate atmospheric re-entry are classified into two categories, according to the correspondent fidelity in the representation of the spacecraft [Lips and Fritsche, 2005]: the object-oriented method and the spacecraft-oriented method. A more in-depth description of these methods is written in Appendix A.

Most available re-entry tools fall under the category of object-oriented methods [Choi et al., 2017], such as ORSAT [Dobarco-Otero et al., 2005], DRAMA [Pontijas Fuentes et al., 2019] and DEBRISK [Omalý and Spel, 2012]. These methods represent the complex shapes of satellites as a collection of predefined basic shapes. This kind of tool usually employs simplified methods, greatly reducing computational expense and allowing for a fast assessment of the risk of casualty on the ground or statistical analysis [De Persis and Lemmens, 2023]. For this reason, object-oriented methods are commonly used in the initial spacecraft design phases when a large number of trade-offs need to be accounted for.

Spacecraft-oriented methods, such as PAMPERO [Annaloro et al., 2015] and SCARAB

[Koppenwallner et al., 2005], attempt to meticulously emulate spacecraft geometry and mass distribution, providing more accurate predictions than object-oriented methods at the expense of higher computational costs. The tools provide a more detailed understanding of the occurring fragmentation and demise processes and rigorous analysis of the spacecraft components' behaviour throughout the entire re-entry process. The spacecraft-oriented tools are vastly used in the later project phases when more detailed system-level knowledge is required and casualty risk requirements are verified.

In recent years, due to the computational expense of spacecraft-oriented methodology, some tools were developed using a combination of spacecraft- and object-oriented methods, such as the case of SAMj [Beck et al., 2015] and FOSTRAD [Falchi et al., 2017]. This new approach allows us to capture critical aspects concerning the use of spacecraft-oriented tools while finding a balance between modelling fidelity and computational requirements.

### 3.1 Key Modules for Destructive Re-entry Analysis Tools

At the base level, the tools used for re-entry simulation are composed of common disciplinary modules that are dependent on one another and exchange information among them at each time step. A complete analysis requires a multidisciplinary software system that can account for:

- geometry modelling,
- assessment of flight dynamics and tracking until ground impact or complete demise,
- analysis of the aerodynamic and aerothermal loads,
- analysis of local heating and resultant ablation,
- evaluation of the mechanical loads, structural deformation and fragmentation.

### 3.1.1 Geometry Modelling

**Object-oriented tools:** The spacecraft is represented as a set of simple geometric objects, such as spheres, plates, cylinders and boxes, which are defined by the user. The earlier versions of object-oriented tools represented the spacecraft using a simple parent/children relationship, where the vehicle is modelled as a basic container (parent), encompassing the spacecraft components (children), again represented as simple shapes. Later versions of object-oriented tools have included the ability for unlimited relationships of *connected-to* and *included-in* types. The first relationship allows to account for the shadowing of the different components, and the later relationship is similar to the parent/children, but allows for recursive containerization. More recently, object-oriented methods have evolved to extend the relationship capability between primitive components by including joints to link the primitives [De Persis and Lemmens, 2023]. As additional primitives are included, the geometrical representation of the spacecraft improves, tending to approximate the representation provided by spacecraft-oriented methods.

**Spacecraft-oriented tools:** The spacecraft geometry representation is not restricted to basic shapes. Instead, it is possible to analyse arbitrarily shaped components by importing information from 3D CAD or geometry files. The components have panelized surfaces and the structure is formed by non-conforming volume panels in the case of SCARAB [Koppenwallner et al., 2005], while PAMPERO [Van Hauwaert et al., 2022] uses conforming volume cells. The geometry can be updated along the trajectory based on breakup and demise events. Additionally, the generated debris are not required to have the same shape as the original components affected by the events.

### 3.1.2 Flight Dynamics Trajectory Modelling

**Object-oriented tools:** The trajectory of the spacecraft and debris is usually computed using a 3 Degrees of Freedom (DoF) ballistic model, and therefore the dynamic equations for the object's attitude are not directly solved. Instead, random tumbling or specific attitude patterns based on the object's shape can be specified. However, some object-oriented tools employ a 6 DoF while maintaining the simplicity

of an object-oriented methodology [Beck et al., 2017].

**Spacecraft-oriented tools:** The flight dynamics trajectory modelling is usually performed employing a 6 DoF, although there are spacecraft-oriented tools that also have the option to run it with 3 DoF [Sourgen et al., 2015].

### 3.1.3 Aerodynamics and Aerothermodynamics Modelling

**Object-oriented tools:** The aerodynamic and heat flux coefficients acting on the objects are retrieved using lookup databases that store the relevant information according to the different shapes, orientations and flight conditions. The coefficients are commonly computed using the Schaaf-Chambre method for the free molecular flow regime, the Newtonian method for the continuum flow regime and a bridging function for the transitional regime [Lips and Fritsche, 2005]. The aerothermal heat flux coefficient is given as the sum of the different heat contributions, respectively convective heat flux, radiative heat flux and oxidation heat flux if available in the tool (ORSAT, DEBRISK) [Ostrom et al., 2019, Annaloro et al., 2021], and are computed using engineering correlations, usually assuming constant surface temperature for each object. In the case of the DEBRISK tool [Annaloro et al., 2021] and recent versions of DRAMA [Pontijas Fuentes et al., 2019], both aerodynamic and heat coefficients are retrieved from a large aerothermodynamics database built for the hypersonic continuum regime using CFD simulations. To account for the changes in attitude due to rotation, tumble-averaged values are calculated.

**Spacecraft-oriented tools:** The methods used are similar to the ones employed by object-oriented tools. However, instead of using a lookup table, the loads are computed on the fly using the local inclination approach, for each panel of the primitive's surface, thus relying on approximations for locally flat plates. Later versions of spacecraft-oriented tools included aerothermodynamic corrections based on local radius of curvature, flow stream length, self-shock impingement, and radiative shock heating [Kanzler et al., 2021].

### 3.1.4 Structural and Fragmentation Analysis

**Object-oriented tools:** Fragmentation is typically modelled by assuming a fragmentation altitude where the primitives defined for the simulation are released from the parent object. The altitude is usually fixed at 78 km for the main break-up event, and 95 km for solar panels [Lips and Fritsche, 2005], and some tools can use additional criteria, such as temperature triggers for breakup altitude prediction [niu Wu et al., 2011], where the spacecraft is assumed to break when the surface temperature reaches the defined temperature. The footprint of the fragments varies according to the break-up altitude, the state of the spacecraft at break-up conditions and the fragment characteristics, such as mass, shape and material.

**Spacecraft-oriented tools:** The evaluation of fragmentation is performed at every time step by checking for structural stress failure, either performing Finite Element Analysis (FEM) [Prigent et al., 2017], or analysing local stress considering pre-defined cut views [Koppenwallner et al., 2005]. The failure criterion is normally based on the Von Mises stress [niu Wu et al., 2011].

### 3.1.5 Thermal Analysis

**Object-oriented tools:** The temperature computation is usually performed via a lumped thermal mass model, a  $0D$  approach that assumes the heat conductivity to be instantaneous. Therefore, the temperature of the object is uniform. The object is considered to start demising when the absorbed heat surpasses the characteristic heat of ablation of the considered material. After this point, at every time step, the mass of the object is updated to reflect the excessive heat absorbed. Some tools, such as DEBRISK, DRAMA and SAMj, have the ability to consider heat conduction [De Persis and Lemmens, 2023]. The demise process does not alter the shape or size of the fragments.

**Spacecraft-oriented tools:** Thermal analysis is carried out in each time step, and ablation is verified at the volume panel/cell level. If the cell temperature reaches the melting temperature of the material, excessive heat is utilized to drive local thermal ablation. In spacecraft-oriented tools, heat conduction between single-cell volumes is

considered [Van Hauwaert et al., 2022].

### 3.2 High-fidelity Modelling for Re-entry Analysis

Increased accuracy in the simulation of the physical processes occurring during object descent through the atmosphere could be achieved by the use of high-fidelity methods: CFD/DSMC methods for the simulation of the flow conditions surrounding the object, and finite element and peridynamic methods for the structural, thermal, and fracture analysis. The coupling of higher-fidelity methods allows for a more detailed understanding of phenomena like shock impingement, shock-shock interactions, the degradation of materials through ablation and gas-surface interactions, and the structural dynamics in response to the external and internal forces, material conditions, and temperature, which are critical for accurately predicting the demise process.

However, due to the computational cost of the high-fidelity methods, it is not feasible to perform a full re-entry study just by employing the mentioned methods throughout the simulation. Instead, several analysis tools have surrogate models built from CFD and DSMC simulations [Braun et al., 2020, Van Hauwaert et al., 2022], which are used to improve the aerodynamic and aerothermodynamic estimations over the surface of the objects.

Nevertheless, several high-fidelity tools and toolsets are currently under development, such as the SMURFS (Spacecraft Motion and behavior Under Re-entry for Fragmentation Simulation) toolset, which integrates flow computations in the rarefied regime, thermo-mechanical analysis, and trajectory propagation [De Persis and Lemmens, 2023]. Additionally, the MISTRAL [Van Hauwaert et al., 2022] and BLIZZARD [Ledermann et al., 2022] tools are currently being developed to be coupled with PAMPERO to improve the accuracy of aerodynamic and aerothermodynamic predictions. The tool MISTRAL includes both DSMC and CFD solvers capable of considering thermochemical non-equilibrium gas composition with weak ionisation, while the tool BLIZZARD focuses on modelling shock interaction, fluid-structure interaction, and includes an advanced structural fragmentation model by coupling FEM with a CFD

solver assuming inviscid flow.

### 3.3 Inclusion of Multi-fidelity for Re-entry Analysis

To overcome the computational expenses of high-fidelity methods, the analysis tools have incorporated a number of approaches that limit their interaction with the use of high-fidelity methods. An approach is the creation of offline surrogate models via the computation of large CFD and DSMC databases through the simulation of varied shapes and flow conditions [Van Hauwaert et al., 2022] and the creation of reduced-order models when analysis re-entering objects of complex shapes [Graham et al., 2023].

However, a major limitation in using these methods is the possibility of not adequately capturing the complex flow physics that occurs near the bodies due to their proximity and/or shape. These complex phenomena include shock-shock interaction and shock impingement on the surface of the bodies, which may lead to highly concentrated aerodynamic and aerothermodynamic loads, contributing to rapid changes in the body dynamics and thermal loads. Ultimately, such loads can lead to ablation and fragmentation.

A possible way to overcome this limitation is explored in this work, via the development of a physics-informed multi-fidelity switch that, via spatial awareness of the proximity of the re-entering objects, it allows to switch fidelity model context, only applying high-fidelity methods when necessary to capture the more complex physics while limiting the number of expensive model calls. The proposed multi-fidelity approach is further tested in Section 5.3, after the introduction of the developed re-entry analysis tool.

#### 3.3.1 A Physics-Informed Multi-Fidelity Switch

By judiciously choosing the most appropriate level of fidelity according to the complexity of flow physics, a trade-off between computational cost and physical accuracy during the entire re-entry simulation can be reached. For this matter, a fidelity switch is proposed in this work, predicting if the presence of multiple bodies can give rise

to intricate flow features. The shock impact is expected to be higher for the continuum regime than for the free-molecular regime because the generated shock waves are sharper, stronger gradients are present, and a complex system of waves is generated from the interaction. Therefore, while the overall concept applies to any flow regime, the specific results and implementation presented here focus on the multi-fidelity approach in the continuum regime. An overview of a two-fidelity aerothermodynamics workflow is presented in Figure 3.1.

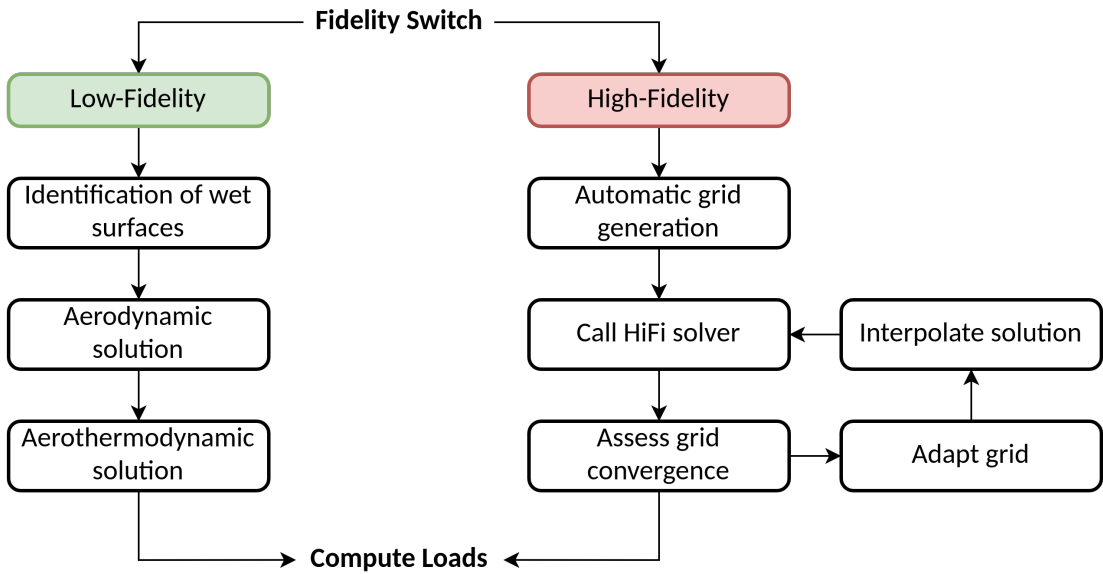


Figure 3.1: Flowchart of the multi-fidelity aerothermal modelling.

Critical events that are heavily influenced by the aerothermodynamics of shock interference are the fragmentation process and dynamics of proximal fragments since the presence of shock waves is expected to have a significant effect on the spreading of the clouds of debris. To detect if the presence of multiple bodies gives rise to intricate flow features, it is necessary to assess the position of the generated shock around the fragments. There are analytical methods to predict the shock position for simple geometries, such as the tangent wedge/cone method and shock expansion theory for attached shocks [Anderson, 2006] and Billig hyperbola formula for detached shocks [Billig, 1967]. For bodies with complex shapes, the vast majority of the methods require the post-processing of the solution obtained from high-fidelity methods such as

CFD/DSMC [Wu et al., 2013].

### 3.3.2 Billig Shock-Envelope

To achieve computationally fast but representative shock estimation even in the case of complex geometries and proximal fragments, it is here proposed to compute the so-called shock envelope around the fragments in the debris cloud. A shock envelope is intended as a single shock wave front that wraps all the shock wave fronts generated by an object or a cloud of objects. Generating a proxy to the shock envelope and identifying its spatial location will allow estimating if shock impingement on the fragments is expected or not to occur and therefore if there is a need to account for higher fidelity in simulating the aerothermodynamics of that interaction. An automatic fidelity switch criteria to choose between low- and high-fidelity models has been developed that uses Billig's formula for estimating the shock around a sphere to generate the shock envelope around the fragments in the cloud of debris. An example of a similar approach was done in the work of Catalano [Catalano et al., 2007], where Billig's expression was used to limit the computational domain over a Vega launcher in a supersonic regime. This method assumes that the detached shock wave generated by a sphere can be written as a hyperbolic function, asymptotic to the freestream Mach angle, or, in the case of a cone or wedge, to the attached shock angle,  $\theta$ . The expression formulated by Billig is given as

$$x = R + \Delta - R_c \cot^2 \theta \left[ \left( 1 + \frac{r^2 \tan^2 \theta}{R_c^2} \right)^{1/2} - 1 \right] \quad (3.1)$$

where  $R$  is the radius of curvature of the geometry at the stagnation point,  $R_c$  is the radius of curvature of the shock at the vertex,  $\Delta$  the stand-off distance, and  $\theta$  the asymptotic angle of the hyperbola. The stand-off distance and the vertex radius of curvature are given by the empirical relation proposed in the work of Ambrosio and Wortman in the continuum regime [Ambrosio and Wortman, 1962] and are respectively formulated as

$$\frac{\Delta}{R} = 0.143 \exp\left(\frac{3.24}{M_\infty^2}\right) \quad (3.2)$$

$$\frac{R_c}{R} = 1.143 \exp\left(\frac{0.54}{(M_\infty - 1)^{1.2}}\right) \quad (3.3)$$

where  $M_\infty$  is the free-stream Mach number.

Billig's formula is only dependent on the free-stream Mach number and the radius of the sphere and does not take into consideration the level of flow rarefaction, as stated in the research of Nicolas et al. [Rembaut et al., 2020], where it has been verified that with the increase in the Knudsen number, the stand-off distance given by the empirical formula further deviates from the experimental results. Therefore, caution must be taken when applying this methodology in transitional and rarefied regimes. To calculate the shock envelope using Billig's approximation, a virtual equivalent sphere is used to represent the object. The calculation is performed in the wind frame, where the free-stream velocity vector points towards the positive X-axis. The centre of the sphere is found by determining the y- and z- coordinates as the midpoint between the maximum and minimum vertex coordinates of the analyzed object. The x-coordinate of the sphere centre is equal to the minimum x-coordinate of the object. The sphere's radius is calculated to be the smallest possible size that would contain the object in the YZ plane, with the centre of the sphere located at the previously calculated position. Subsequently, Billig's formula can be applied to compute the shock envelope. An example of this approach is shown in Fig. 3.2. The approach is tested against two cases of a Mach 9.3 flow, using as geometries a cube and a cylinder, which can be visualized in Fig. 3.3 and Fig. 3.4, respectively. The shock envelope generated by the equivalent sphere contains the shock generated by the object for both cases. As it can be observed in Fig. 3.4, the approach is conservative for elongated bodies in the Y- and Z- direction, while it closely matches the shock for the test where the cylinder is elongated in the flow direction. This difference is caused by the generated virtual sphere, which has to include the entire object in the YZ plane perspective.

Due to the nature of the hyperbolic formula derived by Billig, it is possible to rewrite Eq. 3.1 for an arbitrarily positioned sphere in the wind frame. For a body  $i$

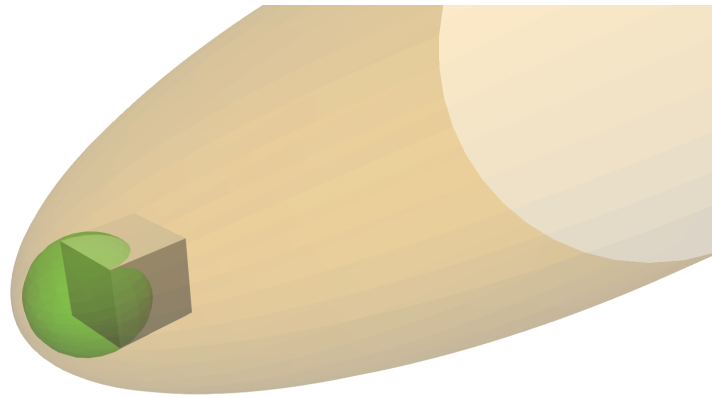
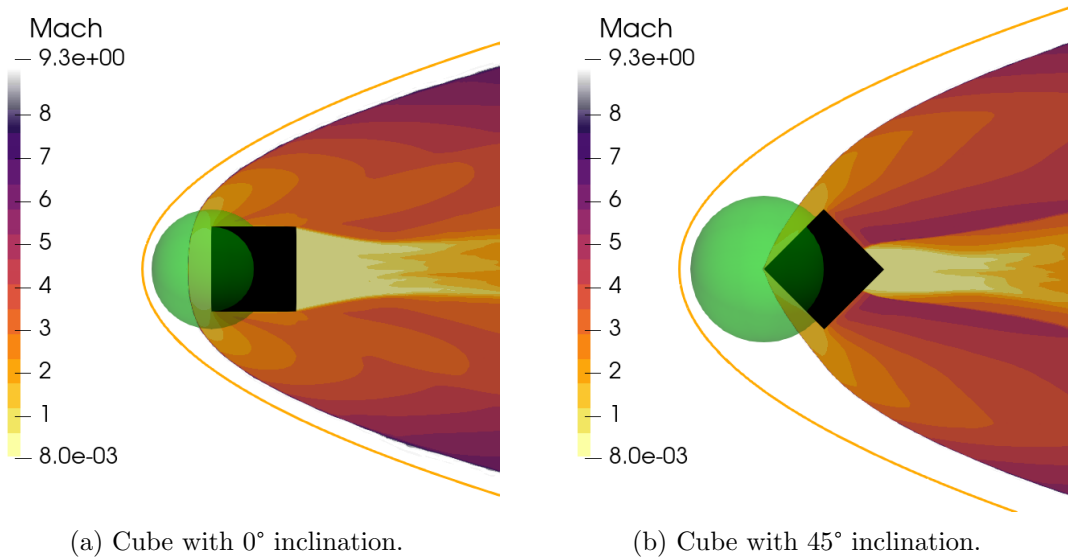


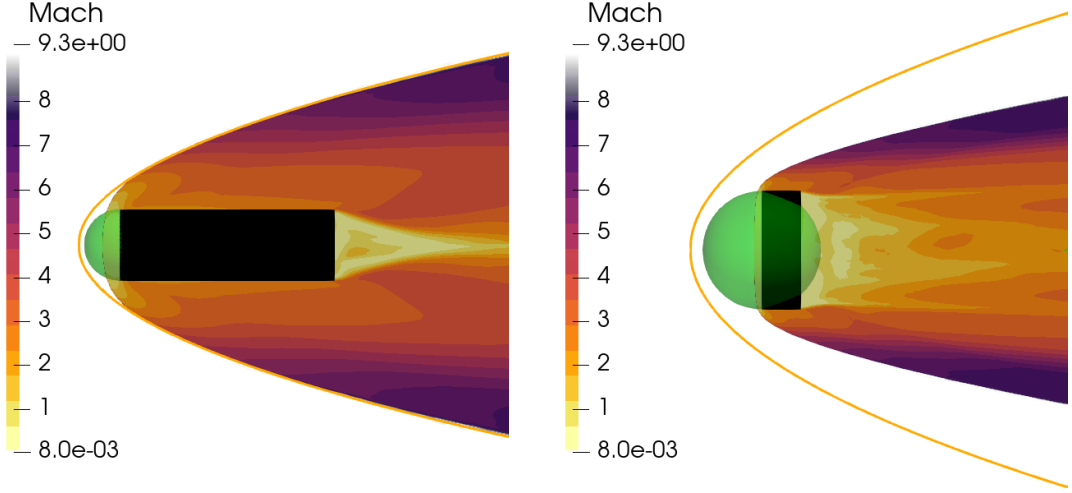
Figure 3.2: Visualization of the virtual sphere and the equivalent shock envelope for a cube geometry.



(a) Cube with  $0^\circ$  inclination.

(b) Cube with  $45^\circ$  inclination.

Figure 3.3: Shock envelope for cubic geometry at Mach 9.3



(a) Cylinder with revolution axis parallel to the flow direction. (b) Cylinder with revolution axis normal to the flow direction.

Figure 3.4: Shock envelope for cylindrical geometry at Mach 9.3

with an equivalent sphere with center at  $(x_{s_i}, y_{s_i}, z_{s_i})$ , and assuming the flow direction to be in the positive X-axis direction, the hyperbolic formula for the shock envelope can be rewritten as

$$(x - x_{s_i}) = -R_c - \Delta + R_c \cot^2 \theta \times \left[ \left( 1 + \frac{(r - r_{s_i})^2 \tan^2 \theta}{R_c^2} \right)^{1/2} - 1 \right] \quad (3.4)$$

where  $r$  is defined as

$$r = \sqrt{y^2 + z^2}. \quad (3.5)$$

Rearranging equation 3.4, the inner side of the hyperbola, which defines the shock envelope, can be defined as

$$R_c \cot^2 \theta \left[ \left( 1 + \frac{(r - r_{s_i})^2 \tan^2 \theta}{R_c^2} \right)^{1/2} - 1 \right] \geq -(R_c + \Delta). \quad (3.6)$$

For a given body  $j$ , with  $i \neq j$ , the coordinates of the  $k_{th}$  vertex of the body are

given as  $(x_{j_k}, y_{j_k}, z_{j_k})$ . If any of the vertices are inside the hyperbola, a high-fidelity solver is used to compute the aerothermal loads. Otherwise, if they are all outside the hyperbola, low-fidelity methods are used. This means that high-fidelity methods are used if any point complies with the following criteria:

$$(x_{j_k} - x_{s_i}) - R_c \cot^2 \theta \left[ \left( 1 + \frac{(r_{j_k} - r_{s_i})^2 \tan^2 \theta}{R_c^2} \right)^{1/2} - 1 \right] \geq -(R_c + \Delta), \quad \text{for } k = 0, 1, \dots, N(3.7)$$

An illustrative example of the proposed methodology for the fidelity switch criteria is presented in Fig. 3.5, where the vertex inside the envelope are flagged. The considered approach not only allows to account for objects leaving the shock envelope but also for fragments re-entering it, thus eventual interaction with the shock generated by a leading fragment can always be accounted for.

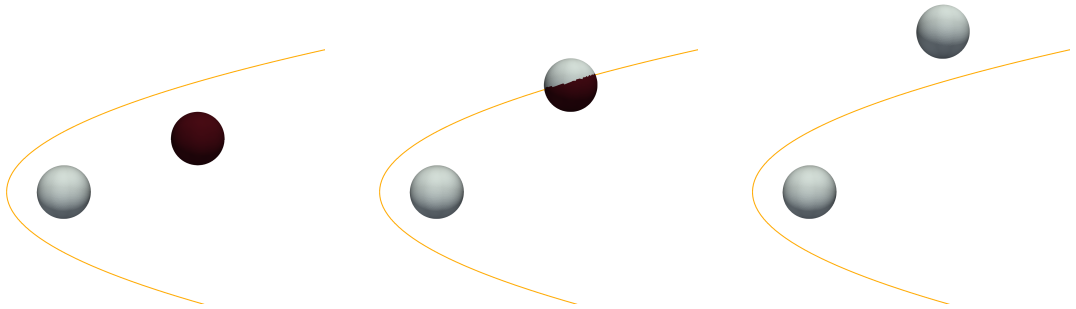


Figure 3.5: Representation of the sphere positioning in relation to the shock envelope.

## Chapter 4

# Development of a Reentry Framework

The tools described in Chapter 3 and in Appendix A have one common approach regarding fragment analysis: after break-up events, the generated debris is analysed individually. In other words, current tools do not account for interactions regarding debris proximity, thus disregarding their impact on the overall reentry process. To improve the current capabilities of reentry tools, the present work describes the development of a new modular framework for atmospheric reentry simulation, providing new methodologies to account for proximal interaction. The present implementation is currently available as a Python-based open-source software named TITAN, created from the need to revise and restructure the FOSTRAD tool to improve the computational efficiency of the physico-numerical methods and facilitate the addition of new models.

The present framework integrates the several disciplinary models crucial to the correct simulation of the reentry process, along with the extended capabilities, in a modular and loosely coupled fashion. These modules are: a geometric/inertia/meshing (GIM) module, a two-fidelity aerothermodynamic module, a component-based lumped mass thermal model, a structural model, a material database, a 6 DoF propagator, an atmospheric model and a collision model. A high-level overview of the currently implemented modules is provided in Fig. 4.1, where the individual components are detailed in the following sections.

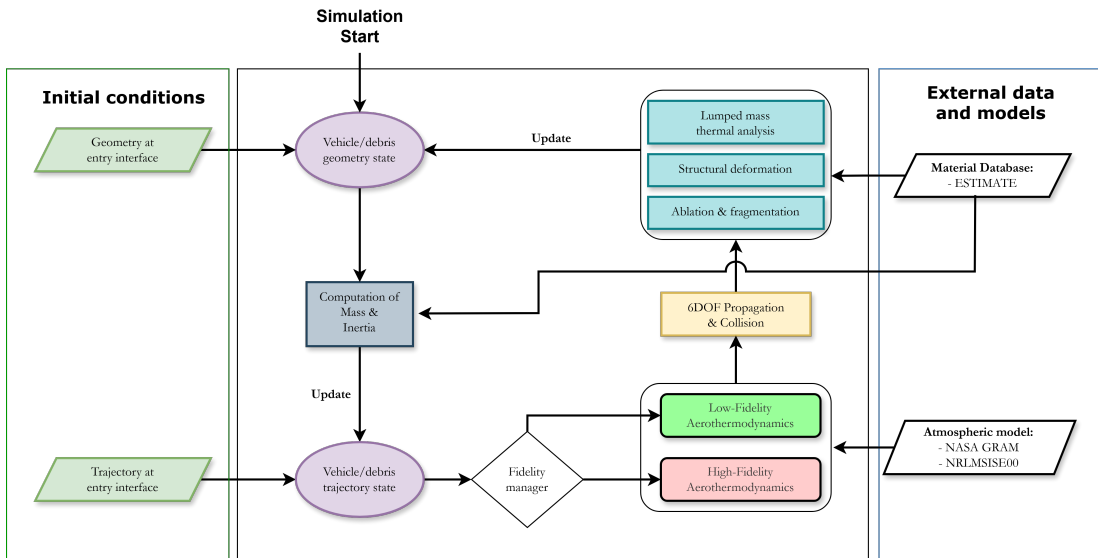


Figure 4.1: High-level overview of TITAN modules flowchart.

The run time of the framework is closely tied to the physical assumptions, simulation time-step, number of simulated components and the resolution of the surface tessellation, structural grid and flow volume, among other parameters. For an exclusive low-fidelity simulation, the run time is estimated to be in the order of seconds or minutes, according to the number and complexity of the fragments. With the inclusion of structural analysis and multi-fidelity capability, the run time estimation can be increased to hours or days, respectively.

## 4.1 Spacecraft Modelling

TITAN adopts a hybrid approach for geometrical modelling where the spacecraft is defined by connecting different components. The components are divided into fragmentable and non-fragmentable components, which are referred to as joints and primitives, respectively. Primitives are non-fragmentable, i.e., fragmentation of the structure is not allowed for this type of component but thermal demise is possible. On the other hand, joint components, which connect the different primitives to form complex objects, can be fragmented and removed from the simulation when a fragmentation criterion is met. Furthermore, joints do not require a physical body, i.e., they can be virtual.

Particularly, this type of joint is used to connect physically touching primitives. The fragmentation criterion depends on the conditions of the connected primitives, such as temperature and altitude. When the criterion is met, the joint linking the primitives is destroyed and the primitives separate.

The level of detail and intricacy in modelling the spacecraft can be varied based on the quantity and complexity of the primitives and their joint arrangements. The connection between joint-primitive bodies allows the separation of different groups of objects to be taken into account when fragmentation occurs during the simulation.

After assessing the connectivity between the different components, the geometry module assembles the multiple meshes and computes the surface element properties (area, normal vector, local radius). These properties are used in the computation of the aerothermodynamic loads, as well as the inertial properties in support of the dynamic computation. An illustrative example of the connectivity between primitives and joints is shown in Fig. 4.2, where the circled joints connect the different primitives (i.e. the solar panels and the main body of the satellite). In the present methodology, each component can be separated or removed from the simulation due to fragmentation or ablation, but cannot break up into smaller fragments as in spacecraft-oriented codes. However, the level of geometrical fidelity can be enhanced by increasing the number of primitives in the simulation, as showcased in Fig. 4.3 regarding a sphere. There is no limit to the number and complexity of primitives and joints. Asymptotically, this process of increasing the number of primitives could lead to a situation that is equivalent to spacecraft-oriented approaches.

The break-up events occurring during the re-entry simulation are modelled by setting either altitude or temperature values to act as a fragmentation trigger event. When the specified value is reached, the fragmented component is removed from the analysis, and the objects linked to the component are detached, forming a cloud of debris of which the debris's relative position and velocity are known at all times. Alternatively, a stress-based fragmentation can also be performed, where, at each time step, the local structural stress is evaluated and, if the Von Mises stress surpasses the material's yield stress, the component is considered to break up and removed from the simulation. A



Figure 4.2: Overview of the primitive-joint concept in the geometry modelling of a spacecraft.

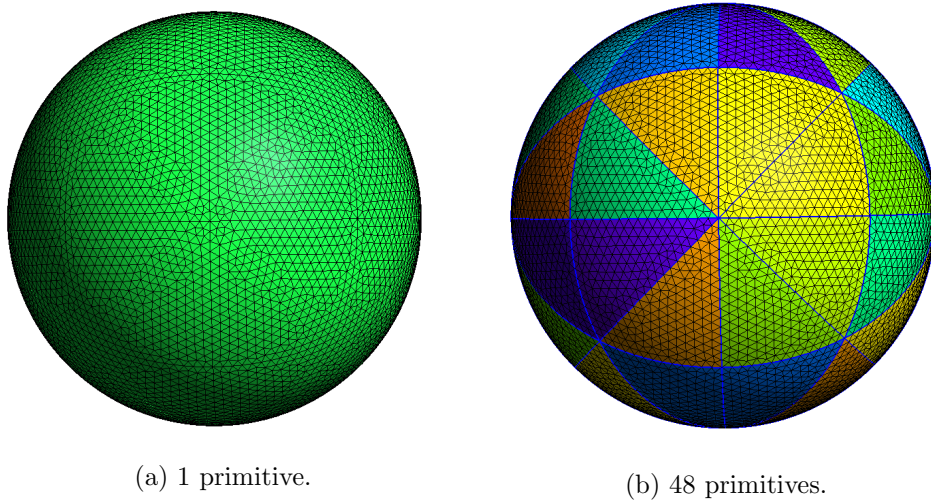


Figure 4.3: Illustration of a sphere subdivision into several components to increase simulation fidelity.

more in-depth explanation is presented in Sec. 4.7.

#### 4.1.1 Surface Mesh Handler

The computation of the aerodynamic and aerothermodynamic loads relies on the use of local panel inclination methods, which require processing the information regarding the panels that are part of the surface tessellation, namely the inclination angle, panel area and the barycenter coordinates. In TITAN, the surface mesh handler processes the geometrical properties and edge connectivity of triangular panels, checking and

removing overlapping panels in the case of components physically touching one another. This process is performed by building a list with the vertex coordinates of each panel and check for duplicates. The removal of overlapping panels is required to generate a closed, non-self-intersecting, edge-manifold mesh, i.e., each edge is bounded by two triangles. This latter step is crucial for TITAN multi-fidelity capabilities, as the mesh needs the mentioned requirements to allow high-fidelity computation.

Lees [Lees, 1956] has demonstrated that for a hemisphere and a blunted cone, surface radius plays a significant role in stagnation point laminar heat transfer. Therefore, after performing the geometry processing, the handler computes the local radius of curvature of the panels to improve heating estimation.

The geometries of the components considered for the simulation are passed to TITAN through a 3-D surface mesh file. The geometry information is read by parsing a *.STL* file, which contains information on the surfaces' triangular facets and vertex coordinates. The mesh files are loaded and transformed into a list of vertices and triangular facets, retaining the original connectivity. Once the lists are defined, they are used to compute the panel properties and the local radius distribution. All computed properties are then utilized for aerodynamic, aerothermodynamic, and re-entry analyses. In the case of objects with curved surfaces, it is important to use a mesh with enough detail to enable accurate load predictions while keeping the computational time low.

For a triangular panel  $i$ , the unitary normal vector can be computed as a function of the vertex coordinates  $A_{i,j}$  for  $j = 1, 2, 3$ , as

$$\hat{n}_i = \frac{(A_{i,2} - A_{i,1}) \times (A_{i,3} - A_{i,1})}{\|(A_{i,2} - A_{i,1}) \times (A_{i,3} - A_{i,1})\|}. \quad (4.1)$$

For the correct estimation of the surface loads, the panels' normal vector has to point outward, reflecting the side of the triangle that will be exposed to the flow. The triangle geometric barycenter is found as the weighted average of the vertex coordinates. If the uniform density is assumed, the geometric barycenter coincides with the panel centre of mass. The barycenter of the  $i$ th triangle is then calculated as

$$A_{i,B} = \frac{A_{i,1} + A_{i,2} + A_{i,3}}{3}. \quad (4.2)$$

The computation of the loads acting on the panel also required the knowledge of the panel's area, which is computed using Heron's formula.

$$Area_i = s(s-a)(s-b)(s-c), \quad \begin{cases} a = \|A_{i,2} - A_{i,1}\| \\ b = \|A_{i,3} - A_{i,1}\| \\ c = \|A_{i,3} - A_{i,2}\| \\ s = \frac{a+b+c}{2} \end{cases}. \quad (4.3)$$

In addition to the normal vector and panel area, predicting aerothermal loads requires the knowledge of the local curvature radius associated with the mesh. The radius is computed using the methodology developed by Falchi [Falchi et al., 2017], also applied in FOSTRAD. The estimation of the local radius of curvature allows us to account for the sharp variations in the surface curvature exposed to the flow which may present a higher heat transfer rate and ablate faster. Illustrative numerical examples of this phenomenon are presented in [?]

The local radius computation for a triangular face and vertices is based on the curvature estimation algorithm proposed by Rusinkiewicz [Rusinkiewicz, 2004]. For the radius estimation, TITAN first estimates the per-vertex normal according to the weighted-average formula proposed by Max [Max, 1999]. The curvature associated with each facet is then computed using the differences between facet normal and the normals of the associated vertex by using the general Gaussian principal curvature relation, defined as

$$R_i = \frac{1}{\sqrt{\kappa_{i,1}\kappa_{i,2}}} \quad (4.4)$$

where  $\kappa_{i,1}$  and  $\kappa_{i,2}$  are the principal Gaussian curvatures of the  $i$ th facet. The local vertex curvatures can also be computed by using a Voronoi-area averaging over the facets with a common vertex [Meyer et al., 2003].

It is known that local vertex and face radii may present very steep variations for

complex geometries, mainly in the vicinity of discontinuous regions. To overcome this issue, Falchi proposes the use of a local radius smoothing algorithm [Falchi et al., 2017], to improve the accuracy in the prediction of aerothermal loads during reentry. Initially, the algorithm imposes a minimum and maximum facet radii, according to a reference value. The radius for a flat surface is infinite, thus a reference maximum local radius is imposed in these extreme cases. A detailed explanation of the smoothing algorithm can be found in [Falchi, 2020].

### 4.1.2 Mass and Inertia

The mass of the assembly and respective centre, as well as the inertia tensor, are automatically computed by TITAN. During atmospheric reentry, the object is subjected to significant aerothermodynamic constraints leading to its deformation, partial or complete ablation, changing the geometrical and inertial properties. Therefore, these parameters must be automatically updated each time ablation or fragmentation occurs.

The computation of the inertial properties for arbitrary shapes lies in the idea of decomposing the object into several tetrahedral elements. In TITAN, the volumetric domains are automatically generated by coupling the open-source software GMSH [Geuzaine and Remacle, 2009], which produces a fully unstructured tetrahedral domain using the frontal Delaunay triangulation method over the components' geometrical surface. Knowing the vertex's position and connectivity information, it is possible to calculate the mass and inertia tensor for each tetrahedron and the contribution to the spacecraft's inertial parameters. To this effect, the formula outlined by Tonon [Tonon, 2005] is applied to calculate the inertia tensor.

Considering an arbitrary tetrahedron  $D$  with vertices  $A_1(x_1, y_1, z_1)$ ,  $A_2(x_2, y_2, z_2)$ ,  $A_3(x_3, y_3, z_3)$ , and  $A_4(x_4, y_4, z_4)$  for an origin point  $Q$  in the Euclidean 3-D space, the volume of a tetrahedron  $D$  is given through the calculation of the Cayley-Menger determinant [Sippl and Scheraga, 1986], which states that the squared volume of a  $k$ -dimensional simplex with  $k + 1$  points in the Euclidean space can be expressed entirely in terms of distance. For a tetrahedron ( $k = 3$ ), the volume is therefore calculated using

$$288Vol_D^2 = \begin{vmatrix} 0 & 1 & 1 & 1 & 1 \\ 1 & 0 & d_{12}^2 & d_{13}^2 & d_{14}^2 \\ 1 & d_{21}^2 & 0 & d_{23}^2 & d_{24}^2 \\ 1 & d_{31}^2 & d_{32}^2 & 0 & d_{34}^2 \\ 1 & d_{41}^2 & d_{42}^2 & d_{43}^2 & 0 \end{vmatrix} \quad (4.5)$$

where  $d_{ij}$  is the distance between vertices  $i$  and  $j$ . Assuming homogeneous tetrahedrons with density  $\rho$ , the mass is thus computed using

$$m_D = \rho Vol_D. \quad (4.6)$$

and the total mass is asserted by summing the mass of the individual  $l$ th tetrahedron of the  $k$ th component belonging to the same assembly

$$m_{assembly} = \sum_{k=1}^{n_{component}} \sum_{l=1}^{n_{tetra}} \rho_k Vol_{k,l}. \quad (4.7)$$

The centre of mass is calculated with a weighted-average equation of the mass

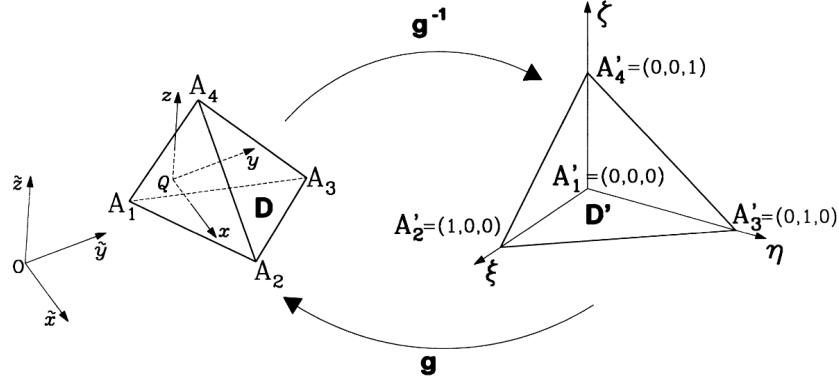
$$CM = \sum_{k=1}^{n_{component}} \sum_{l=1}^{n_{tetra}} \sum_{m=1}^4 \frac{A_{k,l,m}}{4} \frac{\rho_k Vol_{k,l}}{m_{assembly}} \quad (4.8)$$

where  $A_{k,l,m}$  is the  $m$ th vertex of the  $l$ th tetrahedron belonging to the  $k$ th component. This formulation accounts for the possibility of applying different materials to the assembly components.

The inertia tensor of a tetrahedron  $D$  is defined as

$$I_D = \begin{bmatrix} I_{xx} = \int_D \rho (y^2 + z^2) dD & I_{yx} = - \int_D \rho xy dD & I_{zx} = - \int_D \rho xz dD \\ I_{xy} = - \int_D \rho xy dD & I_{yy} = \int_D \rho (x^2 + y^2) dD & I_{zy} = - \int_D \rho yz dD \\ I_{xz} = - \int_D \rho xz dD & I_{yz} = - \int_D \rho yz dD & I_{zz} = \int_D \rho (x^2 + y^2) dD \end{bmatrix} \quad (4.9)$$

To ease the calculation of the integrals required for the inertial tensor in Eq. 4.9, Tonon proposes a change in the coordinate system through an affine transformation  $\mathbf{g}$ , as illustrated in Fig. 4.4. The linear transformation is given by


 Figure 4.4: Transformation  $\mathbf{g}$  and  $\mathbf{g}^{-1}$  (from [Tonon, 2005]).

$$\begin{bmatrix} x \\ y \\ z \end{bmatrix} = \begin{bmatrix} x_1 \\ y_1 \\ z_1 \end{bmatrix} + M \begin{bmatrix} \xi \\ \eta \\ \zeta \end{bmatrix}, \quad M = \begin{bmatrix} x_2 - x_1 & x_3 - x_1 & x_4 - x_1 \\ y_2 - y_1 & y_3 - y_1 & y_4 - y_1 \\ z_2 - z_1 & z_3 - z_1 & z_4 - z_1 \end{bmatrix} \quad (4.10)$$

and  $M$  is equivalent to the Jacobian of the transformation matrix. The determinant of the Jacobian matrix is equal to

$$\begin{aligned} \text{DET}(M) = 6 \text{Vol}_D = & -z_2x_3y_1 - x_2y_4z_3 + y_2x_3z_1 - y_2x_1z_3 - y_2x_4z_1 + x_2y_4z_1 + x_2y_3z_4 \\ & - x_2y_3z_1 - x_2y_1z_4 + x_2y_1z_3 - x_1y_3z_4 + x_1y_4z_3 - y_2x_3z_4 + y_2x_1z_4 \\ & + y_2x_4z_3 + y_1x_3z_4 - y_1x_4z_3 + z_2x_3y_4 - z_2x_1y_4 - z_2x_4y_3 + z_2x_4y_1 \\ & + z_2x_1y_3 - z_1x_3y_4 + z_1x_4y_3 \end{aligned} \quad (4.11)$$

where  $\text{Vol}_D$  is the volume of the tetrahedral  $D$ . The transformation  $\mathbf{g}^{-1}$  normalizes the tetrahedron  $D$  into a tetrahedron  $D'$  as suggested in Fig. 4.4. Because transformation  $g$  is regular and the tetrahedron  $D$  is bounded by regular surfaces, the integration of a continuous generic function over  $D$  can be expressed as

$$\int_D f(x, y, z) dD = \int_{D'} f[x(\xi, \eta, \zeta), y(\xi, \eta, \zeta), z(\xi, \eta, \zeta)] \cdot |DET(M)| dD' \quad (4.12)$$

and because  $D'$  is normal to the plane  $(\xi, \eta)$  and the projection of  $D'$  onto the plane  $(\xi, \eta)$  is normal to the  $\xi$  axis, then

$$\int_D f(x, y, z) dD = |DET(M)| \int_0^1 d\xi \int_0^{1-\xi} d\eta \int_0^{1-\xi-\eta} f[x(\xi, \eta, \zeta), y(\xi, \eta, \zeta), z(\xi, \eta, \zeta)] d\zeta \quad (4.13)$$

which can be used to replace the integrals of the inertia tensor in Eq. 4.9. The detailed solution is expressed in Appendix B. The inertia tensors of each tetrahedron are calculated using the position of the centre of mass as the origin point. Thus, the inertia matrix of the assembly is equal to the sum of the inertia tensors of the tetrahedrons composing the assembly

$$I_{assembly} = \sum_{k=1}^{n_{component}} \sum_{l=1}^{n_{tetra}} I_{k,l}. \quad (4.14)$$

## 4.2 Aerodynamics and Aerothermodynamics Computation

The low-fidelity methods adopted in the present framework follow the hybrid approach of having each component forming the spacecraft represented by a set of facets for which a local evaluation of aerodynamic loads and heat fluxes is performed.

### 4.2.1 Flow Properties Calculation

Before evaluating the aerodynamics and aerodynamic loads, the information on the external and post-shock flow properties is processed. The thermodynamic properties of the mixture are computed using the Mutation++ library [Scoggins and Magin, 2014], which was integrated into TITAN. The library can efficiently compute the thermodynamic, transport and chemical kinetic gas properties for any given custom mixture,

thus facilitating the computation of flow properties for custom atmospheres if required. The interaction between TITAN and the Mutation++ library is illustrated in Fig. 4.5, under the assumption that a single temperature is sufficient to describe the mixture state.

Two atmospheric models are available in TITAN: Earth-GRAM model [White and Hoffman, 2023] and NRLMSISE-00 [Picone et al., 2002]. Both models provide the local partial density of the atmospheric mixture and the local temperature for a given spacecraft or fragment altitude, which are passed to Mutation++ to determine the free-stream parameters (pressure, specific heat ratio, dynamic viscosity, sound speed and total enthalpy) considering the atmospheric mixture to be in thermo-chemical equilibrium.

The conditions at the boundary layer edge and the stagnation point are also computed by the TITAN-Mutation++ coupling. Similar to the works of Goulard [Goulard, 1958] and Sutton and Graves [Sutton et al., 1971], the mixture at the boundary layer edge is also assumed to be at equilibrium, i.e. shock-boundary distance is sufficiently large to allow the mixture to reach chemical equilibrium through recombination and dissociation. However, such an assumption fails for objects with small nose radii and flows with very high enthalpy, where the mixture residence time in the shock layer is not sufficient to reach equilibrium and requires models with higher fidelity to predict the mixture conditions in the boundary layer edge. The temperature and pressure at the boundary layer edge are retrieved from the conservation of the flow total enthalpy, using the post-shock stagnation values as the initial guess. The post-shock parameters are calculated using the Rankine-Hugoniot jump conditions.

The calculation of the mixtures at the wall depends on the modelling of the boundary layer, which can be considered frozen (the mixture at the wall is the same as the boundary layer edge) or in thermochemical equilibrium (the mixture at the wall is in chemical equilibrium), which are the two edge cases analysed by Fay and Riddell [Fay and Riddell, 1958]. For the former hypothesis, the species concentration depends on the degree of surface catalicity given by the gamma model, while for the latter, the mixture properties are directly retrieved, assuming chemical equilibrium for the given

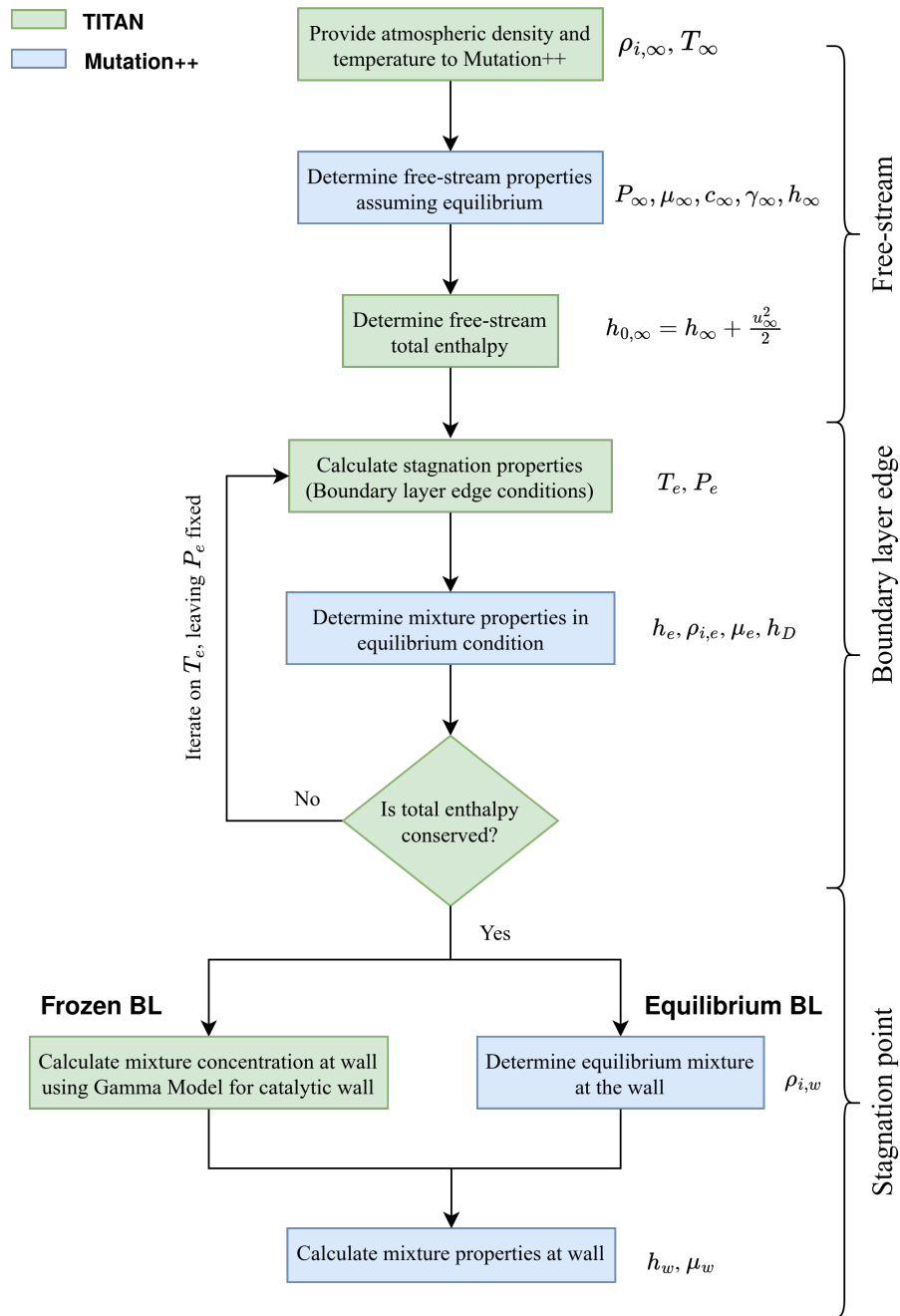


Figure 4.5: Computation of mixture properties at free-stream, boundary layer edge and wall locations using Mutation++.

wall temperature. To determine which assumption to use, it is useful to calculate the Damköhler number, which defines the ratio between the flow transport timescale and the timescale of the occurring reactions ( $Da = \frac{\text{flow timescale}}{\text{chemical timescale}}$ ). For large Damköhler

numbers ( $Da \gg 1$ ), chemical reactions can be considered instantaneous, while for small values ( $Da \ll 1$ ) the atoms fully recombine before hitting the surface [Goulard, 1958]. For the intermediate cases, non-equilibrium high-fidelity models are required to compute the conditions at the boundary layer.

### 4.2.2 Panel Shadowing

The use of panel methods for the computation of the aerothermodynamic quantities at hypersonic regimes assumes that only the panels facing the flow direction are impacted by the external flow, resulting in shadow areas that are not affected. For convex objects, it is enough to assess the angle between the flow direction and the surface facet [Anderson, 2006]. Thus, if

$$\begin{cases} \arccos(-\vec{n} \cdot \vec{V}_\infty) \leq \pi/2, & \text{The flow is impinging the panel} \\ \arccos(-\vec{n} \cdot \vec{V}_\infty) > \pi/2, & \text{The panel is shadowed} \end{cases} \quad (4.15)$$

where  $\vec{n}$  is the normal vector of the panel, pointing outwards, and  $\vec{V}_\infty$  is the free-stream velocity vector. However, if the geometry is concave, self-occlusion needs to be considered and Eq. 4.15 is not sufficient. In self-occluding cases, the spacecraft is partially shielded by itself, as illustrated in Fig. 4.7. Dedicated algorithms are required to determine the shadowed panels, such as ray-tracing algorithms [Glassner, 1989], depth-sorting algorithms [Zhang, 1998] and pixelator algorithms [Mehta et al., 2016]. Currently, TITAN has two methods integrated to assess occlusion culling: a depth-sorting algorithm, and a ray-tracing algorithm.

The depth-sorting method in TITAN performs rasterization rendering using a boolean matrix. The method is based on the projection of the surface mesh into the plane orthogonal to the free-stream velocity vector. Given the location of the panels' geometrical centre, it is possible to sort them by the relative distance to the orthogonal plane, and individually project them, starting from the closest panel. The projection is stored in a 2D Cartesian boolean matrix, as illustrated in Fig. 4.6. To improve the efficiency of the method, the panels are only projected to the boolean matrix and

considered to be facing the flow if the panels are potentially visible using Eq. 4.15 and if the correspondent projection of the panel geometrical centre location falls on an empty cell (panel 1) and 2)). Otherwise, if it falls on a filled cell, the panel is assumed as fully shadowed (panel 3)). An example of the pixelator occlusion culling method is shown in Fig. 4.7, where the solar array of the ATV is partially occluding the cargo bay.

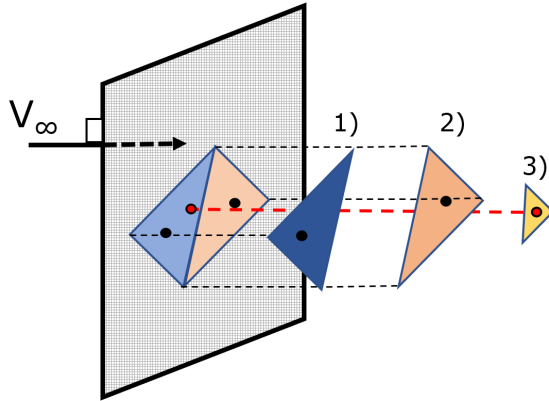


Figure 4.6: Occlusion culling depth-sorting methodology illustration.

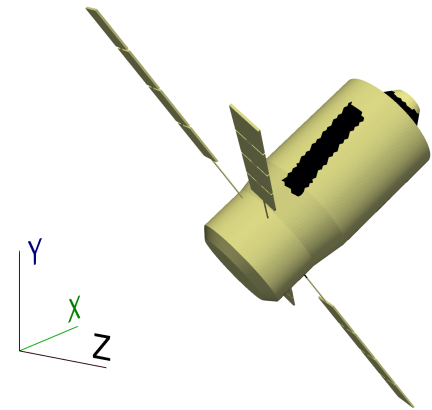


Figure 4.7: Depth-sorting methodology applied to the ATV spacecraft.

The depth-sorting method presents some benefits compared to the colour-based pixelation algorithm implemented in FOSTRAD (see Sec. A.3.1), such as the exclusion of colour-based facets for which the RGB values are dependent on the hardware used, and memory saving. Indeed, each position of the boolean matrix requires 1 bit of memory, in contrast with the 24 memory bits required to store a colour in RGB format. However, both methods present one similar limitation: the detection of visible facets is highly dependent on the size of the pixel/boolean matrix used for rasterization rendering. Ideally, the resolution of the matrix needs to be able to capture panels that present a very small area or high inclination angle, but it may require an excessive amount of memory and computational time at every time step.

An alternative method based on ray-casting is also available in TITAN, easing both memory requirements and computational speed. For each panel barycenter, a ray is

cast in the opposite direction to the free-stream velocity vector. The intersection events between rays and panels are handled by calculating the intersection point between the ray and the plane formed by the object's triangular panels, and checking if the intersection occurs inside the triangle. The panel from which the ray was cast is considered visible if there are no intersections detected.

The ray-casting approach has the possibility for parallel computation, contrary to the depth-sorting algorithm, which requires serial computation due to panel sorting. An example of the limitation of the depth-sorting algorithm due to the requirement of a binary matrix, which is not present in the ray-casting algorithm is presented in Fig. 4.8. Due to the matrix cell size being larger than the panel, it does not adequately capture the pressure distribution near the stagnation area.

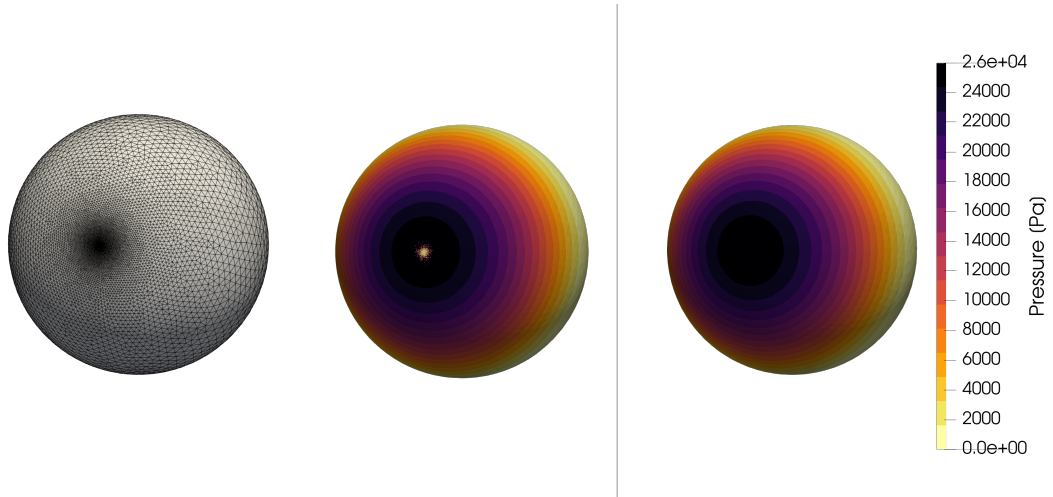


Figure 4.8: Comparison of pressure distribution obtained using the depth-sort algorithm (middle) and the ray-casting algorithm (right) over a sphere with a fine discretization at the stagnation area.

Partial occlusion is also available in the ray-casting methodology. The triangular facets are partitioned using a recursive equilateral division procedure of order  $N = 2$  [Pomelli and Tomasi, 1998]. The triangles are recursively replaced by  $N^2 = 4$  triangles by dividing each side in half and connecting the points. For  $M$  recursion steps, the original panel is partitioned using  $N^{2M}$  triangles with equal area, as depicted in Fig. 4.9. Afterwards, each triangle casts a ray from its respective barycenter in a direction

contrary to free-stream velocity, and intersections with other panels are assessed. The pressure and convective heat acting on the panel are computed using

$$p_{partial} = \left(1 - \frac{n_{R_i}}{n_{R_t}}\right) p \quad (4.16)$$

$$\dot{q}_{conv,partial} = \left(1 - \frac{n_{R_i}}{n_{R_t}}\right) \dot{q}_{conv} \quad (4.17)$$

where  $n_{R_t}$  is the number of rays cast from a given panel, and  $n_{R_i}$  refers to the number of intersected rays.

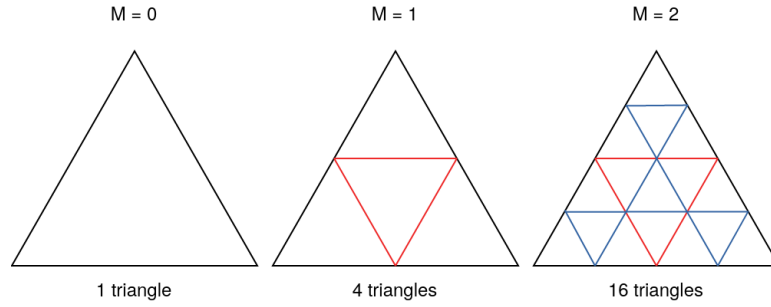


Figure 4.9: Facet subdivision for partial occlusion assessment.

### 4.2.3 Aerodynamics Calculation

After identifying the visible panels, TITAN proceeds to compute the pressure and shear coefficients, which are integrated over the object's surface to obtain the effective aerodynamic force. The aerodynamic loads in the free molecular regime ( $Kn \geq 10^2$ ) are evaluated using the analytical model by Schaaf and Chambre [Schaaf and Chambre, 1958] for pressure and shear stress, as reported in Eq. 2.22 and Eq. 2.23 respectively. The aerodynamic loads in the continuum regime ( $Kn \leq 10^{-4}$ ) are estimated with the Modified Newtonian Theory [Lees, 1956] given by the pressure coefficient expressed in Eq. 2.25 and Eq. 2.26.

For the transitional regime ( $10^{-4} < Kn < 10^2$ ), a bridging function based on the Gaussian error function formulated by Falchi [Falchi et al., 2017] is employed. A logarithmic normalization of the Knudsen number is calculated using Eq. 4.18, where

$Kn_{trans}$  is the respective computed Knudsen values in the transitional regime, and the subscripts  $fm$  and  $c$  represent the free molecular and continuum regime reference values respectively.

$$Kn_{norm} = \frac{\log(Kn_{trans}) - \log(Kn_{c,ref})}{\log(Kn_{fm,ref}) - \log(Kn_{c,ref})} \quad (4.18)$$

Using the normalized Knudsen number  $Kn_{norm}$ , a corrective function is calculated as

$$Kn_{cf} = \frac{2Kn_{norm}}{(1 + \operatorname{erf}(4Kn_{norm} - 2))} \quad (4.19)$$

The corrective function is scaled by taking into account a pivotal point ( $Kn_p = 1$ ), allowing scaling of two regions independently, as showcased in Eq. 4.20 where  $A$  and  $B$  are weighting factors. According to Falchi [Falchi, 2020], the optimal fitting was computed based on the transitional aerodynamics analysis found in the literature [Dogra et al., 1992, Moss et al., 2006], obtaining  $A = 1e - 6$  and  $B = 0.1508$ .

$$Kn_{cf} = \begin{cases} A(Kn_{cf} - 1) + 1, & \text{if } Kn_{cf} < 1 \\ B(Kn_{cf} - 1) + 1, & \text{if } Kn_{cf} > 1 \end{cases} \quad (4.20)$$

The Knudsen bridging function is finally defined by Eq. 4.21. This specific form of bridging function simplifies the mathematical computation of the aerodynamics in the transitional regime, as only one bridging function is necessary for all the aerodynamic coefficients. The pressure and shear coefficients in the transitional regime are given by Eq. 4.22 and Eq. 4.23.

$$Kn_{bridge} = Kn_{cf} \frac{(1 + \operatorname{erf}(4Kn_{norm} - 2))}{2} \quad (4.21)$$

$$C_p = C_{p,c} + (C_{p,fm} - C_{p,c})Kn_{bridge} \quad (4.22)$$

$$\begin{aligned} C_\tau &= C_{\tau,c} + (C_{\tau,fm} - C_{\tau,c})Kn_{bridge} \\ &= C_{\tau,fm}Kn_{bridge} \end{aligned} \quad (4.23)$$

After obtaining the distribution of aerodynamic loads over the panels, the forces and moments are computed. The aerodynamic force is calculated as the integration of pressure and shear loads over the assembly surface

$$\vec{F}_a = 0.5\rho_\infty V_\infty^2 \int_S (C_p \vec{n} + C_\tau \vec{t}) dS \quad (4.24)$$

where  $\vec{n}$  and  $\vec{t}$  are the normal and tangential vectors of the local panel. Additionally, the aerodynamic moment acting on the object concerning the centre of mass is computed as

$$\vec{M}_a = 0.5\rho_\infty V_\infty^2 \int_S [(\vec{r} - \vec{r}_{CM}) \times (C_p \vec{n} + C_\tau \vec{t})] dS, \quad (4.25)$$

where  $\vec{r}$  is the position of the surface panel geometrical centre and  $\vec{r}_{CM}$  is the position of the centre of mass.

#### 4.2.4 Aerothermodynamics Calculation

Like the aerodynamics module, the aerothermodynamics calculation is performed for all the flow regimes. The analytical heat transfer coefficient for the free molecular regime is given as a function of the local flow inclination angle using the Schaaf and Chambre flat plate theory using Eq. 2.14.

In the continuum regime, the heat transfer can be obtained by a set of different correlations and simplified models, namely using Van Driest (Eq. 2.30), Sutton-Graves (Eq. 2.33), Fay-Riddell (Eq. 2.31) and the formulation used in SCARAB (Eq. A.7). The parameters required to use the models are obtained using Mutation++ as described in Section 4.2.1, and assuming a boundary layer in thermo-chemical equilibrium. The velocity gradient at the stagnation point is calculated using the Fay-Riddell approximation as default (Eq. 2.39), although the other alternatives specified in Section 2.2.4

are also available. To account for the inclination of the local panels, the heat flux distribution over the surface is given by Lees distribution formula as

$$q(\theta) = q_s(0.1 + 0.9 \cos \theta). \quad (4.26)$$

For the calculation of the aerothermodynamic properties in the transitional regime, a dedicated bridging model similar to the model developed by Falchi [Falchi et al., 2017] has been integrated into the framework and is given by Eq. 4.27 where  $St$  is the Stanton number. Therefore, the bridging function for the computation of the aerothermodynamic loads is a function of both the local radius and Knudsen number.

$$St = St_c + (St_{fm} - St_c)Kn_{bridge}(Kn, R_N) \quad (4.27)$$

The integrated bridging function was developed using different re-entry heating data with distinct local nose radii.

The effect of wall catalicity is considered with the introduction of the Goulard equation (Eq. 2.35) to the TITAN framework, which introduces the catalytic correction factor  $\varphi$  (Eq. 2.36) to account for heat release due to the atomic recombination occurring at the wall, assuming a frozen boundary layer. However, according to Goulard [Goulard, 1958], the assumptions in his formulation, respectively  $\frac{\mu_e \rho_e}{\mu_w \rho_w} = 1$  and  $h_e \gg h_w$  can lead to the underestimation of the heat transfer for catalytic walls by 20% at most.

To overcome the assumptions in the Goulard formulation, the catalytic correction factor has been added to the Fay-Riddell equation for the frozen boundary layer. With the introduction of the correction factor, the contribution of the heat released due to recombination at the wall is a function of the wall catalicity. Thus, the new expression of Fay-Riddell for partially catalytic surfaces is

$$\dot{q}_s = 0.763 \text{Pr}^{-0.6} (\rho_s \mu_s)^{0.4} (\rho_w \mu_w)^{0.1} \sqrt{\left(\frac{du_e}{dx}\right)_s} (h_s - h_w) \left[1 + (Le^\alpha \varphi - 1) \left(\frac{h_D}{h_s}\right)\right]. \quad (4.28)$$

Note that for non-catalytic walls ( $\varphi = 0$ ), the equation is reduced to the non-catalytic

variant of the Fay-Riddell equations, and for fully catalytic walls ( $\varphi \approx 1$ ), the equation is equal to the fully-catalytic variant. Hence, the introduction of the catalytic correction factor bridges the catalicity extremes. The recombination coefficient used assumes the rates to be equal for both oxygen (O) and nitrogen (N) atoms. The validation of this expression is presented in Sec. 4.8.2.

### 4.3 Trajectory Dynamics

For a complete reentry analysis, it is essential to track all fragments generated during reentry until they reach the ground or disintegrate in the atmosphere. Several state parameters needed to be provided to initialize the trajectory propagation, respectively geodetic latitude, longitude, altitude and aerodynamic velocity. The direction of the initial velocity vector is determined by providing the initial flight path angle and heading angle.

The trajectory is propagated in the Earth-centered, Earth-fixed coordinate system based on the geodetic coordinate system WGS-84, a rotational Cartesian spatial reference system that represents locations in the vicinity of the Earth as X, Y, and Z coordinates from its centre of mass while accounting for Earth's oblateness.

The Earth's rotation is described by its angular velocity, represented by the rotation vector:

$$\vec{\Omega}_E = \begin{bmatrix} 0 \\ 0 \\ \omega_E \end{bmatrix}, \quad (4.29)$$

where  $\omega_E$  is Earth's rotational rate.

TITAN models the motion of the objects using 6 DoF equations, where translational and angular motions are considered, derived from the application of Newton's second law for forces and moments. The sums of all acting forces and torques form the right-hand sides of the equations of motion. The velocity derivative in the Cartesian frame is given by

$$m \frac{d\vec{V}}{dt} = m(\vec{g} + \vec{a}_{cor} + \vec{a}_e) + \vec{F}_a \quad (4.30)$$

where  $\vec{g}$  is the gravitational acceleration vector,  $\vec{F}_a$  is the aerodynamic forces due to shear and pressure,  $\vec{a}_{cor}$  is the Coriolis contribution in the Cartesian frame and  $\vec{a}_e$  is the centrifugal acceleration. Both Coriolis and centrifugal accelerations are needed because the equations of motion are being solved using a rotating frame.

$$\vec{a}_{cor} = -2\vec{\Omega}_E \times \vec{V} \quad (4.31)$$

$$\vec{a}_e = \vec{\Omega}_E \times \vec{\Omega}_E \times \vec{r} \quad (4.32)$$

The position derivative in the Cartesian frame is therefore given by

$$\frac{d\vec{r}}{dt} = \vec{V}. \quad (4.33)$$

The attitude rate is conveniently expressed in the object's body reference frame. The dynamic equations for angular motion are obtained from the Euler's Law as

$$\mathbf{I} \cdot \begin{bmatrix} \dot{p} \\ \dot{q} \\ \dot{r} \end{bmatrix} = \vec{M}_a - \begin{bmatrix} p \\ q \\ r \end{bmatrix} \times \left( \mathbf{I} \cdot \begin{bmatrix} p \\ q \\ r \end{bmatrix} \right) \quad (4.34)$$

The parameter  $\mathbf{I}$  is the object's inertia tensor, expressed in the body reference frame. The parameters  $p$ ,  $q$  and  $r$  are the roll, pitch and yaw angular velocity respectively. At each step, the forces acting on the object's surface are computed and used to update the translational and angular motion states using the Forward Euler integration method. The time step is adapted based on the motion derivatives, with the aim of maintaining numerical accuracy and preventing integration errors and trajectory divergence. The new attitude is then computed using the quaternions formulation [Diebel et al., 2006] to avoid gimbal lock. The quaternions formulation does not present singularities in the rotation and its vector is denoted as  $\mathbf{Q} = (Q_1, Q_2, Q_3, Q_4)$ , and it's evolution is governed by

$$\begin{bmatrix} \dot{Q}_1 \\ \dot{Q}_2 \\ \dot{Q}_3 \\ \dot{Q}_4 \end{bmatrix} = \frac{1}{2} \begin{bmatrix} rQ_2 - qQ_3 + pQ_4 \\ -rQ_1 + pQ_3 + qQ_4 \\ qQ_1 - pQ_2 + rQ_4 \\ -pQ_1 - qQ_2 - rQ_3 \end{bmatrix}. \quad (4.35)$$

#### 4.4 Collision Dynamics

To model the movement of a system after a collision event, there are two crucial steps: identification of a collision and application of a contact law for rigid-body collision. The first step determines the point of contact  $c_i$  and the unit normal vector  $\vec{n}_i$  to the common tangent plane between the bodies at the contact point, as illustrated in Fig. 4.10. A collision mesh is generated using the geometrical mesh as a reference, by translating the nodes by a factor  $\varepsilon$  such that  $(x, y, z)'_i = (x, y, z)_i + \varepsilon \vec{N}_i$ , where  $(x, y, z)$  are the coordinates of the  $i_{th}$  node in the body frame, and  $\vec{N}_i$  is the node unit normal, pointing outwards of the body. Therefore, the collision mesh is derived by inflating the object's original mesh, retaining its shape and vertex connectivity. The collision mesh is purposely only used in the collision model to avoid the intersection between objects. At every iteration, the framework verifies if any collision mesh overlaps, adjusting the time-step such that the overlapping factor  $\delta$  is smaller than the translation factor  $\varepsilon$ , hence avoiding the overlap of the original geometries.

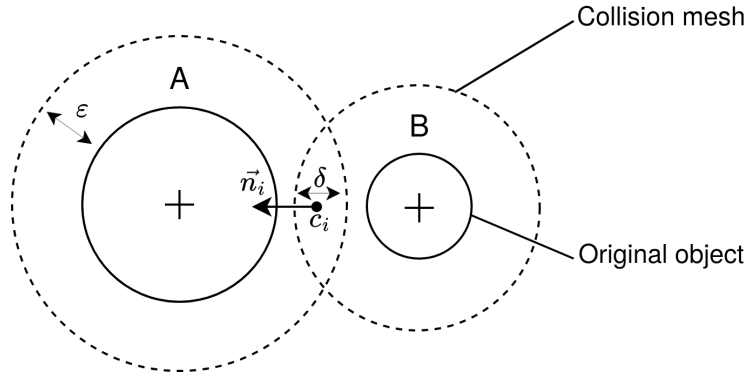


Figure 4.10: Schematic of objects and respective collision mesh at the moment of impact.

When a collision is detected, the moment exchange between the colliding bodies is

computed. Two approaches have been commonly used to model rigid-body collisions: incremental approach [Routh, 1891], in which the force during collision is accounted for in the dynamics through differential equations, and algebraic approach [Whittaker and McCrae, 1988], only dependent on the impulse at the contact area of the colliding bodies

The rigid-body collision model implemented in this framework assumes an instantaneous impulse. To account for simultaneous collisions, the model considers a system of  $N$  bodies that are in contact at  $N_c$  active collision points, i.e. the bodies are actively moving through each other [Harris et al., 2012, Meakin, 2003]. The pair of colliding bodies at the  $i_{th}$  collision point is designated as  $(a_i, b_i)$  and the unit normal vector pointing from  $a_i$  to  $b_i$  is denoted as  $\hat{n}_i$ . The implemented simultaneous method solves active collisions as a linear equation system  $Ap = b$ , where  $p$  is the impulse vector for an inelastic collision. The matrix  $A$  has the dimension  $N_c \times N_c$  and the coefficients have the following form:

$$A_{i,j}^1 = \text{sgn}(a_j, i) \left( \frac{\hat{n}_j}{m_{a_i}} + (J_{a_i}^{-1}(\vec{r}_{a_i,j} \times \hat{n}_j) \times \vec{r}_{a_i,i}) \right) \cdot \hat{n}_i \quad (4.36)$$

$$A_{i,j}^2 = \text{sgn}(b_j, i) \left( \frac{\hat{n}_j}{m_{b_i}} + (J_{b_i}^{-1}(\vec{r}_{b_i,j} \times \hat{n}_j) \times \vec{r}_{b_i,i}) \right) \cdot \hat{n}_i \quad (4.37)$$

$$A_{i,j} = A_{i,j}^1 - A_{i,j}^2 \quad (4.38)$$

where  $m_{a_i}$  and  $J_{a_i}$  are respectively the mass [ $kg$ ] and moment of inertia [ $m.kg^2$ ] in the inertia frame of the colliding body  $a_i$ , with contact point  $i$ , and  $r_{a_i,i}$  is the location of the contact point  $i$  concerning the centre of mass of the colliding body  $a_i$ , and

$$\text{sgn}(i, j) = \begin{cases} -1 & \text{if } i = a_j \\ 1 & \text{if } i = b_j \\ 0 & \text{otherwise} \end{cases} \quad (4.39)$$

The components of the right-hand side vector  $b$  are represented as

$$b_i = (\vec{V}_{b_i} + \vec{\omega}_{b_i} \times \vec{r}_{b_i,i} - \vec{V}_{a_i} - \vec{\omega}_{a_i} \times \vec{r}_{a_i,i}) \cdot \hat{n}_i \quad (4.40)$$

where  $\vec{V}_{a_i}$  and  $\vec{\omega}_{a_i}$  are the linear and angular velocity of the colliding body  $a_i$ , respectively.

After the computation of vector  $p$ , a restoration step is applied to account for the coefficients of restitution at the different contact points. Thus, the final collision impulses are given as

$$p'_i = (1 + e_i)p_i. \quad (4.41)$$

Using the restored impulse vector, the post-collision linear velocity  $\vec{V}'_k$  and angular velocity  $\vec{\omega}'_k$  for the  $k_{th}$  body are computed as

$$\vec{V}'_k = \vec{V}_k + \sum_{j=1}^{Nc} sgn(k, j) \frac{p_j}{m_k} \hat{n}_j \quad (4.42)$$

$$\vec{\omega}'_k = \vec{\omega}_k + J_k^{-1} \sum_{j=1}^{Nc} sgn(k, j) p_j \vec{r}_{k,j} \times \hat{n}_j \quad (4.43)$$

## 4.5 Thermal and ablation modelling

A component-based lumped mass approach ( $0D$ ) is used to model and simulate the thermal ablation of the re-entering object. It is assumed that each component of the spacecraft, i.e. primitives and joints, will undergo a convection-radiation dominated heat exchange process while heat conduction inside the component is assumed to be instantaneous. As a result of this process, each component will have a uniform temperature resulting from the solution of a  $0D$  heat transfer mechanism,

$$mc_p \frac{dT}{dt} = \dot{q}_{net} = \dot{q}_{conv} - \dot{q}_{rad,out} \quad (4.44)$$

where  $m$  is the mass of the component and  $c_p$  is the temperature-dependent specific heat,  $\dot{q}_{net}$  is the total heat flux acting on the component, given as the sum of convective heating and radiative cooling using Stefan-Boltzmann's law (Eq. 2.3). Currently,

incoming radiation and heat conduction between components are not available in the thermal model.

The ablation process on a component starts when it reaches the melting temperature. The amount of heat remaining after the component reaches the melting temperature ( $T_{melt}$ ) is given by Eq. 4.45, where  $\Delta t$  is the time step of integration, and  $m_0$  and  $T_0$  are respectively the mass and temperature of the object at the previous time step.

$$Q_f = \dot{q}_{net}\Delta t - m_0c_p(T_{melt} - T_0) \quad (4.45)$$

The mass lost due to ablation is then given by the ratio  $\frac{-Q_f}{Q_{melt}}$  where  $Q_{melt}$  is the latent heat of fusion. After the ablation process, the mass of the component is given as

$$m_f = m_0 + \Delta m = m_0 + \frac{-Q_f}{Q_{melt}}. \quad (4.46)$$

The mentioned methodology is applied at every trajectory propagation step, thus enabling continuous ablation throughout reentry. The time-step used in the methodology is therefore the time interval between the propagation steps. During the ablation process, only the mass and inertia tensor of the component are affected, not affecting the size and shape. A common issue is verified when a component's mass is close to zero. In this case, the components suffer a substantial deceleration and demise is not correctly predicted. To address this issue, a limit on the fragments' mass has been introduced. Therefore, if the components' mass is below the threshold of 0.05 kg, it is considered demised.

## 4.6 Material modelling

Each component used in modelling the spacecraft has an assigned material, whose properties are retrieved from a material database linked to TITAN, illustrated in Fig. 4.11. The material database follows the same database layout as the European Space maTerIal deMisability dATabasE (ESTIMATE) [Agency, 2020], providing a seamless integration with ESTIMATE<sup>1</sup>, but also allowing for custom materials.

<sup>1</sup>Access to ESTIMATE database needs to be requested through the ESA Space Debris Office.

The ESTIMATE database is used in DRAMA reentry tool [Pontijas Fuentes et al., 2019] and provides the characteristics and thermophysical properties of the material and follows the guidelines suggested in DIVE [European Space Agency, 2020] for examining and evaluating the destruction of man-made objects in space during re-entry. The values presented in the database were retrieved from measurement data of Plasma Wind Tunnel testing and calibrated during the MADRE activity [Bonvoisin et al., 2023, Holbrough et al., 2021].

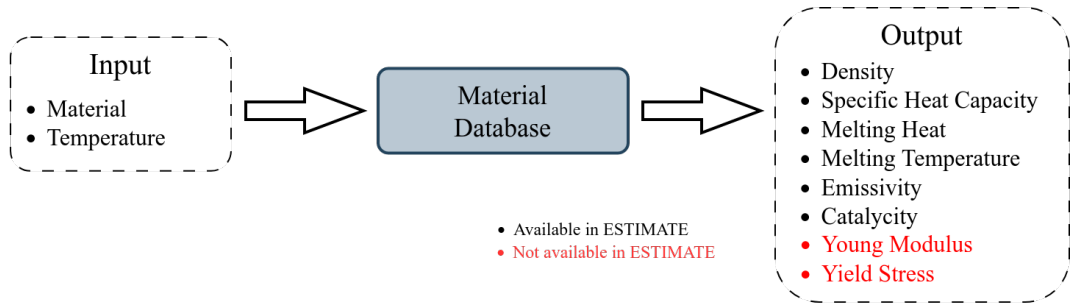


Figure 4.11: Material database information flow.

In addition to the parameters available in the ESTIMATE database, TITAN also enables retrieving the Young modulus and yield stress fields from an in-house database as a function of the component temperature, used in the structural analysis of the joint components.

## 4.7 Structural Analysis

During reentry, the aerodynamic and dynamic loads interaction on the spacecraft components may give rise to structural deformation of the joints, ultimately leading to fragmentation events that have an impact on the overall reentry process. The structural deformation of the joint components in TITAN is assumed to have a linear elastic behaviour dependent on the temperature of the component, thus plasticity is not accounted for. Additionally, the materials are assumed to be homogeneous and isotropic. The governing equations for an elastic body,  $\Omega$ , under a body force  $f$  is given by

$$\begin{aligned}
-\nabla \cdot \boldsymbol{\sigma}(u) &= f \quad \text{in } \Omega \\
\boldsymbol{\sigma}(u) &= \lambda \text{Tr}(\boldsymbol{\varepsilon}(u))I + 2\mu\boldsymbol{\varepsilon}(u) \\
\boldsymbol{\varepsilon}(u) &= \frac{1}{2}(\nabla u + (\nabla(u))^T)
\end{aligned} \tag{4.47}$$

where  $\lambda$  and  $\mu$  are Lamé's elasticity parameters defining the material properties of  $\Omega$ ,  $I$  is the identity tensor,  $\boldsymbol{\sigma}$  is the stress tensor given by the Hooke's law,  $\text{Tr}$  is the trace operator,  $\boldsymbol{\varepsilon}$  is the symmetric strain tensor and  $u$  is the displacement vector.

The mechanical stress analysis in TITAN is performed by using the open-source partial differential equation (PDE) solver FEniCS 2019.1.0 [Alnæs et al., 2015], which was coupled to the main framework [Peddakotla et al., 2022b]. FEniCS has a high-level Python and C++ interface which enables translating the mathematical models required to perform structural analysis into finite element code in order to perform Finite Element Analysis (FEA) while supporting parallel computing. The existent Python interface allows a fast integration with TITAN.

To statistically determine the solution to an elastic system under stress, Dirichlet boundary conditions are traditionally used to impose a displacement constraint, serving as an attachment element. However, for the analysis of re-entering spacecraft, no natural boundary condition exists for Dirichlet imposition. To overcome this limitation, the principle of superposition is utilised, which states that for a linearly elastic structure, the load effects caused by two or more loadings are equal to the sum of the loads considered separately. Therefore, the FEA is performed twice, using separate sets of Dirichlet boundary conditions and superimposing the resultant displacement vectors to determine the overall displacement of the structure. An example of this application is shown in Fig. 4.12. The cube on the left is first constrained by imposing a zero displacement boundary condition on nodes located on and within the cube. The elastic system is solved to obtain the displacement solution shown in Fig. 4.12a. The same process is performed to constrain the displacements on the right cube, obtaining the displacement field shown in Fig. 4.12b. These two solutions are then superimposed to determine the total displacement field of the complete structure.

After obtaining the displacement solution, the stress field on the spacecraft is com-

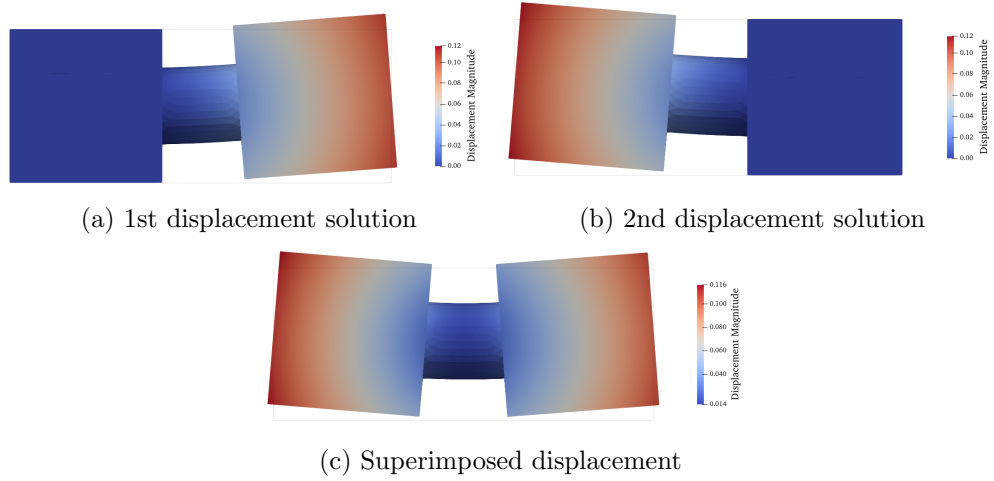


Figure 4.12: Example of the superposition method for two cubes attached with a cylindrical joint.

puted. The structural failure of a joint is determined by the von Mises yield criterion, used to identify when yielding occurs. In the current version of the framework, it is assumed that joints fragment instantaneously when the computed von Mises stress exceed the yield stress of the material. Using the stress tensor,  $\boldsymbol{\sigma}(u)$  the von Mises stress,  $\sigma_{vm}$  is computed using

$$\sigma_{vm} = \sqrt{\frac{3}{2} s_{ij} s_{ij}} \quad (4.48)$$

$$\mathbf{s}(u) = \boldsymbol{\sigma}(u) - \frac{Tr(\boldsymbol{\sigma}(u))}{3} \mathbf{I}$$

where  $s$  is the deviatoric stress tensor and fragmentation occurs when

$$\sigma_{vm} \geq \sigma_y \quad (4.49)$$

where  $\sigma_y$  is the yield stress of the material.

## 4.8 Verification and Validation cases

### 4.8.1 Aerodynamic and Aerothermodynamic

The validation of the discussed low-fidelity models is performed through the comparison of the computed results with TITAN against experimental and numerical data, along with the available results from state-of-the-art spacecraft-oriented tools, retrieved from the work of Annaloro et al. [Annaloro et al., 2017a]. Three validation cases are performed: a sphere simulation for the validation of the models in the transitional and rarefied regime, and a hollow hemisphere and ARD capsule for the validation of the models in the continuum regime.

#### Transitional and Rarefied Regime - Sphere Case

A 1.6-meter-diameter sphere re-entry case was selected for the accuracy analysis of the low-fidelity models for the transitional and rarefied regime. The computed results were computed using a mesh with approximately 5,000 facets, and are compared with those obtained by the re-entry spacecraft-oriented tool PAMPERO [Annaloro et al., 2015], SCARAB [Koppenwallner et al., 2005] and FAST/MUSIC [Sourgen et al., 2015], as well as DSMC calculations from Dogra et al. [Dogra et al., 1992]. The considered flow conditions are expressed in Table 4.1. The altitude range considered encompasses the lower limit of the transitional regime at 90 km, approaching the free-molecular limit at 200 km. Free-stream velocity is set to 7.5 km/s. The wall temperature of the sphere is set to be 350 K, uniformly distributed along the surface, and the gas-surface interaction is assumed to be diffuse with full thermal accommodation, as according to [Dogra et al., 1992].

Figure 4.13 presents the difference in drag coefficient, pressure and heat-flux coefficients at the stagnation point with respect to the DSMC computation from Dogra's simulations for several altitudes, which are characterized by the different Knudsen numbers. There is a very good agreement for all the tools regarding the stagnation pressure and drag coefficient, where the maximum deviation reported comes from SCARAB (7.7%) and PAMPERO (15.8%) at 110 km, respectively. The results computed by

Table 4.1: Free-stream conditions for the 1.6-meter-diameter sphere case [Dogra et al., 1992].

	Altitude [km]	Density [kg/m <sup>3</sup> ]	Temperature [K]	Pressure [Pa]	Knudsen
a)	90	3.43E-6	188	1.862E-1	0.01
	100	5.66E-7	194	3.234E-2	0.063
	110	9.67E-8	247	7.296E-3	0.375
	120	2.27E-8	368	2.657E-3	1.675
b)	130	8.23E-9	500	1.345E-3	4.828
	140	3.86E-9	625	8.085E-4	10.573
	160	1.32E-9	822	3.798E-4	31.458
c)	200	3.29E-10	1026	1.278E-4	122.907

the framework present a maximum deviation of 2.7% for the pressure coefficient and 4% for the drag coefficient along all the computed altitudes. These results increase the confidence in using the proposed bridging methodology for the computation of the aerodynamic values. Regarding the heat flux coefficient at the stagnation point, except for TITAN, all the tools present an error superior to 10% in the transitional regime for  $Kn < 2$ . The framework is able to compute the heat flux with a maximum deviation of 8.7% for an altitude of 110 km.

A more detailed comparative analysis is performed for the altitudes of 90, 130, and 200 km, illustrated in Fig. 4.14, 4.15, and 4.16 respectively. Analyzing the images, it is clear that the discrepancy between the different codes is larger for pressure distribution when shifting towards the free-molecular regime, and for the heat-flux distribution when shifting towards the continuum regime. Overall, the distribution provided by the framework is in good agreement with the reference DSMC solution, except for the heat-flux at 90 km, where the distribution is overestimated, but approximates the reference value at the stagnation point.

### Continuum Regime - Hollow Hemisphere

To analyze the performance of the low-fidelity models for the continuum regime, a comparative analysis of the pressure and heat rate distribution of a hollow hemisphere with 4 meters of diameter and thickness of 0.1 meters was performed, using a mesh with 21,000 cells. In the simulation, the concave region was facing the flow direc-

## Chapter 4. Development of a Reentry Framework

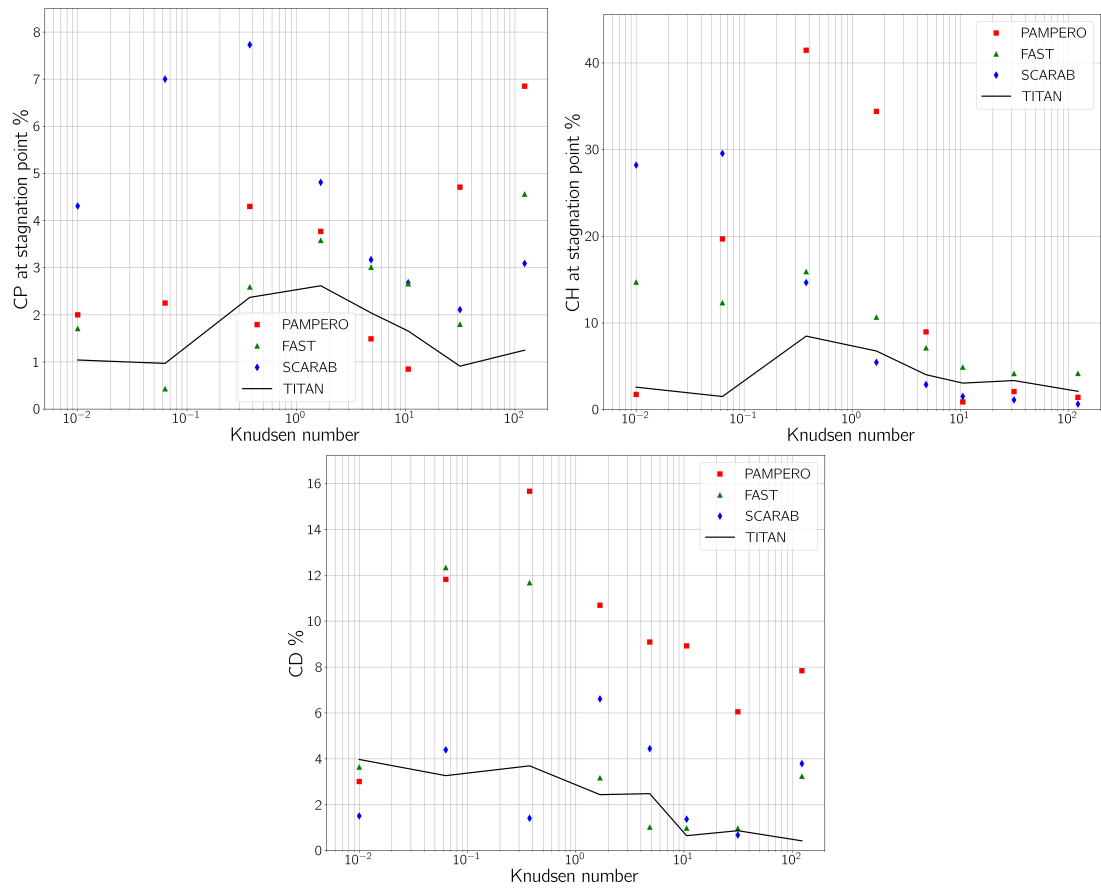


Figure 4.13: Comparison of aerodynamic and aerothermal coefficient deviation concerning the reference DSMC solution.

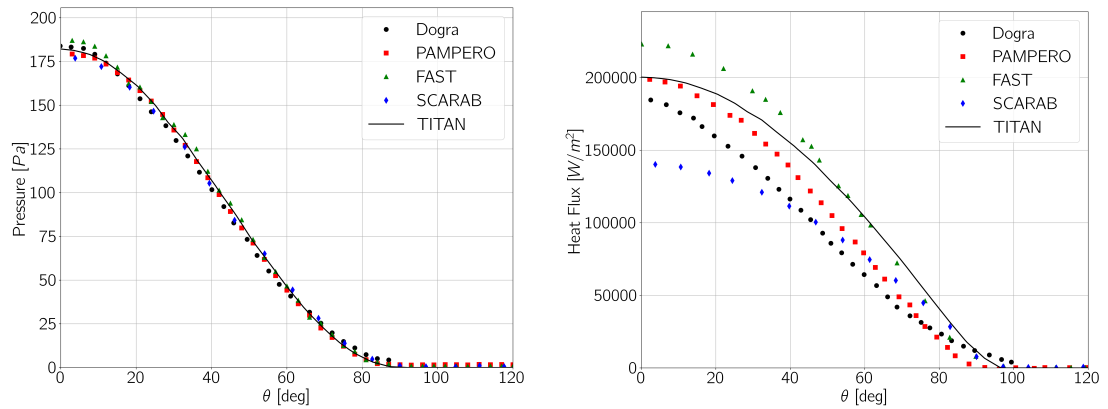


Figure 4.14: a) Pressure and heat-flux surface distribution from sphere stagnation point at 90 km

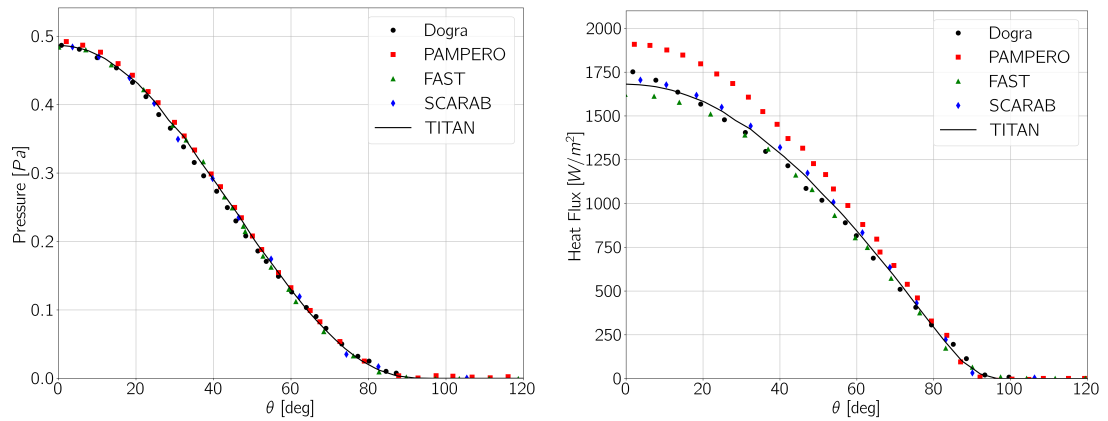


Figure 4.15: b) Pressure and heat-flux surface distribution from sphere stagnation point at 130 km

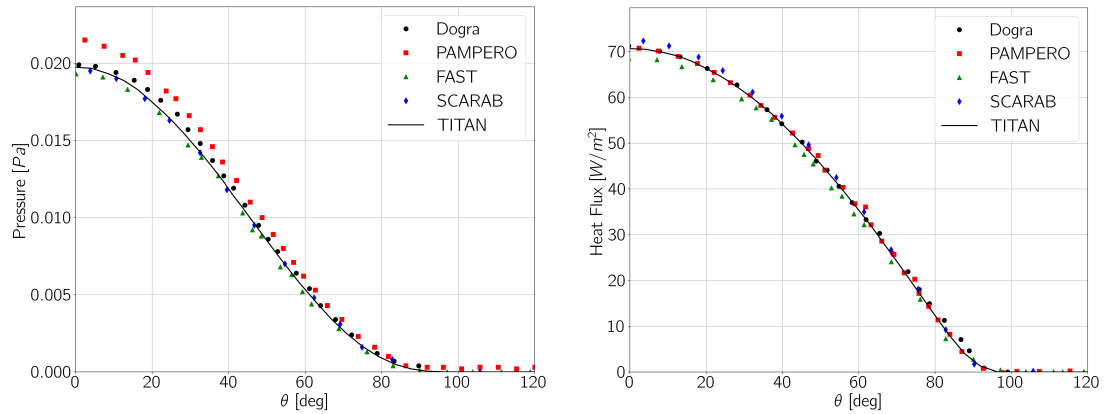


Figure 4.16: c) Pressure and heat-flux surface distribution from sphere stagnation point at 200 km

tion. The obtained solution is again compared against results that were obtained by the spacecraft-oriented tools, and the reference solution was computed using the CFD solver MISTRAL [Annaloro et al., 2017a]. It is known that predicting the pressure distribution using Modified Newtonian theory yields fairly accurate results for convex bodies [Boison, 1959] but becomes increasingly inaccurate for concave bodies with the increase of concave curvature [Rao, 1973]. For this simulation, a wall temperature of 700 K is uniformly distributed along the objects' surface and the free-stream conditions selected for this case study are showcased in Table 4.2.

The comparison of pressure and heat-flux distribution along the symmetry plane is showcased in Fig. 4.17. All of the low-fidelity tools present similar results, with the

Table 4.2: Free-stream conditions for the hollow hemisphere case.

Altitude [km]	$\rho_\infty$ [kg/m <sup>3</sup> ]	$T_\infty$ [K]	$P_\infty$ [Pa]	$M$
58	3.64E-4	250.61	26.3	15

difference that the computed results follow the solution obtained by SCARAB more closely with respect to the heat-flux computation, as both tools use the same heat rate equation for catalytic walls. However, all the low-fidelity results are inaccurate in relation to the reference CFD solution, showing the inability of local panel methods to simulate concave geometries.

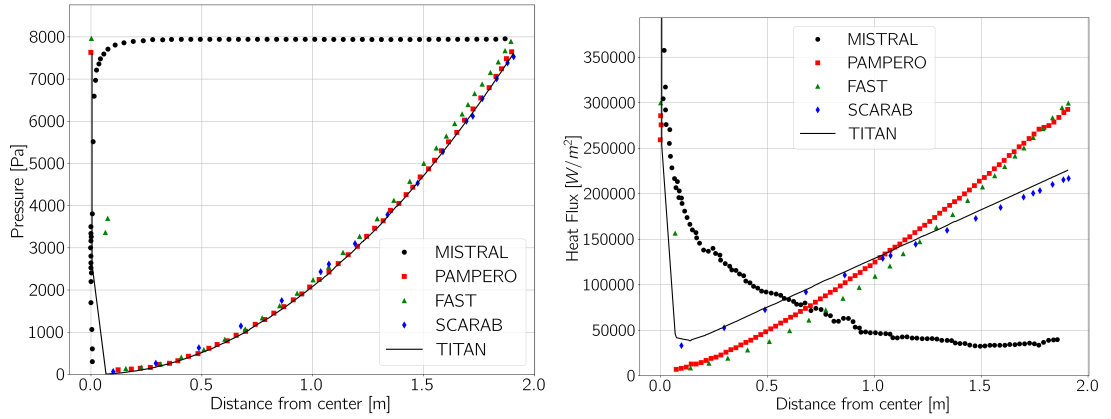


Figure 4.17: Pressure and heat-flux distribution for the hollow hemisphere.

### Continuum Regime - ARD Capsule

The Atmospheric Reentry Demonstrator (ARD) capsule was Europe’s first complete re-entry mission. The ARD was launched in 1998, where it was injected into a sub-orbital path, reaching a peak altitude of 830 km, and subsequently re-entered Earth’s atmosphere at an altitude of 120 km above the Pacific Ocean, with an average speed of 7 km/s. The capsule had an Apollo-like shape, with a spherical nose radius of 3.36 m followed by a conical surface that is connected to the nose through a 0.14 m radius curve. Overall, the capsule presented an external diameter of 2.8 m and a height of 2.04 m. Further information on the geometry can be found in Fig. 4.18.

The numerical analysis of the ARD re-entry using the proposed framework has been performed for an altitude of 65.83 km when the peak heating was recorded. The

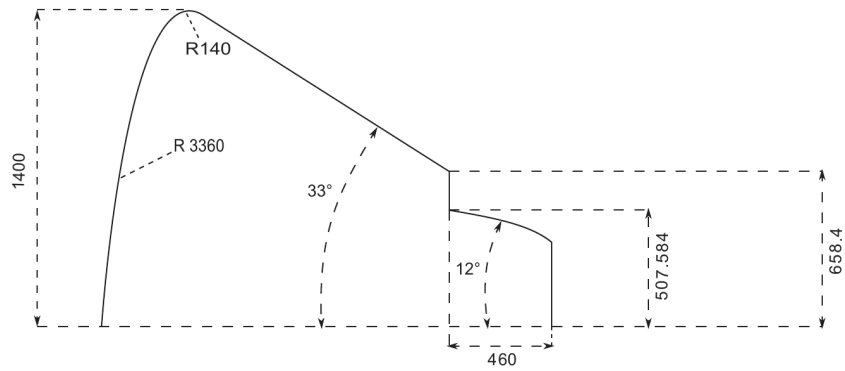


Figure 4.18: ARD geometrical configuration [Walpot, 2002] in mm.

capsule wall is assumed to be fully catalytic and has a fixed temperature of 1500 K. The mesh used for the simulation has approximately 58,000 cells, where 50,000 are used to discretize the surfaces exposed to the flow. The parameters specified in Table 4.3 were used for the simulation and are shown in Fig. 4.19, illustrating the pressure coefficient and heat flux computed at the symmetry plane for an angle of attack of  $20^\circ$ . The flight pressure and heat rate data acquired from the thermocouples and pressure sensors onboard the ARD are also plotted [Paulat and Boukhobza, 2007].

Table 4.3: Free-stream conditions for the ARD case.

$\rho_\infty$ [kg/m <sup>3</sup> ]	$T_\infty$ [K]	$P_\infty$ [Pa]	$M$	$T_w$ [K]	AoA <sup>o</sup>
1.5869E-4	224.5	10.23	24	1500	20

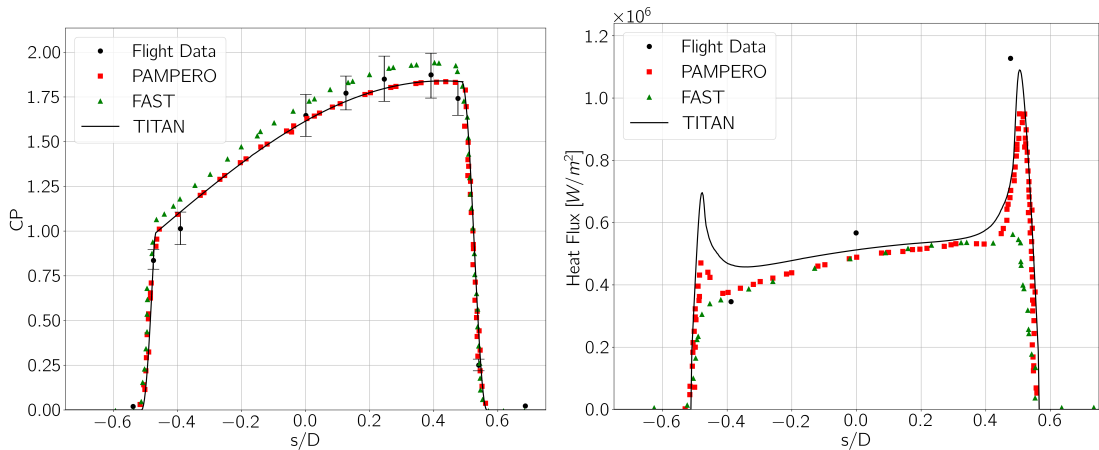


Figure 4.19: Pressure and heat-flux distribution for the ARD capsule.

The results obtained for the ARD analysis using the framework are compared again with the re-entry spacecraft-oriented tools PAMPERO and FAST/MUSIC [Annaloro et al., 2017a]. The pressure coefficient computed along the symmetry plane is in good agreement with the flight data, showing a slight under-prediction of  $\approx 2\%$  at the stagnation area, but matching the results of PAMPERO, while FAST/MUSIC overestimates the pressure coefficients. However, all three tools are contained within the error associated with the flight data.

Analyzing the heat rates, the maximum heat flux recorded reaches  $\approx 1.15 \text{ MW/m}^2$ , slightly under-predicted by TITAN, followed by PAMPERO and FAST/MUSIC, respectively. The two peaks presented in the plot correspond to the transition between the spherical nose and the conical surface, thus presenting a different radius of curvature that impacts the heat rate computation. The smoothness of the computed solution transition between the heat rate peaks is due to the use of a smoothness algorithm for the computation of the facet curvature to enhance the accuracy of the computed heat rates. Although the framework manages to reasonably compute the peak heat flux, it overestimates the heat distribution at the trailing edge further from the stagnation point, where FAST/MUSIC and PAMPERO provide a reasonable prediction when compared to the flight data.

### 4.8.2 Stagnation Heat Transfer for Partially Catalytic Wall

To model partially catalytic surfaces, the Goulard equation and the Fay-Riddell equation with the catalicity correction factor have been introduced into TITAN, and are demonstrated in this section by analysis of the stagnation point of a 0.5 meters radius sphere with a 1000  $K$  surface temperature, and a 0.05 meters radius sphere with a 300  $K$  surface temperature, with varying catalicity rate. The results are compared with the solution obtained from the VKI Stagnation-line code [Munafo, 2014], a quasi-1D non-equilibrium solver that enables the determination of flow properties along the stagnation streamline of hypersonic flows over spheres and cylinders. The stagnation-line code is coupled with the Mutation++ physicochemical library, enabling gas-surface interactions. The free-stream conditions used for the simulation of both spheres are

expressed in Table 4.4, similar to the conditions employed by Prévèreaud for the development of a bridging function for partially catalytic walls [Prevèreaud et al., 2019]. For the simulation using the VKI stagnation-line code, only one temperature is used to model the mixture energy.

Table 4.4: Free-stream conditions for model verification.

H (km)	u (km/s)	$T_\infty$ (K)	$P_\infty$ (Pa)
40	3.0	226.7	250.60
58	4.8	242.3	21.06
70	6.0	221.7	3.67

The conditions at the boundary layer edge are required to use the Goulard and Fay-Riddell models and are assumed to be at thermochemical equilibrium. For reference, the position of the boundary layer is considered to be located where the flow total enthalpy is 99% of the free-stream total enthalpy ( $h_0 \approx 0.99h_{\infty,0}$ ). The values of temperature at the boundary layer edge for thermochemical equilibrium and the temperature obtained from the stagnation line simulations are compared in Table 4.5. The equilibrium temperature is obtained following the flowchart illustrated in Fig. 4.5, and is independent of the local radius, in contrast with the non-equilibrium temperatures, which depend on the size of the sphere. The increase in radius directly affects the shock stand-off distance, allowing the flow to move towards the equilibrium state. This is verified by the relative difference in temperature, where the case with the larger sphere presents temperatures at the boundary layer edge closer to the temperature at equilibrium for the tested altitudes. A similar observation is made in Table 4.6, where the species mass fraction at the boundary layer edge of the sphere with a larger radius is closer to the equilibrium state.

Table 4.5: Temperature at boundary layer edge.

H (km)	$T_{eq}$ (K)	$T_{neq}$ (R=0.5m)(K)	$T_{neq}$ (R=0.05m)(K)
40	3091.5	3232.3	3734.5
58	5080.4	5298.1	6826.5
70	5333.0	6779.7	11473.2

The surface heat flux as a function of the catalicity coefficient rate and the flow

Table 4.6: Species mass fraction at boundary layer edge.

H (km)	Mode	$Y_N$	$Y_O$	$Y_{NO}$	$Y_{N_2}$	$Y_{O_2}$
40	Equilibrium	1.95761E-5	5.92107E-2	4.43246E-2	7.46373E-1	1.50073E-1
	R = 0.5	1.34981E-5	4.63960E-2	2.68211E-2	7.55005E-1	1.71764E-1
	R = 0.05	4.10136E-6	9.72580E-3	1.01738E-3	7.66698E-1	2.22554E-1
58	Equilibrium	7.30601E-2	2.29933E-1	5.30995E-3	6.91544E-1	1.52734E-4
	R = 0.5	3.87238E-2	2.24580E-1	1.40216E-2	7.21879E-1	7.95910E-4
	R = 0.05	1.61091E-2	1.34933E-1	4.79592E-2	7.29394E-1	7.16048E-2
70	Equilibrium	2.24909E-1	2.31859E-1	1.94494E-3	5.41266E-1	2.15199E-5
	R = 0.5	1.59491E-1	2.25090E-1	1.27126E-2	6.02383E-1	3.24949E-4
	R = 0.05	1.77144E-2	7.24725E-2	1.17167E-2	7.38049E-1	1.60048E-1

temperature at the stagnation line assuming a non-catalytic wall obtained from the stagnation line code are plotted in Fig. 4.20 for the sphere with radius  $R = 0.5$  m. The concentration of species in the stagnation line and a non-catalytic surface is given by Fig. 4.21 for the altitudes of 40, 58 and 70 km respectively. The heat flux obtained using the Goulard and Fay-Riddell models using the Olivier velocity gradient (Eq. 2.41) and the shock-standoff estimation by Freeman (Eq. 2.42) is also plotted in Fig. 4.20a for comparison with the computational results from the stagnation line code. Both models follow the heat flux trend, which increases as the wall becomes more catalytic. Thus, the results show good promise in using both models to quickly capture the impact of catalicity on the surface heat flux.

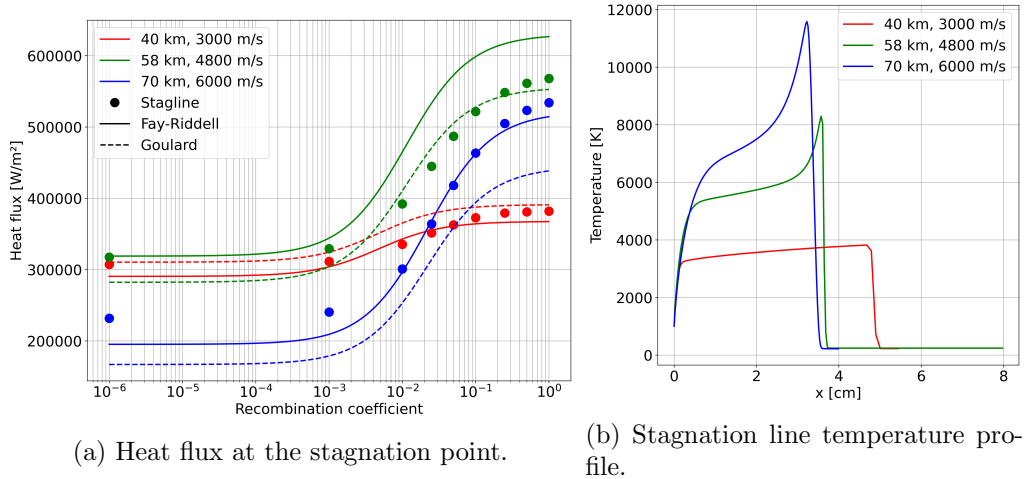


Figure 4.20: Stagnation line results for sphere with radius  $R = 0.5$  m and heat flux prediction using the low-fidelity models.

## Chapter 4. Development of a Reentry Framework

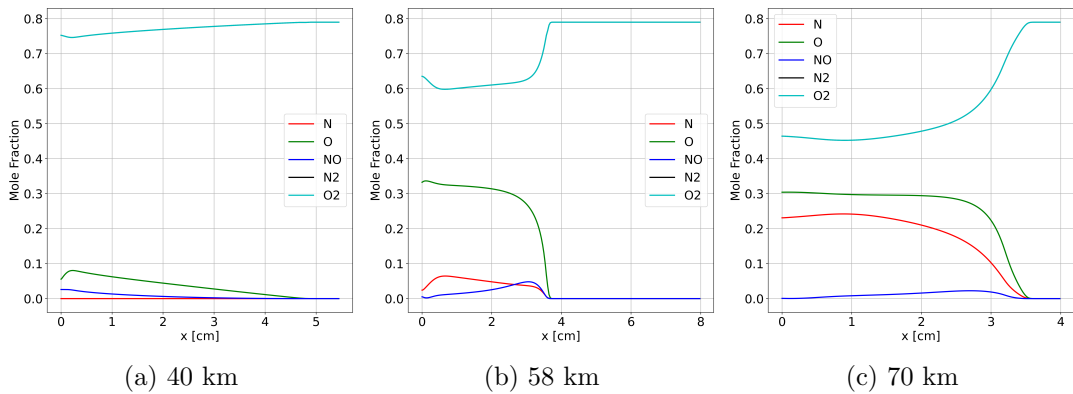


Figure 4.21: Species molar fraction at stagnation line assuming non-catalytic wall for a sphere with radius  $R = 0.5$  m.

The same comparison was performed for the smaller sphere, where Fig. 4.22 shows a comparison of the heat flux given by the low-fidelity models and by the stagnation line code and the temperature evolution along the stagnation line, and Fig. 4.23 shows the molar fraction. For this case, as the equilibrium at the boundary layer edge does not hold due to insufficient residency time at the shock layer, the heat flux is greatly underestimated by the low-fidelity models for no-catalytic walls due to the underestimation of diffusive heat from recombination. This is observed by comparing the O and N species mass fraction in Table 4.6, which is substantially higher for the equilibrium assumption.

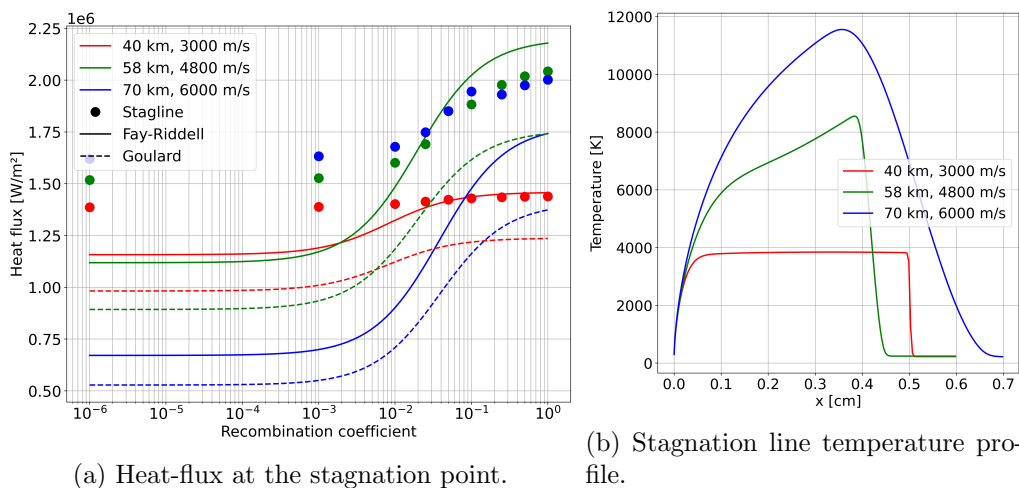


Figure 4.22: Stagnation line results for sphere with radius  $R = 0.05$  m and heat flux prediction using the low-fidelity models.

## Chapter 4. Development of a Reentry Framework

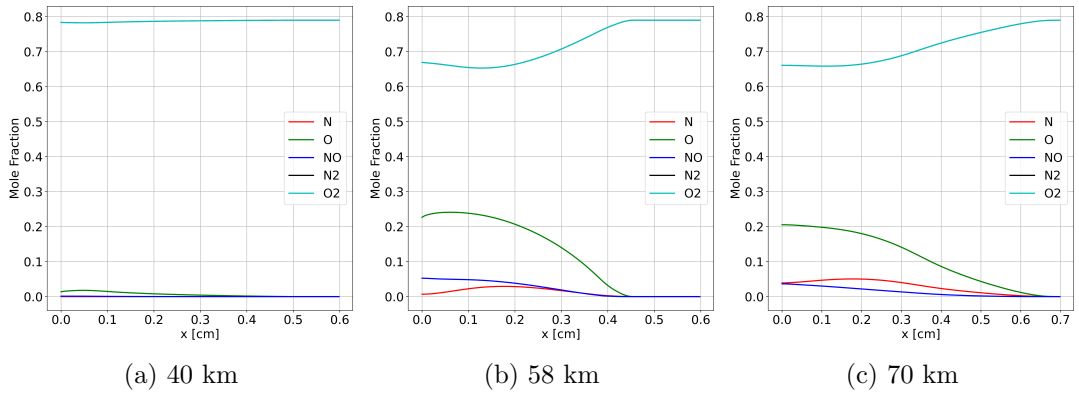


Figure 4.23: Species molar fraction at stagnation line assuming non-catalytic wall for a sphere with radius  $R = 0.05$  m.

However, when using the boundary layer edge conditions retrieved from the stagnation line code, and employing them in the low-fidelity models, results can be improved for no-catalytic and partially catalytic walls, as shown in Fig. 4.24. These results demonstrate that, even when the boundary layer edge equilibrium assumption fails, a good prediction may still be achievable by providing a reasonable estimation of the non-equilibrium conditions.

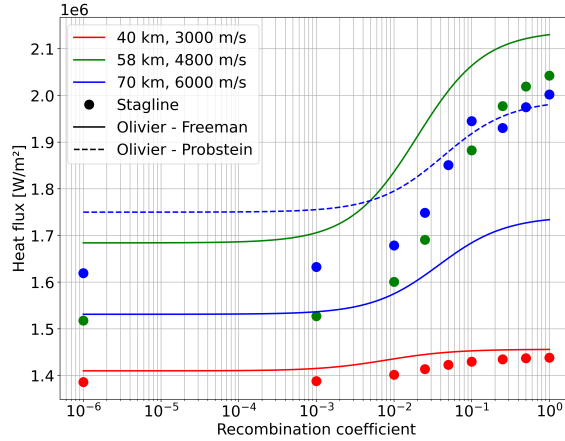


Figure 4.24: Heat flux at the stagnation point for the sphere with radius  $R = 0.05$  m, using the boundary layer edge conditions from the stagnation line code.

### 4.8.3 Structural Analysis Validation

Structural modelling is performed within the re-entry simulation through the coupling of FEniCS and TITAN, as explained in Sec 4.7. To verify the implementation, structural analysis is performed during the re-entry of a conceptual Automated Transfer Vehicle (ATV) geometry, inspired by the unclassified information available at [Koppenwallner<sup>1</sup> et al., 2005], and the initial re-entry conditions are expressed in Table 4.7. The structural simulation is conducted on the volumetric mesh generated by the open-source software GMSH, re-using the mesh originally used for the computation of the mass and inertia of the spacecraft. An example of the generated mesh is shown in Fig. 4.25a. The spacecraft volumetric mesh is partitioned into subdomains, which are used within FEniCS to dynamically impose the Dirichlet boundary conditions and to identify the joints where fragmentation occurs, as seen in Fig. 4.25b. The mesh is only generated at the start of the trajectory simulation or when fragmentation occurs, leading to a change in the underlying geometry.

Table 4.7: ATV trajectory at the start of the re-entry simulation.

Parameter	Value
Altitude [km]	120
Velocity [km/s]	7.57
Flight path angle [°]	-1.45
Pitch angle velocity [°/s]	10

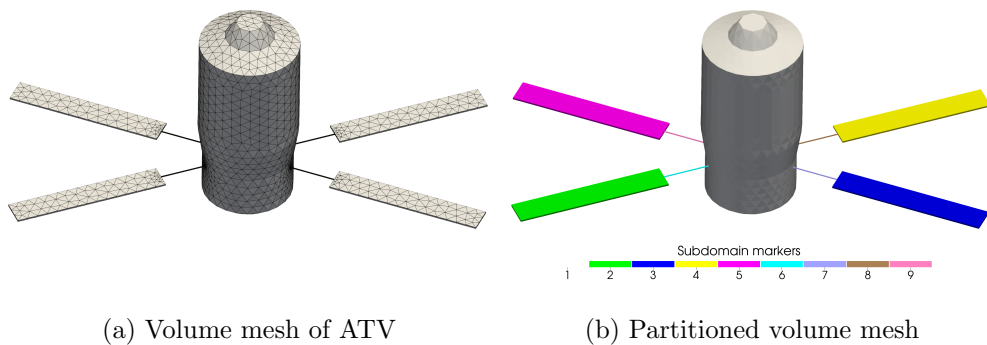


Figure 4.25: Volume mesh with subdomain decomposition generated using GMSH.

The aerodynamic and inertial loads acting on the spacecraft are computed within

TITAN. The aerodynamic loads are computed via the integral distribution of pressure over the objects' surface, while the inertial loads are the centrifugal forces experienced due to the rotation of the body around its centre of mass, characterised by the angular velocity  $\vec{\omega}$ . The contribution of the centrifugal force is given as  $-m\vec{\omega} \times (\vec{\omega} \times \vec{r})$  and is applied to each volumetric element with mass  $m$  and located at  $\vec{r}$  relative to the spacecraft's centre of mass. The joints were modelled as aluminium alloy, and the information on the young modulus and yield stress as a function of temperature (Table 4.8) was included in the material database. The properties are linearly interpolated and maintained constant for temperatures above 500 K. The value for the cylindrical joint thickness was adjusted to get the right total mass for the material selected, according to the unclassified information retrieved from [Koppenwallner<sup>1</sup> et al., 2005]. Using the volume mesh, nodal forces and material properties, the system of linear elastic equations defined in Sec. 4.7 are solved to obtain the nodal displacements, as shown in Figure 4.26b. Using the displacement information, the von Mises stress distribution is obtained using Equation 4.48, illustrated in Fig. 4.26c.

Table 4.8: Material properties of Al6061-T651 as a function of temperature [Summers et al., 2015].

Temperature [K]	E [GPa]	Yield stress (MPa)
24	68	295
200	59	240
300	47	95
500	12	8

Following the structural analysis step, the nodal displacements are passed to TITAN, which is used to update the geometry to account for changes in the surface inclination and inertia tensor. Furthermore, the von Mises stress of the joint components is analysed. If the computed von Mises stress exceeds the yield stress criterion, the joint is considered fragmented and is removed from the simulation. TITAN then proceeds to assess the connectivity between the remaining components and computes the new inertia properties and centre of mass of the newly generated fragments. The evolution of the joint temperature, yield stress and maximum von Mises stress obtained through structural analysis are illustrated in Fig. 4.27a and Fig. 4.27b respectively.

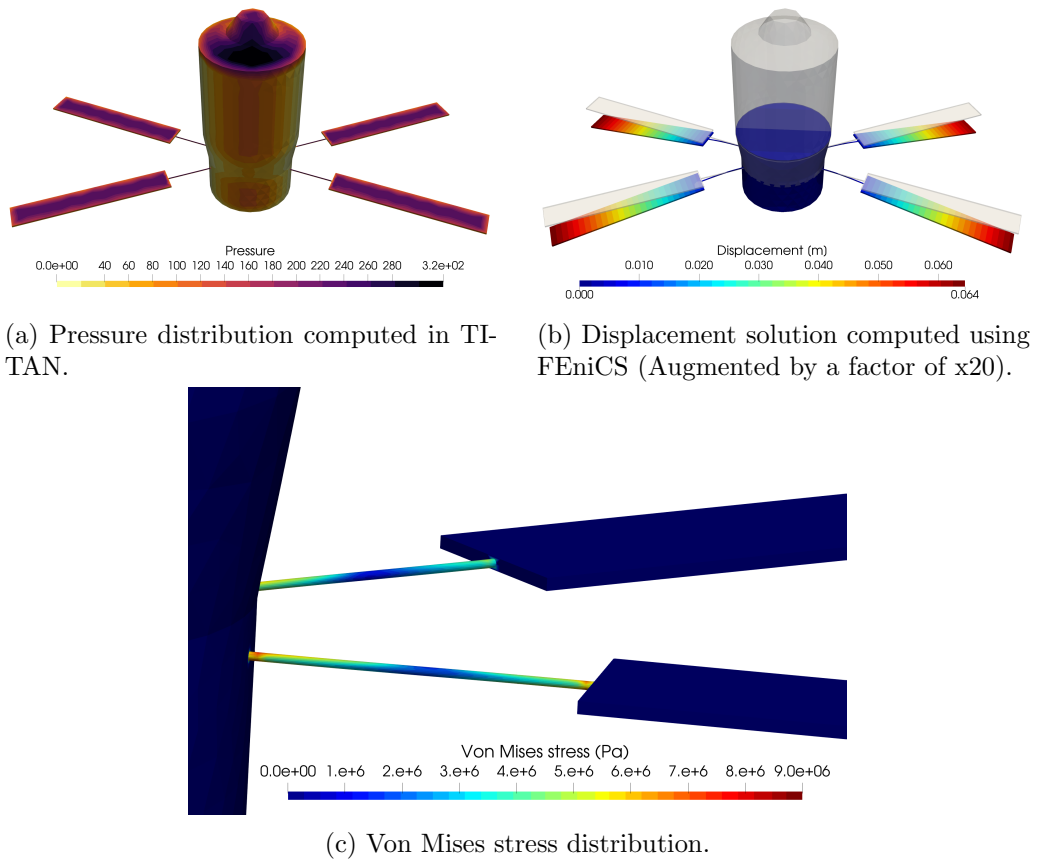


Figure 4.26: Pressure distribution, displacement and von Mises solution on ATV geometry at an altitude of 82 km.

The joint breakup occurs at approximately 80 km of altitude when the von Mises stress surpasses the yield stress, separating the panels from the ATV main body.

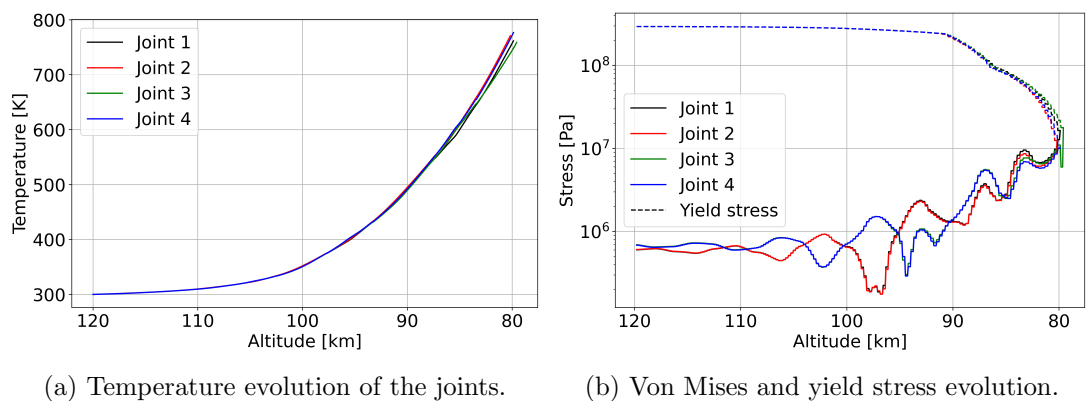


Figure 4.27: Evolution of the joint temperature and stress during re-entry.

#### 4.8.4 Collision Dynamics Validation

The impact mechanics implemented in TITAN are verified by conducting a set of simple problems and comparing the computed trajectory with known analytical solutions. The aerodynamic and gravitational forces are neglected, such that the dynamics of the objects are solely impacted by the collision. Lastly, the collision model is validated through the numerical reconstruction of an experimental test case of a collision with friction.

##### Multi-Sphere Collision.

Consider the configuration illustrated in Fig. 4.28, where sphere A is moving towards sphere B at constant velocity. Assuming the absence of friction forces, the analytical post-collision velocity for sphere A is given as

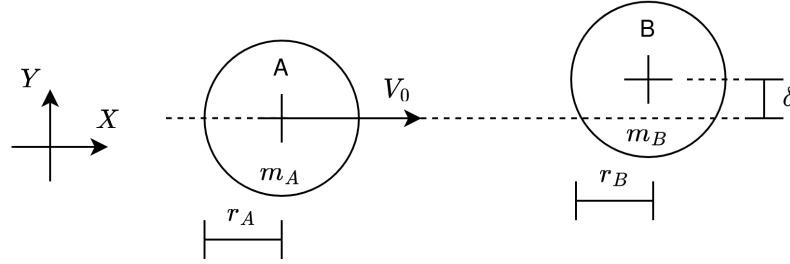


Figure 4.28: Sphere-sphere collision arrangement.

$$u_A = V_0 - 2 \frac{m_B}{(m_A + m_B)} \frac{\left( (r_A + r_B)^2 - \delta^2 \right)}{(r_A + r_B)^2} V_0 \quad v_A = -2\delta \frac{m_B}{(m_A + m_B)} \frac{\sqrt{(r_A + r_B)^2 - \delta^2}}{(r_A + r_B)^2} V_0, \quad (4.50)$$

and for sphere B as

$$u_B = 2 \frac{m_A}{(m_A + m_B)} \frac{\left( (r_A + r_B)^2 - \delta^2 \right)}{(r_A + r_B)^2} V_0 \quad v_B = 2\delta \frac{m_A}{(m_A + m_B)} \frac{\sqrt{(r_A + r_B)^2 - \delta^2}}{(r_A + r_B)^2} V_0, \quad (4.51)$$

where  $V_0$  is the pre-collision velocity of sphere A,  $u$  and  $v$  are the X- and Y-velocity components, respectively,  $m$  is the sphere mass,  $r$  is the radius [m] and  $\delta$  is the offset

distance [m] of the centers of mass in the Y direction.

The simulation of the sphere-sphere collision assumed a perfectly elastic collision (coefficient of restitution  $\varepsilon = 1$ ) and the parameters of sphere A were defined as  $V_0 = 5$  m/s,  $r_A = 1$  m, and  $m_A = 1$  kg. Two scenarios were tested for a sphere B with radius  $r_B = 1$  m, setting different sphere mass  $m_B$  and offset distance  $\delta$ . The results reported in Fig. 4.29 show that the computed values are in good agreement with the analytic position for both tested scenarios.

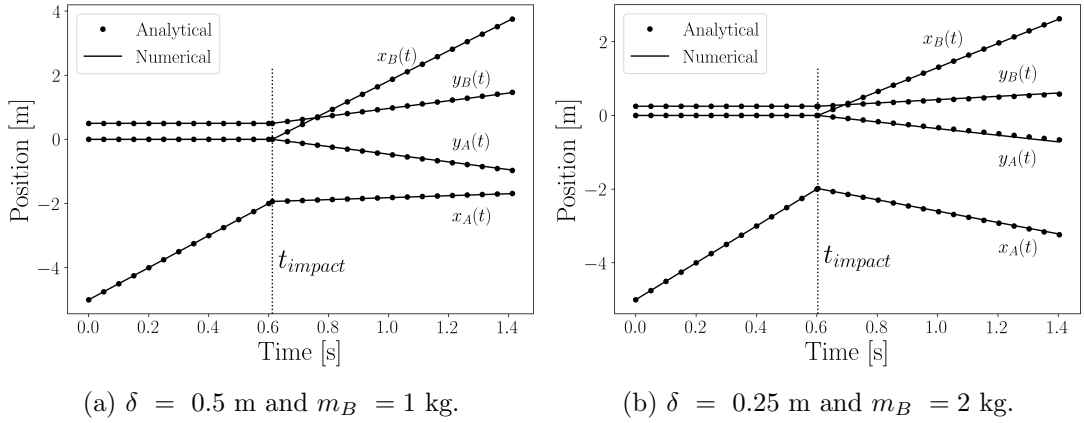


Figure 4.29: Sphere-Sphere collision

The verification of simultaneous multi-collision is also conducted by modifying the number and arrangement of the spheres according to Fig. 4.30 such that sphere B, sphere C and sphere D are in contact. When sphere A collides with the group, three points of simultaneous collision are expected: sphere A - sphere B, sphere C - sphere B and sphere D - sphere B. For this analysis, the radius of the spheres was imposed to be  $r = 0.1$  m, the velocity of sphere A was set to  $V_0 = 1$  m/s and the mass of the spheres was fixed at  $m = 1$  kg. The computed and analytical trajectory of the spheres is compared in Fig. 4.31, showing a good agreement between the analytical and predicted trajectories.

### Sphere-Rod collision.

The impulse vector is generally not aligned with the object's center of mass, inducing a change in the body's rotational velocity. For this purpose, the collision between a

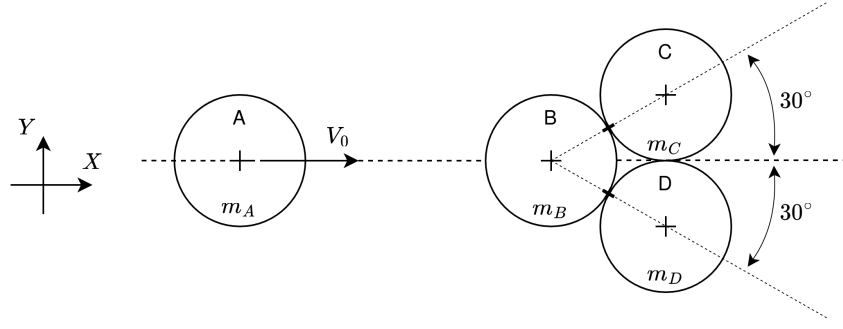


Figure 4.30: Multi-sphere collision arrangement.

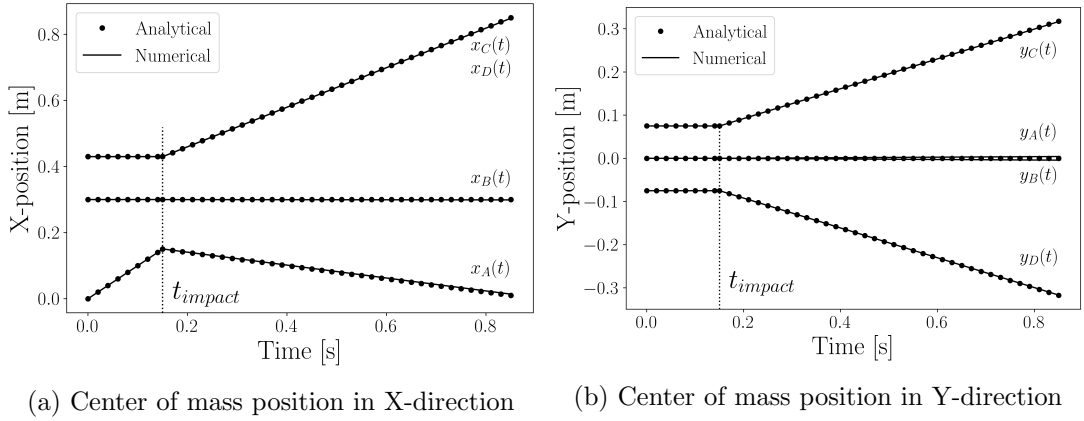


Figure 4.31: Multi-sphere collision results.

sphere of mass  $m_S = 2$  kg and radius  $r_s = 1$  m and an unconstrained rod of mass  $m_R = 1$  kg, length  $l = 1.2$  m and radius of  $r_R = 1$  m was simulated, as illustrated in Fig. 4.32a. Disregarding aerodynamic drag, the momentum transferred from the sphere during the collision at the lower end of the resting rod induces the rod to spin indefinitely. The analytical equations of the post-collision velocity are given for the sphere as

$$u_s = \left[ 1 - (1 + \varepsilon) / \left[ 1 + \frac{m_S}{m_R} + \frac{m_S l^2}{4I_R} \right] \right] V_0, \quad (4.52)$$

and for the rod as

$$u_r = (1 + \varepsilon) V_0 / \left[ \frac{m_R}{m_S} + 1 + \frac{m_R l^2}{4I_R} \right] \quad \omega_r = l(1 + \varepsilon) V_0 / \left[ \frac{2I_R}{m_S} + \frac{2I_R}{m_R} + \frac{l^2}{2} \right] \quad (4.53)$$

where  $V_0$  is the initial sphere velocity,  $I_R$  is the rods' moment of inertia and  $\varepsilon$  is the coefficient of restitution.

A comparison between the analytical and predicted trajectory of the rod's lower end is shown in Fig. 4.32b, for a coefficient of restitution of  $\varepsilon = 0.8$  and  $\varepsilon = 1.0$ . The comparison shows a good agreement between the results for the simulated time window.

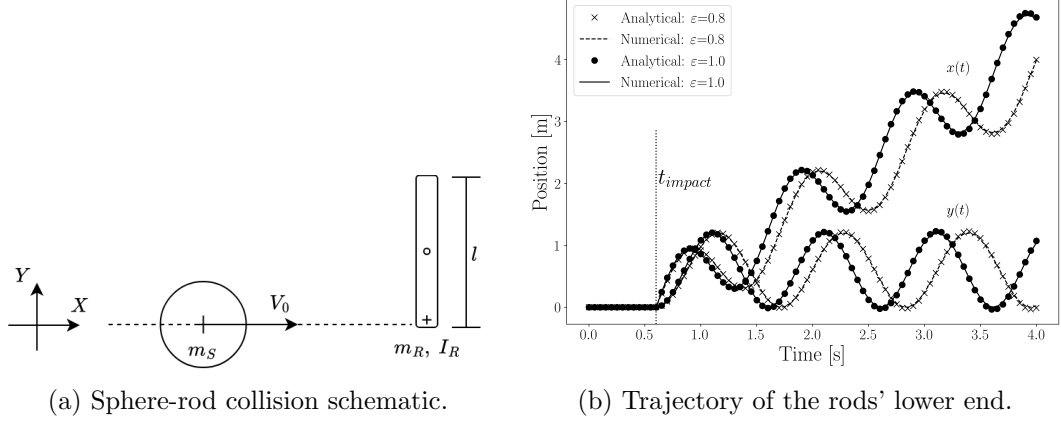


Figure 4.32: Setup and results for the sphere-rod collision case.

### Cylinder-wall collision.

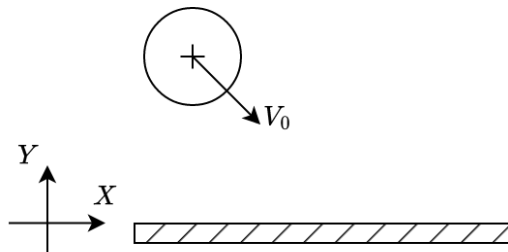
A two-dimensional impact experiment was numerically rebuilt using the collision model implemented in this framework. The experiment was conducted by Martin et al. [Fandrich and Hogue, 1995] using air tables, which injected air through regularly spaced holes to avoid friction forces from the contact between the table surface and the puck. A collision between a cylindrical puck and the table wall was selected for the reconstruction, due to the possibility of direct comparison between the predicted and experimental position of the puck. To emulate the experimental environment, friction forces were only accounted for during impact. The cylindrical puck parameters and initial conditions are expressed in Table 4.9 and the setup schematic is shown in Fig. 4.33a.

For the simulation, a coefficient of restitution  $\varepsilon = 0.50$  was used as specified by Martin et al. [Fandrich and Hogue, 1995]. The friction between the wall and the puck is also considered by employing Coulomb's law of friction [Popov, 2010] and setting

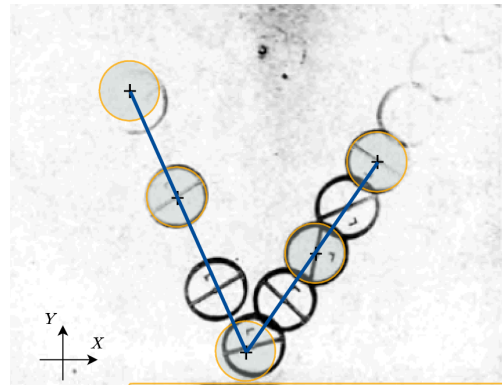
the friction coefficient to  $\mu = 0.07$ , half of the value determined experimentally. This assumption is supported by Martin et al. [Fandrich and Hogue, 1995], where the author mentions that during the validation of the computational model, using half of the experimentally determined friction coefficient resulted in a better agreement between the theoretical output and the experimental data. The experimental and predicted positions of the cylindrical puck before and after colliding with the table wall are superposed in Fig. 4.33b, showing the conducted simulation is in good agreement with the experimental observation. The results demonstrate the ability of the framework to predict the position of the puck and validate the implementation of the collision model.

Table 4.9: Geometrical, inertial and initial conditions of the cylindrical puck.

$r$ [mm]	$m$ [g]	$I$ [g.mm <sup>2</sup> ]	$V_x$ [mm/s]	$V_y$ [mm/s]
102	94	122200	521	-1169



(a) Puck-wall collision schematic.



(b) Comparison between predicted (orange) and observed (black) [Fandrich and Hogue, 1995].

Figure 4.33: Setup and results for the puck-wall collision case.

## Chapter 5

# Integration of a High-fidelity Fluid Solver for Proximal Aerodynamics Interaction

The aerodynamics of proximal fragments affect the trajectories and ground dispersion for meteor entries [Passey and Melosh, 1980, Register et al., 2020], and analogously, for satellite re-entries [Marwege et al., 2018]. The presence of multiple fragments can result in smaller bodies being entrained within the bow shock formed by the larger leading object over considerable distances. Eventually, fragments can be trapped in the wake of the larger object, leading to a collimation effect [Barri, 2010, Artemieva and Shuvalov, 2001]. In addition, shock interaction patterns can occur and impinge on the surface, generating highly localized pressure and heat loads, thus affecting the overall dynamics and expediting the demise process [Register et al., 2020]. In some cases, the fragments follow the leading bow shock, in a phenomenon called shock surfing [Laurence and Deiterding, 2011].

Over the years, several methods have emerged to address the proximal-body aerodynamic interaction for cylindrical (2D) and spherical (3D) objects. Laurence et al. [Laurence et al., 2007, Laurence and Deiterding, 2011] have developed analytical methods based on the Blast Wave Theory [Sedov, 1959] and Modified Newtonian Theory [Lees, 1955] to determine the drag and lift experienced by cylinders and spheres when en-

trained in the bow shock and during shock impingement. Further developments to accommodate real gas effects at thermochemical equilibrium were conducted by Prevereaud et al. [Prevereaud et al., 2013]. However, these methods are unsuitable for analyzing the interactions for general configurations of arbitrarily shaped fragments [Register et al., 2020]. To overcome this limitation, Marwege et al. [Marwege et al., 2018] proposed a numerical approach to predict the pressure distribution of entrained fragments using superposing numerical flows from a computed database. However, the approach is limited to two-body interactions and has been tested for spherical bodies, as complex geometries would require excessive computational resources.

The use of CFD solvers to evaluate the proximal-body aerodynamic and aerothermodynamic interaction allows for arbitrary configurations and geometries while capturing the emerging shock interaction patterns. To improve the current capabilities of the state-of-the-art re-entry analysis tools, this chapter describes the integration of a higher-fidelity non-equilibrium solver (SU2-NEMO [Maier et al., 2021, Maier et al., 2023]) into TITAN, enabling to capture the shock features that simplified methodologies are not able. To increase grid accuracy, an anisotropic mesh adaptation tool (AMG) is used. A summary of the tools is provided, and more in-depth information can be found in Appendix C. The influence of anisotropic grid adaptation on the prediction of flowfield and surface quantities is analysed in this project for hypersonic flows in air as an alternative to structured grids for cases where the structured grid generation/adaptation is not straightforward, such as for destructive atmospheric re-entry. The current chapter also explores the use of a quasi-steady methodology to decouple the dynamics computation from the CFD solver, simplifying the simulation process.

## 5.1 Coupling of SU2-NEMO and Mesh Adaptation

To expand the capabilities of the reentry framework in solving complex flow structures arising from the objects' proximity, the quasi-steady approach illustrated in Fig. 5.1 has been implemented into the framework, allowing to obtain grid-converged solutions while capturing the directional flow features. In this approach, the dynamics of the objects are computed assuming a steady-state solution at each time step. The quasi-

steady high-fidelity loop can be summarised as follows: creation of a computational domain, flow simulation using a CFD solver, adaptation of the mesh, and computation of aerodynamic forces to propagate the object dynamics.

As shown in Fig. 5.1, before proceeding to the flow simulation, the volumetric grid used to simulate the flow around the bodies is automatically generated and manipulated by referencing third-party tools through the framework. The domain is generated by the open-source software GMSH [Geuzaine and Remacle, 2009], which produces a fully unstructured tetrahedral computational domain using the frontal Delaunay triangulation method. The computational volume is delimited by a semi-ellipsoid with two axes, corresponding to the axis of revolution and the radial axis. The centre of the semi-ellipsoid is determined by the geometrical centre, accounting for all the objects in the CFD simulation, and the axis of revolution is parallel to the direction of the flow. The length of the axis of revolution is specified to be a minimum of three times the greatest distance between the vertices of the objects in the direction of the flow, while the radial axis is set to be at least twice the largest distance within the plane perpendicular to the flow direction. The dimensions of the cell elements on the initial grid exhibit a linear increase, from roughly the size of the surface panels in the vicinity of the objects up to 5 times greater at the boundary of the domain. Additionally, to partially recover the solution from errors generated through the misalignment of tetrahedral elements with the shock wave, a prismatic boundary layer is generated using the tool Bloom, a boundary layer mesh generator for complex geometries developed by INRIA.

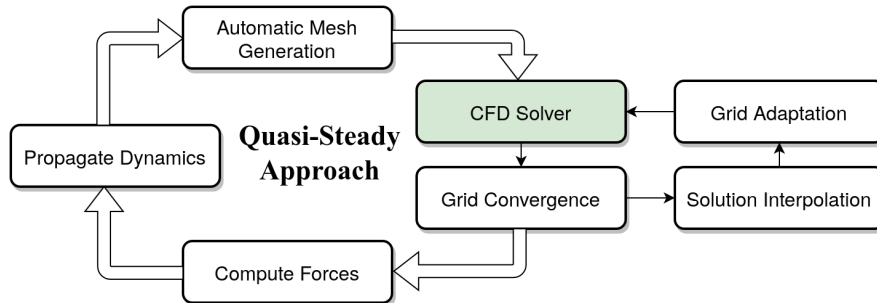


Figure 5.1: Flowchart of the quasi-steady approach for high-fidelity modelling.

High-fidelity solutions are calculated using the SU2-NEMO CFD solver [Maier et al., 2023, Maier et al., 2021], which has been extensively tested for hypersonic regimes. The SU2-NEMO extends the capability of the classical Navier-Stokes code in the baseline SU2 framework [Economon et al., 2016] to account for a chemically-reacting, non-equilibrium flow using the two-temperature model by Park [Park, 1993]. By default, a reactive gas flow using Navier-Stokes equations is used for the CFD simulations, if not otherwise specified before the initialization of the simulation. The solver adopts a classical edge-based Finite Volume Method (FVM) approach for the numerical discretization of the computational domain. Several upwind schemes are available for computing inviscid fluxes, with a special focus on Flux Vector Splitting (FVS) schemes. The solution is reconstructed through the implementation of the Monotonic Upstream-centered Scheme for Conservation Laws (MUSCL), allowing to obtain second-order approximation accuracy. For the determination of viscous flux, the average values at the dual-grid interface are used, and gradient information is derived through the Weighted Least Squares method.

To achieve a grid-converged solution, anisotropic grid adaptation of the volumetric mesh and the generation of refined prismatic boundary layers are done to enable accurate computation of the physical surface heating and shear stress. The mesh is anisotropically adapted through the use of the AMG library [Loseille and Loehner, 2011, Loseille and Menier, 2014, Loseille et al., 2015]. The adaptation process produces local anisotropic elements that follow the direction of the complex multi-directional flow features, such as shock waves, contact discontinuities, and boundary layers. The adaptation is performed by computing an optimal Riemannian metric tensor field from the error estimate of a given background mesh and respective solution. The adaptation procedure is repeated until a grid-converged solution is achieved by assessing if the difference in forces and moment coefficients between consecutive adaptations or the maximum number of grid adaptations is reached.

After the assessment of the loads through the CFD simulation, the forces acting on the surface of the objects are computed by integrating the pressure and shear stress over the individual object panels. The time integration is then performed using the

forward Euler method, computing the new object’s state, and closing the quasi-steady loop.

The adaptation loop was tested for the simulation of a free-flying ring for a hypersonic  $N_2$  flow. The ring geometrical parameters and freestream conditions are specified in Table 5.1 and Table 5.2, respectively. The aerodynamic coefficients are compared with experimental results obtained by Grossir et al. [Grossir et al., 2020] using the hypersonic wind tunnel Longshot at the von Karman Institute. Albeit having a simple geometry, the ring is similar to an inter-stage element of a rocket. The presence of a ring at different angles of attack exhibits complex flow features, such as self-impingement, that need to be carefully addressed in order to compute the correct aerodynamic coefficients. Figure 5.19 showcases the capabilities of anisotropic grid adaptation in capturing the complex shock interference formed by the ring. A comparison between the numerical and experimental aerodynamic coefficients for different angles of attack ( $0^\circ$ ,  $30^\circ$ ,  $45^\circ$  and  $90^\circ$ ) is provided in Fig. 5.3, where the numerical coefficients are in good agreement with the experimental data, highlighting the benefits of using an adaptation loop for high-fidelity modelling.

Table 5.1: Ring geometrical details.

Parameters	Annular ring
Diameter	60 mm
Height	$h = 15$ mm
Thickness	$t = 2$ mm
Reference length	$l_{ref} = 60$ mm
Reference surface	$S_{ref} = 900$ mm <sup>2</sup>
Reference point	center of gravity
Angle of attack	$0^\circ, 30^\circ, 45^\circ, 90^\circ$

Table 5.2: Freestream parameters.

$V_\infty$ [m/s]	$P_\infty$ [Pa]	$T_\infty$ [K]
2046	560.7	75

Chapter 5. Integration of a High-fidelity Fluid Solver for Proximal Aerodynamics Interaction

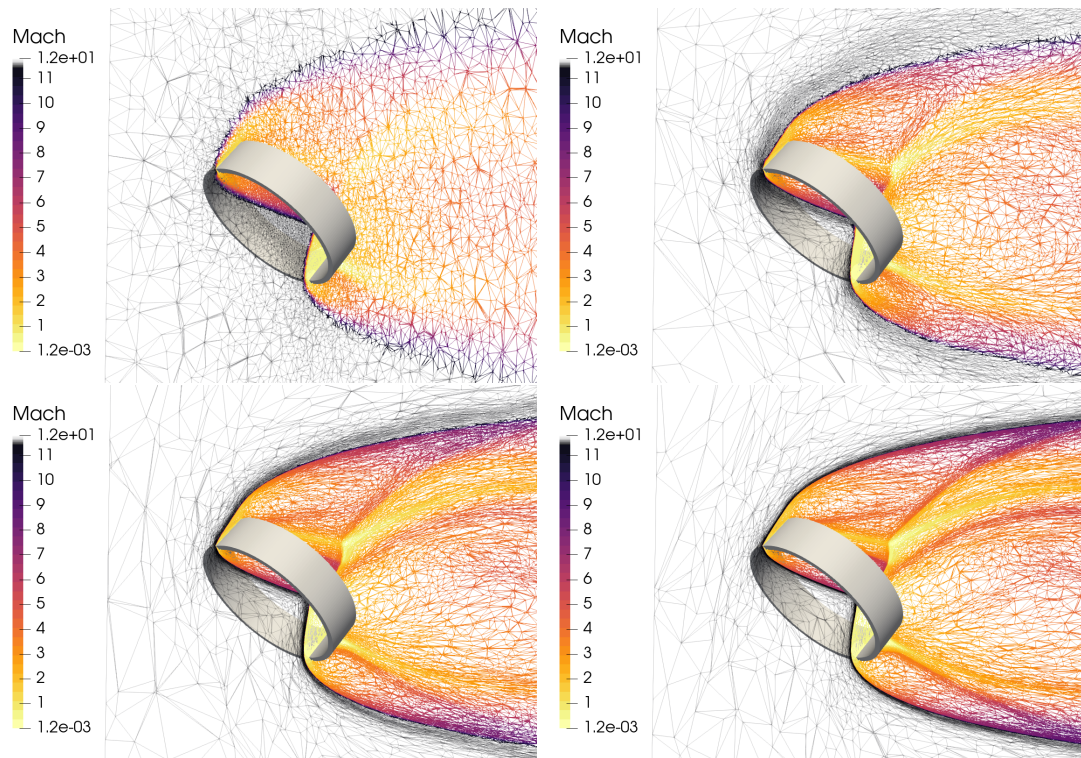


Figure 5.2: Grid adaptation for a ring with 45° angle of attack.

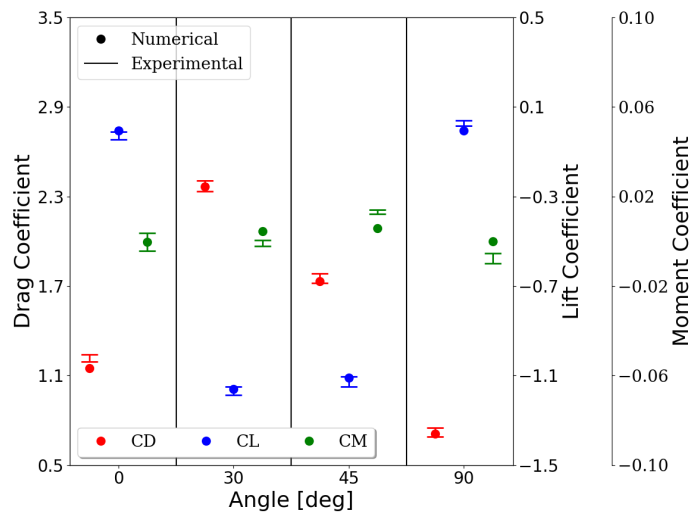


Figure 5.3: Ring aerodynamic coefficients for different angles of attack.

### 5.1.1 Verification of Anisotropic Adaptation in Hypersonic Flows

The use of anisotropic grids for hypersonic flows was evaluated for several cases before integration into TITAN, as described in this section. The test cases were simulated to assess the effect of grid element type and orientation on the solution obtained with anisotropic unstructured grids around 3D geometries. First, a three-dimensional sphere is analysed and results are compared with the available reference data in the literature. The isolated blunt body generates a single shock wave without any interaction with other flow features, thus enabling the analysis in greater detail of the effects of grid misalignment with the shock and the generation of momentum in the wrong direction. A case regarding a single cylinder is presented in Appendix D, where a comparison between a solution obtained using anisotropic grid adaptation and a generated structured grid is performed, as it is known that the problem of misalignment between the shock and the mesh is known to be less problematic for quadrilateral/hexahedral grids.

After demonstrating the use of anisotropic grids for flows around single blunt bodies with numerical and experimental data comparison, a three-dimensional proximal spheres test case is examined. The ability of anisotropically adapted grids to achieve good surface predictions and alignment with the different directional flow features generated due to shock-shock interactions is demonstrated. The three-dimensional proximal spheres results are validated with experimental data provided by DLR Institute of Aerodynamics and Flow Technology through experimentation using the hypersonic wind tunnel H2K [Sebastian Willems, 2018]. A two-cylinder test case is also presented in Appendix D, where the anisotropic results are compared with the integral quantities from reference literature data and with the results obtained through the generation of a structured grid that closely follows the directional flow features.

For the analysed cases, it is of major importance to use a structured grid across the boundary layer to overcome surface heating problems introduced by the use of tetrahedral grids in the capture of the bow shock, as shown by Nompelis et al. [Nompelis et al., ]. The error in heating prediction is caused by the introduction of entropy errors when the faces of the local elements are not aligned with the shock, which propagate and contaminate the shock layer [Carpenter and Casper, 1999].

### 3D Single Sphere

To assess how the anisotropic grids handle the prediction of surface pressure and thermal quantities, a three-dimensional flow over a single sphere is considered in this section. The 1 decimeter radius sphere is subjected to the free-stream and boundary conditions shown in Table 5.3, which correspond to a Mach 12 flow. For a better comparison with Candler et al. [Candler et al., 2007] and Gnoffo et al. [Gnoffo, 2009] results for this particular test case, a perfect gas air model was considered. Figure 5.4 illustrates the evolution of the heat flux and pressure surface contours through the grid adaptation. The details of the grids can be observed in Table 5.4. All grids have a hexahedral boundary layer with 80 elements normal to the surface.

Table 5.3: Free-stream and wall values for the single sphere case.

$T_\infty$ [K]	$T_w$ [K]	$\rho_\infty$ [kg/m <sup>3</sup> ]	U [m/s]
300	800	0.0216	4167

Table 5.4: Grid details for the single sphere case.

Grid	Nodes	Elements	Average AR	Maximum AR
Isotropic grid - level 0	448,754	703,444	1.568	5.503
Anisotropic grid - level 1	977,849	3,876,455	2.026	11.817
Anisotropic grid - level 2	1,385,755	6,329,490	4.840	25.591
Anisotropic grid - level 3	1,955,103	9,744,654	9.652	55.388

An analysis of the spurious momentum generation near the stagnation line throughout the adaptation levels is shown in Fig. 5.5. While the first row of sub-figures representing the first anisotropic grid generated contains elements that are introducing wrong values of momentum, it becomes clear that as adaptation progresses, the error is corrected, until the error introduced at the shock area is minimized in the last level of adaptation.

The first row of sub-figures in Fig. 5.4 shows the surface contours obtained using an unbiased isotropic grid, and illustrates how the non-alignment of the elements in the shock area affects the prediction of the surface loads. While only one level of anisotropic grid adaptation is required to observe vast improvements in the symmetry capture of

## Chapter 5. Integration of a High-fidelity Fluid Solver for Proximal Aerodynamics Interaction

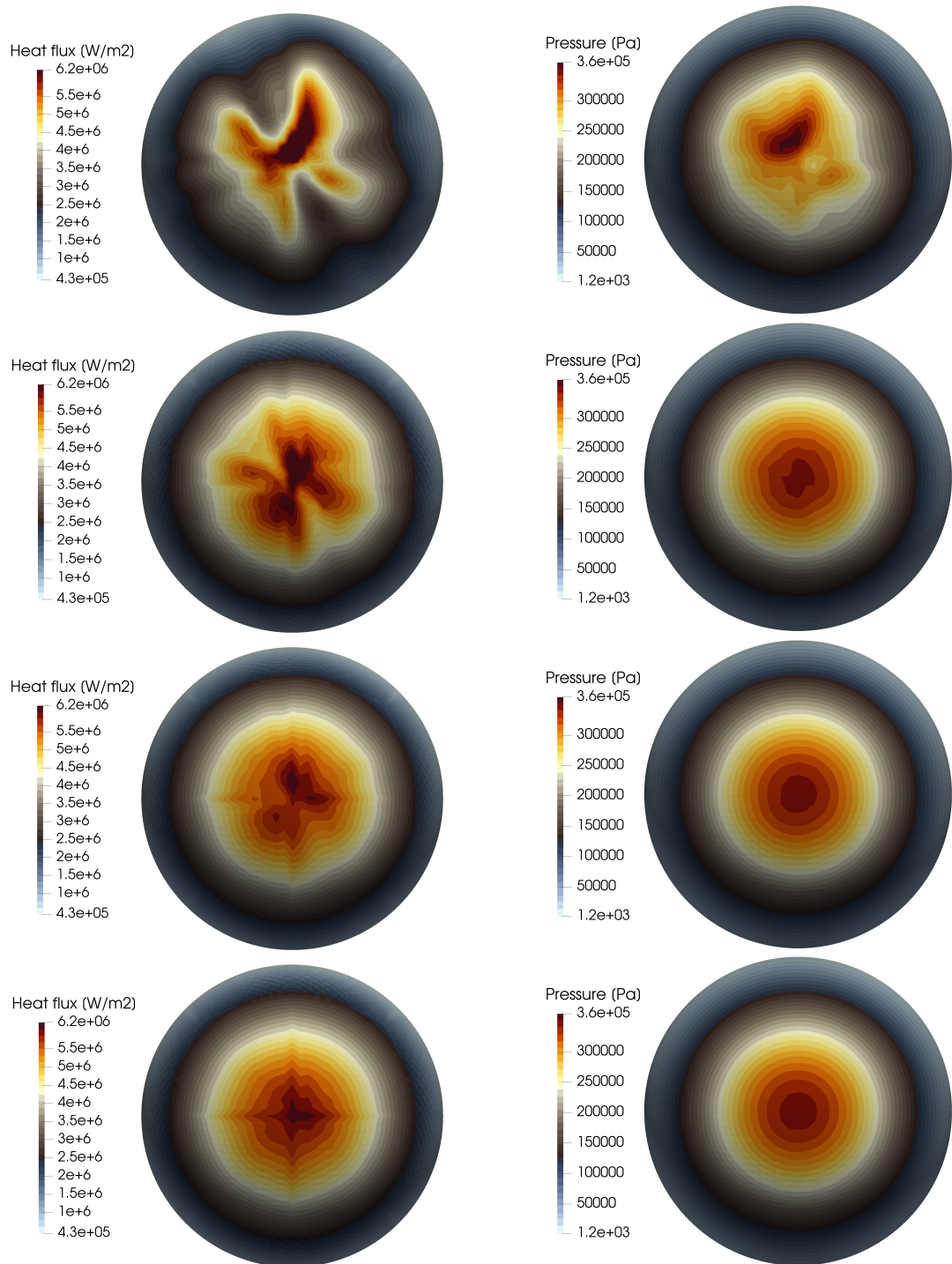


Figure 5.4: Heat flux (left) and pressure (right) contours of the single sphere case for different levels of adaptation (Top figures correspond to the first grid and bottom figures correspond to the final adapted grid).

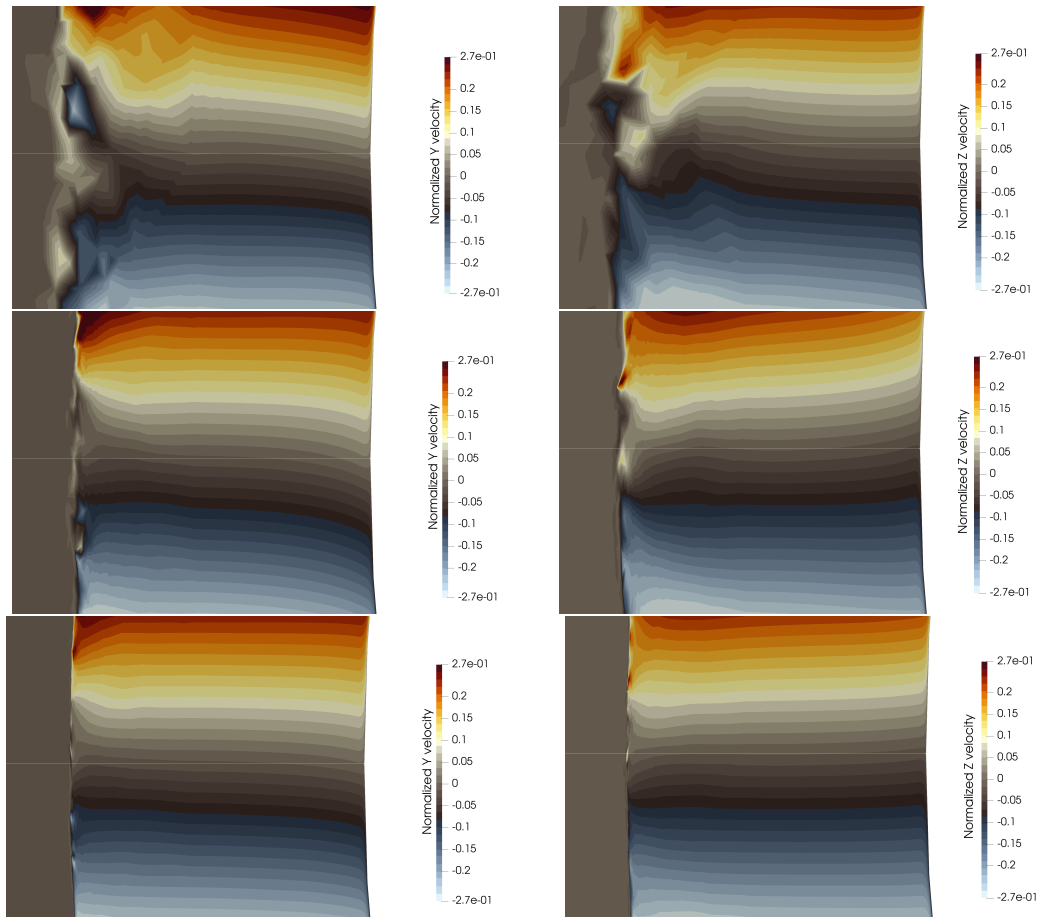


Figure 5.5: Contours of normalized y- velocity  $[v/u_2]$  (left) and z- velocity  $[w/u_2]$  (right) components contours of the single sphere case for different levels of adaptation (Top figures correspond to the first grid and bottom figures correspond to the final adapted grid).

the surface pressure near the stagnation point, the predicted heating is more sensitive to the local grid orientation at the shock, thus requiring more iterations to obtain a near symmetric solution without the use of flux reconstruction methods [Gnoffo, 2009].

The heat flux and pressure plots (Fig. 5.6) of the +y and +z plane for the different anisotropic grids show a symmetry improvement throughout the adaptation process. The last row of sub-figures corresponds to the plots of the last adapted grid. The plots show that symmetry was achieved in the prediction of surface pressure and, although symmetry was not achieved for the heat flux, the plots show a clear convergence of the heating prediction in the +y and +z plane, and it's comparable with the solution obtained from LAURA [Gnoffo, 2009] and US3D [Candler et al., 2007] solvers, showing the applicability of anisotropic grids for 3D cases.

### 3D Proximal Spheres

The effectiveness of the adaptation process for a three-dimensional viscous flow over a proximal-sphere configuration is assessed in this section. The free-stream flow conditions, wall temperature and species mass fractions are written in Table 5.5, and the case geometry is illustrated in Fig. 5.7.

Initially, an isotropic grid is used for the computation of the flowfield and prediction of the surface quantities. The final solution and numerical grid are then used to drive the adaptation process of AMG for the generation of the anisotropic grid. For simulations where the solution is not known beforehand, grid adaptation is necessary to achieve good predictions. Details regarding the grids used for the simulation, the computed aerodynamic coefficients and the peak value of the Stanton number for the aft sphere can be found in Table 5.6. The evolution of the aerodynamic coefficients and Stanton number throughout the different levels shows that the smallest difference occurs for the last grid adaptation. Additionally, it can be observed that the degree of anisotropy increases with the levels of adaptation. All three grids employed a prismatic boundary layer around the two spheres to partially recover the solution from errors generated through the misalignment of tetrahedral elements with the shock wave. For simplicity, only the final grid used is illustrated, in Fig. 5.8, where a higher level of local mesh

## Chapter 5. Integration of a High-fidelity Fluid Solver for Proximal Aerodynamics Interaction

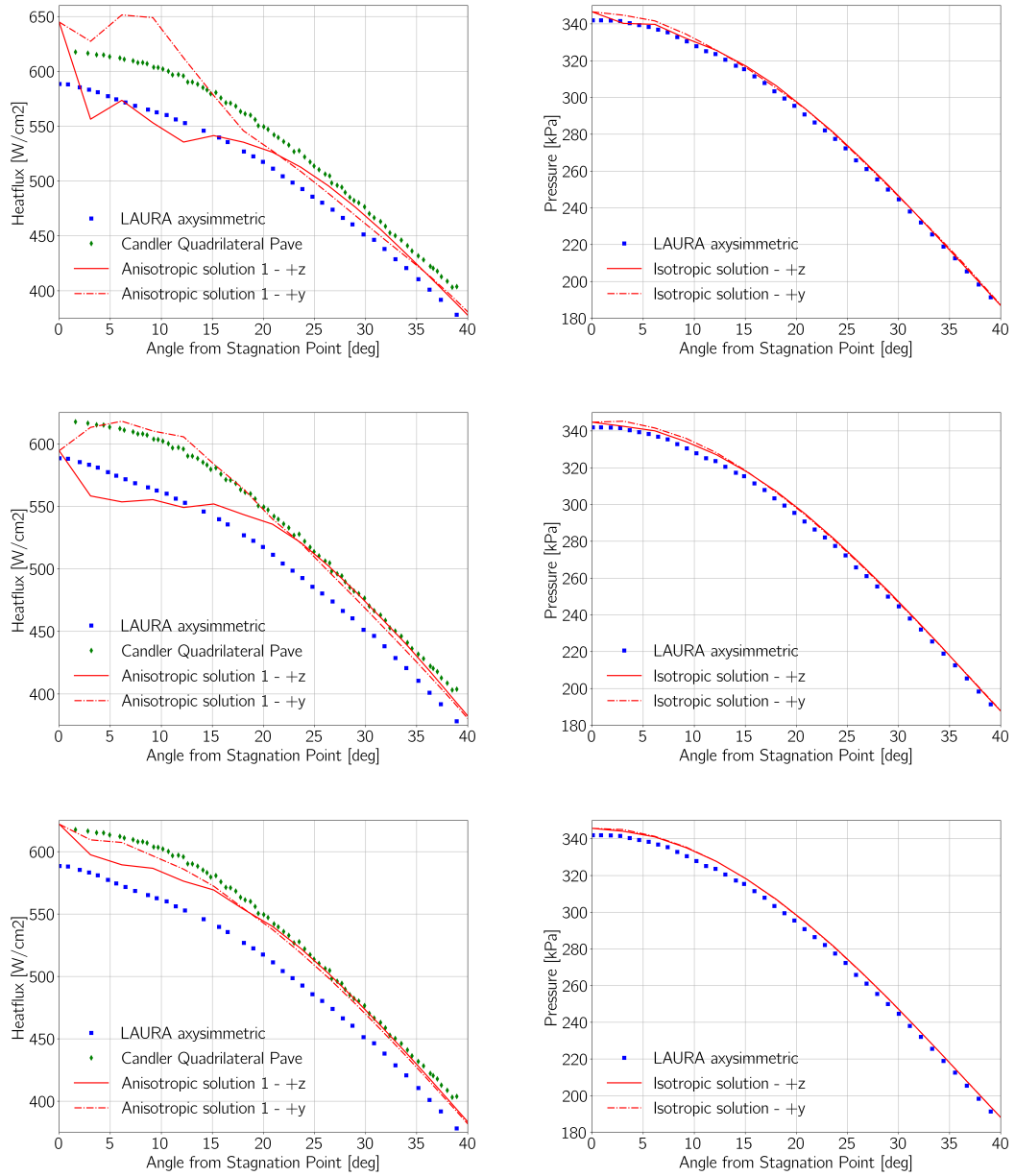


Figure 5.6: Heat flux (left) and pressure (right) plots of the different anisotropic grids for the +y and +z plane (Top figures correspond to the first adapted grid and bottom figures correspond to the final adapted grid).

refinement and element orientation at the shock waves and shock-shock interaction region can be observed.

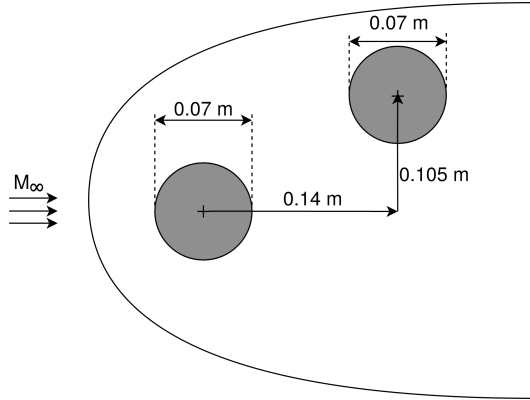


Figure 5.7: Geometry configuration of the three-dimensional two-spheres case.

Table 5.5: Free-stream and wall values for the two-spheres case.

$T_\infty$ [K]	55.56
$T_w$ [K]	293.15
$P_\infty$ [Pa]	125.61
$U$ [m/s]	1048.0
N [%]	0.0
O [%]	0.0
NO [%]	0.0
N2 [%]	77.0
O2 [%]	23.0

Table 5.6: Grid details for the two-spheres case.

	Initial grid	Level 1	Level 2	Level 3
Nodes	4,834,102	6,799,812	8,337,524	9,767,945
Elements	12,045,150	23,739,949	32,954,899	41,532,117
Avg. AR	1.553	2.512	4.175	4.274
Max. AR	6.313	15.399	48.097	58.971
$C_L$	-0.13926	-0.13982	-0.14196	-0.14150
$C_D$	0.29303	0.29383	0.29755	0.29682
St	0.43858	0.19508	0.15506	0.16218

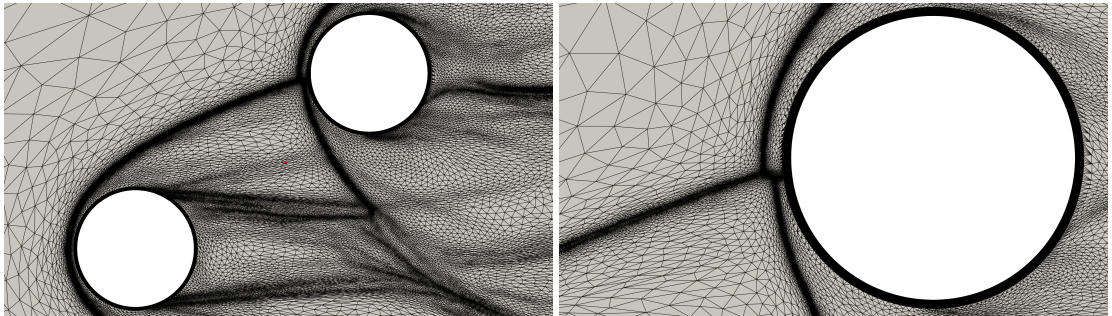


Figure 5.8: Detailed visualization of the final anisotropic grid used for the two-spheres case.

Figure 5.9 shows the numerical Schlieren on the left and Mach contours on the right for the different numerical grids, starting from the isotropic grid at the top. It



is clear that throughout the different levels of adaptation, the shock discontinuity and the shock-shock interaction pattern of type IV, according to Edney criteria [Edney, 1968], are sharply captured. The major flow difference can be observed when the grid is adapted for the first time, where the shock impingement on the aft sphere is captured, showing the importance of anisotropic grid adaptation and element alignment in the capture of complex features, when the solution is not known beforehand. A comparison between the numerical Schlieren of the most refined anisotropic grid and the experimental Schlieren [Sebastian Willems, 2018] obtained from experiments conducted at the hypersonic wind tunnel H2K at DLR Institute of Aerodynamics and Flow Technology is shown in Fig. 5.10. Overlaying the Schlieren images at the region of the shock-shock interaction, it can be visualized the clear superposition of the experimental and numerical shock waves, supporting the validity of the anisotropic approach used in this work to perform proximal-body simulations.

The surface pressure plot shown in Fig. 5.11 illustrates the importance of grid alignment in the location of the pressure peak, where the largest difference is shown between the isotropic grid and the first adapted grid obtained. The last two grid levels show similar pressure profiles, showing that grid convergence was achieved. The obtained pressure field for the final grid, illustrated in Fig. 5.12, shows a smooth contour without any considerable oscillation.

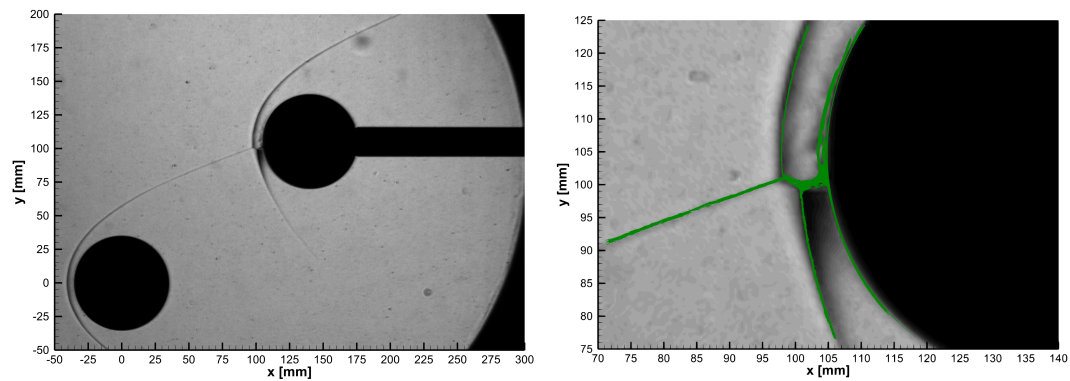


Figure 5.10: Experimental Schlieren (left) and superposition of experimental and numerical Schlieren in green (right) at the shock-shock interaction region.

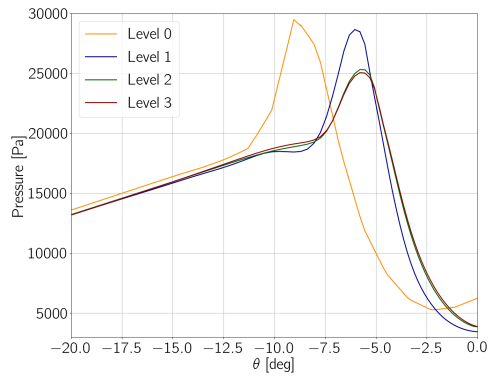


Figure 5.11: Pressure plot at the symmetry plane of the aft sphere.

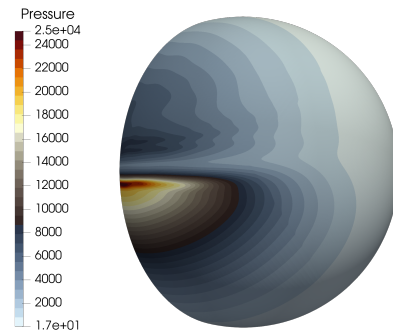


Figure 5.12: Pressure contour at the surface of the aft sphere.

## 5.2 A Quasi-Steady Approach for the Aerothermodynamic Interaction

The quasi-steady approach is verified in this section for two experimental campaigns: a two-sphere separation in supersonic flow, and a shock-interfered free-flying ring in hypersonic flow. Using the quasi-steady approach, it is assumed the solution is steady-state at each time interval, from which the dynamics are propagated using the forward Euler time scheme.

### 5.2.1 Numerical reconstruction of two-sphere dynamical separation

An experimental campaign to analyze the dynamic separation of two spheres in supersonic flow has been carried out by Laurence et al. [Laurence et al., 2012]. The spheres were suspended in the test section using single threads of dental floss to ensure a weak suspension link capable of detaching upon the flow's arrival. The detachment occurs within 1 ms after the arrival of the initial shock, from which the spheres start to fly freely according to the aerodynamic forces experienced, with a negligible initial velocity. The spheres' displacements, velocities, and accelerations were determined through a visualization-based tracking technique, detailed in [Laurence et al., 2007].

The proposed quasi-steady approach is used to conduct the numerical simulation, and compared against the experimental results retrieved from Laurence et al. [Lau-

rence et al., 2012]. Following the numerical setup applied by Laurence, a 3D inviscid compressible perfect fluid in equilibrium was modelled. The upwind numerical flux was computed using the AUSM scheme, and the solution was reconstructed with the MUSCL technique and the Venkatakrisnan-Wang limiter to obtain a second-order accuracy. The initial state of the spheres and the coordinate systems are illustrated in Fig. 5.13. The geometrical and mass properties, along with the initial position and free-stream properties are reported in Table 5.7 and 5.8, respectively.

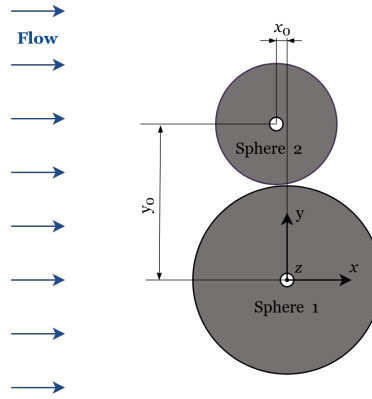


Figure 5.13: Schematic of the configuration setup and reference frame.

Table 5.7: Geometrical and mass properties of the model.

Model properties	Sphere 1	Sphere 2
Radius	$r_1 = 25.4 \text{ mm}$	$r_2 = 12.7 \text{ mm}$
Reference surface	$S_{ref} = \pi \cdot r_1^2 = 2026.83 \text{ mm}^2$	$S_{ref} = 506.71 \text{ mm}^2$
Reference point	center of sphere	—
Density	$\rho_s = 1122 \text{ kg/m}^3$	$\rho_s = 1122 \text{ kg/m}^3$
Mass	$m_1 = 77.016 \text{ g}$	$m_2 = 9.627 \text{ g}$

Table 5.8: Initial conditions and free-stream parameters.

$x_0$ [mm]	$y_0$ [mm]	$M_\infty$	$p_\infty$ [Pa]	$\rho_\infty$ [kg/m <sup>3</sup> ]	$T_\infty$ [K]
0.0665	38.1	4	1400	0.07	69.67

To correctly compare the numerical simulation with the experimental data, a non-dimensional time computed as  $t' = \sqrt{\frac{\rho_\infty}{\rho_s}} t \frac{V_\infty}{r_1}$  is used, as applied in the work of Laurence et al. to analyze different experimental configurations. The initial configuration at  $t'$

$t = 0$  has an alignment angle between the sphere centres of  $-0.1^\circ$  counterclockwise. A variable time step was employed to limit the translation of the small secondary sphere with respect to the flow direction. Thus, at each time iteration, the secondary sphere was restricted to move a maximum value of 3 millimetres. At each simulated instant of time, the computational grid was anisotropically adapted for three levels to obtain grid-converged solutions using AMG for the automatic adaptation loop. The Mach number is used for the computation of the metric tensor field, along with a complexity number of 100,000 and a p-norm of 4 to find the optimal mesh. After three levels of adaptation, the number of cells in the mesh increased by a factor of 120%, from roughly 1.0 million to 2.2 million cells, adapted to capture the strong variations in the Mach field due to shock-shock interactions and discontinuities. Figure 5.14 presents the adapted grids obtained for different instants of time. During the simulated time window, the shock generated by the larger sphere is impinging the upper smaller sphere, making it follow the shock discontinuity for a limited time in a phenomenon referred to as shock-wave surfing [Laurence and Deiterding, 2011], similarly experienced in the experimental campaign [Laurence et al., 2012]. The anisotropic adaptation at each step of the time propagation allowed the generation of mesh that follows the shock discontinuities, leading to a better alignment of the shock and the domain cells. The computational cost was approximately 2000 CPUh, distributed over 40 CPUs, where the mesh adaptation overhead contribution was estimated to be 0.15%.

A comparison between the experimental and numerical Schlieren is illustrated in Fig. 5.15 for  $t' = 0$  and  $t' = 1.66$ , respectively, where the black circles represent the experimental spheres and the red and green contours are the numerical spheres position and shock-wave, respectively. The non-dimensional time is used for both numerical and experimental simulations. At  $t' = 0$ , the spheres in the numerical simulation can move freely. However, the instant of the sphere release in the experiment is not precise due to the duration uncertainty of the flow start-up, as specified by Laurence. Nonetheless, the computation of the dynamics using the quasi-steady approach correctly predicts the position of the secondary sphere at a time of  $t' = 1.66$ , as shown in the right subfigure of Fig. 5.15.

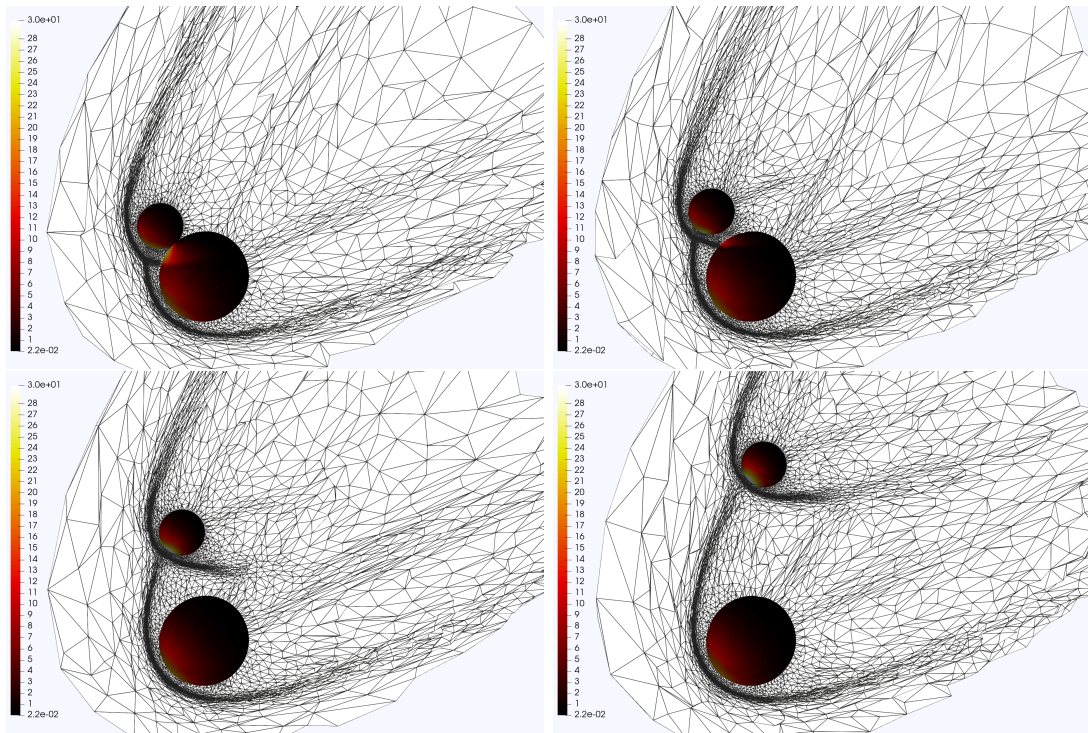


Figure 5.14: Visualization of the final adapted grid and pressure distribution at  $t' = 0$ , 1.04, 2.08 and 3.16.

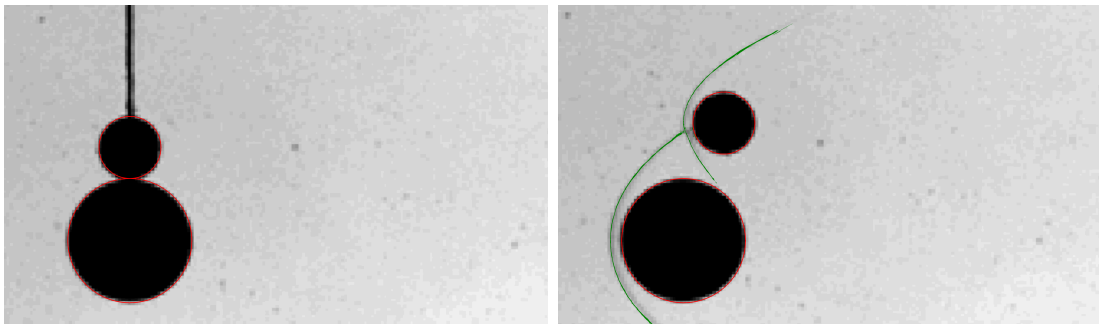


Figure 5.15: Comparison of experimental Schlieren and numerical sphere position and shock front for  $t' = 0$  (left) and  $t' = 1.66$  (right) [Laurence et al., 2012].

In Fig. 5.16 a comparison of force coefficients between the numerical simulation and experimental data for both the primary and secondary spheres is made. Between  $t' = 0$  and  $t' = 1.5$  the force coefficients present a large discrepancy compared to the experimental data due to the flow start-up period at the testing facility. After this period ( $t' \geq 1.5$ ), the numerical predictions show a good agreement with the available data for the simulated time window.

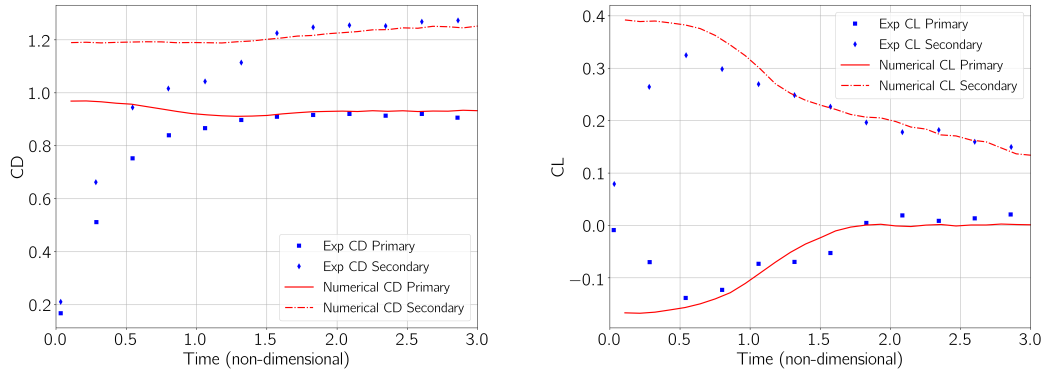


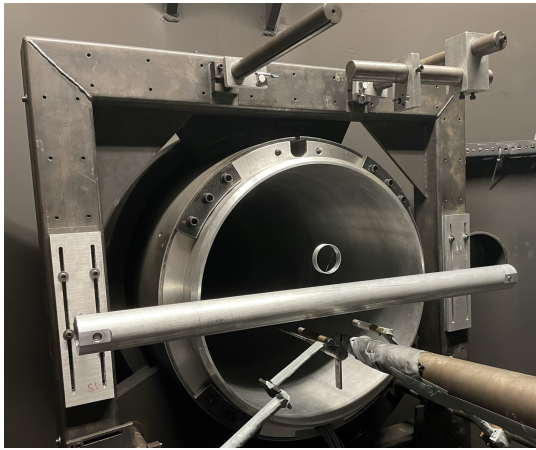
Figure 5.16: Drag coefficient (left) and Lift coefficient (right).

### 5.2.2 Numerical reconstruction of a shock-interfered free flying ring

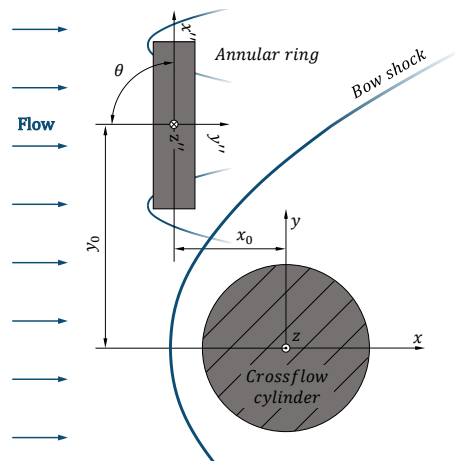
Recent studies in the VKI Longshot wind tunnel investigated the interference scenario of an annular ring geometry with a two-dimensional bow shock in Mach 14 cold hypersonic nitrogen flow [Kovács et al., 2023]. This research aimed to examine the influence of the interaction on the aerodynamics of a free-flying ring using free-stream flight conditions studied previously by Grossir et al. [Grossir et al., 2020]. The research was selected as a test campaign for the Aerothermodynamics and Design for Demise (ATD3) Working Group, a group dedicated to the verification, validation and comparison of numerical methods for space object reentry simulation tools. The detached shock wave was generated by a crossflow cylinder, given that this proximal body interaction can be interpreted as the interference scenario of an interstage rocket element with the fuselage.

The experimental setup is illustrated in Fig. 5.17a and the initial state of the models and the reference coordinate systems are sketched in Fig. 5.17b. The parameters of the test articles are summarized in Table 5.9. The annular ring model was initially suspended with thin wires upstream to the transversely mounted cylinder. Upon the arrival of the flow, the support wires release the model, which thenceforth flies freely. The experiment was recorded with a high-speed camera coupled with a Z-type horizontal Schlieren system. The flight trajectory of the ring and the corresponding aerodynamic forces were retrieved via contour detection-based image processing algo-

rithms and a linearized aerodynamic model detailed in [Kovács et al., 2023]. A set of probes (heat-flux, Pitot, static pressure) were introduced to the core flow below the cylinder model, enabling the rebuilding of the flow conditions based on free-stream measurements [Grossir and Dias, 2018] providing improved accuracy compared to nozzle methods. After the establishment of the flow and the rupture of the support wires, the free flight is initiated at  $3.8 \text{ ms}$ . Simulations are advised to start from the conditions corresponding to this time instant. The presence of the two-dimensional detached shock of the cylinder caused strong flow-normal aerodynamic forces promoting a shock wave surfing configuration. An in-depth description of the experimental results and the data processing methods are presented in [Kovács et al., 2022], where the dataset (flow conditions, flight trajectory, aerodynamic coefficients, Schlieren images, etc.) is available in a tabulated form.



(a) Photo of the experimental setup in the VKI Longshot [Kovács et al., 2022].



(b) Schematic of the model configuration.

Figure 5.17: Model arrangement of the free-flight ring and steady crossflow cylinder test case.

Numerical results obtained with the current simulation framework are compared below with measurement data of the described experiment in terms of flight trajectory and aerodynamic coefficients. Figure 5.18 showcases the evolution of the free stream flow conditions during the useful test duration of the experiment, starting from  $t = 3.8 \text{ ms}$  until when the ring reaches the edge of the core flow at  $t = 12.45 \text{ ms}$ . The plotted data was computed using a cubic interpolation of the tabulated data provided

Table 5.9: Properties of the annular ring and the cylinder model.

Model properties	Annular ring	Cylinder
Diameter	$D = 60 \text{ mm}$	$D = 60 \text{ mm}$
Height	$h = 15 \text{ mm}$	—
Thickness	$t = 2 \text{ mm}$	—
Reference length	$l_{ref} = D = 60 \text{ mm}$	$l_{ref} = \infty$
Reference surface	$S_{ref} = D \cdot h = 900 \text{ mm}^2$	—
Reference point	center of gravity	center of cylinder
Mass	$m = 13.30 \text{ g}$	—
Moment of inertia	$I = 5848.7 \text{ g} \cdot \text{mm}^2$	—

in [Kovács et al., 2022].

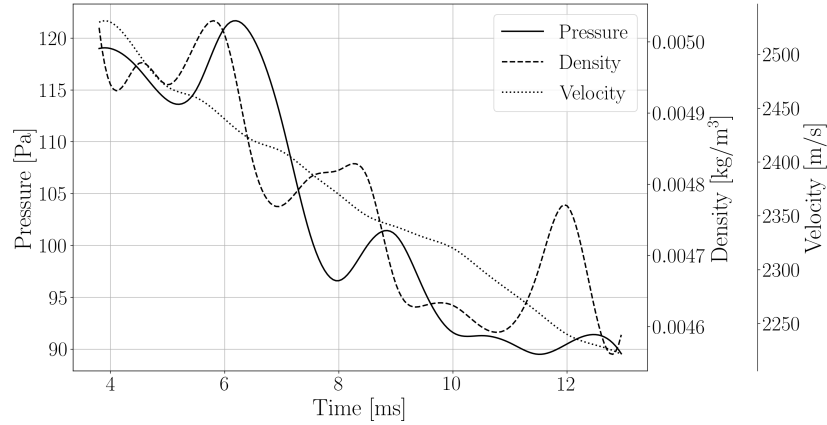


Figure 5.18: Evolution of the freestream flow conditions during the useful test duration of the experiment.

For the numerical rebuild of the experiment, the framework accounts for the changes in the attitude and position of the ring by employing the quasi-steady approach already verified for a double sphere case. The motion of the ring is accounted for by translating and rotating the ring mesh concerning the fixed cylinder. The initial conditions to initialize the simulation are shown in Table 5.10 in the frame referenced in Fig. 5.17b, and correspond to the instant the last wire holding the ring ruptures, at  $t = 3.8 \text{ ms}$ . At this instant of time, the shock wave generated by the presence of the cylinder at the exit of the nozzle already contributes to the pressure and skin friction distribution, affecting the dynamics of the ring. In this scenario, the use of a low-fidelity method for aerodynamic computation will not capture the influence of the shock, leading to

increased uncertainty in the computation of the aerodynamic loads. Therefore, for the numerical rebuilding of the experiment, high-fidelity solvers are required to capture the impact on the ring dynamics while crossing the shock wave. At each time step, the considered free-stream properties used in the CFD simulation were retrieved from the interpolation of the experimental free-stream data reported in Fig. 5.18.

Table 5.10: Initial conditions for the shock-impinged ring case.

$x_0$ [m]	$y_0$ [m]	$\theta_0$ [°]	$U_x$ [m/s]	$U_y$ [m/s]	$\omega_z$ [rad/s]
-3.377E-2	7.743E-2	87.96	3.603	0.3525	-8.443

To accommodate the mesh into capturing the physics and discontinuities occurring by the presence of the ring and the cylinder, the grid was adapted three times using the AMG library. Figure 5.19 shows a comparison between the isotropic base mesh generated using GMSHs' frontal Delaunay algorithm and the anisotropic mesh after three levels of adaptation, fitted to the hessian matrix of the Mach field in the computational domain to better capture the shock discontinuities. Throughout the adaptation process, the number of cell elements increases from 6.8 million to approximately 11.6 million.

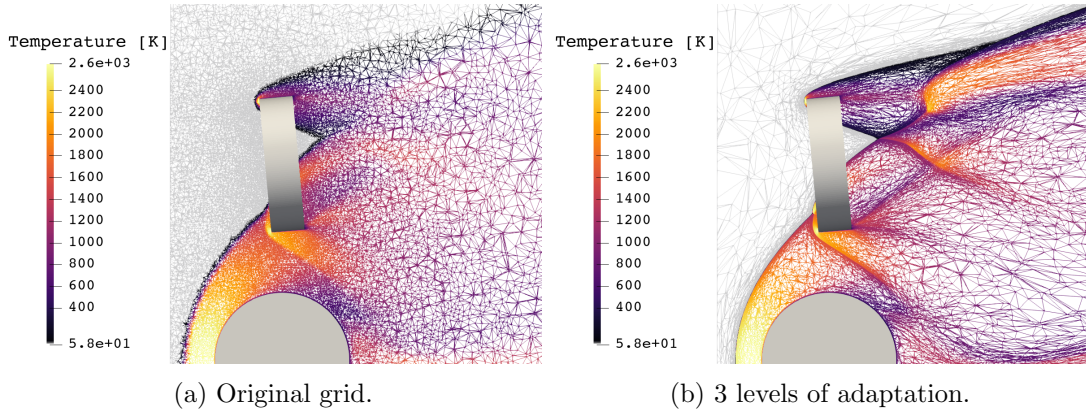


Figure 5.19: Visualization of anisotropic grid adaptation for  $t = 10$  ms.

A time window from  $t_0 = 3.8$  ms and  $t_f = 11.0$  ms was simulated using a constant time-step of  $\Delta t = 0.4$  ms, after verifying that the time-steps of  $\Delta t = 0.2$  and  $\Delta t = 0.4$  using a calorically-perfect gas model were negligibly distinct when comparing the

computed results. Having assessed the time-step value, the framework was then set to run a CFD viscous simulations using SU2-NEMO and assuming a laminar flow. The AUSM scheme was selected for the computation of the inviscid fluxes and, to enhance accuracy, the solution was reconstructed using MUSCL with the Venkatakrishnan-Wang limiter. The dynamic viscosity and thermal conductivity of the  $N_2$  flow were computed using a multi-scale Chapman-Enskog perturbative solution of the Boltzmann equation [Scoggins and Magin, 2014]. The computational cost was approximately 57600 CPUh, distributed over 80 CPUs, where the mesh adaptation overhead contribution was estimated to be 0.01%, taking approximately 6 hours to perform the adaptation for the simulated time steps.

Figure 5.20 illustrates the evolution of pressure distribution over the surface of the ring for  $t = 5, 7, 9$  and  $11$  ms. As the ring starts to cross the shock wave induced by the cylinder, the lower rear edge of the ring starts to be affected by the flow structures emerging from the shock-shock interaction between the ring and cylinder (Fig. 5.20a). Moving further downstream, the prominent shock interactions start to shift from the rear edge to the front edge of the ring's lower surface (Fig. 5.20b), until around  $t = 8.2$  ms, inducing lifting motion. After this point, the ring's lower surface travels downstream of the cylinder's front shock, inducing pitch rotation counterclockwise. The cylinder's shock front reached the level of the ring's lower edge at approximately  $t = 9.0$  ms (Fig. 5.20c), and crosses further the ring's front surface until the end of the simulation at  $t = 11$  ms (Fig. 5.20d).

The drag, lift and moment coefficients are plotted in Fig. 5.21 for the simulated time window and compared with the experimental results in [Kovács et al., 2023], where a detailed explanation regarding the uncertainty of the aerodynamic and moment coefficients retrieved from the experiment data can be found. Although the computed aerodynamics coefficients tend to overestimate the absolute value of the experimental coefficients, the trend concerning time is similar. From  $t = 3.8$  ms until  $t = 8.2$  ms the load contribution from the shock-shock interaction is applied on the lower surface, moving from the rear end to the front end. During this period, the acting loads are mainly forcing a lifting motion onto the ring. Afterwards, until the end of the simulation

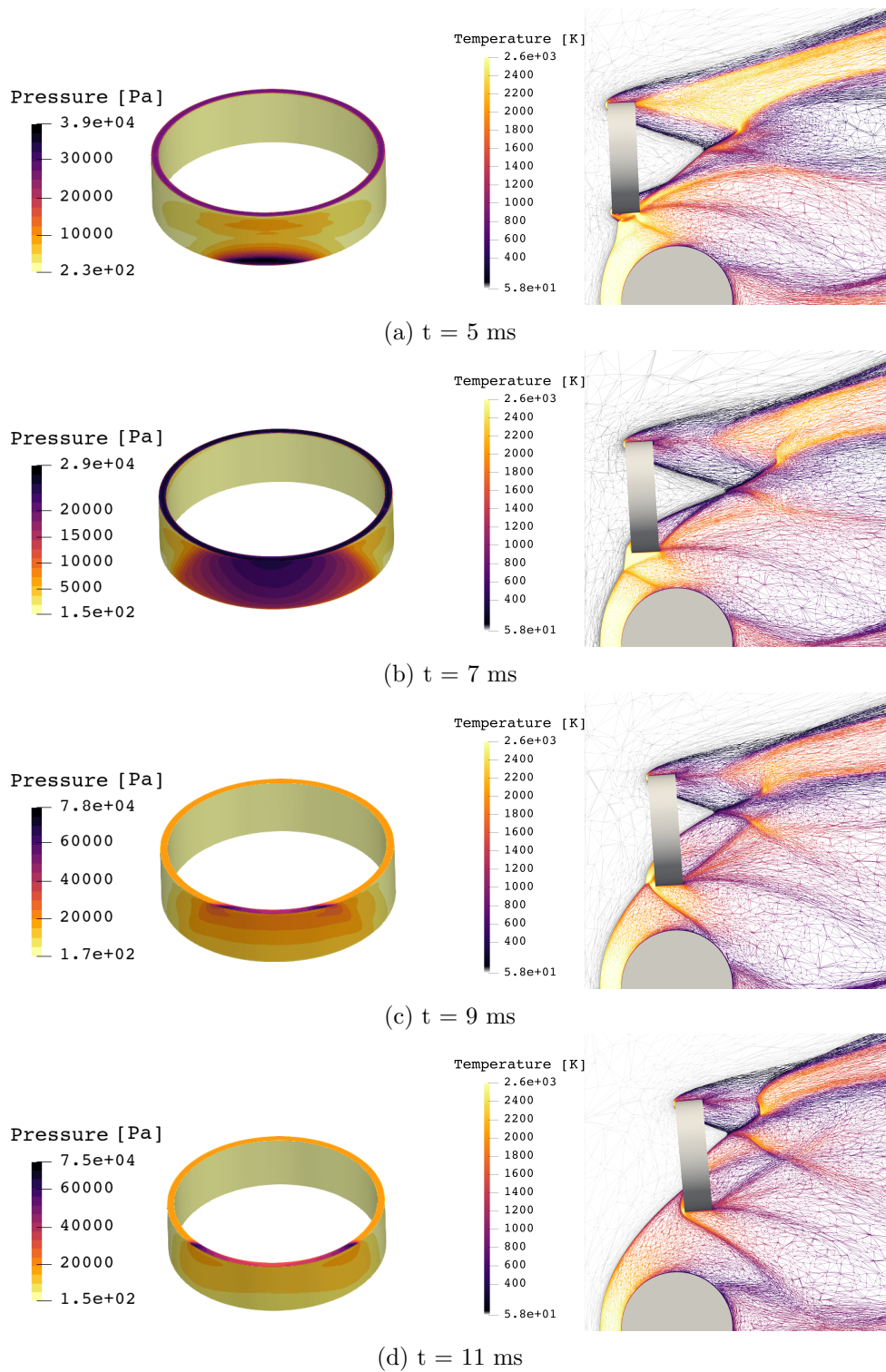


Figure 5.20: Pressure distribution over the ring's surface and correspondent last level of mesh adaptation for several instants of time.

at  $t = 11$  ms, the cylinder's shock front crosses the lower front edge of the ring, starting to induce a counterclockwise pitch moment and increasing the drag coefficient. The values obtained using the modified Newtonian method are also plotted in Fig. 5.21, and the discrepancy between computing the aerodynamic loads using a CFD solver and a low-fidelity method is reported in Table 5.11. The difference in the coefficients is due to the inability of the low-fidelity model to capture the influence of the shock wave in the distribution of the loads. The absence of the cylinders' shock is noticeable by the lack of lift forces through the simulated time window. Since the shock is not accounted for in the low-fidelity simulation, the pitch moment occurring at  $t = 8.2$  ms as the shock impinges the ring front surface is neglected, and there is no variation of drag and lift coefficients, in opposition to the high-fidelity and experimental results.

To assess the feasibility of the coefficients calculated using the quasi-steady propagation approach with the CFD solver, standalone simulations with localised adaptation at the regions of interest near the ring, using the experimental trajectory and position as reference, were performed and reported in Fig. 5.21. In contrast with the adaptation process undergone in this framework, which adapts the grid globally, the localized adaptation conducted for the standalone simulations was focused primarily on adapting the vicinity of the ring to assess if the impact of shock-shock interactions was being adequately captured in the high-fidelity quasi-steady approach. Except for the drag coefficient at  $t = 6$  ms, where the difference is 10%, the remaining points using both approaches are similar, following the same trend.

Table 5.11: Discrepancy parameters between numerical CFD and low-fidelity coefficients.

	Drag	Lift	Moment
min	0.004	0.016	0.002
max	0.202	1.165	0.078
mean	0.067	0.713	0.026

Figure 5.22 shows the position and attitude of the ring for the simulated time window using the quasi-steady high-fidelity approach. A comparison between the numerical and experimental trajectory is done by plotting the absolute difference. Albeit

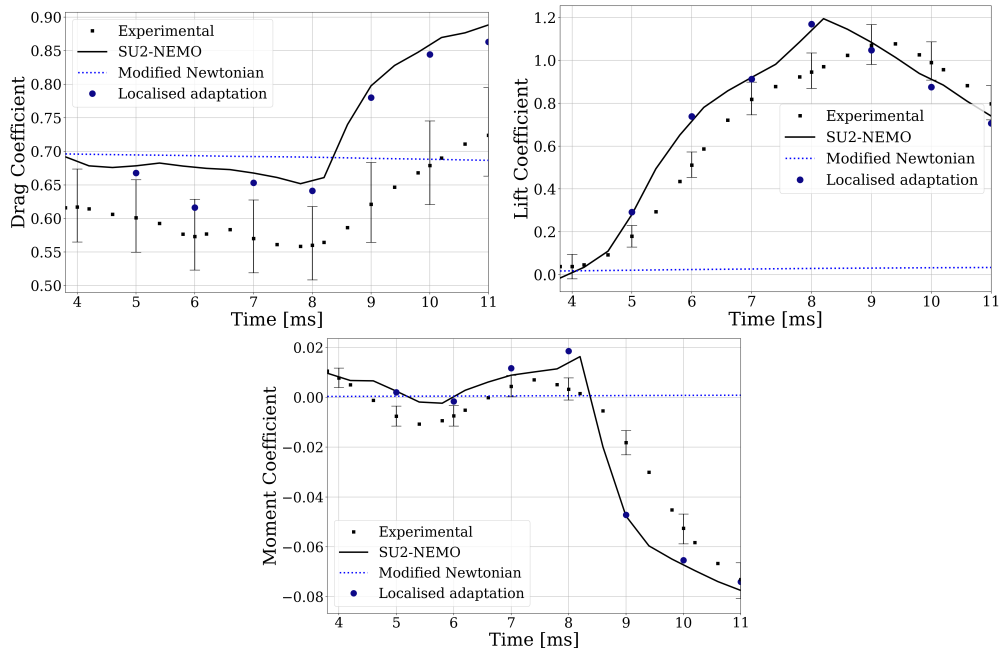


Figure 5.21: Aerodynamic coefficients for different instants of time.

the difference in the aerodynamic coefficients, the error in the position and attitude computation is not as pronounced, reaching a maximum deviation of 2.5 mm for the X-position, 1.75 mm for the Y-position and  $0.53^\circ$  for the angle of attack. The results show the promising application of the quasi-steady propagation used in this framework for addressing the dynamics of bodies in close proximity.

### 5.3 Validation of the Multi-Fidelity Criteria

A conceptual test case of a simplified ATV re-entry scenario was conducted to evaluate the effectiveness of the automatic fidelity switching mechanism that was proposed in Section 3.3.1 and its impact on the dynamics of the fragments. The initial trajectory conditions and fragmentation trigger used in this simulation are summarised in Table 5.12 and the ATV geometry is shown in Fig. 5.23.

The trajectory is propagated until 78 km of altitude when the joints are set to fragment due to the specified altitude criterion, occurring at  $t = 172$  s. Until the moment of fragmentation, there is only one assembly present in the simulation. As a result,

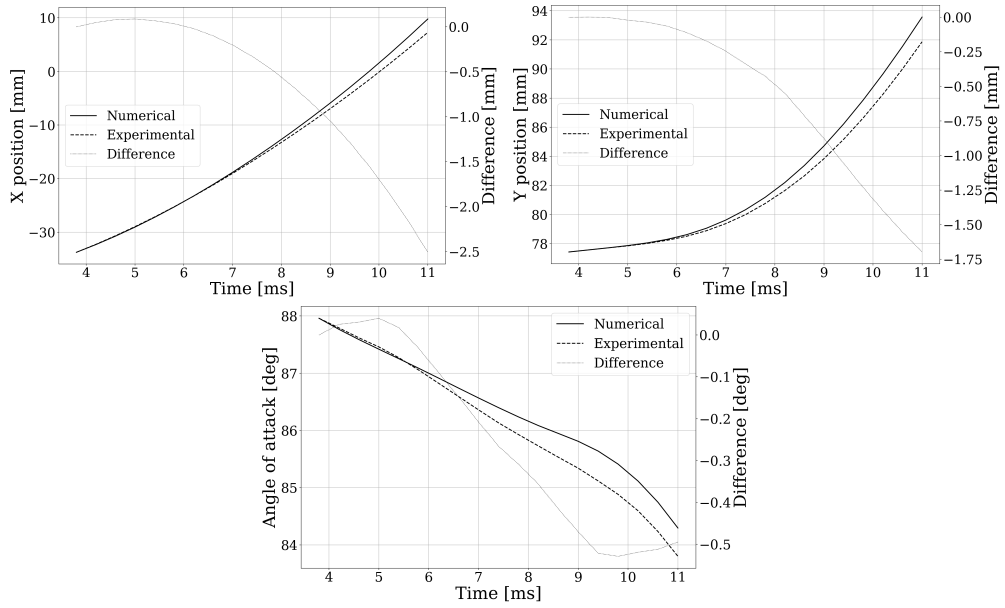


Figure 5.22: Position and attitude evolution of the ring.

Table 5.12: Initial trajectory conditions and geometry details.

Parameter	Value
Altitude [km]	120
Velocity [km/s]	7.57
Flight path angle [°]	-1.45
Initial pitch angle velocity [°/s]	10
Fragmentation trigger altitude [km]	78
Number of facets [ $\times 10^3$ ]	40
Time step [s]	0.25

low-fidelity models are employed to calculate the surface loads until the moment of fragmentation. After the break-up event, the objects are re-entering at Mach 26, leading to the formation of shock waves. Using the described shock envelope methodology, it is possible to estimate if the fragments are subjected to the influence of the shock generated by leading objects, requiring the use of high-fidelity methods for accurate predictions of surface loads. The forces and moments applied to the fragments were computed for a time interval of  $\Delta t = 2.0$  s using a time step of  $dt = 0.05$  s for both low- and high-fidelity methods to compare the differences.

The results shown in Fig. 5.24 illustrate the forces and moments experienced by a single solar panel, circled in red in Fig. 5.25. The plots show the forces and moments

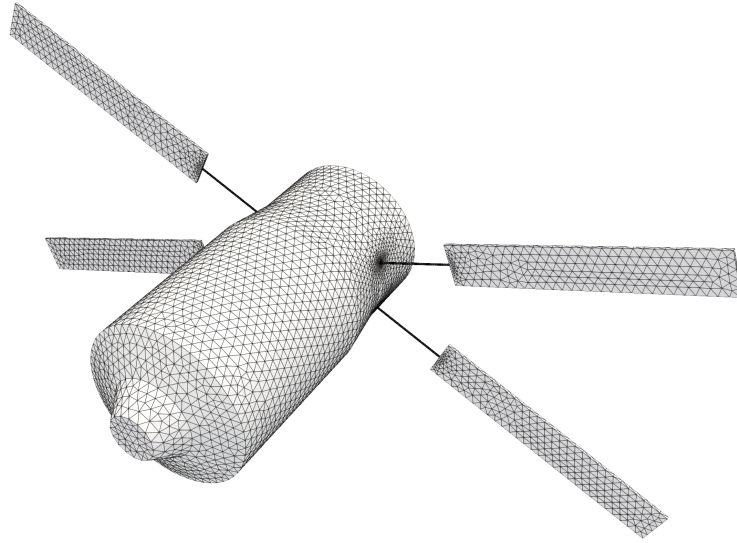


Figure 5.23: Simplified conceptual geometry configuration of the ATV for methodology validation.

computed for both low and high-fidelity models. The blue background indicates the time interval where the panel is inside a shock envelope generated by the main body or leading panels, thus requiring the use of high-fidelity tools, and the yellow background indicates the time interval where the panel is not inside generated by neighboring objects, and as such low-fidelity models can be used. The difference in the methods is more pronounced when the fragment is inside the shock envelope due to the influence of the shock generated by the leading body. As the fragment leaves the shock envelope, the forces and moments computed using both methods become comparable as there is no further interaction with shock waves. Therefore, after exiting the envelope, low-fidelity methods are sufficient to capture the object's dynamics.

Three different scenarios were sequentially identified and marked with a black dashed line in Fig. 5.24. After the joint fragmentation, due to the proximity of the solar panels and the main body, high-fidelity methods are required to fully capture the loads applied to the fragments. Afterwards, the tracked solar panel leaves the shock influence of the remaining fragments. At this stage, the framework can separate the panel whose dynamics can be captured using the Modified Newtonian Theory from the fragments that require the use of CFD. This selection process enables the reduction

## Chapter 5. Integration of a High-fidelity Fluid Solver for Proximal Aerodynamics Interaction

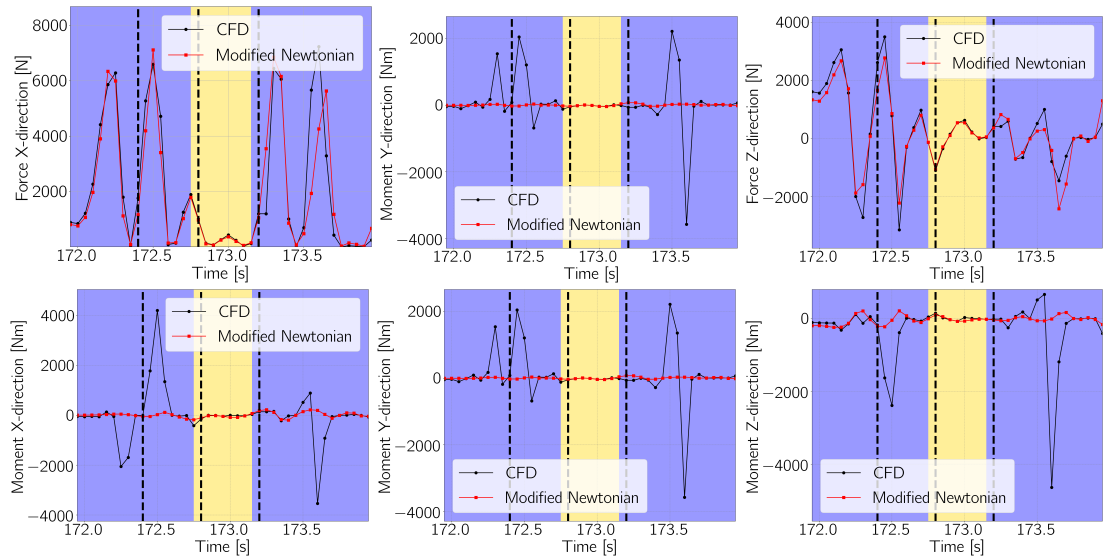


Figure 5.24: Solar panel forces and moments comparison.

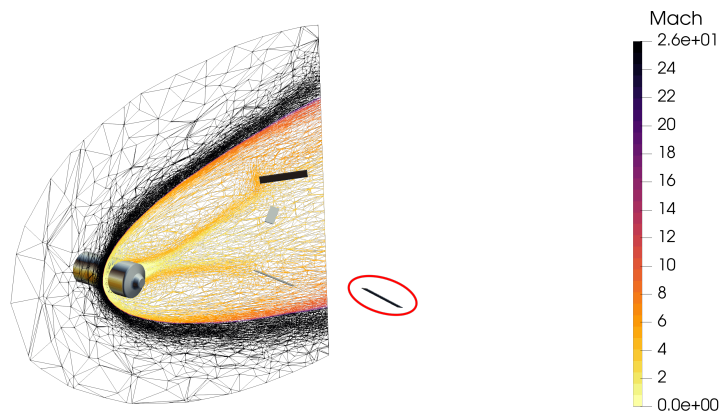
of the number of objects in the high-fidelity simulation, thus minimizing the computational cost. Lastly, a scenario was observed where different clusters of fragments were formed. These clusters do not interact with each other, but the shock influence is still prominent inside each one individually, requiring the use of high-fidelity models. To address them, TITAN can run separate high-fidelity simulations, reducing the time and complexity of the flow computation.

In the absence of shock interacting with the fragments, it is expected that the forces and moments computed by both CFD and the Modified Newtonian method to be similar. The use of an analytical function to assess the position of the objects concerning the generated shock envelopes allows us to quickly assess the level of fidelity required to adequately compute the applied loads at the given instant of time.

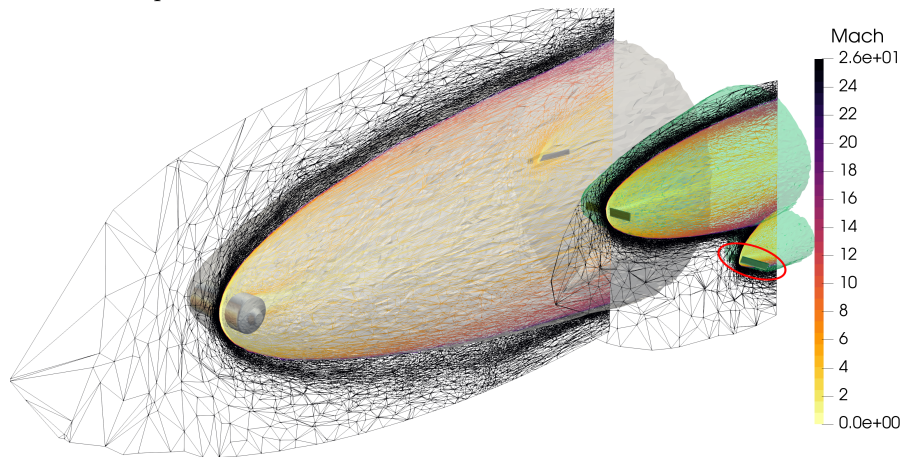
Chapter 5. Integration of a High-fidelity Fluid Solver for Proximal Aerodynamics Interaction



(a) Full CFD simulation at  $t = 172.4s$ . Due to their proximity, objects can't be split into separate clusters for CFD computation.



(b) Solar panel isolation at  $t = 172.8s$ . Low-fidelity model is used for the circled solar panel



(c) Formation of separate fragment clusters at  $t = 173.3s$ .

Figure 5.25: ATV dynamics after fragmentation.

## Chapter 6

# Application to Spacecraft re-entry

### 6.1 Automated Transfer Vehicle

The ATV (Automated Transfer Vehicle) was designed by ESA to serve the International Space Station (ISS) as an autonomous resupply and waste removal vehicle. A collaborative campaign was carried out by ESA and NASA to observe the re-entry of the ATV named Jules Verne (ATV-1) which re-entered Earth's atmosphere over the South Pacific Ocean in September 2008 [Lohle et al., 2011]. The campaign was successful in capturing a short clip of the re-entry trajectory, leading to numerous studies with various re-entry analysis tools emerging. The vehicle is composed of a main body connected to four solar arrays as shown in Fig 6.1. Both the main body and solar arrays are constructed such that they may fragment into individual objects upon satisfying the fragmentation criteria. Overall, the ATV main body has an external diameter of 4.5 m, and a length of 10.3 m, whilst the solar arrays have a span of 21.0 m, amounting to a total mass of 16 tons.

Several fragmentation events were inferred from the observations recorded in ESA and NASA's joint ATV campaign and analysis suggests initial solar array fragmentation at an altitude of approximately 88 km, followed by a further notable explosive event at an altitude of approximately 78 km [Boyd et al., 2013]. The fragmentation criteria

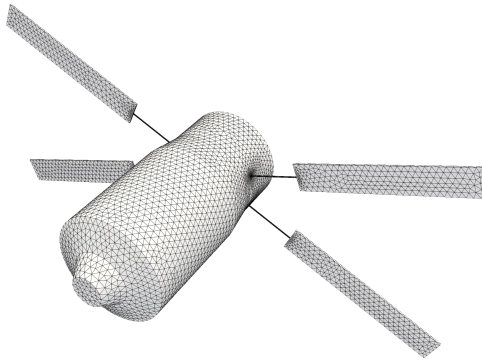


Figure 6.1: ATV geometry and surface mesh details.

used in this study was informed by work carried out with SCARAB [Fritsche et al., 2000]. As such, the first fragmentation event, corresponding to the fragmentation of the four solar arrays from the main ATV body is assumed to occur at an altitude of 92 km.

The present test case is used as a means to assess the impact of the multi-fidelity approach on the fragments dynamics, instants after the fragmentation, comparing the obtained results with a purely low-fidelity analysis. Until the break-up event, the simulation is conducted using the low-fidelity methodology. The initial conditions used for this case were also informed by the re-entry analysis report, defined using geodetic coordinates for the trajectory in Table 6.1. In addition, the ATV wall temperature is set to 300 K, uniformly distributed along the surface which is assumed to be non-catalytic. Thermal ablation is neglected in the analyzed case.

Table 6.1: Initial trajectory conditions for the ATV case.

Parameter	Value
Altitude [km]	120
Velocity [km/s]	7.57
Flight path angle [°]	-1.45
Initial pitch angle velocity [°/s]	10
Number of facets [ $\times 10^3$ ]	50

Figure 6.2 shows the altitude, drag, and pitch values until the break-up event at  $t = 122s$ . As the satellite descends through the atmosphere, the drag force substantially increases. As the satellite reaches the specified altitude criteria for the solar array

breakup, the applied forces start to impact the pitch rate that has been provided at the beginning of the simulation, changing the spinning direction.

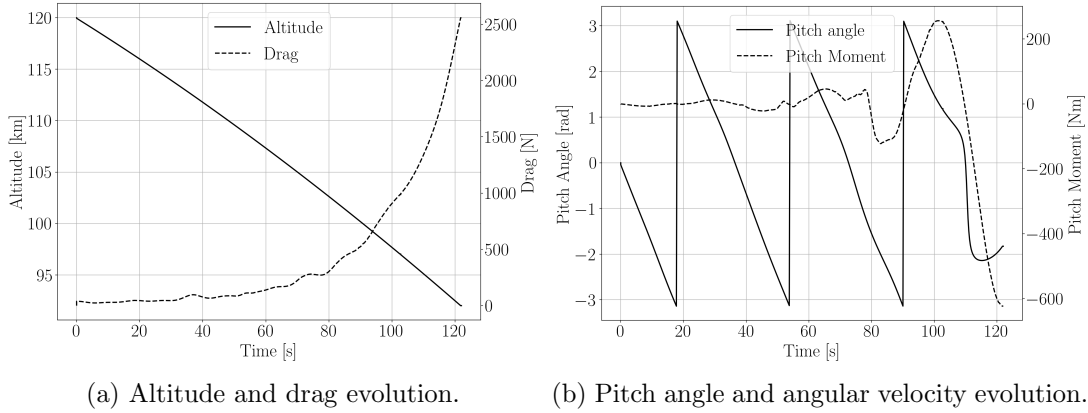


Figure 6.2: Parameters evolution until fragmentation event.

After the break-up event, the framework activates the shock envelope methodology specified in Section 3.3.1, allowing a decision between the use of low- or high- fidelity methods to be made on the basis of the discussed criteria. During the simulated time window of  $\Delta t = 5s$ , all resulting fragments remained within the shock envelope computed using Billig's formulation. As a result, the high-fidelity methodology was used to compute all aerodynamic forces. The maximum number of grid adaptations between high-fidelity simulations was limited to 2. Figure 6.3 shows the computed shock envelopes produced by the ATV main body after the fragmentation event, which is intersecting the solar panels. As the break-up event occurred in the continuum regime, the CFD solver SU2-NEMO is employed. A comparison between the pressure distribution using both fidelity methods is shown in Fig. 6.4 for the instant after fragmentation. The ATV on the left-hand side corresponds to the multi-fidelity approach and the ATV on the right-hand side corresponds to the low-fidelity simulation. A detailed visualization of the adapted grid in the post-shock region is provided, indicating that the generated shock is impinging the solar panels, thus substantially affecting their dynamics in the subsequent iterations. The pressure distribution for the main body is similar for both cases mainly due to the lack of shock interference, indicating that dynamics are similar using both methods.

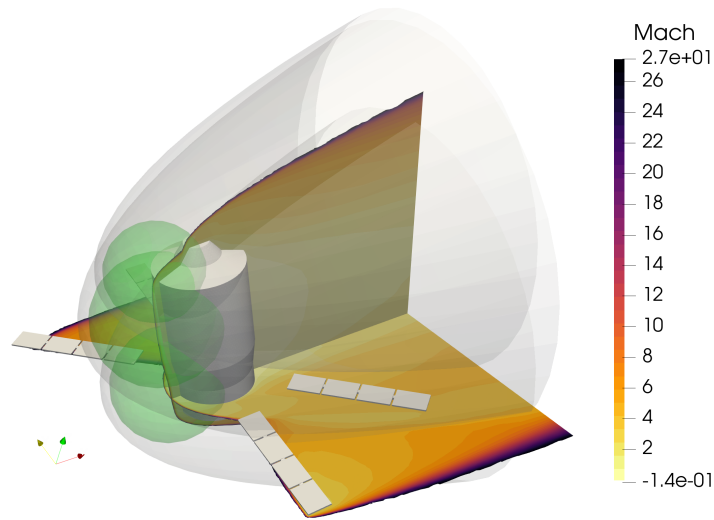


Figure 6.3: Post-fragmentation fidelity management.

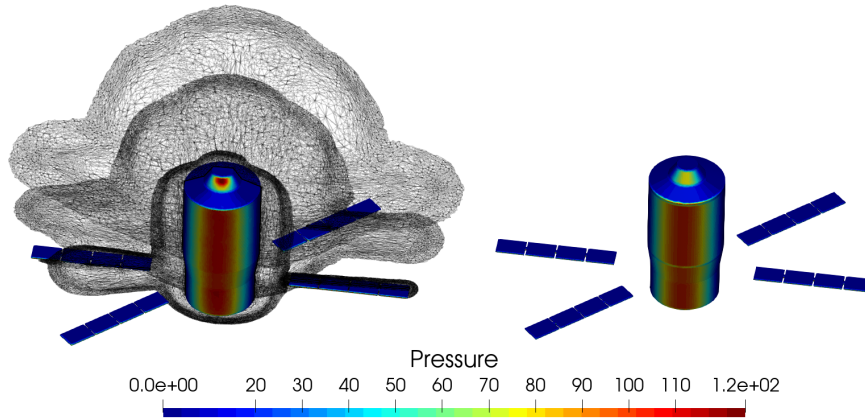


Figure 6.4: High-fidelity (left) and low-fidelity (right) pressure distribution comparison.

To understand the impact of both fidelity methods in the dynamics propagation, a comparison between the obtained result using the high-fidelity methodology (in blue) and using the Modified Newtonian Theory (in green) is showcased in Fig. 6.5. Figure 6.6 reports the CFD solution after the solar arrays have fragmented.

Due to the shock impingement generating localized regions of high pressure, the attitude of the fragments changes substantially, when compared with the results obtained through the Modified Newtonian Theory. The difference in displacement showcases a maximum difference of 45.6 meters for the simulated time window. The drag experi-

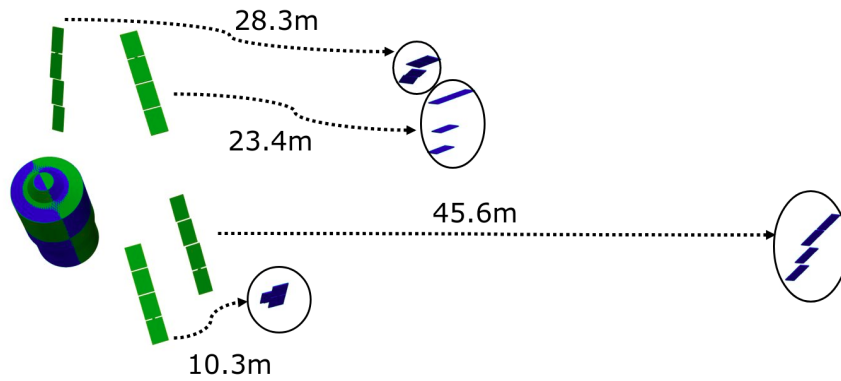


Figure 6.5: Fragments disposition comparison after 5 seconds of simulation (distance in meters).

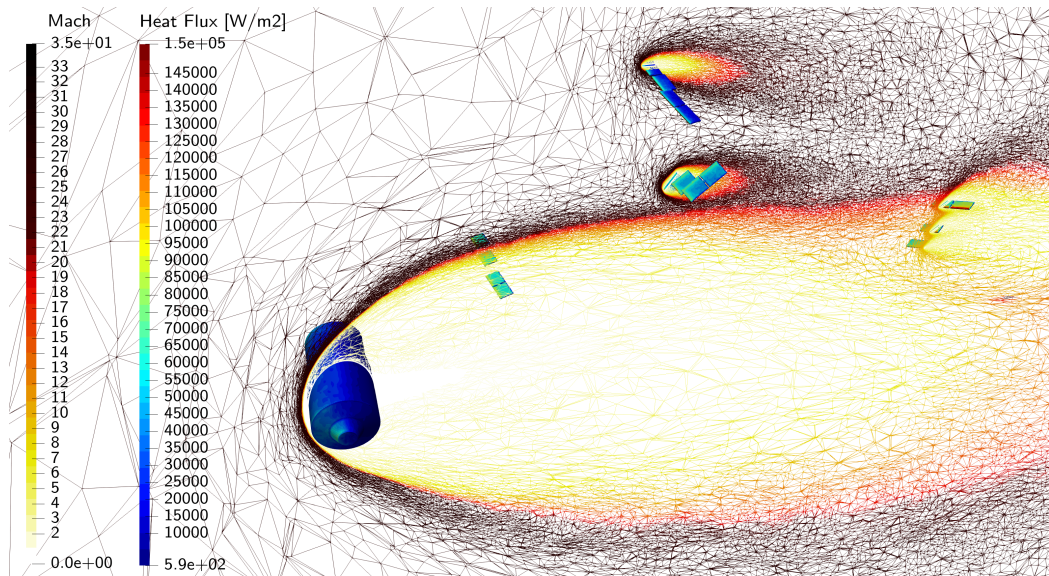


Figure 6.6: High-fidelity solution after 5 seconds of simulation, at 92 km of altitude.

enced by the fragments is higher, reducing the re-entry velocity by an average of 30 m/s when compared to the Modified Newtonian results. These small changes in velocity and position of the objects are important for successful tracking operations, as well as to determine the potential casualty of reaching the ground and respective location.

## 6.2 Attitude and Vernier Upper Module

The Attitude and Vernier Upper Module (AVUM) is the upper stage of the VEGA rocket, designed to provide precise orbital injection and attitude control to insert the payload into the desired orbit [Battie et al., 2012]. The Inter-Agency Space Debris Coordination Committee (IADC) together with the European Space Agency, have coordinated a re-entry case campaign to gather and analyze the AVUM re-entry data for improving the quality of the re-entry predictions [Virgili et al., 2017]. The AVUM upper stage underwent an uncontrolled destructive re-entry on the 2<sup>nd</sup> November 2016. Two surviving objects were found in southern India: a COPV (Carbon Over-wrapped Pressure Vessel) tank and a titanium fuel tank [Virgili et al., 2017, Dumon et al., 2022].

The materials used to model the AVUM components were retrieved from the ESA ESTIMATE library [Agency, 2020] and the publicly available data for the approximate materials is disclosed in Table 6.2. The geometrical model, shown in Fig. 6.7, was modelled with reference to the provided DRAMA model to mimic the connections and thermal fragmentation triggers between the various components. The heat flux is evaluated using the Van Driest model [van Driest, 1958] for the continuum regime, and the thermal processes are accounted for using the lumped mass approach. A temperature trigger of 750 K based on the melting temperature of aluminium was set for the release of the titanium tanks [Dumon et al., 2022]. The initial conditions at the re-entry interface are provided in Table. 6.3. The simulation was conducted until all the components demised or impacted the ground. For this test case, elastic collision was assumed, neglecting friction forces.

Table 6.2: Material list of the main AVUM components [Dumon et al., 2022]

Component	Material
Payload Launch Adapter (PLA)	CFRP + Aluminium AA7075
Carbon Over-wrapped Pressure Vessel (COPV) tank	CFRP
Roll and Attitude Control Subsystem (RACS) tank	Titanium TiAl6v4
Titanium tanks	Titanium TiAl6v4
Nozzle	Inconel718
Skirt	Aluminium AA7075

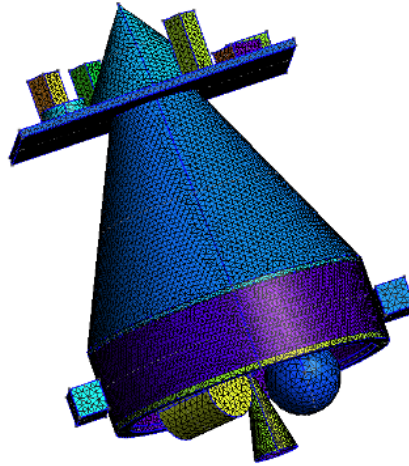


Figure 6.7: AVUM model used in the re-entry simulation.

Table 6.3: Trajectory conditions and geometry details at the entry interface

Parameter	Value
Altitude [km]	120.007
Velocity [km/s]	7.67
Flight path angle [°]	-0.088
Heading angle [°]	45.429
Angle of Attack [°]	0
Side Slip [°]	0
Latitude [°]	-61.229
Longitude [°]	35.955
Roll/Pitch/Yaw [°/s]	[0/10.6/10.6]
Number of facets [ $\times 10^3$ ]	60
Time step [s]	0.1

To test the collision model for the AVUM case, two simulations were carried on: one employing the model and one where collision is disregarded and the objects are considered isolated. Both simulations required around 2.5 CPUh to complete and presented similar fragmentation times. The first fragmentation event occurred at  $t = 426$  s and an altitude of 76.6 km when the payload base plate reached critical temperature and released the payload-related components. The event was followed by the skirt demise at  $t = 441$  s and an altitude of 73.6 km, resulting in the separation of the payload launch adapter (PLA), the Carbon Over-wrapped Pressure Vessel (COPV) and Roll and Attitude Control Subsystem (RACS) tanks from the main frame holding the

titanium tanks and the thrust chamber. After fragmentation, the separated objects maintain the angular rate of the parent object and their velocity is equivalent to the parent objects' velocity with the contribution of the release velocity. The instants after the skirt's demise can be visualized in Fig. 6.8, showing the impact of collision on the dynamics of the components. For each instant of time, the left image shows the relative position of the fragments as resulting from the application of the collision model, while the right image shows the position and attitude of the fragments without any collision model applied. Due to the lack of physical collision modelling, the components pass through one another instead of colliding, which is particularly noticeable in Fig. 6.8b and 6.8c with the crossing of the payload adapter over the titanium tanks and the thrust chamber. This situation is caused by the lack of structural connection due to the skirt demise. After 0.375 seconds of the demise event, the AVUM structure of the two simulations presents an opposite orientation due to the collision of the released objects, as depicted in Fig. 6.8f. The release of the titanium tanks occurs when the plate holding the tanks reaches the prescribed temperature trigger, at  $t = 464$  s, and lastly, the thrust chamber fragments at  $t = 467.6$  s.

The resultant ground spread and comparison with the position of the retrieved titanium tank and the COPV tank are shown in Fig. 6.9 and the details regarding the altitude of the tanks release and the ground spread are reported in Table 6.4. The altitude release of the COPV tank is the same for both simulations, as there were no previous collision events. However, the collision events that occur after the skirt demise have changed the AVUM attitude and limited the heat exposure of the tanks, delaying its release when compared to the collisionless simulation. The titanium tanks' ground spread is calculated using the value of the maximum distance between tanks, and the distance between the COPV and the titanium tanks is computed using the titanium tanks' average location. The simulations underpredicted the ground impact location by over 4400 km when compared to the location of the retrieved parts, which can relate to the uncertainty of the models and the data used for the simulation. However, both the predicted titanium tanks ground spread and distance between the COPV and the tanks present the same order of magnitude as the predictions from SCARAB and PAMPERO

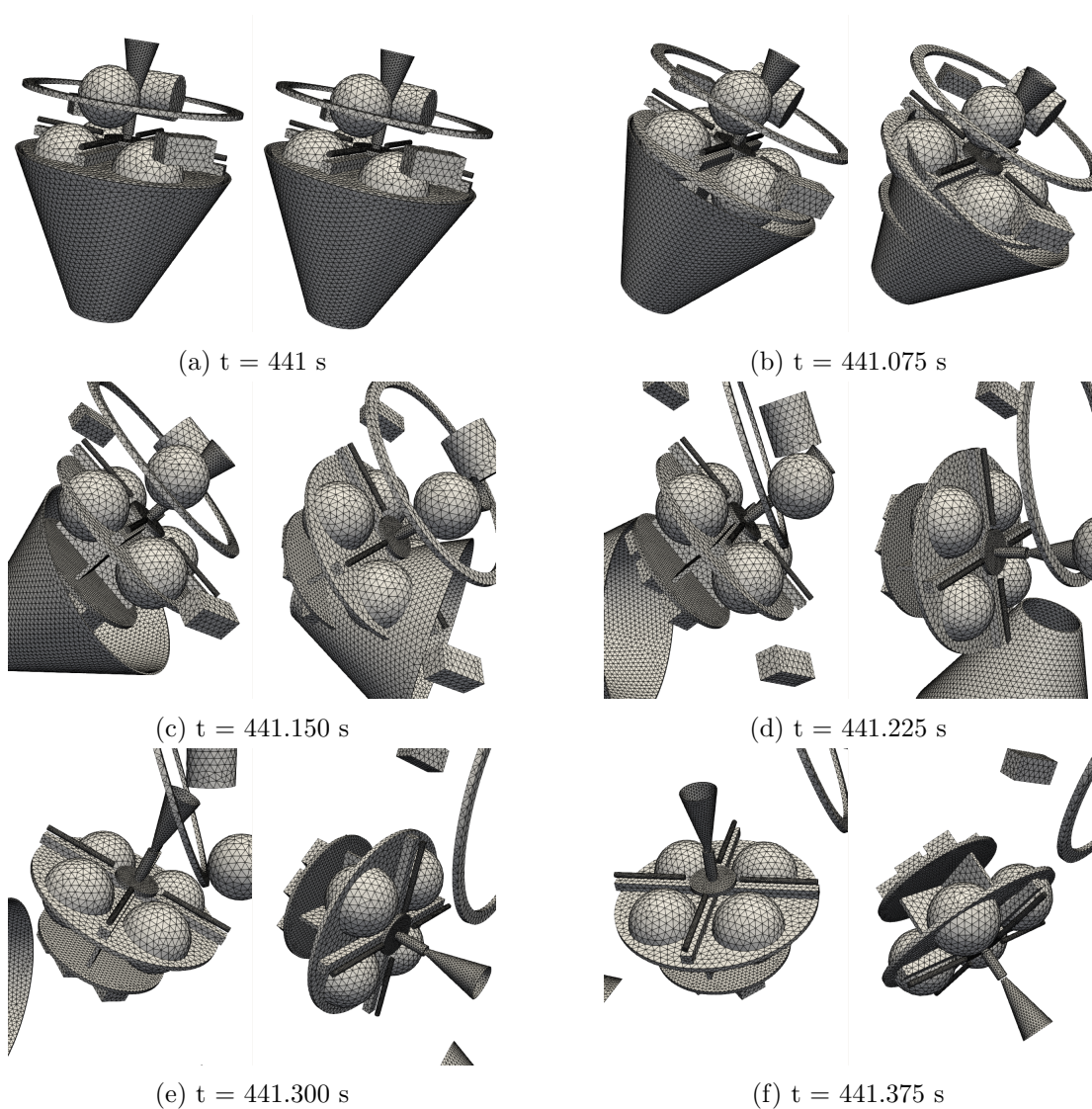


Figure 6.8: AVUM snapshots after skirt demise (Left panel accounts for collision, Right panel neglects collision).

[Dumon et al., 2022]. The predicted distance between the COPV and titanium tanks is also supported by the observed ground distance of 67.48 km between the retrieved components. The modeling of collision interaction has reduced the distance between the titanium tank and the COPV by 11% and has more than halved the titanium tanks' spread distance. Analyzing Fig. 6.9b, the PLA and nozzle ground impact location show a non-negligible difference of approximately 100 km between the collision and collisionless simulation. The obtained results show that accounting for collision of

proximal bodies can affect the ground collision, influencing the debris spread distance and impact location, and should not be disregarded.

Table 6.4: COPV and Titanium tanks release and ground spread details.

	SCARAB [Dumon et al., 2022]	PAMPERO [Dumon et al., 2022]
Ti tanks release [km]	73.4	63.4
COPV release [km]	82.2	77.7
Ti Tanks-COPV distance [km]	101.5	61.9
Ti Tanks spread [km]	9.2	12.3

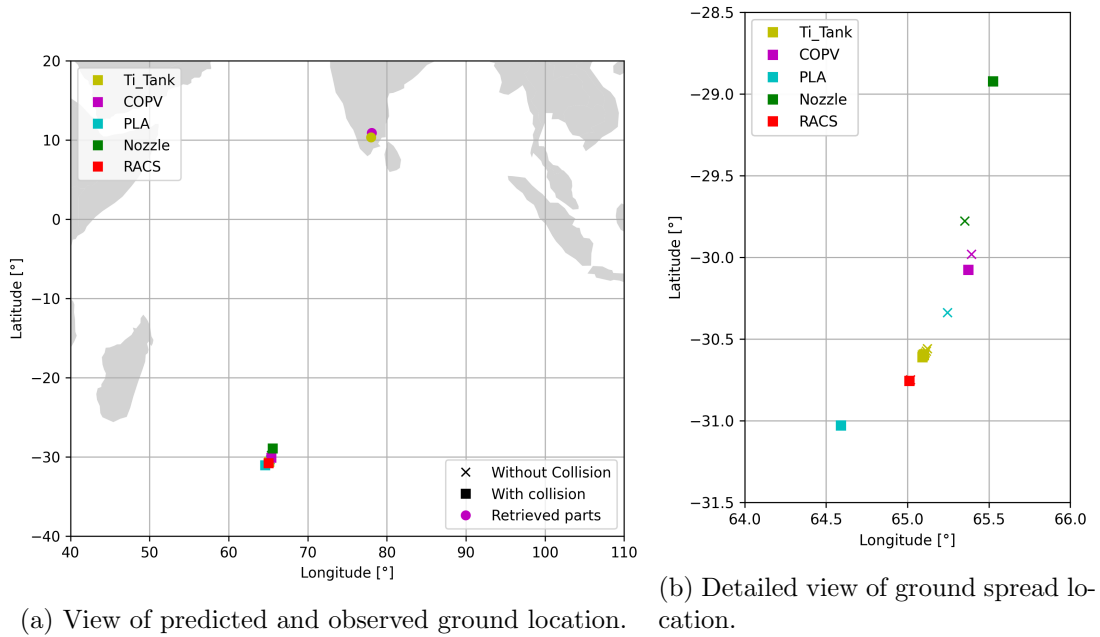


Figure 6.9: Impact location of surviving components of the AVUM

The impact of shock interaction due to objects' proximity on ground impact collision and distance spread was assessed by using the quasi-steady high-fidelity approach. The use of the approach was limited to a time window of 0.6 seconds after the release of the titanium tanks at  $t = 464$  s, using an initial time-step of  $\Delta t = 25$  ms and changing to a time-step of  $\Delta t = 10$  ms after the verification of a collision event. The simulation was set to use Navier-Stokes equations, AUSM for the upwind scheme, MUSCL for the solution reconstruction, and the viscosity computed using the Chapman-Enskog equations. The computational cost for the simulated time windows was approximately

14000 CPUh distributed over 40 cores. Per each time iteration, the mesh was set to anisotropically adapt twice. In Fig. 6.10, a slice of the adapted volumetric mesh at the wake of the objects and the pressure distribution is presented for the AVUM structure immediately following the tank release (Fig. 6.10a) and at the end of the quasi-steady propagation (Fig. 6.10b) using both low- and high-fidelity methods. In both instants, the shock impact on the pressure distribution is demonstrated by the highly localized pressure loads acting on the surface of the tanks, influencing their dynamics, as visualized through the crossbeam and plate positioning. After running the quasi-steady time window, the trajectory was propagated using the low-fidelity model. The retrieved ground impact location and spread distance were compared to the fully low-fidelity simulation with the collision model activated. The ground spread distance presents no discernible difference, and the ground impact collision location differs for less than 1.5 kilometres. For the specified time window, the influence of shock interactions on the ground impact location is less predominant than the collision influence, but further analysis with an extended period of quasi-steady simulation is required to better assess the shock impact.

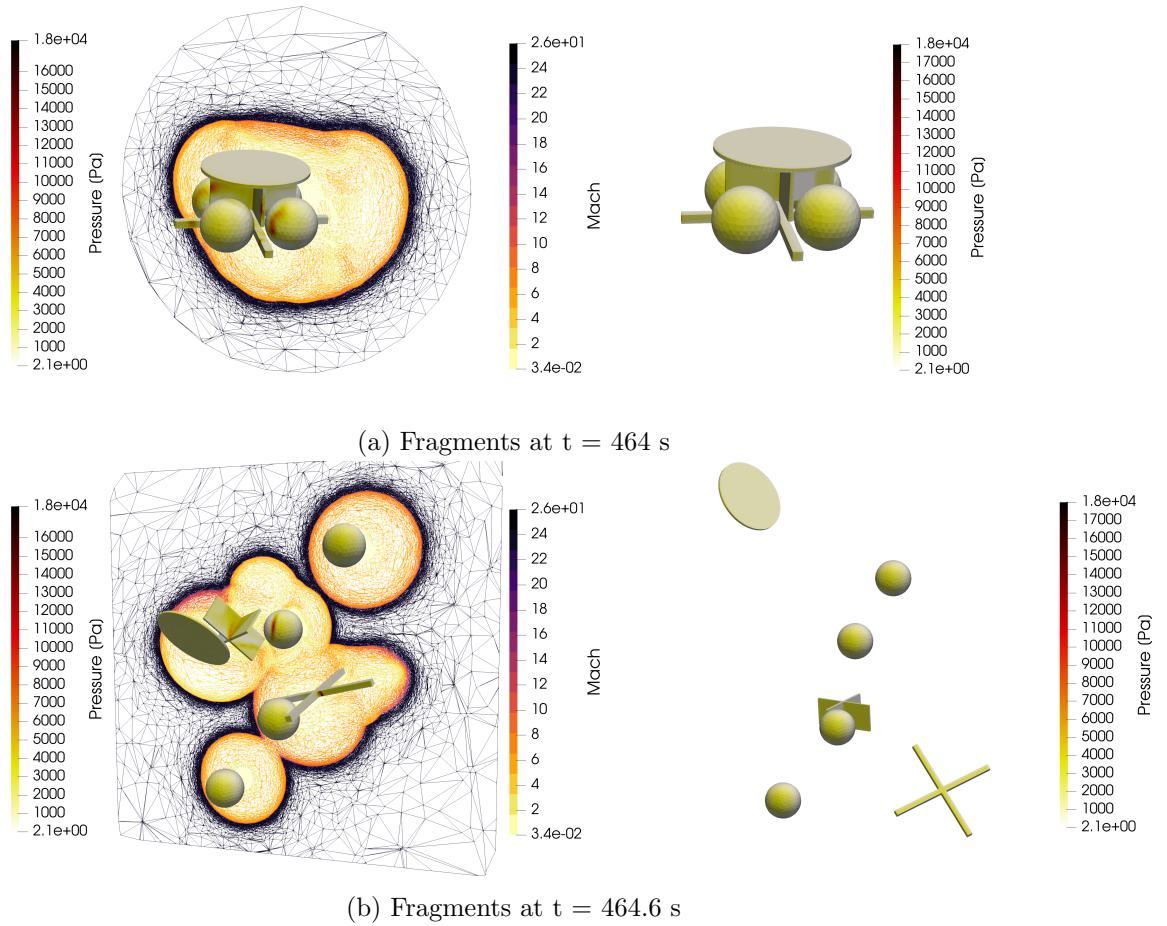


Figure 6.10: Pressure distribution over the surface of the fragments using the quasi-steady propagation with high-fidelity computation (left) and low-fidelity methods (right), and Mach distribution over a slice of the adapted mesh instants after the release of the titanium tanks.

## Chapter 7

# Conclusions

In this work, a methodology to improve the modelling of the instants after break-up and demise events is proposed, which can serve as an extension to the capabilities of current reentry tools to account for occurring interactions due to fragments being in close proximity. Although more scenarios of complex flow features could also occur (i.e. self-shock impingement), the present work is particularly focused on the interactions produced by the presence of multiple bodies.

The approach has been tested alongside the development of a new reentry simulation framework using a modular architecture, aimed to speed up and ease integration of new internal features and external libraries. The framework integrates several modular and loosely coupled disciplinary models. These modules consist of a geometric/inertia/meshing module, a two-fidelity aerothermodynamic module, a component-based lumped mass thermal model, a structural model, a material database, a 6 DoF propagator, an atmospheric model and an elastic collision model. The framework also allows the import of geometric files with arbitrary custom shapes and connectivity between objects, material selection, and fragmentation trigger specification (altitude, temperature, stress), providing flexibility in modelling the reentering spacecraft. The developed framework currently stands as an hybrid approach regarding reentry tools classification: it presents a similar approach of primitive-joint relationship as the new generation of object-oriented tools, but enables the use of higher fidelity models characteristic of spacecraft-oriented tools to perform reentry analysis.

The research questions reported in Sec. 1.2 have been explored throughout this work. For clarity and convenience, the questions are repeated in this section, and the findings can be summarised as follows:

**Research Question 1: Is it possible to develop a computationally efficient and accurate tool that can model flow interaction in the moments after breakup and demise events?**

- Through the implementation of a two-fidelity aerothermodynamic module, the frameworks extend the fidelity considered in standard re-entry analysis tools, by including the ability to compute the acting aerodynamic and thermal loads using high-fidelity models. The high-fidelity modelling of the aerodynamic and aerothermal loads in this work was achieved through the integration of the non-equilibrium two-temperature CFD solver SU2-NEMO for the continuum and the slip flow regime. The inclusion of the solver into the framework allowed for improved accuracy in situations where the proximity of the bodies is likely to generate complex flow features that need to be adequately resolved.
- The implemented low-fidelity aerodynamic and aerothermodynamic methods are based on a local panel inclination approach while accounting for the local radius of curvature to improve heat load prediction. The methods have been compared to reference study cases analysed by other reentry tools: a sphere, a hollow semi-sphere and the ARD capsule. A facet visibility and partial occlusion algorithm based on a ray tracing method has been implemented and tested for different cases, overcoming the limitation of pixel-based methodologies concerning computational speed and memory.
- To achieve a computationally efficient and accurate approach in simulating each considered time-step, the ability to seamlessly switch between both fidelity models was explored in the framework. By introducing a physics-informed switch criterion, the framework was able to apply the high-fidelity models only during the time-steps the criterion is triggered. This step is critical to reduce the num-

ber of calls to the high-fidelity model, thus reducing the computational cost while producing higher-fidelity predictions of the flow and surface load distribution.

**Research question 1.1: How to automatically detect the required local fidelity level in a conservative manner?**

- The introduced criterion to automatically select the level of fidelity based on the Billig formulation to compute a shock envelope has proven effective in identifying conditions where high-fidelity computation is needed as well as situations where a return to low-fidelity methods will not compromise the overall accuracy in the prediction of pressure and heat fluxes. An analysis of the shock-envelope limits and the computed shock location enabled to verify the conservative nature of the approach, thus avoiding to erroneously use low-fidelity methods when shock interactions are expected. The automatic fidelity switch has been tested using a simplified ATV test case, where both low- and high-fidelity models were used at each simulated time-step and the predicted forces and moments acting on the solar panels were compared. The obtained results illustrate the capability of the proposed criterion in correctly choosing to use the high-fidelity model at the time-steps when the forces and moments comparison presented a larger discrepancy. The results presented illustrate the ability of this method to maintain a reasonable degree of accuracy in computing the dynamics of the bodies in the instants after the breakup process.
- Furthermore, the use of the shock-envelope allowed to separate the fragments that may be affected by shock interference (inside an envelope), from those that will not be affected (not inside an envelope). This separation allows to locally select where to use high-fidelity models, and where to use low-fidelity models, further reducing computational cost. Although not explored in this work, this separation could allow to run CFD simulations in parallel, for clusters of objects that are known not to interact with each other.

**Research question 1.2: Is an anisotropically adapted unstructured grid capable of adequately resolving the load distribution on the surface of objects?**

- In order to converge the results obtained through the high-fidelity model, an anisotropic grid adaptation over the unstructured tetrahedral flow grid is proposed in this work. The use of tetrahedral grids is proven to be advantageous for automating the grid generation at every time-step the CFD solver is called, as the objects position and attitude evolution in time are not known before-hand, and also allow to ease grid generation over complex objects. For the grid adaptation, the metric-based anisotropic mesh adaptation tool PyAMG is applied. The adaptation is driven by the Hessian matrix computed using the Mach field, as it allows to capture shock discontinuities due to sharp gradient changes.
- A study on the influence of the type and alignment of anisotropic unstructured grid elements is presented for a hypersonic AIR-5 flow. Single- and multi-body tests using spheres and cylinders were conducted, and a comparison with the available literature data reveals that results obtained with anisotropic grids provide an accurate prediction of surface aerodynamic and aerothermodynamic quantities, as well as on the accurate prediction of shock-shock interference location.

**Research question 2: Can the implementation of a common global domain enable to capture the interference in dynamics due to the objects physical proximity?**

- For the framework to account for the interactions that can arise from the proximity of fragments, in particular contact collision and shock interference, this work explores the use of a singular spatial domain common to all generated debris. This approach shifts from the standard used in current atmospheric reentry tools, where the fragments generated through breakup and demise events are individually analysed, and interactions between them are not accounted for.
- The implementation of a rigid-body model is tested to handle impact and momentum exchange between fragments. A perfectly elastic collision at the point

of contact is assumed in this project. The verification of the model is performed against simple problems with known analytical solutions, showing good agreement with the computed dynamics.. Further verification was performed by a quasi-2D experimental test case with applied friction, which was numerically rebuilt, and the predicted translation dynamics matched the experimental observations.

- To evolve the dynamics of the fragments that are impacted by shock interference, a quasi-steady approach is used to propagate the object's trajectory and attitude when high-fidelity methods are applied. This approach assumes a steady-state solution at each time step and was validated against a mach-4 double sphere experiment, showing satisfactory results for aerodynamic forces and sphere positioning. The same methodology was employed to numerically rebuild a recent experiment of a free-flying ring crossing a shock wave, where the computed coefficients and trajectory show reasonable agreement with the experimental data.
- A set of spacecraft reentry test cases was conducted using the developed framework to assess the impact of contact collision and shock interference in the spreading of fragments and ground collision location, which in turn affects the casualty risk. By introducing the methods discussed in this work, it is expected to predict the occurring physics more accurately, thus assessing more reliably the compliance with the design for demise guidelines and reentry mitigation requirements for uncontrolled reentries. Firstly, the framework was used to simulate a conceptual re-entry test case scenario involving the ATV geometry, to analyze the use of the multi-fidelity approach to improve the accuracy of the debris dynamics after fragmentation. The moments after the breakup event are simulated using the shock envelope criteria to assess the level of fidelity required. The positioning comparison between the multi-fidelity approach and a low-fidelity approach shows a deviation between 10.3 and 45.6 meters for the simulated time window of 5 seconds. Additionally, a reduction in average speed by 30 m/s was noticed when employing the multi-fidelity approach due to the higher drag predicted. The framework was also tested to simulate a representative AVUM re-entry sce-

nario, using multiple components with different materials. The demisable joints were modelled to mimic the thermal fragmentation triggers as per the available data sources. The impact of accounting with collision during reentry is analyzed through the simulation of the AVUM re-entry where non-negligible differences of 100 km arise on the difference of ground impact location. The effect of shock interaction in the ground impact location of the titanium tanks has been assessed by employing the quasi-steady high-fidelity approach for a short time window after the tanks' release. Results show minor differences in ground impact. Most of the fragments underwent a complete thermal demise before reaching the ground, while some survived the re-entry impacting the surface. The current simulation under-predicts the ground distance covered by the surviving fragments since the re-entry interface point but provides results aligned with the current uncertainties on the process and the models.

### 7.1 Future Work

The methodologies and approaches explained throughout this work that were included during the development of the divulged reentry framework are presented as propositions for new and existing reentry tools to apply. The framework was developed with flexibility and modularity in mind to ease future developments and further enhance its capabilities.

However, the current version of the tool presents some limitations and lacks a number of features that were out-of-scope for the present work. Additionally, a test case with both CFD and FEM enabled has not been enabled in the current work and is left for future testing. Thus further work is required to turn the framework into a certification tool, and which can be summarised as follows to be tackled in future projects:

#### **Closing the shock envelope method**

Using the Billig method to formulate a shock envelope surrounding the object has proven to be conservative in enclosing the location of the generated shock wave, thus

if objects are inside the shock envelope, high-fidelity methods are applied. However, in some instances, the debris may be entailed in the wake of upstream fragments and/or may never leave the shock envelope, resulting in a high volume of high-fidelity calls, exponentially increasing the computational cost of the simulation. Therefore, completely closing the shock envelope in the downstream direction is of great importance to avoid over-calling high-fidelity methods. For this matter, the application of a blast wave theory to close the shock envelope is envisaged to be implemented in the future.

### **Self-impinging shock waves**

Along with the occurrence of shock-shock interference due to the multi-body presence, self-induced shock impingement is also a phenomenon to be considered as a driver of destruction events. Although self-induced shock impingement was not analysed in this work, it can generate localised high-intensity aerodynamic and heating loads that can lead to fragmentation and thus should be considered in future works.

### **Increasing the order for time propagation**

For this work, the first-order forward Euler was applied to propagate the objects' dynamics in time, as it only requires one evaluation of pressure and heat flux distribution per evaluated time step for both low- and high-fidelity methods. The stability introduced by higher-order time propagation methods, such as Runge-Kutta, would allow an increase in the time interval between steps, which could translate into a reduction of computational cost.

### **FEniCS interface improvements and plasticity effects**

Current collision and structural models assume elastic behaviour, which only requires solving linear equations to model the structural and dynamic behaviour, thus being more computationally efficient in a complete atmospheric reentry simulation. Therefore, the implemented models do not account for energy transformation into plastic deformation, which would be more representative of the undergoing physics with the drawback of requiring solving non-linear equations. In future work, the benefits of

using more detailed modeling to capture plastic behaviour should be assessed against computational performance.

Furthermore, the current interface between the framework and FEniCS solver only allows to solve cases with a limited number of joints. In the current version, the solver can only be called twice per time-step to apply the superposition method for structural analysis, but multi-joint structures with complex primitive dispositions may require more complex methods to perform structural analysis.

### **7.1.1 Improving the ablation model**

The current ablation model implemented in the framework is a lumped mass approach with infinite heat conductivity, i.e., the body always has uniform temperature. In reality, this is not the case, as conductivity is finite. To account for this, a 3D heat model can be considered, by dividing the geometrical objects into several tetrahedrons which allow for heat conduction through their facets.

### **7.1.2 Uncertainty quantification**

Being a self-contained code, future works envisage the use of the framework as a black-box. By repeatedly calling the framework, it is possible to perform statistical analysis and uncertainty quantification of the reentry process, and therefore estimate the drivers of the demise process for the modelled spacecrafts.

# Appendix A

## Tools for Re-Entry Simulation

### A.1 Object-Oriented tools

#### A.1.1 DAS/ORSAT

The Debris Assessment Software (DAS) [Lips and Fritsche, 2005, Johnson, 2011, Opiela and Johnson, 2007, Liou et al., 2021] is an object-oriented tool developed by Lockheed, designed to assist NASA space programs in performing orbital debris assessment as described in NASA Technical Standard 8719.14B, "Process for Limiting Orbital Debris", which establishes debris mitigation guidelines. The tool is mainly used to assess compliance with the requirements, performing fast evaluations of potential risks associated with controlled and uncontrolled satellite re-entry and calculating collision probabilities and lifespan for orbiting spacecraft.

The spacecraft analysed with DAS are modeled as a set of components with simple geometries, and specific material, dimensions and mass. The tool can analyze both solid and hollow components with finite wall thickness. For solid components a lumped thermal mass model is used, assuming a uniform temperature distribution for the component. For hollow components or objects with several materials, an effective density approach is used [Lips and Fritsche, 2005]. If the absorbed heat exceeds the ablation heat, the component is considered to demise. DAS does not allow for partial melting and fragmentation of components leading to a more conservative approach. Thus the surviving components retain the same shape and mass.

## Appendix A. Tools for Re-Entry Simulation

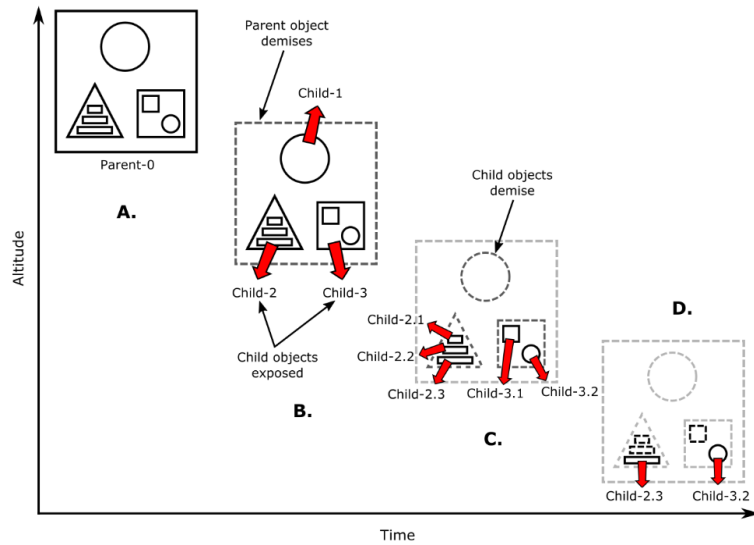


Figure A.1: Parent-child relationship of nested components in the DAS 3.0 re-entry assessment (from [Liou et al., 2021]).

Figure A.1 illustrates an example of the parent-child relationship used in DAS, where the parent object (the spacecraft) is represented at point A.. In the figure, the parent contains three main subcomponents, classified as child objects. It is assumed that the parent object fragments at an altitude of 78 km based on empirical and theoretical values [Liou et al., 2021], exposing the first level of child objects (point B.) to the various forces in the re-entry model. If a component contains more levels of nested children, the child objects are exposed when their immediate parent object demises (point C.). This process allows for a realistic progression of the exposure for nested structures. The components that survive the most intense re-entry forces reach their terminal velocity and start cooling as they approach the ground (point D.).

The DAS tool should be used for first risk assessments. However, if the predicted risk is not compliant with the safety requirements, a higher-fidelity tool is required. The Orbital Debris Object re-entry Survival Analysis Tool (ORSAT) [Ostrom et al., 2019, Johnson, 2011, Dobarco-Otero et al., 2005] is the reference tool used by NASA when a space mission cannot be proven to be compliant after running the initial analyses with DAS.

The ballistic trajectory propagation in ORSAT is performed using a 3 DoF ap-

## Appendix A. Tools for Re-Entry Simulation

proach, where the motion and tumbling for the basic shapes can be specified according to Table A.1. The aerodynamic and aerothermal models are established for the defined shapes and motions. For tumbling motions, the coefficients are taken as the average of the values obtained for the different attitudes. The atmospheric models 1976 U.S. standard atmosphere [United States National Oceanic and Atmospheric Administration and United States Committee on Extension to the Standard Atmosphere, 1976], MSISe-90 atmosphere [Hedin, 1991] and the GRAM-99 atmosphere [Justus and Johnson, 1999] are available.

Table A.1: ORSAT object geometry and motion [Lips and Fritsche, 2005].

Shape	Motion
Sphere	Spinning
	Not spinning
	Broadside and spinning
Cylinder	Random tumbling and spinning
	End-on and spinning
	End-over-end tumbling and spinning
Box, Flat plate	Not tumbling and normal to the flow
	Tumbling

The aerodynamic analysis only considers the drag coefficient, from hypersonic to subsonic speeds. For the transitional regime, the drag coefficient is calculated using a Knudsen number dependent bridging function, as

$$C_{D_{\text{trans}}} = C_{D_{\text{cont}}} + (C_{D_{\text{cont}}} - C_{D_{fm}}) \left[ \sin \left( \pi \left[ \frac{1}{2} + \frac{1}{4} \log(Kn) \right] \right) \right]^3. \quad (\text{A.1})$$

The box model in ORSAT assumes a constant drag coefficient of 1.42 in continuum flow and a constant free-molecular flow drag coefficient of 2.55 [Rochelle et al., 1997]. For cylinders, the continuum and free molecular drag coefficients are 1.22 and 2.0, respectively [Rochelle et al., 1997]. These values are interpolated using Eq. A.1 for the transitional flow regime.

The averaged aerothermodynamic loads are computed using a heat flux model as a function of shape and motion. The loads are computed according to the different flow

## Appendix A. Tools for Re-Entry Simulation

regimes. In the hypersonic continuum regime, the Detra, Kemp and Riddell formulation for a spherical stagnation point is used as the primary model [Kemp and Riddell, 1957]

$$\dot{q}_{\text{st}_{\text{cont}}} = \frac{110285}{\sqrt{R_N}} \left( \frac{\rho_\infty}{\rho_0} \right) \left( \frac{V_\infty}{V_0} \right)^{3.15}, \quad (\text{A.2})$$

where  $\rho_0 = 1.225 \text{ kg/m}^3$  is the atmospheric density at sea level,  $V_0 = 7924.8 \text{ m/s}$  is a velocity of reference,  $\rho_\infty$  and  $V_\infty$  are respectively the free-stream density and velocity, and  $R_N$  is the nose radius. The heat flux in the free molecular regime is computed as

$$\dot{q}_{\text{st}_{\text{fm}}} = \frac{\alpha_T \rho_\infty V_\infty^3}{2}. \quad (\text{A.3})$$

where  $\alpha_T$  is a thermal accommodation coefficient, set to 0.9 [Lips and Fritsche, 2005]. For the transitional regime, several types of bridging functions are available as functions of Knudsen number and geometrical shape, as expressed in Table A.2. To adjust the stagnation point heat flux for the different shapes and motions, the effective radii of curvature and motion-dependent averaging factors are applied.

Table A.2: ORSAT transition regime bridging function for aerothermal loads [Lips and Fritsche, 2005]

Shape	Bridging method
Sphere, Cylinder	$0.001 \leq \text{Kn} \leq 0.01$ : Logarithmic Stanton number bridging
	$0.01 \leq \text{Kn} \leq 10$ : Computation of Stanton number using the model by [Cheng, 1961, Cropp, 1965]
Box, Flat plate	Exponential bridging function: $\dot{q}_{\text{trans}} = \dot{q}_{\text{cont}} \left[ 1 - \exp\left(-\frac{\dot{q}_{\text{fm}}}{\dot{q}_{\text{cont}}}\right) \right]$

ORSAT offers the flexibility to define multiple break-up altitudes and the distinction between aerodynamic mass and thermal mass to use in trajectory computation and heating analysis, respectively. Therefore, the internal components can be exposed to the flow subsequently at several calculated breakup altitudes. The tool also calculates the structural failure of solar array hinges. The thermal conductive models can employ a lumped mass approach, 1D models for boxes and flat plates, and 2D models for spheres and cylinders [Dobarco-Otero et al., 2005].

### A.1.2 DRAMA/SESAM

The Debris Risk Assessment and Mitigation Analysis (DRAMA) [Lips and Fritsche, 2005, Pontijas Fuentes et al., 2019, Kanzler et al., 2017, Braun et al., 2020] is a support tool for the verification of space mission compliance in Europe. The tool covers numerous assessments related to risks associated with space debris, such as prediction of debris and meteoroid flux for specific targets, forecast of the number of avoidance manoeuvres and respective uncertainty, prediction of orbital lifetimes, analysis of de-orbiting procedures and analysis of atmospheric re-entry.

SARA (spacecraft entry Survival And Risk Analysis module) is one software application included in DRAMA, and is used to compute the casualty risk for both controlled and uncontrolled atmospheric re-entry scenarios. The SARA module is composed of two sub-modules: SESAM (Spacecraft Entry Survival Analysis Module) and SERAM (Spacecraft Entry Risk Analysis Module). The SESAM module simulates the atmospheric survivability of reentering spacecraft and its fragments, while the SERAM module performs the casualty risk assessment based on the ground impact location. SESAM is classified as an object-oriented tool, presenting physical models similar to the ones available in ORSAT. Figure A.2 shows a high-level system context of the latest SESAM module, defining the communication between the aerothermodynamics, dynamics and environmental models.

The objects used to model the spacecraft can have two types of relationship between them: *included-in* and *connected-to*. The former relationship represents a connection between two primitives that partially hide one another from the incoming flow and share thermal conductive area, while the latter relationship is the parent-child concept, similar to DAS and ORSAT. The spacecraft fragmentation has evolved in the recent SESAM version [Pontijas Fuentes et al., 2019] from a single event at 78 km of altitude into a fragmentation process dependent on the type of relationship between primitives and the integrated time histories of the aerothermodynamic loads. The current default fragmentation trigger is a thermal criterion, while still allowing for user-defined triggers for particular bodies, such as altitude, heat flux, dynamic pressure, load factor and temperature.

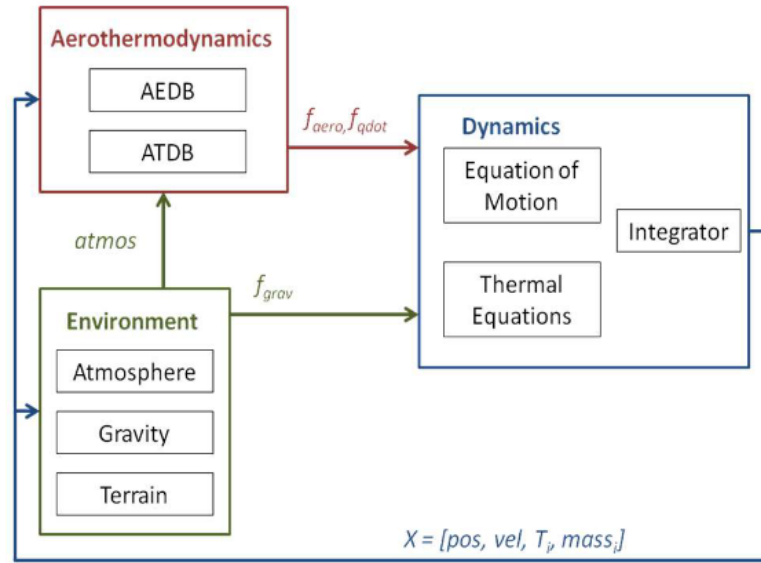


Figure A.2: SESAM High-level System Context (from [Kanzler et al., 2017])

Trajectories are propagated using a 3 DoF and different attitude modes can be specified for the primitives: fixed attitude, random tumbling and tumbling around a given axis. For every fragment shape, the coefficients for drag, lift, and side force are determined as a combination of the individual primitives that make up the fragment. Shading factors are applied to take into account the influence of shadowing effects between primitives, through the use of a voxelator technique [Pontijas Fuentes et al., 2019]. Regarding the atmospheric model, the values are retrieved from the US Standard Atmosphere 1976 and the Horizontal Wind Model 2014 [Drob et al., 2015].

In the later versions of SESAM, the heat balance considers the incoming and rejected radiation heat. Heat conduction is considered for the *connected-to* relationships. Two distinct ablation models are available and depend if the material is either metallic or Carbon Fiber Reinforced Polymers (CFRP). For metallic materials, SESAM uses the standard lumped mass nodal approach. However, a layered approach is employed for CFRP-like materials, and pyrolysis and oxidation effects are considered in the thermal analysis. When the temperature reaches the melting temperature, mass losses are considered during the trajectory propagation. The material's thermal properties can be modelled as temperature-dependent, including parameters such as emissivity, specific

## Appendix A. Tools for Re-Entry Simulation

heat capacity, and heat conductivity.

An explosion model based on NASA’s EVOLVE 4.0 [Johnson et al., 2001] has also been implemented to generate a list of new fragments following an explosion event. Two distinct triggers are available: altitude trigger and temperature trigger.

### A.1.3 DEBRISK

DEBRISK [Omaly and Spel, 2012, Annaloro et al., 2020, Annaloro et al., 2021] is an object-oriented re-entry analysis tool and certification tool for CNES. Similar to other object-oriented tools, DEBRISK represents the spacecraft as a collection of independent objects modelled as simple forms (box, sphere, cylinder and flat plates). Recent versions have introduced the capability to model more complex shapes, such as open cylinders, open truncated cones and spherical caps [Annaloro et al., 2021].

The trajectory of the satellite and its fragments are computed using PATRIUS CNES flight dynamics library using a 3 DoF propagation [Goester et al., 2021]. The objects’ attitude motion is assumed to be randomly tumbling, except for boxes and flat plates, where an End-over-End movement is applied. Fragmentation occurs when the spacecraft altitude reaches the default value of 78 km or the altitude specified by the user. At this altitude, the satellite breaks up and all the fragments are released. However, the fragments contained in the satellite can include other child objects, as in a parent-child relationship, which are released when parent fragment is completely ablated [Goester et al., 2021]. After break-up and demise events, the child object inherit the state vector of the parent objects.

Since DEBRISK V3 [Annaloro et al., 2021], an aerothermodynamics database has been created for the hypersonic continuum regime using CFD computations. This initiative was aimed to increase the accuracy in the computation of the aerodynamic and heat coefficients, replacing the formulations from Klett’s work [Klett, 1964] used in former DEBRISK versions. A comparison between the coefficients retrieved from the database and computed using Klett’s formula has shown that the latter underestimates the survivability of debris.

Thermal modelling considers the contributions of convective, radiative and oxida-

tion heat transfer. The temperature of the object is determined using the lumped mass approach, assuming uniform temperature. Upon reaching the melting temperature, the object starts to ablate. Two ablation models are available: a continuous ablation model and a layered model similar to SESAM. In the former model, the ablated mass is calculated from the energy transferred into the object during the time step interval and the object's shape is updated by uniformly recessing the object's surface. Regarding the latter model, the object is composed of several layers of equal mass, and the object's shape and mass are only updated once a layer is removed.

## A.2 Spacecraft-Oriented tools

### A.2.1 SCARAB

For an initial evaluation of compliance with ESA regulations regarding space debris mitigation, it is recommended to use the SESAM tool, described in Sec. A.1.2. However, as the evaluation assessment progresses, more reliable tools with higher fidelity methods available are required for comprehensive ground risk assessments.

SCARAB (Spacecraft Atmospheric re-entry and Aerothermal Break-Up) is an ESA software tool being developed by HTG since 1995 [Koppenwallner et al., 2005, Lips et al., 2007, Kanzler et al., 2021]. The software was designed for analyzing the mechanical and thermal destruction of spacecraft during controlled or uncontrolled re-entry, pioneering the usage of the spacecraft-oriented methodology. This integrated software package encompasses various aspects, including 6 DoF flight dynamics, aerodynamics, aerothermodynamics, thermal, and structural analysis. Its primary purpose is to conduct re-entry risk assessments, quantifying, characterizing, and monitoring surviving fragments during the re-entry process. SCARAB has undergone validation using in-flight measurements and re-entry observations [Kanzler et al., 2021], and its performance has been compared to other re-entry prediction tools, including ORSAT.

The spacecraft modelling in SCARAB involves various hierarchy levels, enabling the assembly of the complex system through the combination of subsystems, compounds, elements, and basic primitives at the lowest level. The primitives have similar

## Appendix A. Tools for Re-Entry Simulation

shapes as the geometries used in object-oriented tools and can have a material assigned to them. The surface of each primitive is partitioned into triangular surface panels for analysis using local panel inclination methods. For each modelled element, the SCARAB modeller processes the information regarding including mass, location of the centre of mass, and the moment of inertia matrix. Regarding the relationship between different compounds and primitives, the user can select between three types: *connected* (there is a physical connection and thermal conduction), *touching* (there is only thermal conduction) and *separate* (there are gaps between the objects and neither physical connection nor thermal conduction is considered). Several break-up triggers are available in SCARAB for *connected* interfaces, namely altitude, dynamic pressure, and temperature triggers [Kanzler et al., 2021]. A combination of triggers is available, but as soon as the first trigger is activated, the interface relationship changes from *connected* to *separate*, indicating that break-up occurred. If a model object has no connected relationships, it separates, creating a break-up event.

The aerodynamics module from SCARAB determines the aerodynamic loads depending on the spacecraft shape and attitude, and the current flow conditions. The integral aerodynamic force and torque coefficients are calculated from the resulting pressure and shear stress distribution over the spacecraft surface, acting on the unshadowed surface panels. The local pressure and shear stress coefficients for the free molecular regime follow the Schaaf and Chambre model [Schaaf and Chambre, 1958]. For continuum flow, the shear stress coefficient is assumed negligible, and the local pressure coefficients are calculated according to a modified Newtonian theory with applied correction factors  $k_{N1}$  and  $k_{N2}$  [Lips et al., 2007]:

$$C_{p,cont} = k_{N1}C_{p,max} \cos^2 \theta + k_{N2}. \quad (\text{A.4})$$

The correction factors are computed as

$$k_{N1} = \begin{cases} 1 & \cos \theta \geq 0.73 \\ 1 - \frac{0.73 - \cos \theta}{0.73} & 0 < \cos \theta < 0.73 \\ 0 & \text{otherwise} \end{cases} \quad (\text{A.5})$$

## Appendix A. Tools for Re-Entry Simulation

$$k_{N2} = \begin{cases} \frac{0.73 - \cos \theta}{0.73} \left[ (\gamma + 1) \cos^2 \theta + \frac{4}{Ma_\infty^2(\gamma + 1)} \right] & 0 < \cos \theta < 0.73 \\ 0 & \text{otherwise} \end{cases} \quad (\text{A.6})$$

For the transitional regime, SCARAB employs different bridging functions to compute the coefficients. To reduce computation time by avoiding the computation of aerodynamic coefficients, a database is created [Fritsche et al., 2000]. This database contains aerodynamic coefficients in the fixed body coordinate system for a range of angles of attack, side slip angles and atmospheric conditions. The flight dynamics module scans the aerodynamic coefficient database to retrieve the coefficients. However, if no match is found, new coefficients are calculated by the aerodynamic module and stored in the database, dynamically updating it during the trajectory calculation.

The computation of the aerothermal loads is also dependent on the flow regime and the shape of the objects. For the continuum regime, a formulation based on the modified Lees theory is used

$$St_{\text{cont}} = \frac{2.1}{\sqrt{Re_{\infty, \text{stag}}}} (0.1 + 0.9 \cos \theta), \quad (\text{A.7})$$

where  $Re_{\infty, \text{stag}}$  is a Reynolds number based on the free-stream density flux and the stagnation-point temperature, given by

$$Re_{\infty, \text{stag}} = \frac{\rho_\infty V_\infty R_N}{\mu(T_{\text{stag}})}. \quad (\text{A.8})$$

The dynamic viscosity at the stagnation point ( $\mu(T_{\text{stag}})$ ) is obtained using the power law, with  $\omega = 0.72$

$$\frac{\mu(T_{\text{stag}})}{\mu_\infty} = \left( \frac{T_{\text{stag}}}{T_\infty} \right)^\omega. \quad (\text{A.9})$$

Regarding the free molecular regime, the local heat flux is calculated using the Schaaf and Chambre model and assuming an inert wall, i.e. not accounting for chemical reactions or catalysis near the surface [Lips and Fritsche, 2005]. The heat flux equation is expressed as

## Appendix A. Tools for Re-Entry Simulation

$$St_{fm} = \frac{1}{2\sqrt{\pi}\mathcal{S}_\infty^3} \left[ \left( \mathcal{S}_\infty^2 + \frac{\gamma}{\gamma-1} - \frac{(\gamma+1)T_w}{2(\gamma-1)T_\infty} \right) \chi(\mathcal{S}_\infty \sin \theta) - \frac{1}{2} e^{-(\mathcal{S}_\infty \sin \theta)^2} \right] \quad (\text{A.10})$$

and,

$$\chi(\mathcal{S}) = e^{-\mathcal{S}^2} + \sqrt{\pi}\mathcal{S} [1 + \text{erf}(\mathcal{S})]. \quad (\text{A.11})$$

A Knudsen number bridging function is used to combine free-molecular and continuum heat fluxes in the transitional flow regime.

$$St_{trans} = \frac{St_{fm}}{\sqrt{1 + \left(\frac{St_{fm}}{St_c}\right)}}. \quad (\text{A.12})$$

SCARAB computes aerodynamics and aerothermal heating exclusively on the visible panels. The shadow analysis is based on geometric area projections in the flow direction. Therefore, the leeward panels ( $\cos \theta < 0$ ) and the panels occluded by upstream surfaces are assumed shadowed, as illustrated in Fig. A.3.

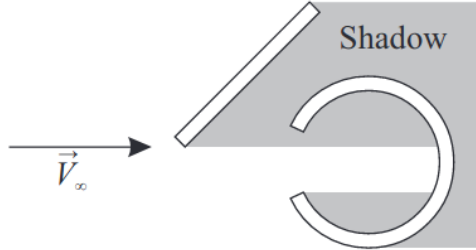


Figure A.3: Shadow analysis schematic (from [Lips et al., 2007]).

After the computation of heat flux, the thermal module calculates the energy balance of the surface panels, as depicted in Fig. A.4. The equation for the heat flux balance for a simple element is

$$\dot{q} = \dot{q}_{conv} + \dot{q}_{cond} + \dot{q}_{rad} = mc \frac{dT}{dt}, \quad (\text{A.13})$$

where  $m$  is the mass of the panel element and  $c$  is the specific heat capacity of the

## Appendix A. Tools for Re-Entry Simulation

material. Each panel has a uniform temperature, corresponding to one thermal node. The heat flux loss due to radiation is computed according to the Stephan-Boltzmann law. Conductive heat exchange between neighbour panels is accounted for and depends on the temperature gradients between the thermal nodes and the thermal conductivity of the material. If the melting temperature of a panel is reached, the panel temperature remains constant and the panel mass is reduced according to Eq. A.13. The mass properties are continuously updated during the re-entry analysis, and molten volume panels are automatically removed.

Along with metallic materials, SCARAB can also model the ablation of CFRP materials, which require different modelling due to the occurrence of physical phenomena [Lips et al., 2017], namely pyrolysis, oxidation and sublimation. A full description of the model may be found in [Fritsche, 2013]. Since the original release, SCARAB has improved the material modelling and has included liquid and gaseous tank contents, non-metallic ceramics, glasses, plastics, and orthotropic, multi-layered composites (e.g. honeycombs, fiber reinforced plastics) [Lips et al., 2004].

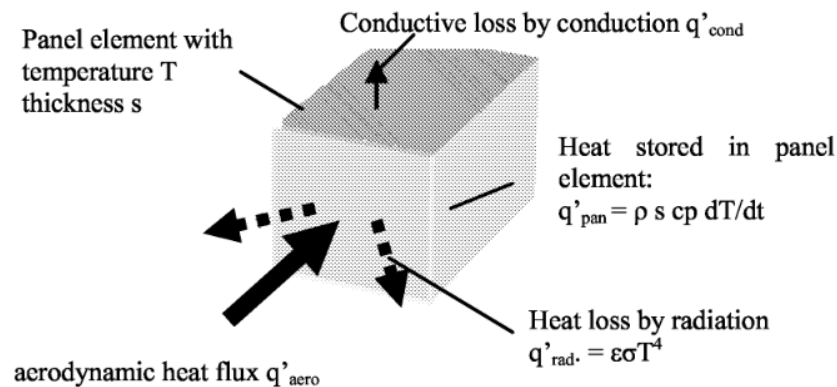


Figure A.4: Heat flow balance for wall surface panel (from [Koppenwallner et al., 2005]).

Structural analysis is also performed at each simulation step, by analysing the impact of the aerodynamic and inertia forces in the structure, causing internal stresses and ultimately mechanical fragmentation. In contrast with thermal fragmentation which is considered for all the volume panels, mechanical fragmentation is only determined for a limited number of user-defined cut planes that go through one or more joints. Joint

## Appendix A. Tools for Re-Entry Simulation

components are defined as an element connecting other elements. The stress present in the cut plane is evaluated based on the forces and torques acting on the spacecraft parts separated by the cut. The stresses at any point of the 2-D section with coordinates  $(y,z)$  are determined by

$$\sigma = \frac{F_x}{A} + \frac{M_y z}{J_y} + \frac{M_z y}{J_z}, \quad \tau = \frac{M_x \rho}{J_\rho}. \quad (\text{A.14})$$

Here,  $\sigma$  is the maximum normal stress,  $\tau$  is the maximum shear stress,  $A$  is the total effective section,  $\rho$  is the density and  $J$  is the moment of inertia. If the equivalent stress surpasses the ultimate tensile strength of the material, which is dependent on the temperature, fragmentation occurs. The failure condition is given as

$$\sigma_{eq} = \sqrt{\sigma^2 + 3\tau^2} \geq \sigma_{ult}(T). \quad (\text{A.15})$$

In the latest version of SCARAB (SCARAB4) [Kanzler et al., 2021], a new Advanced Demise and Ablation Model (ADAM) was introduced, extending the tool capabilities to simulate the demise of distinct material types, including metals, insulators, ceramics and CFRP composites. A new aerothermodynamics model is also available and includes new features that take into consideration the flow stream length and geometry conditions, shock impingement on large structures and radiative shock heating.

### A.2.2 PAMPERO

The PAMPERO re-entry tool [Van Hauwaert et al., 2022, Spel et al., 2021, Annaloro et al., 2015] has been developed by CNES since 2008, and follows a spacecraft-oriented methodology similar to SCARAB. The trajectory and attitude of the spacecraft are simulated using a 6 DoF approach, and integrated with the classical Runge-Kutta method.

Aerodynamics are calculated based on the local panel inclination. In the continuum regime, the Modified Newtonian Theory is employed. For the free molecular regime, computations rely on the analytical law proposed by Bird [Bird, 1994]. In the transitional rarefied regime, a Knudsen-dependent bridging function is applied [Blanchard,

## Appendix A. Tools for Re-Entry Simulation

1991]. At each time step, the viewing factors are computed to determine what are the windward panels, for the integration of the aerodynamic loads.

The stagnation point convective heat fluxes for the exposed faces are estimated using analytical formulas or correlations derived from DSMC and CFD results. The developed empirical formulations for the convective heat flux computation are function of the local curvature radius and local pressure. For the continuum regime, the formulations by Verant-Sagnier [Sagnier and Verant, 1998] and Detra-Kemp-Riddell [Kemp and Riddell, 1957] are available. For the free-molecular regime, the equilibrium kinetic theory is used to estimate the heat flux. A bridging function developed by Legge [Legge, 1987] is used for the transitional regime. PAMPERO also accounts for radiative heat flux losses through the object’s surface but disregards radiation originating from the shock layer. A 3D thermal module using finite volume methods is used to calculate heat conduction inside the object, taking into consideration the material properties and temperature.

PAMPERO’s structural thermal module handles the ablation of a volume cell, assumed to occur when the melting temperature is reached. If more energy than the energy required needed to fully ablate the cell is provided, the energy excess is then spread to its neighbours. While ablating, the size and shape of the cell remain constant, but the mass and inertia properties are continuously revised. Once the entire mass is has been ablated, the cell is removed and the external surface and geometry properties are updated.

At each trajectory and thermal-ablation step, a verification of the fragments’ survivability is conducted, i.e. if the fragments’ condition reaches a defined criterion, the complete fragment is removed from the simulation. Current criteria consist of minimum mass, minimum altitude, minimum energy, maximum acceleration, maximum spin rate, the minimum number of cells and complete thermal ablation.

PAMPERO is in undergoing a verification and validation process campaign, comparing solutionseomparisons with various CFD, DSMC, and experimental cases [Annaloro et al., 2017a, Annaloro et al., 2017b], and has been demonstrating good agreement with the results, including validations against SCARAB simulations.

## A.3 Hybrid tools

### A.3.1 FOSTRAD

The Free Open Source Tool for re-entry of Asteroids and Debris (FOSTRAD) [Mehta et al., 2015, Falchi et al., 2017] is a re-entry tool developed at the University of Strathclyde using the Matlab environment, and combines both spacecraft- and object-oriented approaches. The re-entry analysis framework has been coupled with uncertainty quantification tools, providing the ability to perform uncertainty quantification regarding atmospheric conditions, geometric parameters and initial re-entry state [Mehta et al., 2015, Falchi et al., 2017].

Similar to spacecraft-oriented tools, FOSTRAD uses local panel inclination methods to analyse the aerodynamic and aerothermodynamic loads on the object’s surface. The information regarding the geometry of the objects is provided via *.STL* files, which contain information on the unstructured triangular mesh, namely the facet normal and the corresponding vertex positions and connectivity. To avoid the misidentifying of visible panels due to mesh coarseness, the mesh handler in FOSTRAD proceeds to refine the mesh via an area-based or length-based approach. The local radius of curvature is computed via a specialized algorithm described in [Falchi et al., 2017] to improve aerothermodynamic analysis in complex objects with sharp edges.

The mesh handler originally developed for FOSTRAD was modified to allow the modelling of spacecraft with multiple objects [Falchi, 2020]. Two types of objects are allowed: full bodies and thin shells with predefined thicknesses. The mass and inertia properties are calculated using a voxelization algorithm, in which the geometry volume is replaced with cubic voxels with the selected resolution. A limitation of this method when applied to thin shells is the requirement that the grid resolution is higher than the shell thickness [Falchi, 2020].

The trajectory propagation is performed using a 4th-order Runge-Kutta method, and both 3 DoF with random tumbling or 6 DoF are available. The re-entry simulation is considered concluded when all the objects have ablated or a reference altitude of 10 km is reached. Break-up events are also available through the specification of a breakup

## Appendix A. Tools for Re-Entry Simulation

altitude, where all the components forming the spacecraft are released from the main body.

In regards to the computation of the aerodynamic and aerothermodynamic loads, FOSTRAD determines the Knudsen number at each time step and accordingly selects the adequate method as illustrated in Table A.3. Two distinct bridging functions are applied: a local radius-based bridging function for the aerothermodynamics load, and a Knudsen-based bridging function for the aerodynamics. Detailed information regarding the development of the bridging functions can be found in [Falchi, 2020].

Table A.3: Aerodynamic and Aerothermodynamic models in FOSTRAD.

	Rarefied Regime $Kn > 10^2$	Transitional Regime $10^{-3} < Kn < 10^2$	Continuum Regime $Kn < 10^{-3}$
Aerodynamics	Schaaf and Chambre	Bridging function	Modified Newtonian
Aerothermodynamics	Schaaf and Chambre	Bridging function	Van Driest Fay-Riddell SCARAB

To save computational time, the local panel analysis is only performed on the visible panels. The visibility facet detection algorithm is based on two techniques: a back-face culling method and an attitude-dependent occlusion culling using a unique pixelation method [Mehta et al., 2016]. The pixelation method applies colour IDs to identify the visible faces using the following steps:

- Assign a random unique colour ID in RGB format to each facet;
- Generate a digital picture of the coloured object using a projection parallel to the free-stream direction and store it in RAM;
- Compare the colours that are visible in the generated image to the colour ID assigned to the facets. If matching, the flow is acting on the facet.

However, there are some technical limitations regarding this method. During the generation of the digital image, some graphic cards perform interpolation to smooth colour transitioning between facets, causing panels to be wrongly identified as visible or shadowed. Thus, this method is hardware-dependent.

## Appendix A. Tools for Re-Entry Simulation

During the re-entry process, thermal ablation is considered through a lumped mass approach, similar to the common method employed by object-oriented tools. The temperature is uniformly distributed over the surface of the object, and ablation starts to occur when the temperature reaches the material melting point, from which the mass is blown away at each time step without altering the geometry.

### A.3.2 SAMj

The Spacecraft Aerothermal Model (SAMj) destructive re-entry code [Beck et al., 2017, Beck et al., 2018, Beck et al., 2021, Beck et al., 2015] was developed through a collaboration between Belstead Research and Fluid Gravity Engineering. It makes use of several modules linked within an integrated Java framework and, similar to FOSTRAD, utilizes both object- and spacecraft-oriented approaches. To provide a reasonable estimation of the casualty risk promptly, the geometrical modelling of the spacecraft was simplified regarding spacecraft-oriented tools, but without compromising the capture of important physical processes occurring during re-entry.

Before proceeding to simulate the re-entry case, the spacecraft modelling in SAMj requires information about the components to simulate and their respective linkage. With this information, the tool generates an unstructured mesh to be used in the aerodynamics and aerothermodynamics calculation.

The tool initially propagates the trajectory using a 6 DoF model, switching to a 3 DoF tumble average model after the separation of singular components from the main spacecraft. During the 3 DoF modelling, the continuum aerodynamics are predicted using the Modified Newtonian approach and free molecular aerodynamics is calculated using the methodology of Schaaf and Chambre. For the aerothermodynamics prediction, the Schaaf and Chambre model is also applied in the free molecular regime, but the Modified Lees [Lees, 1956] approach is used in the continuum regime, which was originally designed as a conservative engineering estimate for blunt bodies. When fragmentation occurs, if the released fragments are constituted by individual components, a tumble average 3DOF representation is used to propagate the fragment's trajectory. In this scenario, the aerothermodynamic heating in the continuum regime is predicted

## Appendix A. Tools for Re-Entry Simulation

using running length models for simple shapes, as indicated in [Merrifield et al., 2015], showing improvements concerning standard methodologies when compared to CFD simulations.

The fragmentation events are driven by the material ablation and by the failure of the joints which link the components together. For the latter, it has been demonstrated that joint failure can occur at relatively low temperatures, in comparison to the melting point of aluminium [Beck et al., 2017]. Therefore, SAMj allows the use of adhesive, potted and bolted joints, whose failure criteria are force- and temperature-based:

- Adhesive joint fails at temperatures above 150°C and forces of 250 N
- Potted joint fails at temperatures above 450°C and forces of 500 N
- Bolted joint fails at temperatures above 550°C and forces of 5000 N

Once a joint fails, the resulting fragments are determined.

The thermal modelling in SAMj is dependent on the type of material. For conductors, a bulk heating approach is used, while for isolators, a heat-balance integral technique was developed [Beck and Merrifield, 2015]. Furthermore, the tool accounts for catalicity effects for titanium, steel, aluminium and silicon carbide, experiencing a reduction in convective heat flux when compared to a fully-catalytic surface approach. For charring ablators, internal thermal decomposition is modelled through blowing and surface oxidation [Beck et al., 2017].

## Appendix B

# Inertial tensor of a tetrahedron

The inertial tensor of a tetrahedron  $D$  for a generic coordinate system with direction  $x, y, z$  is expressed as

$$I_D = \begin{bmatrix} I_{xx} = \int_D \rho (y^2 + z^2) dD & I_{yx} = - \int_D \rho xy dD & I_{zx} = - \int_D \rho xz dD \\ I_{xy} = - \int_D \rho xy dD & I_{yy} = \int_D \rho (x^2 + y^2) dD & I_{zy} = - \int_D \rho yz dD \\ I_{xz} = - \int_D \rho xz dD & I_{yz} = - \int_D \rho yz dD & I_{zz} = \int_D \rho (x^2 + y^2) dD \end{bmatrix} \quad (\text{B.1})$$

The moments of nertia for axes  $x, y$  and  $z$  are respectively given as

$$I_{xx} = \rho \cdot |\text{DET}(M)| \cdot (y_1^2 + y_1y_2 + y_2^2 + y_1y_3 + y_2y_3 + y_3^2 + y_1y_4 + y_2y_4 + y_3y_4 + y_4^2 + z_1^2 + z_1z_2 + z_2^2 + z_1z_3 + z_2z_3 + z_3^2 + z_1z_4 + z_2z_4 + z_3z_4 + z_4^2) / 60, \quad (\text{B.2})$$

$$I_{yy} = \rho \cdot |\text{DET}(M)| \cdot (x_1^2 + x_1x_2 + x_2^2 + x_1x_3 + x_2x_3 + x_3^2 + x_1x_4 + x_2x_4 + x_3x_4 + x_4^2 + z_1^2 + z_1z_2 + z_2^2 + z_1z_3 + z_2z_3 + z_3^2 + z_1z_4 + z_2z_4 + z_3z_4 + z_4^2) / 60, \quad (\text{B.3})$$

$$I_{zz} = \rho \cdot |\text{DET}(M)| \cdot (x_1^2 + x_1x_2 + x_2^2 + x_1x_3 + x_2x_3 + x_3^2 + x_1x_4 + x_2x_4 + x_3x_4 + x_4^2 + y_1^2 + y_1y_2 + y_2^2 + y_1y_3 + y_2y_3 + y_3^2 + y_1y_4 + y_2y_4 + y_3y_4 + y_4^2) / 60,$$

## Appendix B. Inertial tensor of a tetrahedron

and the products of inertia as

$$\begin{aligned} I_{yz} = & -\rho \cdot |\text{DET}(M)| \cdot (2y_1z_1 + y_2z_1 + y_3z_1 + y_4z_1 + y_1z_2 + \\ & + 2y_2z_2 + y_3z_2 + y_4z_2 + y_1z_3 + y_2z_3 + 2y_3z_3 + \\ & + y_4z_3 + y_1z_4 + y_2z_4 + y_3z_4 + 2y_4z_4) / 120, \end{aligned}$$

$$\begin{aligned} I_{xz} = & -\rho \cdot |\text{DET}(M)| \cdot (2x_1z_1 + x_2z_1 + x_3z_1 + x_4z_1 + x_1z_2 + \\ & + 2x_2z_2 + x_3z_2 + x_4z_2 + x_1z_3 + x_2z_3 + 2x_3z_3 + \\ & + x_4z_3 + x_1z_4 + x_2z_4 + x_3z_4 + 2x_4z_4) / 120, \end{aligned}$$

$$\begin{aligned} I_{xy} = & -\rho \cdot |\text{DET}(J)| \cdot \{2x_1y_1 + x_2y_1 + x_3y_1 + x_4y_1 + x_1y_2 + \\ & + 2x_2y_2 + x_3y_2 + x_4y_2 + x_1y_3 + x_2y_3 + 2x_3y_3 + \\ & + x_4y_3 + x_1y_4 + x_2y_4 + x_3y_4 + 2x_4y_4) / 120. \end{aligned}$$

## Appendix C

# SU2-NEMO and anisotropic adaptation

### C.1 The open-source solver SU2-NEMO

The open-source software suite SU2 [Economon et al., 2016] has been developed to perform high-fidelity analysis of partial differential equations (PDE) and the creation of PDE-constrained systems. The suite was mostly written in C++, allowing the construction of high-level object-oriented structures and promoting code re-usability and flexibility to effortlessly integrate new state-of-the-art features. In the past few years, new numerical methods, tools and solvers have been gradually incorporated into the SU2 infrastructure. The requirement of simulating chemically reactive multi-species and non-equilibrium flows led to the development of the SU2-NEMO (Non-Equilibrium MOdels) solver [Palacios et al., 2013, Maier et al., 2021]. The thermochemistry models used in SU2-NEMO are provided through the coupling of the solver with the Mutation++ library [Scoggins and Magin, 2014]. The use of the library ensures an appropriate closure of the governing equations for a wide range of temperatures and the use of multi-temperature models for non-equilibrium flows, with the aid of high-fidelity physical models. The coupling has been thoroughly validated [Garbacz et al., 2021]. The library can efficiently compute the thermodynamic, transport and chemical kinetic gas properties for any custom mixture. The transport properties are computed using bi-

nary collision integral mixing methods (Gupta-Yos and Wilke) or the Chapman-Enskog relations.

SU2 and SU2-NEMO adopt a classical edge-based Finite Volume Method (FVM) approach for the numerical discretization of the computational domain. Several upwind schemes can be chosen to calculate the inviscid fluxes, with a special focus on the flux vector splitting (FVS) schemes. To enhance accuracy, the solution is reconstructed using MUSCL (Monotonic Upstream-centered Scheme for Conservation Laws) with the Venkatakrisshnan-Wang limiter. The viscous flux is calculated using the average values at the dual-grid interface and the gradient information is retrieved using the Weighted Least-Squares approach.

### C.1.1 Governing equations and physical models

While SU2 uses the conventional Navier-Stokes equations with a single temperature, the governing equations in SU2-NEMO are obtained by extending the classical Navier-Stokes equations to account for a chemically-reacting, non-equilibrium flow using the two-temperature model by Park [Park, 1993]. Using this model, the translational energy mode is assumed to be at equilibrium with the rotational mode, while the vibrational mode is assumed to be at equilibrium with the electronic mode. The equations can be written as

$$\frac{d\mathbf{U}}{dt} + \nabla \cdot \mathbf{F}^i(\mathbf{U}) - \nabla \cdot \mathbf{F}^v(\mathbf{U}) = \mathbf{Q}(\mathbf{U}), \quad (\text{C.1})$$

where  $\mathbf{U}$  are the conservative variables,  $\mathbf{Q}$  are the source terms,  $\mathbf{F}^i$  and  $\mathbf{F}^v$  are the inviscid and viscous fluxes, respectively. The vectors are given by

$$\mathbf{U} = \begin{pmatrix} \rho_1 \\ \vdots \\ \rho_{n_s} \\ \rho \mathbf{u} \\ \rho e \\ \rho e^{v-e} \end{pmatrix}, \quad \mathbf{F}^i = \begin{pmatrix} \rho_1 \mathbf{u} \\ \vdots \\ \rho_{n_s} \mathbf{u} \\ \rho \mathbf{u} \otimes \mathbf{u} + p \bar{I} \\ \rho \mathbf{u} h \\ \rho \mathbf{u} e^{v-e} \end{pmatrix}, \quad \mathbf{F}^v = \begin{pmatrix} \mathbf{J}_1 \\ \vdots \\ \mathbf{J}_{n_s} \\ \bar{\tau} \\ \bar{\tau} \cdot \mathbf{u} + \sum_s \mathbf{J}_s h_s + \mathbf{q}^{t-r} + \mathbf{q}^{v-e} \\ \sum_s \mathbf{J}_s h_s^{v-e} + \mathbf{q}^{v-e} \end{pmatrix}, \quad \mathbf{Q} = \begin{pmatrix} \dot{\omega}_1 \\ \vdots \\ \dot{\omega}_{n_s} \\ 0 \\ 0 \\ \dot{\Omega} \end{pmatrix}, \quad (\text{C.2})$$

in which  $\rho$  is the density,  $\mathbf{u}$  is the velocity vector,  $p$  is the static pressure,  $h$  is the total enthalpy per unit mass of the mixture,  $e$  is the energy per unit mass,  $\bar{\tau}$  is the viscous stress tensor,  $\mathbf{q}$  is the conduction heat flux,  $\mathbf{J}$  is the mass diffusion flux,  $\dot{\omega}$  is the net rate of species production,  $\dot{\Omega}$  is the source term of vibrational energy and  $n_s$  is the number of species in the mixture. The subscript index  $s$  stands for the  $s^{\text{th}}$  chemical species in the mixture and the superscript t-r and v-e stand for the translational-rotational and vibrational-electronic modes, respectively. If the quantity does not have a subscript, it is related to the full mixture. The term  $\bar{I}$  denotes the identity matrix.

Individual chemical species are assumed to behave as an ideal gas. Under this assumption, the total pressure of the mixture is defined using Dalton's law as

$$p = \sum_{s=1}^{n_s} p_s, \quad (\text{C.3})$$

where  $p_s$  is the partial pressure of each species. The partial pressure can be determined by using the ideal gas law

$$p_s = \rho_s \frac{R_u}{M_s} T_{tr}, \quad (\text{C.4})$$

where  $R_u$  is the universal gas constant,  $M_s$  is the molar mass of species  $s$  and  $T_{tr}$  is the translational-rotational temperature of the mixture. The total specific energy of the flow is given as the sum of the internal and kinetic energies

$$e = \sum_{s=1}^{n_s} c_s e_s + \frac{1}{2} |\mathbf{u}|^2, \quad (\text{C.5})$$

## Appendix C. SU2-NEMO and anisotropic adaptation

where  $c_s$  is the mass fraction of species  $s$ ,  $|\mathbf{u}|$  is the magnitude of the flow velocity vector and  $e_s$  is the specific internal energy of the species, given by

$$e_s = e_s^t(T_{\text{tr}}) + e_s^r(T_{\text{tr}}) + e_s^v(T_{\text{ve}}) + e_s^e(T_{\text{ve}}) + e_s^0. \quad (\text{C.6})$$

where  $e_s^0$  is the energy of formation,  $e_s^t$ ,  $e_s^r$ ,  $e_s^v$  and  $e_s^e$  are the translational, rotational, vibrational and electronic energy contribution, respectively. The thermal nonequilibrium calculations are performed using the Rigid-Rotor/Harmonic-Oscillator (RRHO) model.

To account for the species production and destruction caused by the occurring chemical processes, the species source term  $\dot{\omega}_s$  are included in the conservative equations, which are given by

$$\dot{\omega}_s = M_s \sum_{r=1}^{n_r} (\nu''_{s,r} - \nu'_{s,r}) \left[ k_{f,r} \prod_{j=1}^{n_s} \hat{\rho}_j^{\nu'_{j,r}} - k_{b,r} \prod_{j=1}^{n_s} \hat{\rho}_j^{\nu''_{j,r}} \right], \quad (\text{C.7})$$

where  $n_r$  and  $n_s$  are the number of reactions  $r$  and the number of species  $s$ , respectively,  $\nu'_s$  is the forward reaction stoichiometry coefficient,  $\nu''_s$  is the backward reaction stoichiometry coefficient,  $\hat{\rho}_j$  is the molar density,  $k_{f,r}$  is the forward reaction rate and  $k_{b,r}$  is the backward reaction rate.

### C.1.2 Inviscid Flux Scheme

The high-fidelity simulations presented in this work were performed using the newly implemented AUSM+M scheme [sheng Chen et al., 2020], which is proposed to increase robustness and performance for all flow speeds. This accomplishment is the result of three new key formulations: pressure diffusion term for mass flux, velocity diffusion term for pressure flux and numerical sound speed.

The AUSM+M scheme follows the general governing equations of the AUSM family with a few modifications. The inviscid flux is expressed as

$$\mathbf{F}_{1/2} = \frac{\dot{m} + |\dot{m}|}{2} \phi_L + \frac{\dot{m} - |\dot{m}|}{2} \phi_R + \mathbf{P}_{1/2}, \quad (\text{C.8})$$

Appendix C. SU2-NEMO and anisotropic adaptation

$$\phi = \begin{Bmatrix} 1 \\ \mathbf{u} \\ h \\ e^{v-e} \end{Bmatrix}, \quad \mathbf{P}_{1/2} = \begin{Bmatrix} 0 \\ p_s \bar{\mathbf{I}} \cdot \mathbf{n} + \mathbf{p}_{u_n} \\ 0 \\ 0 \end{Bmatrix}, \quad \dot{m} = M_{1/2} c_{1/2} \begin{cases} \rho_L & \text{if } M_{1/2} \geq 0; \\ \rho_R & \text{if } M_{1/2} < 0; \end{cases} \quad (\text{C.9})$$

where  $\dot{m}$  is the mass flux,  $\mathbf{P}_{1/2}$  is the pressure flux,  $p_s$  is the interface pressure,  $p_u$  is the velocity diffusion term, and  $c_{1/2}$  and  $M_{1/2}$  are the value of the numerical sound speed and Mach number at interface, respectively. The numerical sound speed is calculated using the definition suggested by Kim et al. [Kim et al., 2001] to satisfy the Prandtl relation across oblique shocks.

The interface Mach number is calculated using a new formulation for the pressure diffusion term  $M_p$

$$M_{1/2} = M_L^+ + M_R^- + M_p, \quad (\text{C.10})$$

$$M_p = -(1-f)(1-g) \frac{1}{2} \frac{p_R - p_L}{\rho_{1/2} c_{1/2}^2}. \quad (\text{C.11})$$

The subscripts "L" and "R" and superscripts "+" and "-" stand for the left and right states across the cell interface, respectively. The split Mach numbers  $M_L^+$  and  $M_R^-$  are calculated using the same approach as in the AUSM+UP scheme [Liou, 2006]. The term  $g$  is the multidimensional pressure-based sensing function [sheng Chen et al., 2018] used to detect strong shock wave and to preserve shear layers and the term  $f$  is the Mach number limiting function used for a good transition through all range of speeds. The functions are expressed as

$$g = \frac{1 + \cos(\pi h)}{2}, \quad h = \min_k(h_k), \quad h_k = \min \left( \frac{P_{Lk}}{P_{Rk}}, \frac{P_{Rk}}{P_{Lk}} \right), \quad \text{and} \quad (\text{C.12})$$

$$f = \frac{1 - \cos(\pi M)}{2}, \quad M = \min(1, \max(|M_L|, |M_R|)), \quad (\text{C.13})$$

where the index  $k$  indicates the adjacent interfaces for both cells being evaluated. The

interface pressure is calculated using

$$p_s = \frac{p_L + p_R}{2} + (\psi_L^+ - \psi_R^-) \frac{p_L - p_R}{2} + f_o(\psi_L^+ + \psi_R^- - 1) \frac{p_L + p_R}{2}, \quad (\text{C.14})$$

$$f_o = \min(1, \max(f, M_\infty^2)), \quad (\text{C.15})$$

where the function  $f_o$  is a scaling Mach number function dependent of function  $f$  defined in equation C.13. The term  $M_\infty$  is the free-stream Mach number and the terms  $\psi_L^+$  and  $\psi_R^-$  are the pressure-splitting functions used in the AUSM+UP scheme. To avoid the propagation of perturbation and occurrence of carbuncle, an additional dissipation mechanism is implemented in AUSM+M. The velocity diffusion is expressed as

$$p_{u_n} = -g \cdot \frac{\gamma(p_L + p_R)}{2c_{1/2}} \psi_L^+ \psi_R^- (u_{R_n} - u_{L_n}). \quad (\text{C.16})$$

where  $u_{R/L_n}$  is the velocity component in the  $\mathbf{n}$  direction.

## C.2 Adaptive Mesh Generation

The pyAMG library developed by the GAMMA team at INRIA <sup>1</sup> [Loseille and Loehner, 2011, Loseille and Menier, 2014, Loseille et al., 2015] is used to generate the anisotropic grids for this work test cases by coupling the SU2 solver and the AMG mesh adaptation tool via python interface. The pyAMG software is a Python wrapper for the Adaptive Mesh Generation library (AMG-lib), a fast and robust mesh adaptation tool capable of generating anisotropic grids around 2D and 3D complex geometries. The local anisotropic elements follow the direction of the complex multi-directional flow features, such as shock waves, contact discontinuities and boundary layers. This is done by computing an optimal Riemannian metric tensor field from the error estimate of a given background mesh and respective flowfield solution, containing information

---

<sup>1</sup><https://pyamg.saclay.inria.fr/>

## Appendix C. SU2-NEMO and anisotropic adaptation

of the elements' edge size and orientation for the adaptation process. The computed interpolation error is second-order in space and can be approximated using the Hessian matrix  $\mathcal{H}(\mathbf{x})$ , calculated using a double  $\mathbf{L}^2$ -projection [Vallet et al., 2007]. To ensure that the computed metric field is positive definite, the absolute value of the Hessian matrix is used, given as

$$|\mathcal{H}| = \mathcal{R} |\Lambda| \mathcal{R}^\top. \quad (\text{C.17})$$

The optimal metric field is given by the  $\mathbf{L}^p$ -norm normalization of the Hessian matrix for a mesh complexity constraint  $\mathcal{N}$  specified before the adaptation process:

$$\mathcal{M}(\mathbf{x}) = \mathcal{N}^{\frac{2}{3}} \left( \int_{\Omega} (\det |\mathcal{H}(\mathbf{x})|)^{\frac{p}{2p+3}} d\Omega \right)^{-\frac{2}{3}} (\det |\mathcal{H}(\mathbf{x})|)^{-\frac{1}{2p+3}} |\mathcal{H}(\mathbf{x})| \quad (\text{C.18})$$

where  $\mathcal{N}$  is a measure of the desired number of Degrees Of Freedom (DOFs) in the final adapted mesh,  $\left( \int_{\Omega} (\det |\mathcal{H}(\mathbf{x})|)^{\frac{p}{2p+3}} d\Omega \right)^{-\frac{2}{3}}$  is a global normalization used to reach the desired number of DOFs, and  $(\det |\mathcal{H}(\mathbf{x})|)^{-\frac{1}{2p+3}}$  is a local normalization to assess the sensitivity to small variations. The PyAMG tool recursively uses anisotropic local operators such as point insertion, edge swapping, edge collapse and point smoothing to improve the output grid through the computed metric field and imposed quality constraints to guarantee the robustness and quality of the final grid [Loseille, 2017].

## Appendix D

# 2D cases for anisotropic mesh validation in hypersonic flow

### D.1 2D Single Cylinder

Let us consider a simulation of a non-equilibrium hypersonic flow past a single cylinder, using the free-stream conditions and mass fractions in Table D.1. This non-trivial test case has been used as validation of the physico-chemical models used in CFD solvers [Knight et al., 2012] since the shock layer is subject to non-equilibrium chemical and vibrational relaxation. The simulations were performed on the two grids shown in Fig. D.1 for the inviscid and viscous flow. The grids have the same structured boundary layer grid, with 200 equally spaced elements along the cylinder surface, and 135 elements in the normal direction, starting with a first element height of  $10^{-8}$  m from the surface and linearly growing in the normal direction with a progression rate of 1.075. The number of nodes and elements, along with the aspect ratio details can be seen in Table D.2. The anisotropic adaptation was performed using the Mach number of the steady-state solution to compute the Hessian matrix for the anisotropic metric.

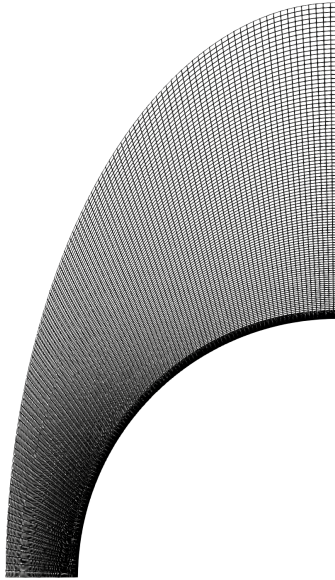
To assess the existence of grid misalignment that may generate numerical issues in the post-shock solution of the anisotropic grid, Fig. D.2 compares the velocity component of the stream in the normal direction for both grids, by normalizing it with the value of the post-shock velocity  $u_2$  at the stagnation line for the inviscid case. Candler

Table D.1: Free-stream and wall values for the single cylinder case.

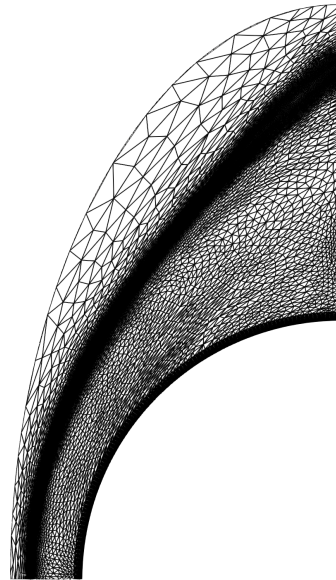
$T_\infty$ [K]	901
$T_w$ [K]	300
$\rho_\infty$ [kg/m <sup>3</sup> ]	1.547e-03
U [m/s]	5956
N [%]	6.5e-05
O [%]	22.83
NO [%]	1.026
N2 [%]	75.431
O2 [%]	0.713

Table D.2: Grid details for the single cylinder case.

Grid	Nodes	Elements	Average AR	Maximum AR
Isotropic grid - level 0	166,694	394,534	1.553	1.600
Anisotropic grid - level 1	244,132	803,567	6.497	35.691
Anisotropic grid - level 2	339,852	1,329,244	10.767	55.913
Structured grid	141,000	189,744	—	—



a) Structured



b) Unstructured Anisotropic

Figure D.1: Grids overview for the single cylinder case.

Appendix D. 2D cases for anisotropic mesh validation in hypersonic flow

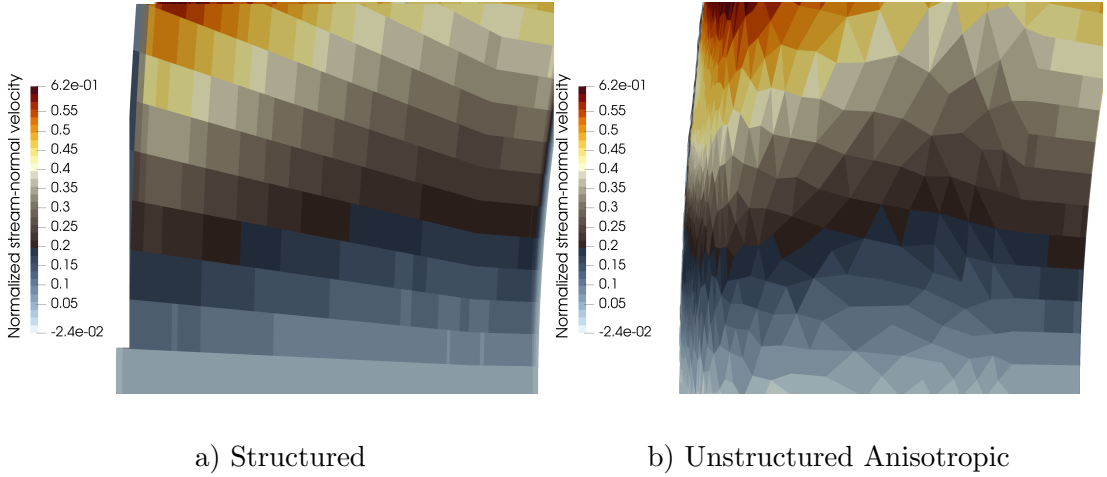


Figure D.2: Normalized stream-normal velocity ( $v/u_2$ ) for the single cylinder case at the stagnation region.

et al. [Candler et al., 2007] show in their work similar comparisons and conclude that the misalignment of the shock with the grid elements induces the formation of momentum in the wrong direction. Candler also mentions that this error rapidly increases with the Mach number and that this problem is more severe for triangular/tetrahedral grids. However, when comparing both grids' results, it is interesting to see that this is not the case for the anisotropic solution. For a better comparison between both grids, the cell-centered value is plotted without smoothing. Both grids present similar values of velocity relatively in the same cell location, with no major spikes of normal momentum generated due to misalignment except for a cell in the anisotropic grid with a minimal velocity error of  $-0.024u_2$ , thus indicating that the anisotropic grid is aligned with the intense shock wave generated by the cylinder.

The plot contours of normalized pressure and temperature are illustrated in Fig. D.3. By analysing the contour plots, it is clear that the anisotropic grid captures more sharply the shock wave. This result is expected since the anisotropic grid was generated to follow the flow features, while the structured grid was not adapted. Thus, the elements of the structured grid do not strictly follow the shock, which is more noticeable when approaching the outlet boundary. Comparing pressure and temperature contours for both inviscid and viscous formulations, no major difference is noticeable except for the expected shock thickness increase for the viscous case.

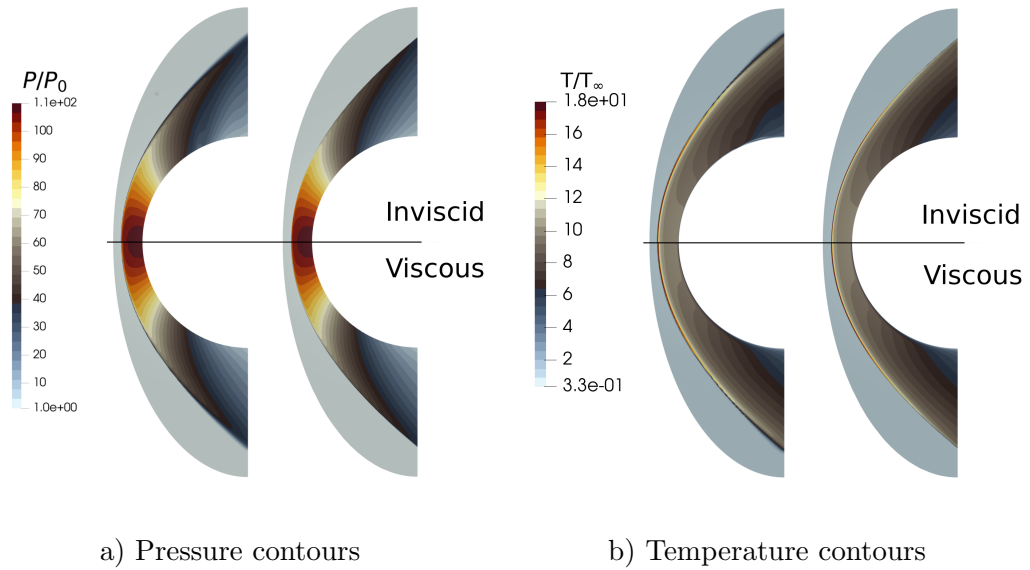


Figure D.3: Flow contours of the single cylinder case for the structured grid (left) and the unstructured grid (right).

The pressure at the surface is plotted in Fig. D.4 for the two grids, and compared to experimental data obtained from the High Enthalpy Shock Tunnel Göttingen, HEG [Karl et al., 2003], using 17 pressure transducers and thermocouples, covering a circumferential angle of  $\pm 60^\circ$  to measure surface pressure and heat flux distributions. The solution obtained for both grids is in good agreement with the experimental data. For a better comparison between the two grids, only a small region near the stagnation point is considered. Since the solution is not known before the generation of the structured grid, it is not possible to guarantee the local alignment of the structured grid elements with the shock wave as the distance from the stagnation line increases, therefore predicting with higher accuracy the surface quantities near the stagnation point. Both the structured and anisotropic grids show a similar pressure profile.

Similar plots near the stagnation point are obtained for the heat flux distribution in Fig. D.5. Once again, the plot only covers the area near the stagnation region since, from an engineering point of view, it is the most important region to be accurately predicted since the peak values that can lead to structural failure and crack initialization are located there. The results obtained from using an anisotropic grid are identical to the solution from a structured grid. The heat flux distribution from the numerical

## Appendix D. 2D cases for anisotropic mesh validation in hypersonic flow

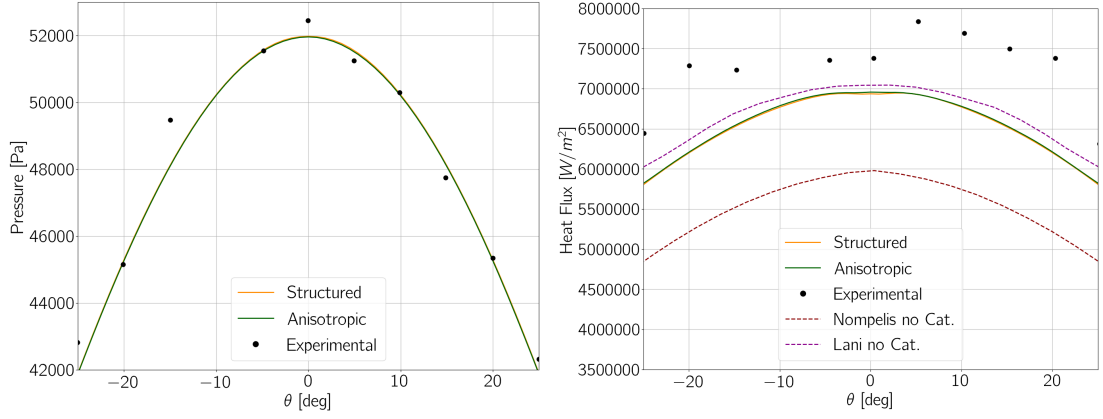


Figure D.4: Surface pressure plot for the single cylinder. Figure D.5: Surface heat flux plot for the single cylinder.

simulations is underestimated when compared to the experimental data since there is no catalytic effect applied at the wall. Nevertheless, the results obtained in this work are comparable with the results published in [Knight et al., 2012]. In particular, the obtained results are similar to the non-catalytic simulation results of Andrea Lani and are in better agreement with the experimental data than the results of Nompelis.

## D.2 2D Proximal Cylinders

The hypersonic flow around a complex vehicle or several bodies often has the presence of multiple shock waves, which are at the origin of shock-shock interactions and shock impingement on the surface of the body. The accurate capture of these interactions is of utter importance to understand how it will affect the aerothermal loads of the objects downstream. The 2D case of proximal bodies is simulated, using the free-stream conditions in Table D.3 and the geometry in Fig. D.6, such that the interaction occurs in the vicinity of the aft cylinder.

Both Euler and Navier-Stokes simulations were conducted using the grids in Fig. D.7 and Fig. D.8 respectively, in the regions of interest, i.e., where the shock interaction occurs. The structured grid was generated using multiple structured blocks as the position of the shock waves and their interaction were known beforehand. Therefore, the structured blocks were introduced to follow the flow features as aligned as possible.

Appendix D. 2D cases for anisotropic mesh validation in hypersonic flow

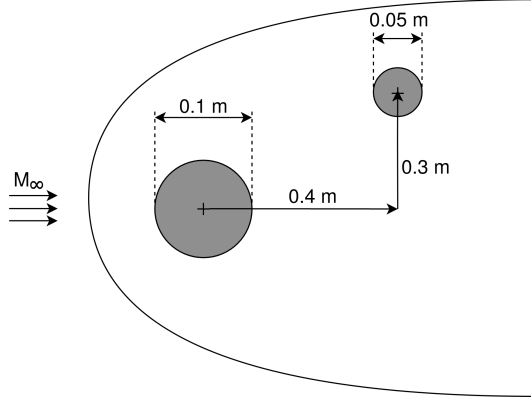


Figure D.6: Geometry configuration of the two-dimensional two-cylinder case

Table D.3: Free-stream and wall values of the two-cylinder case.

$T_\infty$ [K]	210
$T_w$ [K]	300
$\rho_\infty$ [kg/m <sup>3</sup> ]	4.495e-05
U [m/s]	2911
N [%]	0
O [%]	0
NO [%]	0
N2 [%]	77
O2 [%]	23

Just like in the previous case, the anisotropic grid was created through the adaptation of the isotropic grid. For the inviscid case, a structured boundary layer was not used to assess the grid impact on the pressure distribution when compared to the results obtained with the structured mesh. Both grid details are described in table D.4 and table D.5 for the inviscid and viscous case, respectively.

Table D.4: Grid details for the inviscid proximal cylinder case.

Grid	Nodes	Elements	Average AR	Maximum AR
Isotropic grid - level 0	149,652	298,135	1.01	1.68
Anisotropic grid - level 1	120,388	239,992	5.29	73.948
Structured grid	478,030	237,900	—	—

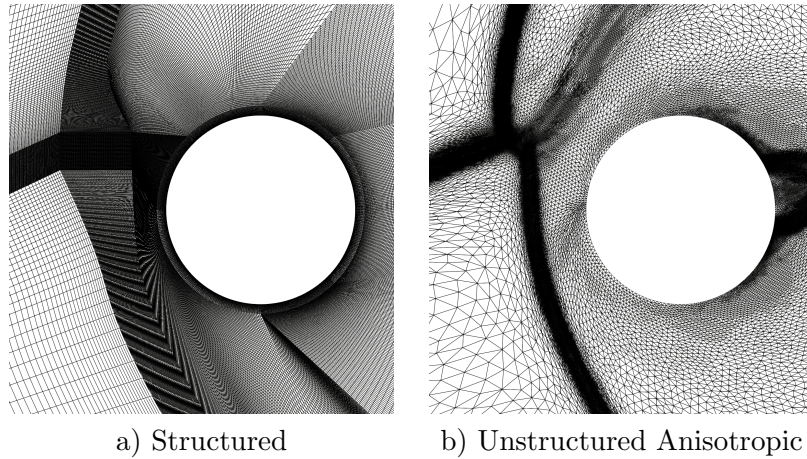


Figure D.7: Grids overview for the two-cylinder case using inviscid formulation.

Table D.5: Grid details for the viscous proximal cylinder case.

Grid	Nodes	Elements	Average AR	Maximum AR
Isotropic grid - level 0	578,658	1,657,059	1.556	5.618
Anisotropic grid - level 1	290,720	698,653	4.623	58.852
Anisotropic grid - level 2	545,358	1,808,059	6.16	71.780
Anisotropic grid - level 3	692,845	2,493,869	6.32	77.938
Structured grid	778,620	516,800	—	—

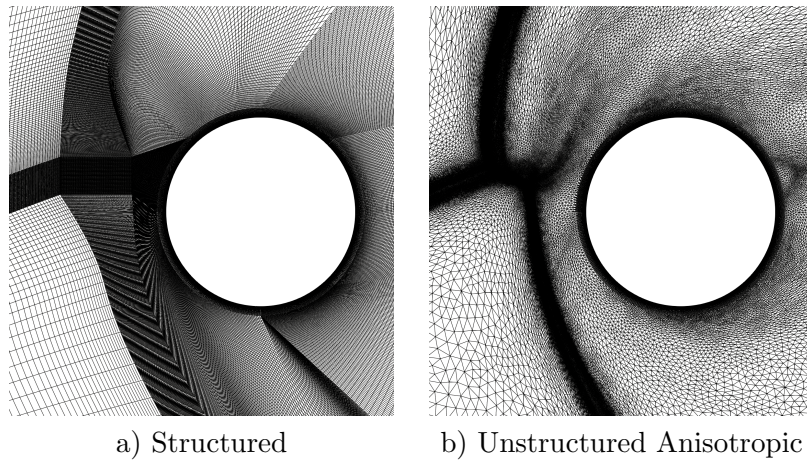


Figure D.8: Grids overview for the two-cylinder case using viscous formulation.

## Appendix D. 2D cases for anisotropic mesh validation in hypersonic flow

The pressure and temperature contours near the aft cylinder for the inviscid case are illustrated in Fig. D.9 and Fig. D.10, respectively. The shock interaction pattern is sharply captured using both anisotropic and structured grids. The shock-shock interference can be characterized as being of type VII according to the work of Yamamoto et al. [Yamamoto et al., 1999], where the supersonic jet produced does not strike the body but follows to the upper downstream region instead. The jet unsteadiness, common for these types of interactions, can be observed in the case of the structured grid. A weaker degree of unsteadiness is also observed for the anisotropic grid.

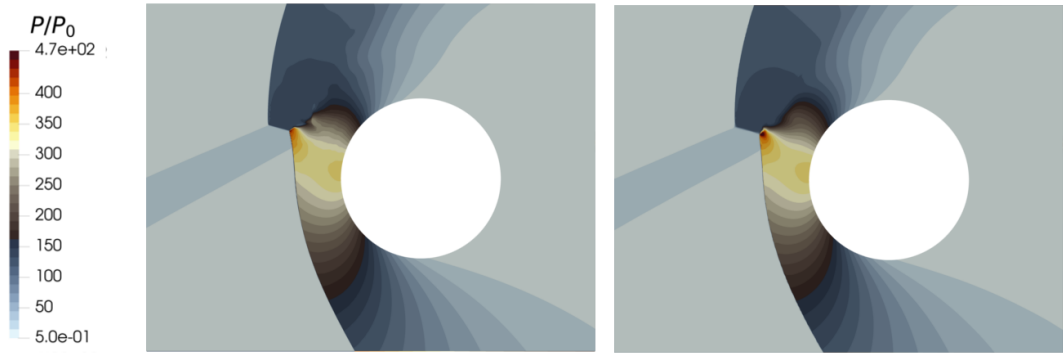


Figure D.9: Normalized pressure contours for the structures and anisotropic grids, respectively, at the shock-shock interference region using inviscid formulation.

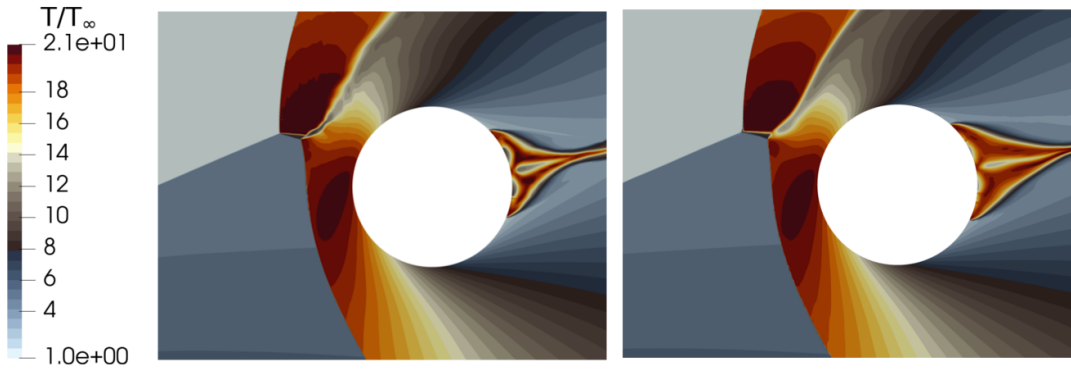


Figure D.10: Normalized temperature contours for the structured and anisotropic grids, respectively, at the shock-shock interference region using inviscid formulation.

Comparing the pressure distribution at the cylinder, in Fig. D.11, the structured and anisotropic grids have an almost coincident pressure profile. The lift and drag coefficients provided by SU2-NEMO solver using the inviscid formulation with the

Appendix D. 2D cases for anisotropic mesh validation in hypersonic flow

anisotropic grid are compared to the reference values of Laurence et al. [Laurence et al., 2007] in Fig. D.13 and Fig. D.14 respectively, showing a perfect agreement with the available data.

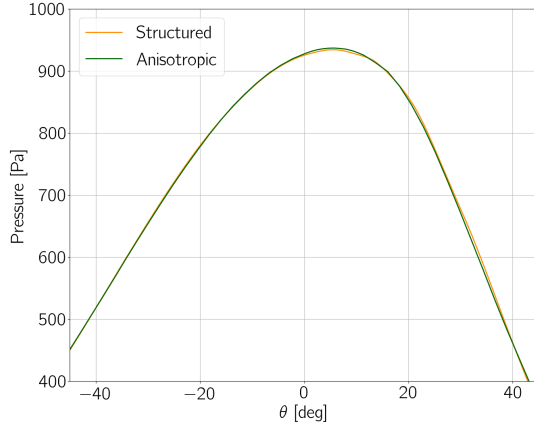


Figure D.11: Surface pressure plot of the aft cylinder for the two-cylinder case using inviscid formulation.

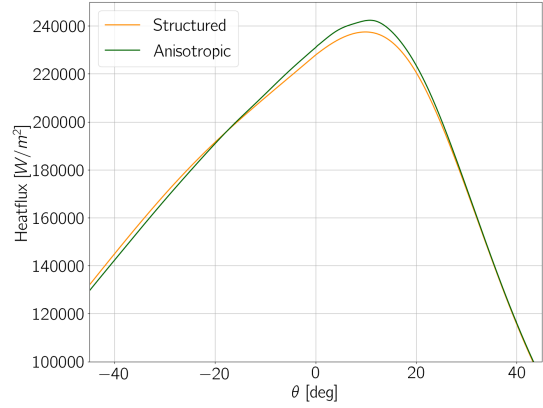


Figure D.12: Surface heat flux plot of the aft cylinder for the two-cylinder case using viscous formulation.

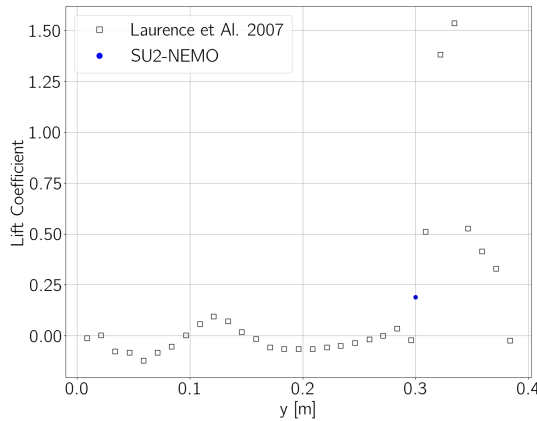


Figure D.13: Lift coefficient of the aft cylinder for a vertical displacement of 0.3 meters.

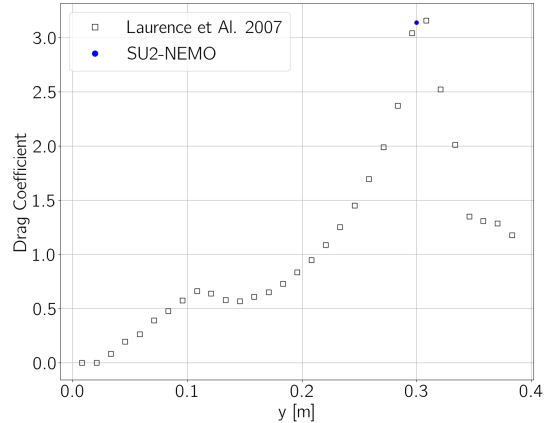


Figure D.14: Drag coefficient of the aft cylinder for a vertical displacement of 0.3 meters.

Regarding viscous simulations, normalized pressure and temperature contours are illustrated in Fig. D.15 and Fig. D.16, respectively. The presence of diffusivity due to viscosity resulted in the three grid contour plots being similar, with no presence of a contact discontinuity as opposed to the inviscid case.

Appendix D. 2D cases for anisotropic mesh validation in hypersonic flow

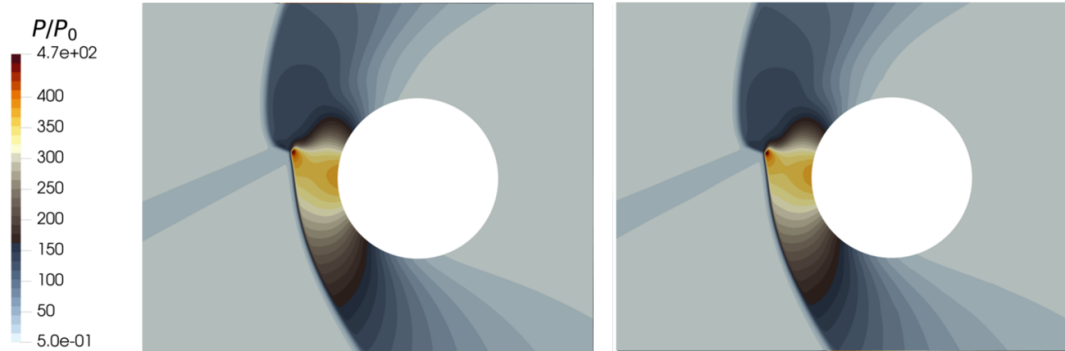


Figure D.15: Normalized pressure contours for the structured and anisotropic grids, respectively, at the shock-shock interference region using viscous formulation.

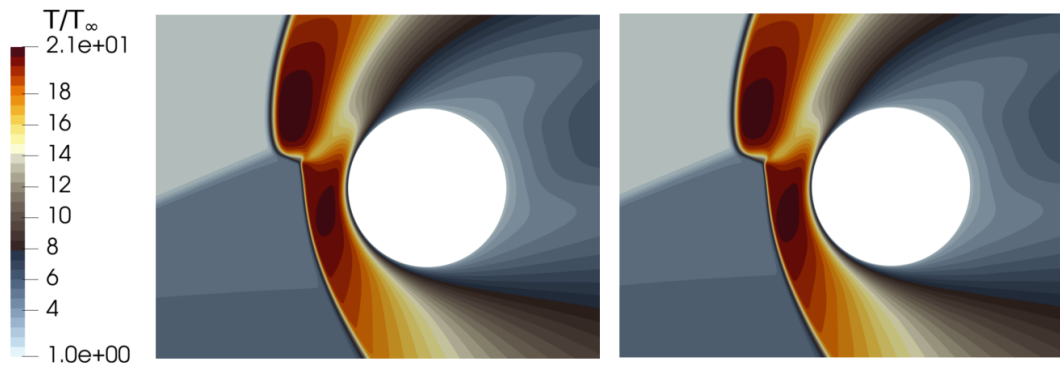


Figure D.16: Normalized temperature contours for the structured and anisotropic grids, respectively, at the shock-shock interference region using viscous formulation.

## Appendix D. 2D cases for anisotropic mesh validation in hypersonic flow

Analysing the heat flux profile in Fig. D.12, only a small discrepancy is present, without any obvious oscillations. Compared to the structured grid, the anisotropic grid slightly overestimates the heat flux. However, it is important to remember that the structured grid was constructed to follow the shock wave as close as possible, but no adaptation was performed on the structured grid, therefore it is not possible to fully guarantee the orthogonality of the elements at the location of the shock-shock interference.

# Bibliography

- [Agency, 2020] Agency, E. S. (2020). Estimate: European space material demisability database.
- [Alnæs et al., 2015] Alnæs, M. S., Blechta, J., Hake, J., Johansson, A., Kehlet, B., Logg, A., Richardson, C., Ring, J., Rognes, M. E., and Wells, G. N. (2015). The FEniCS Project Version 1.5. *Archive of Numerical Software*.
- [Ambrosio and Wortman, 1962] Ambrosio, A. and Wortman, A. (1962). Stagnation-point shock-detachment distance for flow around spheres and cylinders in air. *Journal of the Aerospace Sciences*, 29(7):875–875.
- [Anderson, 2006] Anderson, J. (2006). *Hypersonic and High-temperature Gas Dynamics*. AIAA education series. American Institute of Aeronautics and Astronautics.
- [Annaloro et al., 2017a] Annaloro, J., Galera, S., Kärräng, P., Prevereaud, Y., Vérant, J.-L., Spel, M., Van Hauwaert, P., and Omaly, P. (2017a). Space debris atmospheric entry prediction with spacecraft-oriented tools. In *7th European Conference on Space Debris*.
- [Annaloro et al., 2017b] Annaloro, J., Galera, S., Kärräng, P., Prigent, G., Lips, T., and Omaly, P. (2017b). Comparison between two spacecraft-oriented tools: Pampero & scarab. *Journal of Space Safety Engineering*, 4(1):15–21.
- [Annaloro et al., 2021] Annaloro, J., Galera, S., Thiebaut, C., and Omaly, P. (2021). DEBRISK V3: new generation of object-oriented tools. In *8th European Conference on Space Debris*, page 196.

## Bibliography

- [Annaloro et al., 2020] Annaloro, J., Galera, S., Thiebaut, C., Spel, M., Van Hauwaert, P., Grossir, G., Paris, S., Chazot, O., and Omaly, P. (2020). Aerothermodynamics modelling of complex shapes in the debris atmospheric reentry tool: Methodology and validation. *Acta Astronautica*, 171:388–402.
- [Annaloro et al., 2015] Annaloro, J., Omaly, P., Rivola, V., and Spel, M. (2015). Elaboration of a new spacecraft-oriented tool: Pampero. In *Proceedings of the 8th European Symposium on Aerothermodynamics for Space Vehicles 2-6 March*.
- [Artemieva and Shuvalov, 2001] Artemieva, N. A. and Shuvalov, V. V. (2001). Motion of a fragmented meteoroid through the planetary atmosphere. *Journal of Geophysical Research: Planets*, 106(E2):3297–3309.
- [Barri, 2010] Barri, N. (2010). Meteoroid fragments dynamics: Collimation effect. *Solar System Research*, 44:55–59.
- [Battie et al., 2012] Battie, F., Fossati, T., Gallucci, S., and Volpi, M. (2012). Vega launch vehicle upper stage re-entry survivability analysis. In *2012 IEEE First AESS European Conference on Satellite Telecommunications (ESTEL)*, pages 1–7. IEEE.
- [Bayer-Buhr et al., 2022] Bayer-Buhr, D., Vimal, M., Prakash, A., Gross, U., and Fieback, T. (2022). Determination of thermal accommodation coefficients on  $\text{CaSiO}_3$  and  $\text{SiO}_2$  using molecular dynamics and experiments. *International Journal of Heat and Mass Transfer*, 183:122219.
- [Beck et al., 2019] Beck, J., Holbrough, I., Merrifield, J., Briot, D., Spel, M., Minisci, E., Omaly, P., and Lemmens, S. (2019). Progress in probabilistic assessment of destructive entry.
- [Beck et al., 2017] Beck, J., Holbrough, I., Merrifield, J., Joiner, N., and Bainbridge, S. (2017). Progress in hybrid spacecraft/object oriented destructive re-entry modelling using the sam code. In *7th European conference on space debris, Darmstadt*.

## Bibliography

- [Beck et al., 2021] Beck, J., Holbrough, I., Merrifield, J., and Lemmens, S. (2021). Probabilistic Comparison of Destructive Re-entry Tools. In *8th European Conference on Space Debris*, page 202.
- [Beck et al., 2018] Beck, J., Holbrough, I., Merrifield, J., and Leveque, N. (2018). *Design-for-Demise Analysis using the SAM Destructive Re-Entry Model*, pages 233–246.
- [Beck and Merrifield, 2015] Beck, J. and Merrifield, J. (2015). A heat balance integral method for destructive re-entry codes. In *8th European Symposium on Aerothermodynamics for Space Vehicles*.
- [Beck et al., 2015] Beck, J., Merrifield, J., Markelov, G., Holbrough, I., and Molina, R. (2015). Verification and application of the sam re-entry model. In Sgobba, T. and Rongier, I., editors, *Space Safety is No Accident*, pages 437–443, Cham. Springer International Publishing.
- [Bertin, 1994] Bertin, J. J. (1994). *Hypersonic Aerothermodynamics*. American Institute of Aeronautics Astronautics, Reston, VA.
- [Billig, 1967] Billig, F. S. (1967). Shock-wave shapes around spherical-and cylindrical-nosed bodies. *Journal of Spacecraft and Rockets*, 4(6):822–823.
- [Bird, 1994] Bird, G. (1994). *Molecular Gas Dynamics and the Direct Simulation of Gas Flows*. The Oxford engineering science series. Clarendon Press.
- [Blanchard, 1991] Blanchard, R. C. (1991). Rarefied-flow aerodynamics measurement experiment on the aeroassist flight experiment vehicle. *Journal of Spacecraft and Rockets*, 28(4):368–375.
- [Blay et al., 2019] Blay, V., Barrios Rivas, J. L., and Xiao, Z. (2019). Separation of air components and pollutants by the earth’s gravitational field. *Chemosphere*, 232:453–461.
- [Boison, 1959] Boison, J. C. (1959). An experimental investigation of blunt body stagnation point velocity gradient. *ARS Journal*, 29(2):130–135.

## Bibliography

- [Bonvoisin et al., 2023] Bonvoisin, B., Meisnar, M., Merrifield, J., Beck, J., Lips, T., Guelhan, A., Schleutker, T., Herdrich, G., Pagan, A., Kaschnitz, E., Liedtke, V., Helber, B., Lopes, S., Gouriet, J. B., Chazot, O., and Ghidini, T. (2023). Demisability assessment of space materials. *CEAS Space Journal*, 15(1):213–235.
- [Boyd et al., 2013] Boyd, I. D., Martin, A., Wiebenga, J. E., and Jenniskens, P. (2013). Hypersonic flow and radiation analysis of the automated transfer vehicle jules verne. *Journal of Spacecraft and Rockets*, 50(1):124–136.
- [Braun et al., 2020] Braun, V., Funke, Q., Lemmens, S., and Sanvido, S. (2020). Drama 3.0 - upgrade of esa’s debris risk assessment and mitigation analysis tool suite. *Journal of Space Safety Engineering*, 7(3):206–212. Space Debris: The State of Art.
- [Candler et al., 2007] Candler, G., Barnhardt, M., Drayna, T., Nompelis, I., Peterson, D., and Subbareddy, P. (2007). Unstructured grid approaches for accurate aeroheating simulations. In *18th AIAA Computational Fluid Dynamics Conference*.
- [Candler, 2019] Candler, G. V. (2019). Rate effects in hypersonic flows. *Annual Review of Fluid Mechanics*, 51(1):379–402.
- [Carpenter and Casper, 1999] Carpenter, M. H. and Casper, J. H. (1999). Accuracy of shock capturing in two spatial dimensions. *AIAA Journal*, 37(9):1072–1079.
- [Catalano et al., 2007] Catalano, P., Marini, M., Nicoli, A., and Pizzicaroli, A. (2007). Cfd contribution to the aerodynamic data set of the vega launcher. *Journal of Spacecraft and Rockets*, 44(1):42–51.
- [Cheng, 1961] Cheng, H. K. (1961). *Hypersonic shock-layer theory of the stagnation region at low Reynolds number*. Cornell Aeronautical Laboratory.
- [Choi et al., 2017] Choi, E.-J., Cho, S., Lee, D., Kim, S., and Jo, J. (2017). A study on re-entry predictions of uncontrolled space objects for space situational awareness. *Journal of Astronomy and Space Science*, 34:289–302.

## Bibliography

- [Cropp, 1965] Cropp, L. (1965). Analytical methods used in predicting the re-entry ablation of spherical and cylindrical bodies. Technical report, Sandia Corp., Albuquerque, N. Mex.
- [Cui et al., 2022] Cui, Z., Zhao, J., Yao, G., Zhang, J., Li, Z., Tang, Z., and Dongsheng, W. (2022). Competing effects of surface catalysis and ablation in hypersonic reentry aerothermodynamic environment. *Chinese Journal of Aeronautics*, 35(10):56–66.
- [De Persis and Lemmens, 2023] De Persis, C. and Lemmens, S. (2023). An overview of the destructive re-entry analysis tools available in europe: State of the art, latest advances, and open points. *Journal of Space Safety Engineering*.
- [Diebel et al., 2006] Diebel, J. et al. (2006). Representing attitude: Euler angles, unit quaternions, and rotation vectors. *Matrix*, 58(15-16):1–35.
- [Dobarco-Otero et al., 2005] Dobarco-Otero, J., Smith, R. N., Bledsoe, K. J., DeLaune, R. M., Rochelle, W. C., and Johnson, N. L. (2005). *The Object Reentry Survival Analysis Tool (ORSAT)*.
- [Dogra et al., 1992] Dogra, V., Moss, J., Wilmoth, R., and Price, J. (1992). Hypersonic rarefied flow past spheres including wake structure. In *30th Aerospace Sciences Meeting and Exhibit*.
- [Dongari et al., 2009] Dongari, N., Sharma, A., and Durst, F. (2009). Pressure-driven diffusive gas flows in micro-channels: from the knudsen to the continuum regimes. *Microfluidics and Nanofluidics*, 6:679–692.
- [Drob et al., 2015] Drob, D. P., Emmert, J. T., Meriwether, J. W., Makela, J. J., Doornbos, E., Conde, M., Hernandez, G., Noto, J., Zawdie, K. A., McDonald, S. E., Huba, J. D., and Klenzing, J. H. (2015). An update to the horizontal wind model (hwm): The quiet time thermosphere. *Earth and Space Science*, 2(7):301–319.
- [Dumon et al., 2022] Dumon, J., Constant, E., Spel, M., Lips, T., Kanzler, R., Pagan, A., Buntz, M., Herdrich, G., Santana, C., Sanvido, S., Lemmens, S., and Annaloro, J. (2022). Rebuild and data exploitation of the avum re-entry event for break-up

## Bibliography

- model development. In *2nd International Conference on Flight Vehicles, Aerothermodynamics and Re-entry Missions Engineering (FAR)*.
- [Economon et al., 2016] Economon, T. D., Palacios, F., Copeland, S. R., Lukaczyk, T. W., and Alonso, J. J. (2016). Su2: An open-source suite for multiphysics simulation and design. *AIAA Journal*, 54(3):828–846.
- [Edney, 1968] Edney, B. (1968). Anomalous heat transfer and pressure distributions on blunt bodies at hypersonic speeds in the presence of an impinging shock. Report 115. Flygtekniska Forsksanstalten, Stockholm: The Aeronautical Research Institute of Sweden.
- [ESA Re-entry Safety WG, 2017] ESA Re-entry Safety WG (2017). ESA re-entry safety requirements. Technical Report ESSB-ST-U-004, Issue 1, European Space Agency.
- [ESA Space Debris Mitigation WG, 2023] ESA Space Debris Mitigation WG (2023). ESA space debris mitigation requirements. Technical Report ESSB-ST-U-007, Issue 1, European Space Agency.
- [ESA Space Debris Office, 2023] ESA Space Debris Office (2023). ESA’s annual space environment report. Technical report, European Space Agency.
- [Estermann, 1955] Estermann, I. (1955). *Gases at Low Densities*. Thermodynamics and Physics of Matter, Princeton University Press.
- [Etkin, 1972] Etkin, B. (1972). *Dynamics of Atmospheric Flight*. Wiley.
- [European Space Agency, 2020] European Space Agency (2020). Dive - demise verification guidelines for analysing and testing the demise of man made space objects during re-entry.
- [Falchi, 2020] Falchi, A. (2020). *Atmospheric re-entry analysis of space objects*. PhD thesis, University of Strathclyde.

## Bibliography

- [Falchi et al., 2017] Falchi, A., Renato, V., Minisci, E., and Vasile, M. (2017). Fostrad : An advanced open source tool for re-entry analysis. In *15th Reinventing Space Conference*, GBR.
- [Fandrich and Hogue, 1995] Fandrich, M. and Hogue, C. (1995). *An Experimental Study of Rigid Body Impacts*, pages 389–396. Springer US, Boston, MA.
- [Fay and Riddell, 1958] Fay, J. and Riddell, F. R. (1958). Theory of stagnation point heat transfer in dissociated air. *Journal of the Aerospace Sciences*, 25:73–85.
- [Fritsche, 2013] Fritsche, B. (2013). Modelling the thermal decomposition of carbon fibre materials during re-entry. In *6th European Conference on Space Debris*, volume 723, page 60.
- [Fritsche et al., 2000] Fritsche, B., Klinkrad, H., Kashkovsky, A., and Grinberg, E. (2000). Spacecraft disintegration during uncontrolled atmospheric re-entry. *Acta Astronautica*, 47(2-9):513–522.
- [Furudate et al., 2006] Furudate, M., Jeung, I.-S., and Matsuyama, S. (2006). Nonequilibrium calculation of flowfield over galileo probe. In *44th AIAA Aerospace Sciences Meeting and Exhibit*.
- [Garbacz et al., 2021] Garbacz, C., Maier, W., Scoggins, J., Economon, T. D., Magin, T., Alonso, J. J., and Fossati, M. (2021). Shock interactions in inviscid air and CO<sub>2</sub>-N<sub>2</sub> flows in thermochemical non-equilibrium. *Shock Waves*.
- [Geuzaine and Remacle, 2009] Geuzaine, C. and Remacle, J.-F. (2009). Gmsh: A 3-d finite element mesh generator with built-in pre- and post-processing facilities. *International Journal for Numerical Methods in Engineering*, 79(11):1309–1331.
- [Glassner, 1989] Glassner, A. (1989). *An Introduction to Ray Tracing*. Morgan Kaufmann Series in Computer Graphics and Geometric Modeling. Elsevier Science.
- [Gnoffo, 2009] Gnoffo, P. (2009). Multi-dimensional inviscid flux reconstruction for simulation of hypersonic heating on tetrahedral grids. In *47th AIAA Aerospace Sciences Meeting including The New Horizons Forum and Aerospace Exposition*.

## Bibliography

- [Goester et al., 2021] Goester, J.-F., Bellucci, A., and FREMEAUX, C. (2021). CNES tools and methods for de-orbit and re-entry trajectories evaluation. In *9th European Conference for Aeronautics and Space Sciences (EUCASS)*.
- [Goulard, 1958] Goulard, R. (1958). On catalytic recombination rates in hypersonic stagnation heat transfer. *Journal of Jet Propulsion*, 28(11):737–745.
- [Graham et al., 2023] Graham, J., Morgado, F., and Fossati, M. (2023). Data-driven modelling of aerothermodynamic loads during atmospheric re-entry. In *AIAA AVIATION 2023 Forum*, page 4202.
- [Grossir and Dias, 2018] Grossir, G. and Dias, B. (2018). Flow characterization of the vki longshot wind tunnel. In *Flow Characterization and Modeling of Hypersonic Wind Tunnels (STO-AVT 325)*, pages 1–32, Sint-Genesius-Rode, Belgium. von Karman Institute for Fluid Dynamics, STO/NATO.
- [Grossir et al., 2020] Grossir, G., Puerto, D., Ilich, Z., Paris, S., Chazot, O., Rumeau, S., Spel, M., and Annaloro, J. (2020). Aerodynamic characterization of space debris in the vki longshot hypersonic tunnel using a free-flight measurement technique. *Experiments in Fluids*, 61.
- [Hankey, 1988] Hankey, W. L. (1988). *Re-entry aerodynamics*. American Institute of Aeronautics and Astronautics, Washington, D.C.
- [Harris et al., 2012] Harris, R., Liever, P., Luke, E., and Dudley, J. (2012). Rigid body collision modeling for multiple-body proximate flight simulation in loci/chem. In *50th AIAA Aerospace Sciences Meeting including the New Horizons Forum and Aerospace Exposition*.
- [Hayes and Probstein, 1959] Hayes, W. and Probstein, R. (1959). *Hypersonic Flow Theory*. Number vol. 1 in Applied mathematics and mechanics : an international series of monographs. Academic Press.

## Bibliography

- [Hedin, 1991] Hedin, A. E. (1991). Extension of the msis thermosphere model into the middle and lower atmosphere. *Journal of Geophysical Research: Space Physics*, 96(A2):1159–1172.
- [Hirschel, 2004] Hirschel, E. H. (2004). *Basics of Aerothermodynamics*. Springer.
- [Holbrough et al., 2021] Holbrough, I., Beck, J., Braun, V., and Lemmens, S. (2021). Madre: upgrading the re-entry risk component of esa’s drama software. In *8th European Conference on Space Debris, Online*.
- [Hurlbut, 1957] Hurlbut, F. C. (1957). Studies of Molecular Scattering at the Solid Surface. *Journal of Applied Physics*, 28(8):844–850.
- [Ilich et al., ] Ilich, Z., Grossir, G., and Chazot, O. *Evaluation of the Stagnation-Point Velocity Gradient in Low-Enthalpy Hypersonic Flows*.
- [Johnson et al., 2001] Johnson, N., Krisko, P., Liou, J.-C., and Anz-Meador, P. (2001). Nasa’s new breakup model of evolve 4.0. *Advances in Space Research*, 28(9):1377–1384.
- [Johnson, 2011] Johnson, N. L. (2011). SPACE DEBRIS MODELING AT NASA. In *3rd European Conference on Space Debris*, ESOC, Darmstadt, Germany.
- [Junfeng Zhao, 2020] Junfeng Zhao, Weiming Feng, J. Y. (2020). A novel two-level optimization strategy for multi-debris active removal mission in leo. *Computer Modeling in Engineering & Sciences*, 122(1):149–174.
- [Justus et al., 2004] Justus, C., Duvall, A., and Johnson, D. (2004). Earth global reference atmospheric model (gram-99) and trace constituents. *Advances in Space Research*, 34(8):1731–1735. Planetary Ionospheres and Atmospheres Including CIRA.
- [Justus and Johnson, 1999] Justus, C. and Johnson, D. (1999). The nasa/msfc global reference atmospheric model: 1999 version (gram-99).
- [Kanzler et al., 2021] Kanzler, R., Fritsche, B., Lips, T., Breslau, A., Pagan, A., Herdrich, G., Spel, M., Sanvido, S., and Lemmens, S. (2021). Scarab4—extension of the

## Bibliography

- high-fidelity re-entry break-up simulation software based on new measurement types. In *8th European Conference on Space Debris*. ESA Space Debris Office Darmstadt, Germany.
- [Kanzler et al., 2017] Kanzler, R., Lips, T., Fritsche, B., Bonetti, D., Pontijas Fuentes, I., Letterio, F., Vicario de Miguel, G., Blanco Arnao, G., Palomo, P., Parigini, C., Bunte, K.-D., Miller, A., Garms, C., Kebschull, C., and Lemmens, S. (2017). Upgrade of drama’s spacecraft entry survival analysis codes. In *7th European Conference on Space Debris*, page 236.
- [Karl et al., 2003] Karl, S., Schramm, J. M., and Hannemann, K. (2003). High enthalpy cylinder flow in heg: A basis for cfd validation. In *33rd AIAA Fluid Dynamics Conference and Exhibit*, page 4252.
- [Kato, 2001] Kato, A. (2001). Comparison of national space debris mitigation standards. *Advances in Space Research*, 28(9):1447–1456.
- [Kemp and Riddell, 1957] Kemp, N. H. and Riddell, F. R. (1957). Heat transfer to satellite vehicles re-entering the atmosphere. *Journal of Jet Propulsion*.
- [Kennard, 1938] Kennard, E. H. (1938). *Kinetic theory of gases : with an introduction to statistical mechanics*. McGraw-Hill Book.
- [Kim et al., 2001] Kim, K. H., Kim, C., and Rho, O.-H. (2001). Methods for the accurate computations of hypersonic flows: I. ausmpw+scheme. *Journal of Computational Physics*, 174(1):38–80.
- [Klett, 1964] Klett, R. D. (1964). Drag coefficients and heating ratios for right circular cylinders in free- molecular and continuum flow from mach 10 to 30. Technical report, United States.
- [Knight et al., 2012] Knight, D., Longo, J., Drikakis, D., Gaitonde, D., Lani, A., Nompelis, I., Reimann, B., and Walpot, L. (2012). Assessment of cfd capability for prediction of hypersonic shock interactions. *Progress in Aerospace Sciences*, 48-49:8–26. Assessment of Aerothermodynamic Flight Prediction Tools.

## Bibliography

- [Koppenwallner et al., 2005] Koppenwallner, G., Fritsche, B., Lips, T., and Klinkrad, H. (2005). Scarab -a Multi-Disciplinary Code for Destruction Analysis of Space-Craft during Re-Entry. In Danesy, D., editor, *Fifth European Symposium on Aerothermodynamics for Space Vehicles*, volume 563 of *ESA Special Publication*, page 281.
- [Koppenwallner<sup>1</sup> et al., 2005] Koppenwallner<sup>1</sup>, G., Fritsche<sup>1</sup>, B., Lips<sup>1</sup>, T., Martin<sup>2</sup>, T., Francillout<sup>2</sup>, L., and Pasquale<sup>3</sup>, E. D. (2005). Analysis of ATV Destructive Re-Entry including Explosion Events. In *Proceedings of the Fourth European Conference on Space Debris*, Darmstadt, Germany. <sup>1</sup>HTG - Hypersonic Technology Göttingen, Katlenburg-Lindau, Germany, <sup>2</sup>CNES, Toulouse, France, <sup>3</sup>ESA-CST, ATV Flight Dynamics and Mission Analysis, Toulouse, France.
- [Kovács et al., 2022] Kovács, D. G., Grossir, G., and Chazot, O. (2022). Hypersonic aerodynamics of a free-flying ring interfering with a two-dimensional curved shock wave - an experimental test case. In *2<sup>nd</sup> International Conference on Flight Vehicles, Aerothermodynamics and Re-entry Mission Engineering (FAR2022)*, pages 1–17, Heilbronn, Germany.
- [Kovács et al., 2023] Kovács, D. G., Grossir, G., Dimitriadis, G., and Chazot, O. (2023). Space debris interaction across a two-dimensional oblique shock wave. *Experiments in Fluids*, 64(8).
- [Laurence et al., 2007] Laurence, S., Deiterding, R., and Hornung, H. (2007). Proximal bodies in hypersonic flow. *Journal of Fluid Mechanics*, 590:209 – 237.
- [Laurence and Deiterding, 2011] Laurence, S. J. and Deiterding, R. (2011). Shock-wave surfing. *Journal of Fluid Mechanics*, 676:396–431.
- [Laurence et al., 2012] Laurence, S. J., Parziale, N. J., and Deiterding, R. (2012). Dynamical separation of spherical bodies in supersonic flow. *Journal of Fluid Mechanics*, 713:159–182.
- [Ledermann et al., 2022] Ledermann, V., Midani, I., Constant, E., Spel, M., Stainier, L., Annarolo, J., Galera, S., Boivin, P., Favier, J., and Henneton, M. (2022). Blizzard

## Bibliography

- rebuilding of the interaction between a fixed cylinder and a free flying ring. In *2<sup>nd</sup> International Conference on Flight Vehicles, Aerothermodynamics and Re-entry Mission Engineering (FAR2022)*, Heilbronn, Germany.
- [Lees, 1955] Lees, L. (1955). Hypersonic flow. *Journal of Spacecraft and Rockets*, 40(5):700–735.
- [Lees, 1956] Lees, L. (1956). Laminar heat transfer over blunt-nosed bodies at hypersonic flight speeds. *Journal of Jet Propulsion*, 26(4):259–269.
- [Legge, 1987] Legge, H. (1987). Hypersonic approximations for heat transfer and shear stress applied to continuum and rarefied plume impingement. *DFVLR-ib*, 222.
- [Liou et al., 2020] Liou, J., Kieffer, M., Drew, A., and Sweet, A. (2020). The 2019 u.s. government orbital debris mitigation standard practices. *Orbital Debris Quarterly News*, 24(1):4–8.
- [Liou et al., 2021] Liou, J.-C., Opiela, J., Vavrin, A., Draeger, B., Anz-Meador, P., and Ostrom, C. (2021). Debris assessment software user’s guide. Technical report.
- [Liou, 2006] Liou, M.-S. (2006). A sequel to ausm, part ii: Ausm+-up for all speeds. *Journal of Computational Physics*, 214(1):137–170.
- [Lips and Fritsche, 2005] Lips, T. and Fritsche, B. (2005). A comparison of commonly used re-entry analysis tools. *Acta Astronautica*, 57(2):312–323. Infinite Possibilities Global Realities, Selected Proceedings of the 55th International Astronautical Federation Congress, Vancouver, Canada, 4-8 October 2004.
- [Lips et al., 2007] Lips, T., Fritsche, B., Homeister, M., Koppenwallner, G., Klinkrad, H., and Toussaint, M. (2007). Re-entry risk assessment for launchers—development of the new scarab 3.1 l. In *Proceedings of the Second IAASS Conference, SP-645, ESA Communication Production Office, ESTEC, Noordwijk, The Netherlands*.
- [Lips et al., 2017] Lips, T., Fritsche, B., Kanzler, R., Schleutker, T., Gülhan, A., Bonvoisin, B., Soares, T., and Sinnema, G. (2017). About the demisability of propellant

## Bibliography

- tanks during atmospheric re-entry from leo. *Journal of Space Safety Engineering*, 4(2):99–104.
- [Lips et al., 2004] Lips, T., Fritsche, B., Koppenwallner, G., and Klinkrad, H. (2004). Spacecraft destruction during re-entry – latest results and development of the scarab software system. *Advances in Space Research*, 34(5):1055–1060. Space Debris.
- [Lohle et al., 2011] Lohle, S., Marynowski, T., Knapp, A., Wernitz, R., and Lips, T. (2011). Analysis of the atv1 re-entry using near-uv spectroscopic data from the esa/nasa multi-instrument aircraft observation campaign. In *7th European Symposium on Aerothermodynamics*, volume 692, page 133.
- [Loseille, 2017] Loseille, A. (2017). Unstructured mesh generation and adaptation. In Abgrall, R. and Shu, C.-W., editors, *Handbook of Numerical Methods for Hyperbolic Problems - Applied and Modern Issues*, pages 263–302. Elsevier.
- [Loseille and Loehner, 2011] Loseille, A. and Loehner, R. (2011). Boundary layer mesh generation and adaptivity.
- [Loseille and Menier, 2014] Loseille, A. and Menier, V. (2014). Serial and parallel mesh modification through a unique cavity-based primitive. In Sarrate, J. and Staten, M., editors, *Proceedings of the 22nd International Meshing Roundtable*, pages 541–558, Cham. Springer International Publishing.
- [Loseille et al., 2015] Loseille, A., Menier, V., and Alauzet, F. (2015). Parallel generation of large-size adapted meshes. *Procedia Engineering*, 124:57 – 69. 24th International Meshing Roundtable.
- [Maier et al., 2023] Maier, W., Needels, J. T., Alonso, J. J., Morgado, F., Garbacz, C., Fossati, M., Tumuklu, O., and Hanquist, K. M. (2023). *Development of Physical and Numerical Nonequilibrium Modeling Capabilities within the SU2-NEMO Code*.
- [Maier et al., 2021] Maier, W. T., Needels, J. T., Garbacz, C., Morgado, F., Alonso, J. J., and Fossati, M. (2021). SU2-NEMO: An Open-Source Frame-

## Bibliography

- work for High-Mach Nonequilibrium Multi-Species Flows. *Aerospace*, 8(7). 10.3390/aerospace8070193.
- [Martin et al., 2012] Martin, A., Scalabrin, L. C., and Boyd, I. D. (2012). High performance modeling of atmospheric re-entry vehicles. *Journal of Physics: Conference Series*, 341(1).
- [Marwege et al., 2018] Marwege, A., Willems, S., Gülhan, A., Aftosmis, M. J., and Stern, E. C. (2018). Superposition method for force estimations on bodies in supersonic and hypersonic flows. *Journal of Spacecraft and Rockets*, 55(5):1166–1180.
- [Max, 1999] Max, N. (1999). Weights for computing vertex normals from facet normals. *Journal of Graphics Tools*, 4(2):1–6.
- [Maxwell, 2011] Maxwell, J. C. (2011). *The Scientific Papers of James Clerk Maxwell*, volume 2 of *Cambridge Library Collection - Physical Sciences*. Cambridge University Press.
- [Meakin, 2003] Meakin, R. (2003). A general simulation method for multiple bodies in proximate flight. In *16th AIAA Computational Fluid Dynamics Conference*.
- [Mehta et al., 2015] Mehta, P., Minisci, E., Vasile, M., Walker, A. C., and Brown, M. (2015). An open source hypersonic aerodynamic and aerothermodynamic modelling tool. In *8th European Symposium on Aerothermodynamics for Space Vehicles*, PRT.
- [Mehta et al., 2016] Mehta, P. M., Arnao, G. B., Bonetti, D., Minisci, E. A., and Vasile, M. (2016). Computer graphics for space debris. In *6th International Conference on Astrodynamics Tools and Techniques*, Darmstadt, Germany.
- [Mehta et al., ] Mehta, P. M., Walker, A., Brown, M., Minisci, E., and Vasile, M. L. *Sensitivity Analysis towards Probabilistic Re-Entry Modeling of Spacecraft and Space Debris*.
- [Merrifield et al., 2015] Merrifield, J., Beck, J., Markelov, G., Leyland, P., and Molina, R. (2015). Aerothermal heating methodology in the spacecraft aerothermal model

## Bibliography

- (sam). In Sgobba, T. and Rongier, I., editors, *Space Safety is No Accident*, pages 463–468, Cham. Springer International Publishing.
- [Meyer et al., 2003] Meyer, M., Desbrun, M., Schröder, P., and Barr, A. H. (2003). Discrete differential-geometry operators for triangulated 2-manifolds. In Hege, H.-C. and Polthier, K., editors, *Visualization and Mathematics III*, pages 35–57, Berlin, Heidelberg. Springer Berlin Heidelberg.
- [Millikan, 1923] Millikan, R. A. (1923). Coefficients of slip in gases and the law of reflection of molecules from the surfaces of solids and liquids. *Phys. Rev.*, 21:217–238.
- [Moe et al., 1993] Moe, M. M., Wallace, S. D., and Moe, K. (1993). Refinements in determining satellite drag coefficients - method for resolving density discrepancies. *Journal of Guidance, Control, and Dynamics*, 16(3):441–445.
- [Morgado et al., 2023] Morgado, F., Fossati, M., Kóvacs, D., and Magin, T. (2023). Rebuilding the vki’s experiment on the interference of a free-flying ring and stationary cylinder using a multi-fidelity numerical methodology. In *AIAA SCITECH 2023 Forum*, page 1386.
- [Morgado et al., 2024a] Morgado, F., G. Kovács, D., and Fossati, M. (2024a). Modeling the interaction of proximal fragments for destructive atmospheric entry analysis. *AIAA Journal*. Accepted for publication.
- [Morgado et al., 2022a] Morgado, F., Garbacz, C., and Fossati, M. (2022a). Impact of anisotropic mesh adaptation on the aerothermodynamics of atmospheric reentry. *AIAA Journal*, 60(7):3973–3989.
- [Morgado et al., 2022b] Morgado, F., Peddakotla, S. A., Garbacz, C., Vasile, M., and Fossati, M. (2022b). Fidelity management of aerothermodynamic modelling for destructive re-entry. In *The 2nd International Conference on Flight Vehicles, Aerothermodynamics and Re-entry Missions Engineering (FAR)*. European Space Agency, DEU.

## Bibliography

- [Morgado et al., 2022c] Morgado, F., Peddakotla, S. A., Garbacz, C., Vasile, M. L., and Fossati, M. (2022c). Multi-fidelity approach for aerodynamic modelling and simulation of uncontrolled atmospheric destructive entry. In *AIAA SCITECH 2022 Forum*, page 1323.
- [Morgado et al., 2024b] Morgado, F., Peddakotla, S. A., Graham, J., Vasile, M., and Fossati, M. (2024b). A multi-fidelity framework for aerothermodynamic modelling and simulation of destructive atmospheric entry. *AIAA Journal*. Accepted for publication.
- [Moss et al., 2006] Moss, J., Boyles, K., and Greene, F. (2006). Orion aerodynamics for hypersonic free molecular to continuum conditions. In *14th AIAA/AHI Space Planes and Hypersonic Systems and Technologies Conference*.
- [Munafo, 2014] Munafo, A. (2014). *Multi-scale models and computational methods for aerothermodynamics*. PhD thesis, Châtenay-Malabry, Ecole centrale de Paris.
- [niu Wu et al., 2011] niu Wu, Z., Hu, R., ru Qu, X., Wang, X., and Wu, Z. (2011). Space debris reentry analysis methods and tools. *Chinese Journal of Aeronautics*, 24:387–395.
- [Nompelis et al., ] Nompelis, I., Drayna, T., and Candler, G. Development of a hybrid unstructured implicit solver for the simulation of reacting flows over complex geometries. In *34th AIAA Fluid Dynamics Conference and Exhibit*.
- [O’Connor, 2008] O’Connor, B. (2008). Handbook for limiting orbital debris, technical report nasa handbook 8719.14. Technical report, National Aeronautics and Space Administration.
- [Olivier, 1993] Olivier, H. (1993). An improved method to determine free stream conditions in hypersonic facilities. *Shock Waves*, 3(2):129–139.
- [Olivier, 1995] Olivier, H. (1995). Influence of the velocity gradient on the stagnation point heating in hypersonic flow. *Shock Waves*, 5(4):205–216.

## Bibliography

- [Omaly and Spel, 2012] Omaly, P. and Spel, M. (2012). DEBRISK, a Tool for Re-Entry Risk Analysis. In Ouwehand, L., editor, *A Safer Space for Safer World*, volume 699 of *ESA Special Publication*, page 70.
- [Opiela and Johnson, 2007] Opiela, J. N. and Johnson, N. L. (2007). Improvements to nasa’s debris assessment software.
- [Ostrom et al., 2019] Ostrom, C. L., Greene, B. R., Smith, A. N., Toledo-Burdett, R. C., Matney, M. J., Opiela, J. N., Marichalar, J. J., Bacon, J. B., and Sanchez, C. M. (2019). Operational and Technical Updates to the Object Reentry Survival Analysis Tool. In *First International Orbital Debris Conference*, volume 2109 of *LPI Contributions*, page 6018.
- [Palacios et al., 2013] Palacios, F., Copeland, S., Lonkar, A., and Alonso, J. (2013). Adjoint-based goal-oriented mesh adaptation for nonequilibrium hypersonic flows. *51st AIAA Aerospace Sciences Meeting including the New Horizons Forum and Aerospace Exposition, Grapevine, TX. AIAA Paper 2013-0552*.
- [Pardini and Anselmo, 2013] Pardini, C. and Anselmo, L. (2013). Re-entry predictions for uncontrolled satellites: results and challenges. Citeseer.
- [Pardini and Anselmo, 2019] Pardini, C. and Anselmo, L. (2019). Uncontrolled re-entries of spacecraft and rocket bodies: A statistical overview over the last decade. *Journal of Space Safety Engineering*, 6(1):30–47.
- [Park, 1993] Park, C. (1993). Review of chemical-kinetic problems of future NASA missions. I - earth entries. *Journal of Thermophysics and Heat Transfer*, 7(3):385–398.
- [Park et al., 2021] Park, S.-H., Navarro Laboulais, J., Leyland, P., and Mischler, S. (2021). Re-entry survival analysis and ground risk assessment of space debris considering by-products generation. *Acta Astronautica*, 179:604–618.
- [Passey and Melosh, 1980] Passey, Q. R. and Melosh, H. (1980). Effects of atmospheric breakup on crater field formation. *Icarus*, 42(2):211–233.

## Bibliography

- [Paulat and Boukhobza, 2007] Paulat, J. and Boukhobza, P. (2007). Re-entry flight experiments lessons learned - the atmospheric reentry demonstrator ard. *Flight Experiments for Hypersonic Vehicle Development*.
- [Peddakotla et al., 2022a] Peddakotla, S. A., Morgado, F., Thillaithevan, D., O’Driscoll, D., Santer, M., Maddock, C., Vasile, M., and Fossati, M. (2022a). Multi-fidelity and multi-disciplinary approach for the accurate simulation of atmospheric re-entry. In *73rd International Astronautical Congress 2022*.
- [Peddakotla et al., 2022b] Peddakotla, S. A., Morgado, F., Thillaithevan, D., O’Driscoll, D., Santer, M., Maddock, C., Vasile, M., and Fossati, M. (2022b). Multi-fidelity and multi-disciplinary approach for the accurate simulation of atmospheric re-entry. In *73rd International Astronautical Congress 2022*, FRA.
- [Picone et al., 2002] Picone, J. M., Hedin, A. E., Drob, D. P., and Aikin, A. C. (2002). NRLMsise-00 empirical model of the atmosphere: Statistical comparisons and scientific issues. *Journal of Geophysical Research: Space Physics*, 107(A12):SIA 15–1–SIA 15–16.
- [Pomelli and Tomasi, 1998] Pomelli, C. S. and Tomasi, J. (1998). Variation of surface partition in gepol: effects on solvation free energy and free-energy profiles. *Theoretical Chemistry Accounts*, 99(1):34–43.
- [Pontijas Fuentes et al., 2019] Pontijas Fuentes, I., Bonetti, D., Letterio, F., Vicario de Miguel, G., Blanco Arnao, G., Palomo, P., Parigini, C., Lemmens, S., Lips, T., and Kanzler, R. (2019). Upgrade of esa’s debris risk assessment and mitigation analysis (drama) tool: Spacecraft entry survival analysis module. *Acta Astronautica*, 158:148–160.
- [Popov, 2010] Popov, V. L. (2010). *Coulomb’s Law of Friction*, pages 133–154. Springer Berlin Heidelberg, Berlin, Heidelberg.
- [Prevereaud et al., 2019] Prevereaud, Y., Vérant, J.-L., and Annaloro, J. (2019). Non-catalytic and Finite Catalytic Heating Models for Atmospheric Re-entry Codes. In *First International Orbital Debris Conference (IOC)*, SUGAR LAND, United States.

## Bibliography

- [Prevereaud et al., 2013] Prevereaud, Y., Vérant, J.-L., Moschetta, J.-M., and Sourgen, F. (2013). Debris aerodynamic interaction and its effect on re-entry risk assessment.
- [Prigent et al., 2017] Prigent, G., Carro, J., Crusson, B., and Stainier, L. (2017). A first step toward fragmentation process assessment of re-entering spacecraft: mechanical stress analysis with the spacecraft oriented simulation tool PAMPERO. In *9th IAASS Conference*, Toulouse, France.
- [Rader et al., 2005] Rader, D. J., Castaneda, J. N., Torczynski, J. R., Grasser, T. W., and Trott, W. M. (2005). Measurements of thermal accommodation coefficients. Technical report, Sandia National Laboratories.
- [Rao, 1973] Rao, P. P. (1973). Supersonic Flow Around Concave and Convex Blunt Bodies. *Journal of Fluids Engineering*, 95(1):159–161.
- [Register et al., 2020] Register, P., Aftosmis, M., Stern, E., Brock, J., Seltner, P., Willems, S., Guelhan, A., and Mathias, D. (2020). Interactions between asteroid fragments during atmospheric entry. *Icarus*, 337:113468.
- [Rembaut et al., 2020] Rembaut, N., Jousset, R., and Lago, V. (2020). Aerodynamical behavior of spherical debris in the supersonic and rarefied wind tunnel marhy. *Journal of Space Safety Engineering*, 7(3):411–419.
- [Rochelle et al., 1997] Rochelle, W. C., Kinsey, R. E., Reid, E. A., Reynolds, R. C., and Johnson, N. L. (1997). Spacecraft orbital debris reentry: Aerothermal analysis. In *Proceedings of the Eighth Annual Thermal and Fluids Analysis Workshop: Spacecraft Analysis and Design*.
- [Routh, 1891] Routh, E. (1891). *Elementary Rigid Dynamics*. Number v. 1 in Elementary Rigid Dynamics.
- [Rusinkiewicz, 2004] Rusinkiewicz, S. (2004). Estimating curvatures and their derivatives on triangle meshes. In *Proceedings. 2nd International Symposium on 3D Data Processing, Visualization and Transmission, 2004. 3DPVT 2004.*, pages 486–493.

## Bibliography

- [Sagnier and Verant, 1998] Sagnier, P. and Verant, J.-L. (1998). Flow characterization in the onera f4 high-enthalpy wind tunnel. *AIAA Journal*, 36(4):522–531.
- [Schaaf, 1953] Schaaf, S. A. (1953). Theoretical considerations in rarefied-gas dynamics. In *Heat Transfer Symposium*, pages 237–260.
- [Schaaf and Chambre, 1958] Schaaf, S. A. and Chambre, P. L. (1958). *Flow of Rarefied Gases*. Princeton University Press.
- [Scoggins and Magin, 2014] Scoggins, J. and Magin, T. (2014). Development of mutation++: Multicomponent thermodynamic and transport properties for ionized plasmas written in c++. volume 12.
- [Scott, 1973] Scott, C. D. (1973). Wall boundary equations with slip and catalysis for multicomponent, nonequilibrium gas flows. Technical report.
- [Sebastian Willems, 2018] Sebastian Willems, Patrick Seltner, A. G. (2018). Shock-shock interaction test case. *ESA ATD3 Workshop*.
- [Sedov, 1959] Sedov, L. (1959). In SEDOV, L., editor, *Similarity and Dimensional Methods in Mechanics*. Academic Press.
- [sheng Chen et al., 2020] sheng Chen, S., jie Cai, F., chao Xue, H., Wang, N., and Yan, C. (2020). An improved ausm-family scheme with robustness and accuracy for all mach number flows. *Applied Mathematical Modelling*, 77:1065–1081.
- [sheng Chen et al., 2018] sheng Chen, S., Yan, C., xi Lin, B., yuan Liu, L., and Yu, J. (2018). Affordable shock-stable item for godunov-type schemes against carbuncle phenomenon. *Journal of Computational Physics*, 373:662–672.
- [Sibulkin, 1952] Sibulkin, M. (1952). Heat transfer near the forward stagnation point of a body revolution. *Journal of the aeronautical sciences*, 9:570–571.
- [Sippl and Scheraga, 1986] Sippl, M. J. and Scheraga, H. A. (1986). Cayley-Menger coordinates. *Proc. Natl. Acad. Sci. U. S. A.*, 83(8):2283–2287.

## Bibliography

- [Sourgen et al., 2015] Sourgen, F., Prévereaud, Y., l. Verant, J., Laroche, E., and Moschetta, J.-M. (2015). Music/fast, a pre-design and pre-mission analysis tool for the earth atmospheric re-entry of spacecraft, capsules and de-orbited satellites. In *Proceedings of 8th European Symposium on Aerothermodynamics for Space Vehicles, 2 March 2015 - 6 March*.
- [Spel et al., 2021] Spel, M., Dumon, J., Constant, E., Van Hauwaert, P., Galera, S., and Annaloro, J. (2021). Demisability study of industrial test cases with the spacecraft-oriented code pampero. In *8th European Conference on Space Debris*, Darmstadt, Germany.
- [Summers et al., 2015] Summers, P. T., Chen, Y., Rippe, C. M., Allen, B., Mouritz, A. P., Case, S. W., and Lattimer, B. Y. (2015). Overview of aluminum alloy mechanical properties during and after fires. *Fire Science Reviews*, 4(1):1–36.
- [Sutton et al., 1971] Sutton, K., Graves, R., Aeronautics, U. S. N., Administration, S., and Center, L. R. (1971). *A General Stagnation-point Convective-heating Equation for Arbitrary Gas Mixtures*. NASA technical report. National Aeronautics and Space Administration.
- [Tauber and Sutton, 1991] Tauber, M. E. and Sutton, K. (1991). Stagnation-point radiative heating relations for earth and mars entries. *Journal of Spacecraft and Rockets*, 28(1):40–42.
- [Tonon, 2005] Tonon, F. (2005). Explicit exact formulas for the 3-d tetrahedron inertia tensor in terms of its vertex coordinates. *Journal of Mathematics and Statistics*, 1:8–11.
- [Truitt, 1960] Truitt, R. (1960). *Fundamentals of Aerodynamic Heating*. Ronald Press Company.
- [United States National Oceanic and Atmospheric Administration and United States Committee on United States National Oceanic and Atmospheric Administration and United States Committee on Extension to the Standard Atmosphere (1976). *U.S. Standard*

## Bibliography

- Atmosphere, 1976*. NOAA - SIT 76-1562. National Oceanic and Atmospheric [sic] Administration.
- [Vallet et al., 2007] Vallet, M.-G., Manole, C.-M., Dompierre, J., Dufour, S., and Guibault, F. (2007). Numerical comparison of some hessian recovery techniques. *International Journal for Numerical Methods in Engineering*, 72(8):987–1007.
- [van Driest, 1956] van Driest, E. R. (1956). The problem of aerodynamic heating. *Aeronautical Engineering Review*, 15, 10:26–41.
- [van Driest, 1958] van Driest, E. R. (1958). On the aerodynamic heating of blunt bodies. *Zeitschrift für angewandte Mathematik und Physik ZAMP*, 9(5):233–248.
- [Van Hauwaert et al., 2022] Van Hauwaert, P., Constant, E., Midani, I., Spel, M., Makowski, P., Ledermann, V., Dumon, J., Galera, S., and Annaloro, J. (2022). Pampero v3, a spacecraft-oriented reentry analysis code.
- [Virgili et al., 2017] Virgili, B. B., Lemmens, S., Siminski, J., and Funke, Q. (2017). Practicalities of re-entry predictions—the vega-01 avum case. In *7th European Conference on Space Debris*.
- [Walpot, 2002] Walpot, L. (2002). *Development and application of a hypersonic flow solver (PhD Thesis)*. PhD thesis, Delft University of Technology.
- [White and Hoffman, 2023] White, P. and Hoffman, J. (2023). Earth global reference atmospheric model (earth-gram): User guide. Technical report.
- [Whittaker and McCrae, 1988] Whittaker, E. T. and McCrae, S. W. (1988). *A Treatise on the Analytical Dynamics of Particles and Rigid Bodies*. Cambridge Mathematical Library. Cambridge University Press.
- [Wiedmann and Trumpler, 2022] Wiedmann, M. L. and Trumpler, P. R. (2022). Thermal Accommodation Coefficients. *Transactions of the American Society of Mechanical Engineers*, 68(1):57–64.

## Bibliography

- [Wu et al., 2013] Wu, Z., Xu, Y., Wang, W., and Hu, R. (2013). Review of shock wave detection method in cfd post-processing. *Chinese Journal of Aeronautics*, 26(3):501–513.
- [Yamamoto et al., 1999] Yamamoto, S., Takasu, N., and Nagatomo, H. (1999). Numerical investigation of shock/vortex interaction in hypersonic thermochemical nonequilibrium flow. *Journal of Spacecraft and Rockets*, 36(2):240–246.
- [Zhang, 1998] Zhang, H. (1998). Effective occlusion culling for the interactive display of arbitrary models.